Advances in Theoretical Description of Molecules and their Environment: Density Functional Theory and Continuum Solvation Models

Dissertation
zur
Erlangung der naturwissenschaftlichen Doktorwürde
(Dr. sc. Nat.)

vorgelegt der
Mathematisch-naturwissenschaftlichen Fakultät
der
Universität Zürich
von
Roberto Peverati
aus Italien

Promotionskomitee:
Prof. Dr. Kim K. Baldridge (Vorsitz)
Prof. Dr. Jay S. Siegel
Prof. Dr. Jürg Hutter

Zürich, 2010

Abstract of the Dissertation

Advances in Theoretical Description of Molecules and their Environment: Density Functional Theory and Continuum Solvation Models

by

Roberto Peverati

Doctor of Philosophy in Chemistry

University of Zurich, 2010

Prof. Dr. Kim K. Baldridge (Chair)

Computational chemistry is a branch of chemistry that brings together theoretical chemistry techniques and computer science to enable solving of chemical problems on computers. With such techniques, one can make accurate predictions on aspects of structure and properties of a reaction process, and thereby provide an important supplement to experimental chemistry with added detail or predicting yet unknown chemical outcomes. This thesis work involves both the development and the application of new quantum chemical based computational methodology for prediction of chemical phenomenon. In particular, new theoretical methods are developed that enable greater accuracy in results associated with weakly interacting molecular systems, which can be found in many of today's chemical and biochemical applications. Additionally, since a large portion of chemical processes occur in condensed media, the ability to include such effects into the theoretical methodology is very important for accurate prediction. This work also includes enhancement of methodologies that accommodate the solvent environment to enable study of condensed phase phenomenon in conjunction with experiment. The newly developed methods are exemplified on several important chemical problems in active research.

Zusammenfassung

Advances in Theoretical Description of Molecules and their Environment: Density Functional Theory and Continuum Solvation Models

von

Roberto Peverati

Dr. sc. Nat.

Universität Zurich, 2010

Prof. Dr. Kim K. Baldridge (Vorsitz)

Computional Chemie ist ein Zweig der Chemie, welcher theoretische Chemie und Computerwissenschaften vereint, und damit die Lösung chemischer Probleme am Computer ermöglicht. Mit dieser Technik können präzise Vorhersagen über Struktur und Eigenschaften von Reaktionsmechanismen gewonnen werden, und damit der experimentellen Chemie zusätzliche Details und Vorhersagen über noch unbekannte chemische Ereignisse liefern. Diese Arbeit beinhaltet die Entwicklung und Anwendung einer neuartigen, auf Quantenchemie gestützen Methode zur Vorhersage chemischer Phänomene. Die entwickelten Methoden erlauben präzise Vorhersagen über schwach interagierende molekulare Systeme, welche häufig in chemischen und biochemischen Anwendungen auftreten. Da ein Grossteil dieser chemischen Prozesse in einem verdichteten Medium ablaufen, ist die Miteinbeziehung solcher Effekte für eine präzise Vorhersage von grosser Wichtigkeit. Diese Arbeit beinhaltet auch Erweiterungen von Methoden welche die flüssige Umgebung erfassen, um Studien von Phänomenen in verdichteter Phase in Verbindung mit dem Experiment zu ermöglichen. Die entwickelten Methoden werden an einigen wichtigen Problemen der chemischen Forschung erläutert.

Contents

Chapter 1

Introduction

Overview

1.1 Outcome

The work of this thesis involved the optimization, implementation, and application of several accurate *ab initio* models for calculation of molecular systems, including effects of condensed phase environment. The methods for molecular energies and properties, described in chapter 2, belong to the framework of Density Functional Theory (DFT). Particular emphasis was on the development of methodology for modeling of dispersion interactions. The treatment of environment effects developed in this work belongs to the class of Continuum Solvation Methods (CSMs), and is described in chapter 3. The particular solvation method presented in this work, COSab, was developed in this group and has in the past been used successfully on small organic molecules to predict free energy of solvation in agreement with available experimental data. With the efforts described in this thesis, the algorithm can now be used within the General Atomic Molecular Electronic Structure Systems (GAMESS)[1], on molecules of arbitrary size, with the default solvation cavity able to manage about 200 atoms (arbitrary extension can be easily obtained by simple increasing of the memory demand in the GAMESS source code). The COSab method was also optimized together with the semiempirically corrected DFT-D, enabling application to molecular systems that are complicated by treatment of dispersion interactions in condensed phase environment.

1.2 Background

Computational chemistry is a branch of chemistry that brings together theoretical chemistry techniques and computer science to enable solving of chemical problems on computers. With such techniques, one can make accurate predictions on aspects of structure and properties of a reaction process, and thereby provide an important supplement

to experimental chemistry with added detail or predicting yet unknown chemical outcomes. This thesis work involves both the development and the application of new quantum chemical based computational methodology for prediction of chemical phenomenon. In particular, new theoretical methods are developed that enable greater accuracy in results associated with weakly interacting molecular systems, which can be found in many of today's chemical and biochemical applications. Additionally, since a large portion of chemical processes occur in condensed media, the ability to include such effects into the theoretical methodology is very important for accurate prediction. This work also includes enhancement of methodologies that accommodate the solvent environment to enable study of condensed phase phenomenon in conjunction with experiment. It is very important in the development of any theory to establish accuracy and reliability through application to real-world chemical or biochemical problems of general interest. As such, the newly developed methods are exemplified on several important chemical problems in active research, and compared with experiment where possible.

A large community of theoretical and computational chemists is nowadays active in the vast majority of chemical fields. It is very rare that a modern research paper is published, without a theoretical contribution to explain, or justify, the experimental discoveries. The importance of reliable and accurate computer softwares, and their development, is emerging as a very fundamental, and productive research topic in recent years, particularly after the Nobel Prize awarded to John Pople and Walter Kohn for computational chemistry in 1998[2,3]. It is in this framework that the present thesis work attempts to provide a contribution to the refinement of new theories and the development of computer softwares.

1.3 Project summary and motivation

Considerable efforts have been gone into theoretical chemistry techniques for accurate description of molecules and their environment. Despite the enormous growth of computer speed, the most accurate theoretical methods remain unaffordable for molecules of interests in organic and bio-organic chemistry. Molecular environment, such as solvent, and properties with high-level ab initio methods, are among capabilities even of large supercomputers. The need of computational affordable, but still accurate methods and algorithms, is still a challenge in the recent research in quantum chemistry.

The rigorous approach of wavefunction theory has been supported by the development of affordable algorithms, convenient approximations, and accurate semi-empirical approaches, for calculations with arbitrary accuracy of molecular properties in the environment. The accurate framework of density functional theory (DFT) represent a very nice synthesis of these concepts, with a strong theoretical background, several convenient approximations, and many parametrized functionals used in practical calculations and simulations. The same situation happens for the description of environmental effects, where continuum solvation models (CSM) represent a convenient approach to a complex problem.

Aim of this work is to improve the implementation of both DFT and CSM, within one of the most used quantum chemistry software package: GAMESS. The application of

the newly implemented algorithms to interesting research topic have been conducted, and will be also presented. Each of the next two chapter of this thesis present a major topic of this work, and is divided into three components. In the first part of the chapter, the theory is presented, in the second part, the algorithms and their implementation are described in depth, and in the third part, a specific application is reported in order to briefly illustrate the main concepts of the theoretical developments. Further applications are illustrative of the methodology, as laid out in chapter 4. Conclusions are preented at the end of each chapter, and the full thesis is summarized, together with future work perspectives, in chapter 5 All the program routines coded during this thesis work are explained and entirely reported in the electronic information, included in the thesis CD.

Chapter 2

Density Functional Theory

Overview

2.1 A (very) short history of DFT:

The history of DFT started in 1927: Llewellyn Hilleth Thomas in Cambridge and Enrico Fermi in Rome, working separately, developed a new statistical model to approximate the distribution of electrons in an atom. Following their idea of representing the energy of atoms as a functional of the electron density, Paul Adrien M. Dirac, Carl Friedrich

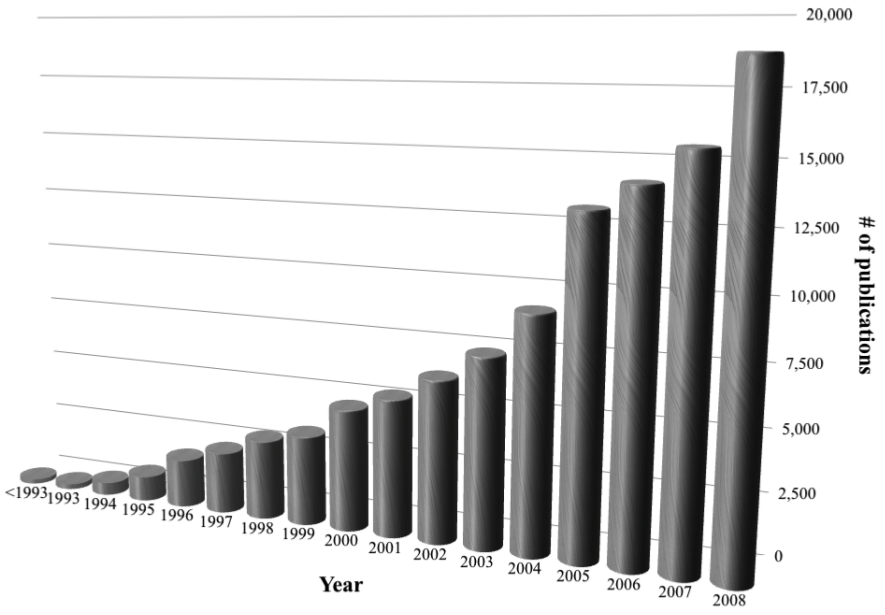

Figure 2.1: Number of articles containing the keyword "DFT" or "density functional theory" (data obtained from ISI Web of Knowledge).

Freiherr von Weizsäcker as first, and Walter Kohn, Pierre Hohenberg and Lu Jeu Sham later, incorporated quantum mechanical effects in the electron density, developing the new density functional theory (DFT). With the fundamental contribution on the software implementation by John Anthony Pople, DFT became a popular method for the calculation of chemical properties of atoms and molecules. Driven by Pople's work, after the second part of 1980s DFT became a widely used method among the young community of quantum chemists. During the 1990s and the first years of 2000s, chemists brought DFT to a higher level, going farther beyond the first models developed by physicists. For sure density functional theory gave a major contribution to computational chemistry, but it's also true that computational chemists were fundamental in the development of density functional methods. Among the recent researchers in the area of density functionals for quantum chemistry, we recall the major contribution of John P. Perdew in his key works on generalized gradient approximations, Axel D. Becke, the first to obtain chemical accuracy with a density functional containing exact exchange, and Donald G. Truhlar for the recent efforts on the modern functionals for quantum chemistry.

The great success of density functional theory in chemistry, particularly in the recent years, is evident from the histogram of Figure 2.1, reporting an estimation of the number of publications using density functional methods in the last fifteen years.

2.2 The mathematical foundations of DFT

The most simple Schrödinger equation is easily written for the nonrelativistic, time-independent, 1-particle case:

$$\left[-\frac{\hbar^2\nabla^2}{2m}+v(r)\right]\psi(r)=\varepsilon\,\psi(r)\,. \tag{2.1}$$

A convenient starting point for a mathematical derivation of density functional theory of atoms and molecules, is the extension of (2.1) to treat N-particles systems:

$$\left[\sum_i^N\left(-\frac{\hbar^2\nabla_i^2}{2m}+v(r_i)\right)+\sum_{i<j}U\left(r_i,r_j\right)\right]\Psi(r_1,r_2\ldots,r_N)=E\Psi(r_1,r_2\ldots r_N) \tag{2.2}$$

in compact way it looks like:

$$\left[\hat{T}+\hat{U}+\hat{V}\right]\Psi(r_1,r_2\ldots r_N)=E\Psi(r_1,r_2\ldots r_N) \tag{2.3}$$

where $\hat{T}$ is the kinetic energy operator:

$$\hat{T}=-\frac{\hbar^2}{2m}\sum_i\nabla_i^2 \tag{2.4}$$

$\hat{U}$ is the Coulomb electron-electron interaction potential:

$$\hat{U}=\sum_{i<j}U\left(r_i,r_j\right)=\sum_{i<j}\frac{q^2}{|r_i-r_j|} \tag{2.5}$$

and finally $\hat{V}$ is the electron-nuclei interaction potential:

$$\hat{V}=\sum_i v(r_i)\,. \tag{2.6}$$

It is interesting to note here that the first two operators are universal: $\hat{T}$ is in fact the same for all nonrelativistic systems, and $\hat{U}$ is analogous for any systems of particles interacting through a Coulomb potential. Whether our system is an atom, a molecule, or a solid thus depends only on the term $v(r_i)$, that ususally it is called external potential, and sometimes it is denoted also $\hat{V}_{ee}$. For example for atoms it is:

$$\hat{V}=-\sum_i\frac{Ze}{|r_i-R|} \tag{2.7}$$

while for molecules and solids:

$$\hat{V}=-\sum_{ik}\frac{Z_k e^2}{|r_i-R_k|}. \tag{2.8}$$

The usual quantum-mechanical approach to Schrödinger equation is to specify the system by chosing $v(r)$, solving the Schrödinger equation for the wavefunction, and then calculates observable through this wavefunction. Among the observables that are calculated in this way, is the particle density:

$$\rho(r)=N\int dr_2\ldots\int dr_N\,\Psi^*(r_1,r_2\ldots r_N)\Psi(r_1,r_2\ldots r_N)\,. \tag{2.9}$$

The density functional approach invert the above procedure: from the electron density $\rho(r)$, one can calculate the wavefunction, and from there, all other observables. This main idea is supported by the fundamental theorems of DFT: the Hohenberg-Kohn theorems, described in the next section.

2.2.1 Hohenberg-Kohn theorems

At the heart of DFT is the first Hohenberg-Kohn (H-K) theorem, that states for *ground-state* densities that equation (2.9) can be inverted to obtain *ground-state* wavefunctions. In simple words, given a *ground-state* density $\rho_0(r)$, it is possible to obtain the corresponding *ground-state* wavefunction $\Psi_0(r_1, r_2 \ldots r_N)$, consequently all ground-state observables are simple *functionals* of the electron density $\rho_0(r)$:

$$O[\rho_0] = \left\langle \Psi[\rho_0] \middle| \hat{O} \middle| \Psi[\rho_0] \right\rangle. \tag{2.10}$$

The second H-K theorem proves that the ground-state electron density minimizes the energy functional:

$$E_v[\rho] = \min_{\Psi \to \rho} \left\langle \Psi \middle| \hat{T} + \hat{U} + \hat{V} \middle| \Psi \right\rangle \tag{2.11}$$

$$E_v[\rho_0] \leq E_v\left[\rho'\right]. \tag{2.12}$$

This theorem provides a variational principle for the electron density, and is crucial for all the further development of DFT. In the same way as in (2.3), $\hat{T}$ and $\hat{U}$ are universal functionals, while $\hat{V}$ is a non-universal functional that depends on the system that can be written explicitly in terms of the particle density ρ:

$$V[\rho] = \int dr\, v(r)\, \rho(r). \tag{2.13}$$

Although the Hohenberg-Kohn theorems are extremely powerful, they do not offer a practical way of computing the ground-state density of a system. In principle the only thing that must be done is the minimization of the energy functional $E_v[\rho]$ with respect to $\rho(r)$:

$$E_v[\rho] = T[\rho] + U[\rho] + \int dr\, v(r)\, \rho(r). \tag{2.14}$$

In practice, the exact functional is not known and we need to used approximations for $T[\rho]$ and $V[\rho]$. The first example of density-functional calculation was the Thomas-Fermi model, but the most modern and useful approach to DFT calculations is the Kohn-Sham formulation described in the next section.

2.2.2 Kohn-Sham DFT

The ground-state energy of a many-electron system can be obtained by minimising the energy functional (2.14), subject to the constraint that the number of electrons N is conserved. Using Lagrange multipliers, (2.14) becomes:

$$\delta\left[T[\rho]+U[\rho]+\int dr\, v(r)\,\rho(r)-\mu\left(\int dr\,\rho(r)-N\right)\right]=0, \tag{2.15}$$

giving the Euler-Lagrange equation:

$$\mu=\frac{\delta T[\rho]}{\delta\rho}+\frac{\delta U[\rho]}{\delta\rho}+v(r). \tag{2.16}$$

The main problem of early theories at this point was the fact that there is no easy expression of T as a functional of ρ, and the minimization of this expression was not possible. The idea of Kohn and Sham was to separate T in a first part, T_s, that represent the kinetic energy of noninteracting particle of density ρ, and the remainder, T_c, that comes from the correlation between particles:

$$T[\rho]=T_s[\rho]+T_c[\rho] \tag{2.17}$$

in this way, while there is no exactly known functional forms for $T_s[\rho]$ (in the Thomas-Fermi model they used a simple local approximation), it can be easily written in terms of the single-particle orbitals $\phi_i(r)$ of a noninteracting system with density ρ:

$$T_s[\rho]=-\frac{\hbar^2}{2m}\sum_i^N\int dr\,\phi_i^*(r)\nabla^2\phi(r). \tag{2.18}$$

This expression is an explicit orbital functional, but an implicit density functional $T_s[\rho]=T_s[\{\phi_i[\rho]\}]$. The same separation is possible for the other universal functional, U, leading to the analogue of the well known Coulomb integral of Hartree-Fock, J, that depends on the electrostatic interaction of the charge distribution ρ, plus the remainder U_r:

$$U[\rho]=J[\rho]+U_r[\rho]. \tag{2.19}$$

The sum between the unknown terms $T-T_s$ and $U-J$ leads to a new universal functional called the *exchange-correlation functional*:

$$\begin{aligned}E_{xc}[\rho] &= T_c[\rho]+U_r[\rho]\\ &= T[\rho]-T_s[\rho]+U[\rho]-J[\rho].\end{aligned} \tag{2.20}$$

The corresponding Euler-Lagrange equation of (2.16) takes the form:

$$\mu=\frac{\delta T_s[\rho]}{\delta\rho}+v_{KS}(r) \tag{2.21}$$

where

$$\begin{aligned}v_{KS}(r) &= v_{ext}(r)+\frac{\delta J[\rho]}{\delta\rho}+\frac{\delta E_{xc}[\rho]}{\delta\rho}\\ &= v_{ext}(r)+v_H(r)+v_{xc}(r)\end{aligned} \tag{2.22}$$

The ground-state density is then calculated by solving a noninteracting-like Schrödinger equation called Kohn-Sham (KS) equation:

$$\left[-\frac{\hbar^2\nabla^2}{2m}+v_{KS}(r)\right]\phi_i(r)=\varepsilon_i\,\phi_i(r) \tag{2.23}$$

and the global wavefunction is then reconstructed as a single Slater determinant made of ϕ_i:

$$\Psi_{KS}=\frac{1}{\sqrt{N!}}\left|\phi_1(r_1),\ \phi_2(r_2)\ldots,\ \phi_N(r_N)\right|. \tag{2.24}$$

It is interesting to stress the analogy between eq. (2.23) and eq. (2.1), to emphasize the fact that density functional theory replace the problem of solving the complicate N-particle Schrödinger equation by that of minimizing a density functional $E[\rho]$ and then, by use of Kohn Sham equations, replace the problem of minimizing $E[\rho]$ by that of solving a noninteracting Schrödinger equation.

Since both v_H and v_{xc} depend on ρ, which depends on the ϕ_i, which in turn depend on v_{KS} , the problem of solving the KS equations is a nonlinear one, just as the Hartree-Fock method. The usual way of solving such problems is to start with an initial guess for $\rho(r)$, calculate the corresponding $v_{KS}(r)$, and then solve the differential equation (2.23) for the ϕ_i. From these a new density can be calculated using (2.9), and the procedure can start again. The process is repeated until it converges in the so-called "self-consistent-field" (SCF) loop. Once the density reached a converged solution ρ_0, the total energy E_0 is easily calculated using this expression:

$$E_0=\sum_i^N\varepsilon_i-\frac{q^2}{2}\int dr\int dr'\,\frac{\rho_o(r)\,\rho_0(r')}{|r-r'|}-\int dr\,v_{xc}(r)\,\rho(r)+E_{xc}[\rho_0]. \tag{2.25}$$

2.3 The exchange-correlation functional and its approximations

One of the main criticisms of DFT is that, unlike most of the wavefunction based methods, it is not systematically improvable. We try to show here that there is a series of approximations to the exchange-correlation potential that leads to a list of functionals with improved accuracy. This DFT analogue to Jacob's ladder was first proposed by Perdew[4] with a nice cartoon representation that we repeat in Figure 2.2. It might be argued that, except for the first two rungs, the ladder is not based on rigorous mathematical expressions of increasing accuracy, but simply on practical considerations based on arbitrary definitions. We agree in general with this last sentence, but we point out that, despite the lack of such mathematical definitions, we can apply Perdew's ladder to real systems and obtain a hierarchy of results with increasing accuracy. In spite of the drawbacks, Perdew's ladder represent a fairly powerful tool for computational chemistry for application of density functional theory.

We will start our description from the first rung in Perdew's ladder: the local density approximation (§ 2.3.1), followed by the second rung: the generalized gradient approximations (§ 2.3.2). We will make then a jump to the fourth rung with the description of functionals that contain exact exchnage (§ 2.3.3). A quick overview on third and higher

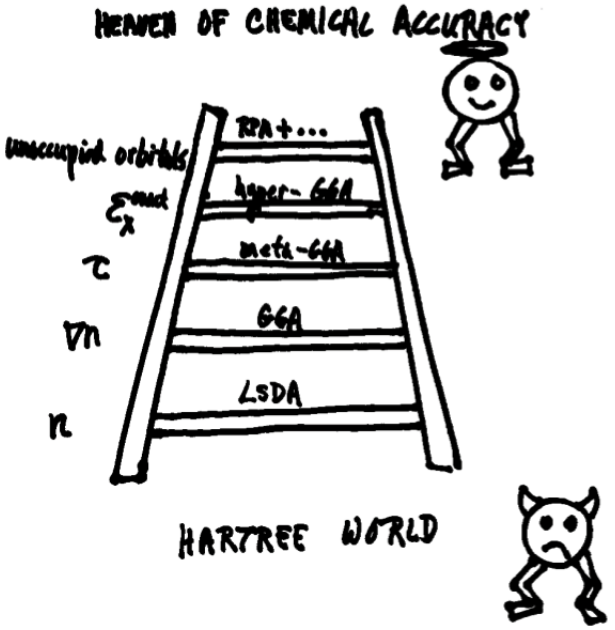

Figure 2.2: Perdew's ladder of density functional approximations to the exchange-correlation energy.

rungs is presented in the last part of this Section (§ 2.3.4), and more formally treated in Section (§ 2.4).

2.3.1 LDA and LSDA

The local density approximation (LDA) and its extension to fermionic systems local spin density approximation (LSDA), are the first and easiest examples of approximations used in Kohn-Sham DFT. The general idea at their basis is simple: consider a homogeneous electron gas, calculate the exchange-correlation energy per particle e_{xc}, and then obtain the global exchange-correlation energy for a generic system by weighting this quantiy by the probability $\rho(r)$, and integrating over all space:

$$E_{xc}^{\mathrm{LDA}} = \int dr\, e_{xc}(\rho(r))\,\rho(r). \tag{2.26}$$

The exchange-correlation energy per particle, e_{xc}, can be further divided into exchange and correlation contributions:

$$e_{xc}(\rho(r)) = e_x(\rho(r)) + e_c(\rho(r)). \tag{2.27}$$

The exchange part, e_x, for a uniform electron gas is a functional of the density, and can easily be obtained from geometrical consideration:

$$e_x^{\mathrm{LDA}} = -\frac{3}{4}\left(\frac{3}{\pi}\rho(r)\right)^{1/3}. \tag{2.28}$$

This expression leads to the well-known $\rho^{4/3}$ dependency of E_x^{LDA}. Analogous analytic expressions for the correlation part e_c are not known, except for the two extreme

cases of high- and low-density. All available correlation functionals use a parametrization of the accurate homogenous electron gas energies obtained with quantum Monte Carlo simulations. The first simulation of homogenous electron gas was performed by Ceperley and Alder, and various mathematical fits to their results are available in modern DFT software:

- Vosko-Wilk-Nusair (VWN)
- Perdew-Zunger (PZ81)
- Cole-Perdew (CP)
- Perdew-Wang (PW92)

The implementation of the PZ81 correlation functional in the GAMESS software was carried out in this thesis work, as a first approach to density functional implementations.

2.3.2 GGA

It has been pointed out by many authors (see *e.g.*, Parr, Yang for a detailed Literature), that the major source of error in the local-density approximation is in the exchange energy. This common problem is present since the Thomas-Fermi model and its improvements, include the conventional gradient expansion of von Weizsäcker. In 1986, Perdew[5] proposed a functional that resembles the correct exchange hole, by introducing the reduced gradient variable s:

$$s_\sigma = \frac{|\nabla\rho|}{\rho^{4/3}}. \tag{2.29}$$

The per-particle exchange functional is:

$$e_x^{\mathrm{GGA}} = -\frac{3}{4}\left(\frac{3}{\pi}\rho\left(r\right)\right)^{1/3} F\left(s\right) \tag{2.30}$$

and the final form of the GGA exchange functional is obtained by integration of (2.30):

$$E_x^{\mathrm{GGA}}\left[\rho\right] = -\frac{3}{4}\left(\frac{3}{\pi}\right)^{1/3}\int dr\, \rho^{4/3} F\left(s\right) \tag{2.31}$$

with:

$$F\left(s\right) = \left(c_0 + c_2\, s^2 + c_4\, s^4 + c_6\, s^6\right). \tag{2.32}$$

The original Perdew functional has $c_0 = 1$, $c_2 = 1.296$, $c_4 = 14$, $c_6 = 0.2$. LSDA can be seen as a zeroth order approximation of this more general method with $c_0 = 1$ and $c_2 = c_4 = c_6 = 0$. Further improvement to (2.31) have been proposed in the recent years through different expressions of $F\left(s\right)$, including some of the most succesful functionals for chemistry, Becke (B88)[6], and solid-state physic Perdew-Burke-Ernzerhof (PBE)[7]. The same scheme has also been applied, with large success, to correlation functionals, leading to a large number of GGA exchange-correlation functionals. The general idea of all GGA functionals, however, is hardly changed from the original formulation: the local-density approximation is improved by including in the functional terms that depend

on the gradient of the density, via some function of the reduced density gradient variable s:

$$E_{xc}^{\mathrm{LDA}}[\rho] \rightarrow E_{xc}^{\mathrm{GGA}}[\rho, \nabla\rho]. \tag{2.33}$$

2.3.3 Hybrid method

If we compare the Hartree-Fock method and density functional theory, we may notice many analogies. These analogies were used in the development of the Hartree-Fock-Kohn-Sham method (HFKS). As Parr and Yang pointed out: *"The conventional Hartree-Fock approximations can be regarded as a density-functional approach in the HFKS method scheme with correlation completely neglected, but not in the KS scheme. Instead of the exact nonlocal exchange potential in HFKS equations, the KS equations use an effective local potential that is not known and has to be approximated"*. After an accurate study on the method, Becke[8] clarified in 1993 that: "E_x is not, strictly speaking, the conventional Hartre-Fock exchange energy, since Kohn-Sham and Hartree-Fock orbitals are not the same thing. From a practical perspective, however, there is very little numerical difference. The HFKS approach has proven very useful in certain atomic applications, but is unable to describe molecular bonding. Although the theory performs somewhat better than Hartree-Fock in thermochemical tests, it falls far short of chemical accuracy. Even the inclusion of beyond-LSDA gradient corrections (for correlation only) does not significantly improve this disappointing situation. The problem lies in the fact that the splitting of E_{xc} into separate exchange and correlation parts is artificial and potentially misleading. Only exchange and correlation together has ultimate physical meaning. Hartree-Fock exchange, although "exact" in a mathematical sense, is a very poor representation of exchange-correlation in molecular systems (for example, Hartree-Fock theory provides absolutely no "left-right" correlation in the H_2 molecule). Local density functionals for E_c cannot repair the fundamental defects of the HartreeFock approximation in molecular bonds. Based as they are on electron gas theory, local E_c functionals model short-range features such as interelectronic cusps, but cannot simulate multiconfiguration mixing."

From the original HFKS method, Becke developed a new kind of exchange functional that includes a fraction of the exact, *nonlocal* exchange, and a complementary fraction of the usual GGA *local* exchange, in the so called Half&Half exchange functional[8]:

$$E_x = \frac{1}{2}E_x^{\mathrm{GGA}} + \frac{1}{2}E_x^{\mathrm{HF}}. \tag{2.34}$$

The exchange-correlation functional might be derived by rigorous analysis of the exchange-correlation hole. Within this rigorous analysis, the mix of HF exchange and DFT exchange is totally justified by the *adiabatic connection*, an expression that links the noninteracting case to the full-interacting case by a smooth function of a parameter λ that varies from 0 to 1:

$$E_{xc} = \int_0^1 d\lambda \left\langle \Psi_\rho^\lambda \left| \hat{V_{ee}} \right| \Psi_\rho^\lambda \right\rangle - J[\rho]. \tag{2.35}$$

Equation (2.34) derives from a simple two-point quadrature of (2.35), evaluating the integrand at $\lambda = 0$ and $\lambda = 1$. At $\lambda = 0$, we simply obtain the non-interacting exchange energy, that is the Hartree-Fock exchange, and at $\lambda = 1$, we have the full exchange+correlation energy. Following these arguments, Becke then suggested the intro-

duction of some semi-empirical mixing of the HF exchange with the exchange-correlation energy functionals:

$$E_{xc} = E_x^{\mathrm{GGA}} + c_x E_x^{\mathrm{HF}} + E_c. \tag{2.36}$$

The vast majority of functionals used in modern quantum-chemistry calculations are semi-empirical hybrids.

2.3.4 meta-GGAs, RSHs, and DFT-D

The main limitation of GGA functionals, including hybrids, is the failure to treat those effects that require a *nonlocal* treatment of correlation. Description of dispersion forces, is the main example of failure of conventional DFT. To overcome this limitation, different strategies have been developed in the recent literature. We provide here just a general classification of these new improvements, and we refer to the next section for a more detailed description of the functional forms. Advances beyond GGAs might be divided into:

1. Meta-GGA functionals that depend also on the Kohn-Sham kinetic energy density, τ, the 3rd rung in Perdew's ladder. The most recent examples in this category are the Minnesota family of functionals of Zhao and Truhlar[9–15], and the τ-HCTH[16] family of functionals of Handy and coworkers, and also including the popular BMK[17] functional of Boese and Martin:

$$E_{xc}^{\mathrm{LDA}}[\rho] \rightarrow E_{xc}^{\mathrm{GGA}}[\rho, \nabla\rho] \rightarrow E_{xc}^{\mathrm{meta-GGA}}[\rho, \nabla\rho, \tau]. \tag{2.37}$$

2. Range separated hybrid (RSH) functionals, where the Coulomb operator is separated into long-range and short-range terms, and these two different parts are treated and mixed in appropriate manners. The first to propose this kind of separation was Savin[18,19], and its applications to DFT functionals leads to the LC-BLYP and CAM-B3LYP functionals[18,19], and the recent ωB97 family of functionals of Chai and Head-Gordon[20–22].

3. Empirically or semi-empirically corrected functionals, usually referred as DFT-D. The main example here is the B97-D functional of Grimme[23].

4. Double-hybrid functionals that include terms derived from correlated wave-function methods, for instance MP2 perturbation theory, and are considered in the 5th rung in Perdew's ladder. This family includes Grimme's B2-PLYP and mPW2-PLYP[24], and Truhlar's double hybrids[25].

5. Van der Waals density functionals (vdW-DF), propsed by Langreth and coworkers[26]. This functional includes a nonlocal correlation term calculated with an integration over the frequency coordinate of a frequency-dependent density response.

It is important to note also that some modern functionals are developed by combining approaches, for example, the RSH-MP2[22] or the B2-PLYP-D[27] methods. In the next section, we will discuss the implementation of DFT functionals in the major quantum chemistry package GAMESS[?].

2.4 A modern family of functionals and its implementation

We turn now the attention to the main DFT work of this thesis: our implementation of a family of modern functionals in GAMESS. The entire set of new functionals is based on a series of mathematical improvements on the same functional form. This first basic formulation is the GGA functional developed by Becke in 1997, and is therefore called Becke-97 (B97)Becke[28]. The functional uses a polynomial series expansion for the gradient term, whose coefficients are determined semi-empirically via fitting to databases of experimental values. The number of coefficients that must be optimized for the GGA functional depends on the truncation of the expansion series. In its original form, a truncation at the third term is used, leading to a set of 9 parameters to be optimized (3 for the exchange and 6 for the correlation). A more advanced truncation is at the fifth term, leading to 15 parameters (5+10). One advantage of this functional form is that the truncation of the series at a term higher than five does not improve the results of the functional, and is never used in practice.

In the next sections, we will first describe the details of the original B97 GGA functional (§ 2.4.1). Next, the meta-GGA extension of the B97 functional form called τ-HCTH will be covered in (§ 2.4.2), and then we will show the range-separated hybrids based on B97 in (§ 2.4.3). The semiempircally corrected DFT-D scheme and the B97-D functional will be presented in section (§ 2.4.4), while the final section (§ 2.4.5) will describe the generation of the FORTRAN routines for the calculation of the functional energies and derivatives, their implementation into the DFT framework of the GAMESS package, and the optimization of the methods. Relevant research applications of the presented functionals are collected in the last Chapter of this Thesis.

2.4.1 The general GGA B97 functionals

The Becke-97 functional is based on two general ideas. The first is a remapping of the dimensionless reduced gradient variable s (2.29), to a set of new finite variables $u\left(s_\sigma^2\right) \in [0,1]$, with specific forms for the exchange and the correlation:

$$u_{x\sigma}\left(s_\sigma^2\right) = \frac{\gamma_{x\sigma} s_\sigma^2}{1+\gamma_{x\sigma} s_\sigma^2} \tag{2.38}$$

$$u_{c\alpha\beta}\left(s_{avg}^2\right) = \frac{\gamma_{c\alpha\beta} s_{avg}^2}{1+\gamma_{c\alpha\beta} s_{avg}^2} \tag{2.39}$$

$$u_{c\sigma\sigma}\left(s_\sigma^2\right) = \frac{\gamma_{c\sigma\sigma} s_\sigma^2}{1+\gamma_{c\sigma\sigma} s_\sigma^2} \tag{2.40}$$

where $\gamma_{X\sigma} = 0.004$, $\gamma_{C\alpha\beta} = 0.002$, $\gamma_{C\sigma\sigma} = 0.2$, and $s_{avg}^2 = \frac{1}{2}\left(s_\alpha^2 + s_\beta^2\right)$. The great advantage of these transformations is that they have linearized the exchange and correlation gradient corrections, and a systematic optimization scheme can be easily created by using a polynomial expansion of the gradient in the new variables u:

$$g = \sum_{i=0}^{M} c_i u^i. \tag{2.41}$$

The second idea is to separate the exchange and the correlation into different contributions arising from the interaction of electrons with the same spin, and electrons with opposite spin. The final general-B97 exchange correlation functional is then:

$$E_{xc}^{\mathrm{GGA}} = E_{x\alpha\alpha}^{\mathrm{GGA}} + E_{x\beta\beta}^{\mathrm{GGA}} + c_x E_x^{\mathrm{HF}} + E_{c\alpha\alpha}^{\mathrm{GGA}} + E_{c\beta\beta}^{\mathrm{GGA}} + E_{c\alpha\beta}^{\mathrm{GGA}}. \tag{2.42}$$

Each term, in (semi-)local form, is expressed as:

$$E_x^{\mathrm{GGA}} = \sum_\sigma \int dr\, e_{x\sigma}^{\mathrm{LSDA}}(\rho_\sigma)\, g_{x\sigma}\left(s_\sigma^2\right) \tag{2.43}$$

$$E_{c\alpha\beta}^{\mathrm{GGA}} = \int dr\, e_{c\alpha\beta}^{\mathrm{LSDA}}\left(\rho_\alpha, \rho_\beta\right) g_{c\alpha\beta}\left(s_{avg}^2\right) \tag{2.44}$$

$$E_{c\sigma\sigma}^{\mathrm{GGA}} = \int dr\, e_{c\sigma\sigma}^{\mathrm{LSDA}}(\rho_\sigma)\, g_{c\sigma}\left(s_\sigma^2\right) \tag{2.45}$$

where the term "semi-local" describes the fact that the energy density depends only on the electron density and orbitals in an infinitesimal neighborhood of the given position (e_x for the exchange and e_c for the correlation). The global exchange-correlation energy is then obtained by integration of the semi-local term over the entire space $E_{xc} = \int dr\, e_{xc}$. However, there is no uniform agreement on this nomenclature, and in general we prefer Truhlar's convention to simply define these terms as local, because they depend only on local values of the density and its gradient. Nonlocal terms can arise only from the integration over all space of broad quantities (like the orbital description of the wavefunction), and are therefore Hartree-Fock-type terms. It is important to clarify from the beginning our definition of local and nonlocal quantities, because they will play a key role in the development of the meta-GGA and of the range-separated functionals.

The optimal coefficients of the expansion series (2.41) are determined by minimization of error functions based on suitable databases of experimental or calculated data. The series is truncated at $M = 2$ (3 terms) for the B97 family of functionals, and at $M = 4$ (5 terms) for the HCTH family of functionals. The coefficient of the nonlocal Hartree-Fock exchange c_x is different from zero only for hybrid GGA functionals.

2.4.2 The general meta-GGA B97 functionals

The form of these functionals is based on a modification of the general GGA B97, with truncation of the sum of $g(s)$ generally at $M = 4$, plus a term that depend on the kinetic energy density τ:

$$\tau = \sum_i |\nabla \phi_i|^2. \tag{2.46}$$

The general-τ-HCTH meta-GGA functional, first proposed by Boese and Handy, is:

$$E_{xc}^{\mathrm{meta-GGA}} = E_x^{\mathrm{GGA}} + E_x^{\mathrm{meta-GGA}} + c_x E_x^{\mathrm{HF}} + E_c^{\mathrm{GGA}} \tag{2.47}$$

where E_x^{GGA} and E_c^{GGA} are the same local terms used in the general-B97 routine, and $E_x^{\mathrm{meta-GGA}}$ is the τ-dependent term:

$$E_x^{\mathrm{meta-GGA}} = \sum_\sigma \int dr\, e_{x\sigma}^{\mathrm{LSDA}}(\rho_\sigma)\, g_{x\sigma}^{\mathrm{meta-GGA}}\left(s_\sigma^2\right) f_{x\sigma}(w_\sigma)$$

where:

$$f_{x\sigma}(w_\sigma) = w_\sigma - 2(w_\sigma)^3 + (w_\sigma)^5$$

$$w_\sigma = \frac{\frac{\frac{3}{5}(6\pi^2)^{2/3}\rho_\sigma^{5/3}}{\tau_\sigma} - 1}{\frac{\frac{3}{5}(6\pi^2)^{2/3}\rho_\sigma^{5/3}}{\tau_\sigma} + 1}$$

and $g_{x\sigma}^{\text{meta}-\text{GGA}}\left(s_\sigma^2\right)$ has the same expression as $g_{x\sigma}\left(s_\sigma^2\right)$ in E_x^{GGA} (2.41), but a different set of parameters. In the original formulation of Boese and Handy, they refer to $E_x^{\text{meta}-\text{GGA}}$ as $E_x^{\text{non}-\text{local}}$, but we prefer to avoid this definition because it can create confusion with the real nonlocal Hartree-Fock term. The confusion in the nomenclature in this case arises from the fact that the τ dependent term is able in part to mimic the nonlocal property of the Hartree-Fock exchange, but in principle it is only semi-local, in the same way as the GGA terms, because it is derived from integration of local quantities.

2.4.3 The range-separated ωB97 family of functionals

The recently proposed ωB97 family of functionals is based on Savin's range-separation of the Coulomb operator:

$$\frac{1}{r_{12}} = \frac{\text{erf}(\omega r_{12})}{r_{12}} + \frac{\text{erfc}(\omega r_{12})}{r_{12}} \tag{2.48}$$

The general form of the ωB97 family of functionals, as firstly proposed by Chai and Head-Gordon, is then a long-range corrected (LC-)GGA functional that can be written as follows:

$$E_{xc}^{\text{LC}-\text{GGA}} = E_x^{\text{SR}-\text{GGA}} + E_x^{\text{LR}-\text{HF}} + c_x E_x^{\text{SR}-\text{HF}} + E_c^{\text{GGA}}. \tag{2.49}$$

Hhere, the long- and short-range Hartree-Fock terms are calculated using Savin's Coulomb operator for the two-electron integrals, instead of the regular $1/r_{12}$ Coulomb operator:

$$\begin{aligned} E_x^{\text{SR}-\text{HF}} &= -\frac{1}{2}\sum_\sigma \sum_{i,j}^{occ.} \int dr_2 \int dr_1 \; \psi_{i\sigma}^*(r_1)\,\psi_{j\sigma}^*(r_1) \\ &\quad \times \frac{\text{erfc}(\omega r_{12})}{r_{12}} \psi_{i\sigma}(r_2)\,\psi_{j\sigma}(r_2) \end{aligned} \tag{2.50}$$

$$\begin{aligned} E_x^{\text{LR}-\text{HF}} &= -\frac{1}{2}\sum_\sigma \sum_{i,j}^{occ.} \int dr_2 \int dr_1 \; \psi_{i\sigma}^*(r_1)\,\psi_{j\sigma}^*(r_1) \\ &\quad \times \frac{\text{erf}(\omega r_{12})}{r_{12}} \psi_{i\sigma}(r_2)\,\psi_{j\sigma}(r_2) \end{aligned} \tag{2.51}$$

$c_x = 0$ for the ωB97 functional, while $c_x \neq 0$ for the ωB97X and ωB97X-D. The short-range part of the DFT functional is obtained by the combination of the short-range LSDA exchange and the correction factor $g(s)$ defined for the previous cases:

$$E_x^{\mathrm{SR-GGA}} = \sum_\sigma \int dr\, e_{x\sigma}^{\mathrm{SR-LSDA}}(\rho_\sigma)\, g_{X\sigma}\left(s_\sigma^2\right) \tag{2.52}$$

and the short range LSDA exchange is calculated as an attenuated LSDA function:

$$e_x^{\mathrm{SR-LSDA}} = -\frac{3}{2}\left(\frac{3}{4\pi}\right)^{1/3} \rho_\sigma^{4/3}(r)\, F(a_\sigma) \tag{2.53}$$

with the attenuation function $F(a_\sigma)$ depending on the dimensionless parameter $a_\sigma = \omega/(2k_{F\sigma})$, where $k_{F\sigma} = \left(6\pi^2\rho_\sigma(r)\right)^{1/3}$ is the Fermi wave vector:

$$F(a_\sigma) = 1 - \frac{8}{3}a_\sigma\left[\sqrt{\pi}\,\mathrm{erf}\left(\frac{1}{2a_\sigma}\right) - 3a_\sigma + 4a_\sigma^3 + \left(2a_\sigma - 4a_\sigma^3\right)\exp\left(\frac{1}{4a_\sigma^2}\right)\right] \tag{2.54}$$

2.4.4 The semiempirically corrected DFT-D

Perhaps motivated by the possibility of a more simplistic approach, several methods for correcting DFT for failures involving noncovalent interactions have involved addition of an empirical correction to the final DFT energy typically of the form C_6R^{-6}, where R represents the interatomic distances and C_6 the dispersion coefficients. Our implementation follows the original formulation of Grimme, as

$$E_{\mathrm{disp}} = -s_6 \sum_{i=1}^{N_{at}-1} \sum_{j=i+1}^{N_{at}} \frac{C_6^{ij}}{R_{ij}^6}\, f_{\mathrm{dmp}}\left(R_{ij}\right) \tag{2.55}$$

the damping function of Wu and Yang (WY) is normally used in this formula to scale the dispersion to zero at short distances:

$$f_{\mathrm{dmp}}^{\mathrm{WY}}\left(R_{ij}\right) = \left[1 + \mathrm{e}^{-d\left(\frac{R_{ij}}{s_R R_0^{ij}} - 1\right)}\right]^{-1}. \tag{2.56}$$

This scheme is general and can be applied not only to DFT but also to all mean field methods that lack a sufficient treatment of dispersion energy. The main parameters in this scheme are (a) the C_6^{ij} coefficients, (b) the R_0 vdW radii, and (c) all of the scale factors. Differences in implementations are mainly in the values of these parameters. For example, R_0 is typically calculated with wave function based methods and scaled by an appropriate factor; C_6 has been calculated from atomic hybridization states and also determined from LDF calculated IPs and static dipole polarizabilities α, and the damping factor, d, typically takes on values between 20-23. C_6^{ij} can be determined via formulas such as $C_6^{ij} = \sqrt{C_6^i C_6^j}$, which has been found by Grimme to be consistent for problems of interest in this work, and the functional dependent scale factors, s_6, typically determined via parameter fitting. The final mean-field (MF) DFT-D energy is the result of the direct addition of this dispersion energy to the computed DFT energy:

$$E_{\mathrm{MF-D}} = E_{\mathrm{MF}} + E_{\mathrm{disp}}. \tag{2.57}$$

A silightly modified damping function was recently proposed by Chai and Head-Gordon (CHG)[21] to avoid a potentially misleading behavior of the WY damping function at very short distances. The expression of the CHG damping function is:

$$f_{\mathrm{dmp}}^{\mathrm{CHG}}\left(R_{ij}\right)=\left[1+a\left(\frac{R_{ij}}{s_R R_0^{ij}}\right)\right]^{-1}. \tag{2.58}$$

An accurate optimization, as well as the analysis of the global performance, have been performed on many dispersion corrected DFT functionals, and will be reported in Section 2.5 together with the relevant research applications, as a working example of applicability of the new family of functionals. Many other research applications will be further presented in the last Chapter 4.

2.4.5 Implementation

Following the definition of the original B97 functional, the first approach for the implementation of these functionals was the separation between exchange and correlation: For the latter then, a FORTRAN routine was generated through a modified version of Knowles' dfauto program (see electronic support information). The generated routine calculates the correlation energy using equations (2.44) and (2.45), and its derivative with respect to ρ_α and ρ_β. The expansion of $g(s)$ up to $M=4$ (5 terms) was used, and the numerical coefficients c_i are passed to the routine as formal parameters. This correlation routine allows the calculation of the correlation energy for all the implemented functionals described above.

The exchange part has been implemented in a different routine composed of three distinct blocks:

1. The LSDA term, implemented using the previous LSDA routine of GAMESS that includes the range-separation of the Coulomb operator (for the ωB97 family of functionals).

2. The GGA part, implemented using the modified dfauto program in the same way as the correlation.

3. The τ dependency for the τ-HCTH family of functionals.

Finally, all three parts are put together in the appropriate way, and the global functional derivatives are calculated using a simple chain-rule formula. The new routines allowed the implementation of a large number of different reparametrizations of the same basic functional form, and because of their modular nature, new sets of parameters can be easily added in the future, leading to different functionals. Dispersion corrections (§ 2.4.4) were also implemented into GAMESS, and have been used in conjunction with the new routines for the B97-D, and the ωB97X-D functionals (the last uses the CHG damping function of Eq. 2.58).

Some of the functionals are hybrid, and a percentage of HF exchange has been added using the standard implementation procedure of GAMESS. The range-separated HF and DFT exchange of the RSH functionals are calculated with the long-range correction scheme of GAMESS, but using a slightly modified routine to allow the multiplication

Table 2.1: newly implemented DFT functionals in the GAMESS code, divided by their nature. GAMESS keywords are given in parenthesis if different from the name of the functional. Hybrid functionals are indicated in italic case.[a]

GGAs	meta-GGAs	RSHs	DFT-D
parametrizations of the general-B97 functional	*parametrizations of the meta-GGA general-τ−HCTH functional*	*parametrizations of the range-separated ωB97 family of functional*	*semi-empirically corrected functionals*
B97	τ−HCTH (tHCTH)	ωB97 (wB97)	B97-D
B97-1	*τ−HCTH hybrid (tHCTHhyb)*	*ωB97X (wB97X)*	*ωB97X-D (wB97X-D)*
B97-2	*BMK*		
B97-3			
B97-K			
B98[b]			
HCTH/93 (HCTH93)			
HCTH/120 (HCTH120)			
HCTH/147 (HCTH147)			
HCTH/407 (HCTH407)			

[a] for RSHs only those that include short-range exchange are considered hybrid, see the main text.
[b] using the *2c* parametrization of the original paper.

with the GGA correction part. The LR-HF integrals are calculated directly using equation (2.51) in the two-electron integrals code of GAMESS. The scaled SR-HF exchange for the ωB97X functional is then obtained indirectly by subtraction of the LR-HF exchange from the total HF exchange (calculated without Savin's modified Coulomb opertors):

$$c_x E_{xc}^{\mathrm{SR-HF}} = c_x \left(E_x^{\mathrm{HF}} - E_x^{\mathrm{LR-HF}} \right) \tag{2.59}$$

thus (2.49) is calculated as:

$$E_{xc}^{\omega\mathrm{B97X}} = E_x^{\mathrm{SR-GGA}} + (1 - c_x) E_x^{\mathrm{LR-HF}} + c_x E_x^{\mathrm{HF}} + E_c^{\mathrm{GGA}}. \tag{2.60}$$

If we compare this expression with the expression for the general-τ-HCTH meta-GGA functional (2.47), we find large similarities between the two. The $\tau-$dependent term of (2.47) is substituted by the long-range Hartree-Fock term (nonlocal by definition) in (2.60). The GGA exchange is limited to short-range in the second case, and the last two terms, the GGA correlation and the scaled HF exchange are the same for both functional forms. Written in this form it is clear that ωB97 is closely related to non-hybrid τ-HCTH functionals ($c_x = 0$), while ωB97X is related to τ-HCTHhyb functionals ($c_x \neq 0$). Regarding the inclusion of the scaled HF exchange, ωB97 can be considered a non-hybrid functional (although it contains a long-range contribution coming from the HF nonlocal exchange), while ωB97X is a full hybrid functional similar to GGA and meta-GGA hybrids.

A summary of all the B97-related functionals available in the new release of GAMESS through our new routines is reported in Table 2.1.

Beyond the B97 family of functionals described above, our contributions for the functional implementation in GAMESS include also some of the largely used functionals: PZ81[29], P86[5], EDF1R.D. Adamson and Pople[30], revPBE[31], B2-PLYP[24]. The first functionals of the previous list have been obtained with the modified dfauto program, whose usage and specification will be presented in the electronic support information. The last

two functionals (revPBE and B2-PLYP) have been implemented through modifications of routines already available in GAMESS.

The source code of all our new routines, are presented in the electronic support informations, included with the Thesis CD.

2.5 Optimization and performance of DFT-D

In this section we mainly report our 2008 paper entitled: "Optimization and performance of DFT-D with respect to basis set and functional for study of dispersion interactions in nanoscale aromatic hydrocarbons"[32].

The article goes through a brief explanation of the theory (omitted here, refer to the previous paragraphs), then shows the optimization that we performed on all the main parameters of the DFT-D method, and finally is concluded with some application examples. We prefer to report here the article in its entirety, including the applications, in order to give an overview on the global performance of the many exchange-correlation functionals that we've just presented. More application examples, will be also reported in the final Chapter of this Thesis (Chapter 4).

2.5.1 Theoretical approach and discussion

Double Parameter Optimization

There has been substantial discussion in the recent DFT-D literature concerning the issue of the optimization of the parameters for the semiempircal correction (§ 2.4.4)[33–35]. On one hand, many consider a fixed value of s_R, and optimize the linear parameter s_6 (as in the original work of Grimme)[23,36]. The atomic dispersion coefficient pre-factors s_6 were originally optimized by Grimme using the TZV2P (also referred as TZV(2d,2p)) basis set, suggesting a fixed value of $s_R = 1.1$. Optimization of the non-linear vdW factor s_R, keeping s_6 at one (as in the work of Jurecka), has also been considered[33], as has a more complete optimization of all empirical parameters of a damping function for C_6R^{-6} for three specific functionals (PBE, BP86, B3LYP) and several basis sets for application to π-stacking interactions in nucleic acids[37]. Given the importance of these parameters on the ultimate predictability of DFT-D, as well as the need to add the appropriate dispersion correction term for the specific functional and basis set being used, we have considered a simultaneous double optimization of the two parameters, showing the behavior of both parameters across various functionals and basis sets. We propose optimal values of both parameters for each case.

The S22 reference set of data provided by Jurecka et. al.[38] has been used for determination of the optimized parameters, a common choice for studies of the present type. As in previous works[23,38], the two parameters were optimized varying their values so that the difference between reference single point energy and the DFT-D for the same geometry is minimized. Accurate geometries were taken for the S22 set from the original paper. All DFT-D calculations were performed with the newly modified GAMESS software.

The B97-D functional tends to be much more insensitive to spurious contamination due to parameterizations in the exchange component, that in some functionals mimics the dispersion effects. This effect can be more clearly observed by plotting the exchange en-

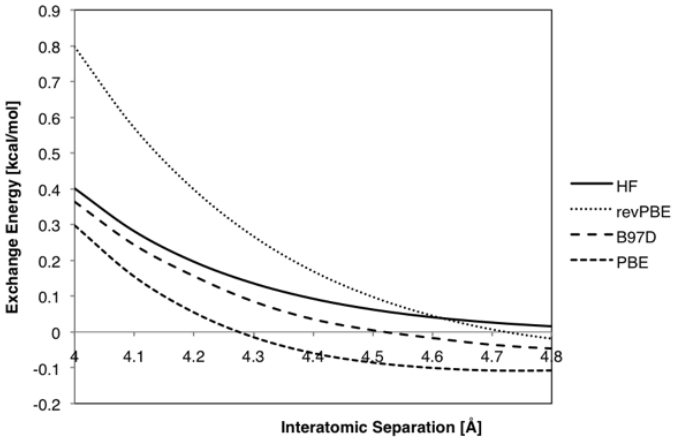

Figure 2.3: Plot of the exchange energy of the functionals, PBE, revPBE, and B97-D, compared to the exact Hartree-Fock exchange in the vdW region, for the Kr_2 dimer.

ergy of the functionals together with the exact Hartree-Fock exchange in the vdW region for a simple dimer of noble gas atoms, for example Kr, as shown in Figure 2.3.

The Zhang and Yang functional, revPBE[31], employs a parametric fit to exact exchange data, and therefore is another candidate for addition of semiempirical dispersion effects. In some cases, revPBE mimics the HF result, however tends to result in more expanded intramolecular geometries and loosely held complexes. While this is partially compensated for by the addition of the attractive dispersion term, the overall effect is still lacking. In addition, one observes a rather large value for s_6 for revPBE, since the correction is taking into account some effects that are typically handled with a correlation terms, which is not present in this functional.

Optimization of the empirical dispersion function parameter across the Dunning cc-pVnZ family of basis sets with $n = 2,3$, and the TZV(2d,2p) basis set used by Grimme in his original paper, was carried out for the B97-D functional. Results are shown in Figure 2.4, where the Mean Absolute Deviation (MAD) is reported as a surface function of the two parameters s_R and s_6 for the S22 system of complexes.

In these diagrams, the lowest energy is given in red, highest energy in blue, and all plots are on the same relative scale. All plots in Figure 2.4 show a large region of red corresponding to optimal s_6 and s_R parameters where the MAD associated with the S22 set of complexes is at a minimum. For the cc-pVDZ basis set, the minimum functional region is 1.0 kcal/mol deep, while for both the triple zeta basis sets, the minimum functional region is 0.5 kcal/mol. One can find the intersection point between horizontal (s_6) and vertical (s_R) within this minimum region, as shown in the right most picture of each set of plots in Figure 2.4. A value of $s_R = 1.1$ always intercepts the minimum-regions, showing that optimization of s_R is not necessarily required, if combined with a good optimized value of the linear s_6 parameter. The intersection with an optimized value of s_6 (solid lines in the associated plots) always lies in the minimum-region. The values of s_6, as optimized by Grimme for TZV(2d,2p), are indicated as dashed lines for the first two sets of plots, to indicate the resulting difference when considering other basis sets.

A similar analysis was performed for the revPBE functional. Our particular interest in this functional is its suitability for our hybrid computations of corannulene on surfaces,

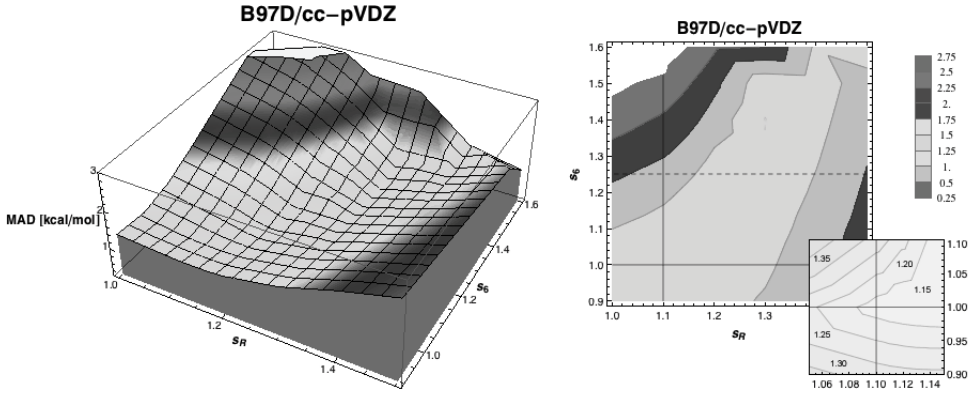

(a)

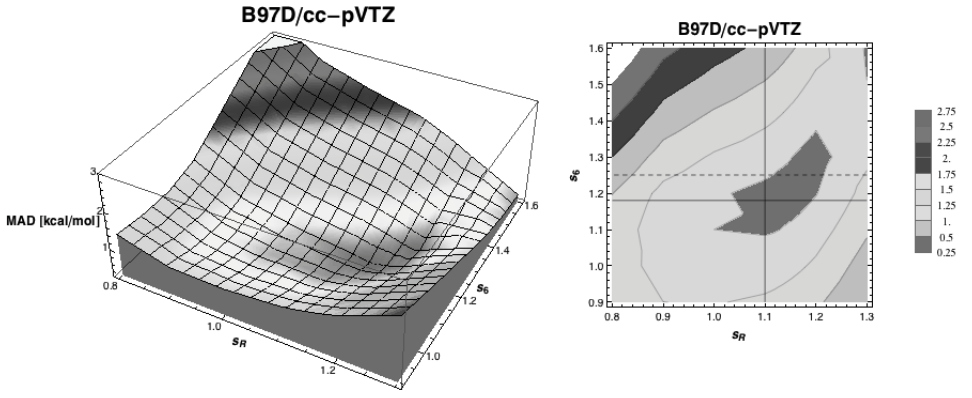

(b)

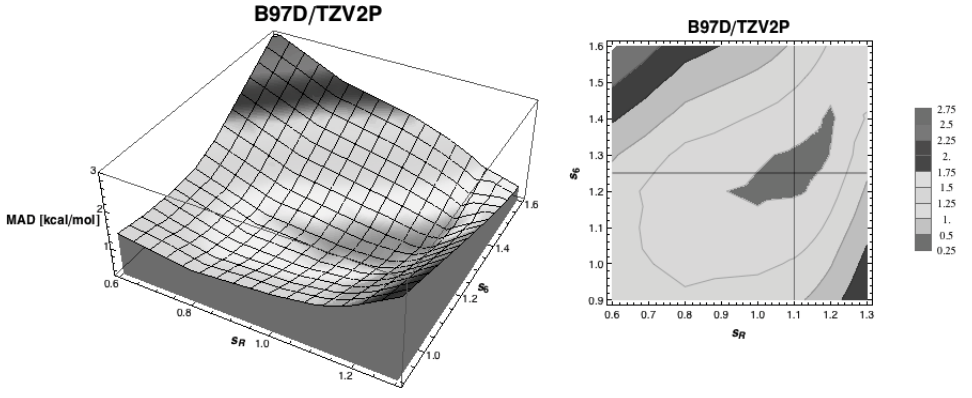

(c)

Figure 2.4: Optimized s_6 and s_R empirical dispersion function parameters for the B97-D functional, with the a) cc-pVDZ, b) cc-pVTZ, and c) TZV(2d,2p) basis sets, respectively. All plots are given on the same relative scale, and a more detailed view of the minimum region is provided in the case of cc-pVDZ.

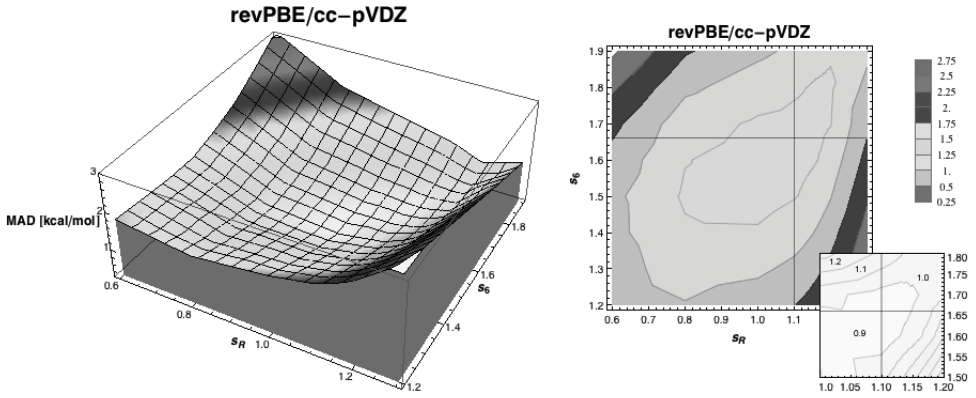

Figure 2.5: Optimizeds_6 and s_R empirical dispersion function parameters for the revPBE functional, with the cc-pVDZ basis set. Plots are shown using the same relative scale as in Figure 2.4, and an inset showing a more detailed view of the minimum is provided.

using the SIESTA software. The revPBE is a good choice for such computations because it is found to be superior in the description of energetics of atomic and molecular bonding to surfaces, as compared to experimental findings. However, up to this point, the attractive dispersion term for this functional was lacking in both SIESTA and GAMESS.

Optimization results for the revPBE functional for one basis set is shown in Figure 2.5, with very similar characteristics for higher order basis sets. As expected, the optimized s_6 value is quite large, at 1.66, since the correction is taking into account some effects that are typically handled with a correlation terms, which is not present in this functional.

Double Hybrid Functional

As clearly shown in the previous Paragraphs, in contrast to the strategy of including the effects of dispersion via an empirical function as discussed so far, an alternative strategy proposed in the literature for improving density functional theory even beyond the so-called 4th rung functionals, is via the "double-hybrid" functionals. These functionals, as initially proposed[25,39], involve a multilevel approach including more advanced ab initio components, within the density functional formalism, for example, Møller-Plesset theory. Double-hybrid functionals were then realized by Grimme in his proposed B2-PLYP set of functionals[24,27], and later by others. In this type of treatment, typically either a hybrid density functional or GGA functional is used together with exact HF exchange, but with a damped correlation functional. The remaining correlation is then treated with a more advanced ab initio method. In the case of B2-PLYP, the GGA functionals are LYP correlation[40] and B88 exchange[6], with 53% exact HF exchange and 27% MP2 energy.

We have now considered optimal s_6 and s_R values for both the cc-pVDZ and cc-pVTZ basis sets. The resulting correlation plots are shown in Figure 2.6. We observe results that are quite different from that found for the GGA and hybrid functionals. The s_6 parameter for the B2-PLYP functional has a smaller optimized value (0.55), due in part to the dispersion contribution being taken into account with the PT2 component of the functional. However, the values are higher than zero because the PT2 component is scaled and takes into account only 27% of the dispersion. The s_R parameter will have a

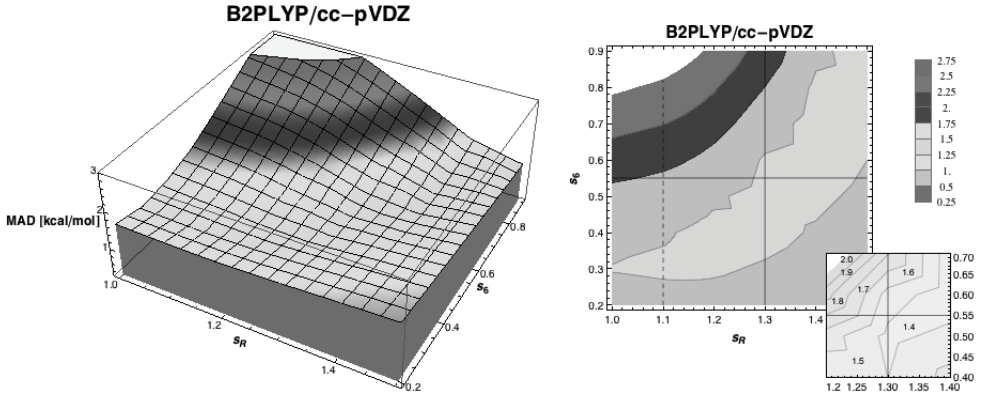

(a)

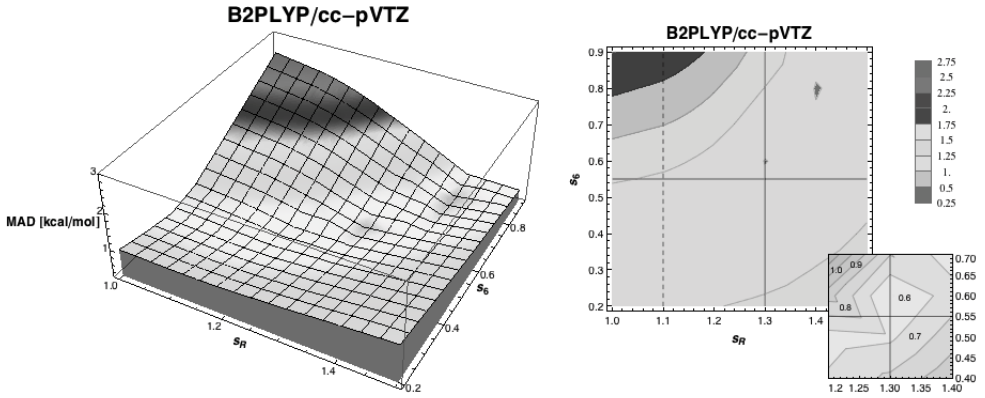

(b)

Figure 2.6: Optimized s_6 and s_R empirical dispersion function parameters for the B2-PLYP double-hybrid functional, with the cc-pVDZ (top) and cc-pVTZ (lower) basis sets. Plots are shown using the same relative scale as those shown in Figures 2.4 and 2.5. Inset graphs are provided showing the minimum region in more detail.

higher value for similar reasons. The differences found between the double-ζ and triple-ζ basis sets appear to be smaller than in the other functionals considered. In fact, the same pair of optimized s_6/s_R values can be utilized with good accuracy with either basis set. Therefore, we suggest values of $s_6 = 0.55$ and $s_R = 1.3$, which represent the best compromise between accuracy and general applicability. Again, the optimized values are shown as solid linesand the optimized values of Grimme are shown as dotted lines in the graphics.

Further Considerations of Basis Sets and BSSE

Following the above analysis, we proceeded to optimized the s_6 parameter for several additional functionals and basis sets, keeping the s_R value fixed to 1.1, as also suggested in the original paper of Grimme, given that this choice looks consistent also for the basis sets and functional types considered here. The first functional considered was the B97-D exchange-correlation functional[23]. The cc-pVnZ basis sets (with $n = 2-4$) were used to investigate the behavior of the optimized s_6 parameter for increasing value of $\zeta\,(n)$. In addition, the reference TZV(2d,2p) optimized parameter of 1.25 was also considered.

Figure 2.7 shows the Median Absolute Deviation (MAD) for the S22 set of molecules, with respect to increasing s_6 value, using the B97-D functional. The optimized s_6 parameter increases with the addition of every $\zeta\,(n)$ to the basis set, as expected. With small basis sets ($n = 2$), one expects the basis set superposition error (BSSE) to be significant. The triple-ζ basis sets have almost the same overall performance as the higher-order quadruple-ζ basis set, with MAD lower than 0.5. The cc-pVTZ basis set, with optimized s_6 parameter of 1.18, has a slightly better overall performance than does the TZV(2d,2p) basis set. Indeed, the original TZV(2d,2p)-optimized parameter of 1.25 of Grimme provides acceptable errors of around 0.5 with the cc-pVTZ basis set. This facts suggests that a reoptimization of the s_6 parameters with basis sets that contain the same number of split shells is not really necessary, while the reduction of the number of split shells (i.e., from triple to double-ζ) can involve a significant increase in BSSE that must be compensated by a corresponding reduction of the optimized-s_6 parameters.

The basis set superposition error (BSSE) plays a key role in the understanding of weakly bounded complexes interaction energies. It is well known that basis sets that are too small will have large BSSE, resulting in poor binding energies and intermolecular distances[36]. Although it has been shown that DFT is much less affected by BSSE than other wavefunction types, a basis set of at least triple-ζ quality is necessary to significantly reduce the BSSE. The counterpoise correction (CP) is the standard method to correct for BSSE, and while the procedure itself has an associated error (typically results in an overestimation of BSSE) and requires additional effort, typically provides good results for the vast majority of cases where it is used.

When the semiempirical-corrected DFT methodologies are employed, optimized parameters inherently account for part of the BSSE, as pointed out in the literature[23,37]. In fact, for small basis sets, BSSE can be of the same order of magnitude as the dispersion corrections, however the two corrections have different asymptotic behavior. To better understand the behavior of dispersion corrections and BSSE with respect to basis set and functional variations, we have performed parameter optimization with and without the CP correction. In Figure 2.7, the optimization of the s_6 parameter for the B97-D functional including counterpoise correction is shown for several basis sets. Interestingly, the CP

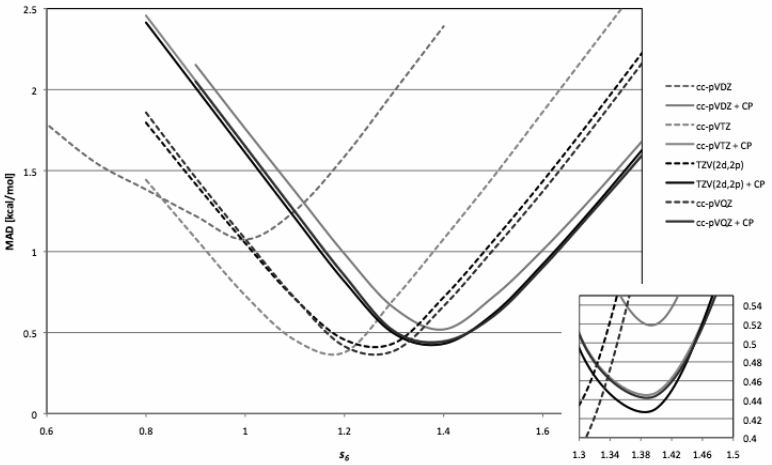

Figure 2.7: Mean Absolute Deviation (MAD) with respect to increasing s_6 value, for the B97-D functional. A detailed view of the minimum region is also provided for the CP corrected curves.

curves for all basis sets considered have a minimum at $s_6 = 1.4$ (general value that we suggest to use when CP corrections are applied with B97-D), a quite large value compared to the ones for non CP-corrected curves. Since we can reasonably expect BSSE for large basis (e.g., cc-pVQZ) to be almost completely reduced to zero, one would expect the optimal s_6 value for the CP-corrected curves to be in the same region, but this is not the case.

Looking at the global performance in terms of MAD of the S22 set, one can see that the MAD is correctly reduced in going from cc-pVnZ to cc-pVnZ + CP for $n = 2$, but slightly increases for $n > 2$ (where the BSSE should be very small also for the noncorrected basis). The loss of accuracy within the same basis sets has to be attributed to the error associated with the CP corrections, since no other source of errors are introduced in the calculations. This difference should actually be a reasonable energetic estimate of the error associated with the CP procedure within the S22 set of molecules. Given a much larger database of molecules, this procedure should be a way to quantify the global performance of the CP methods. Similar considerations can be made for the B3LYP, PBE, and revPBE functionals. Parameter optimizations were performed and results collected in Figure 2.8.

The optimal s_6 parameters show the same behavior for all three functionals, resulting in an increase of this parameter value with dimension of basis set. The revPBE functional actually shows a relatively strange overall performance, its accuracy is in fact reduced with increase in basis set, with the double-ζ basis set having the lowest MAD value. To better analyze the s_6 optimization process, the deviation from reference for cc-pVDZ with the non-optimized and optimized s_6 values for the S22 set of complexes was investigated, in addition to results of DFT without dispersion (Figure 2.9).

As can be expected, one observes the general improvement of results with inclusion of the dispersion correction (DFT *vs*. DFT-D results). The largest errors for DFT-D are found for the first 7 complexes in the S22 set, which are all hydrogen-bonded complexes. Complexes 8 to 15 have predominantly dispersion contributions, while complexes 16 to 22 involve more complicated diverse interactions. In the case of PBE and revPBE, the

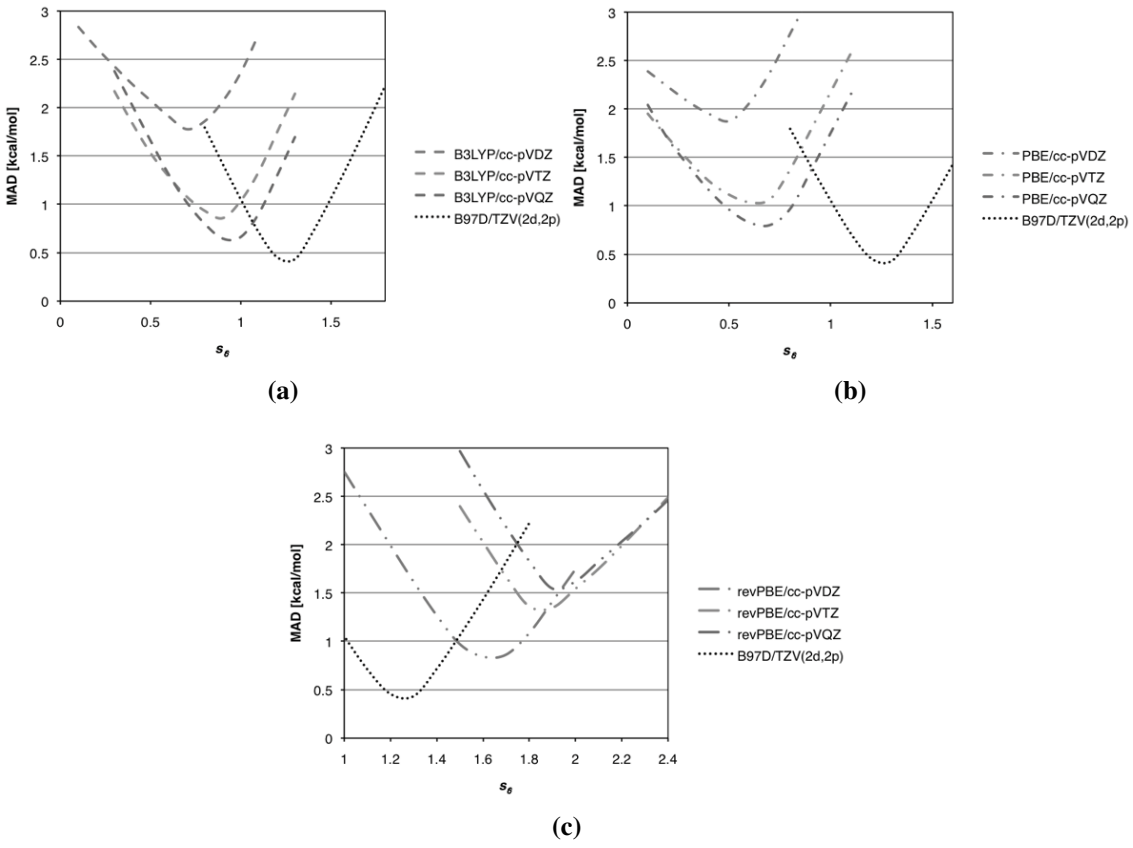

Figure 2.8: Optimization of the s_6 and s_R parameters for the a) B3LYP, b) PBE, and c) revPBE functional at cc-pVnZ, $n = 2-4$, compared to the B97-D functional at the TZV(2d,2p) basis set with optimized $s_6 = 1.25$.

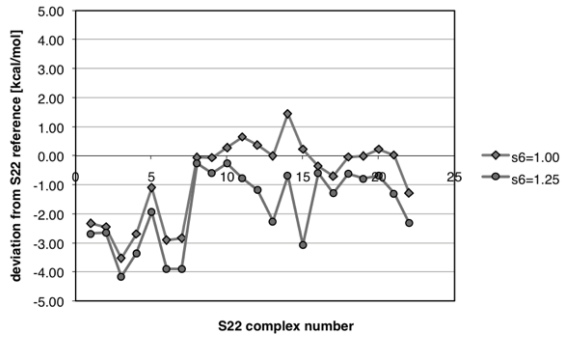

(a) B97-D/cc-pVDZ, $s_6 = 1.25$ *vs.* $s_6 = 1.00$

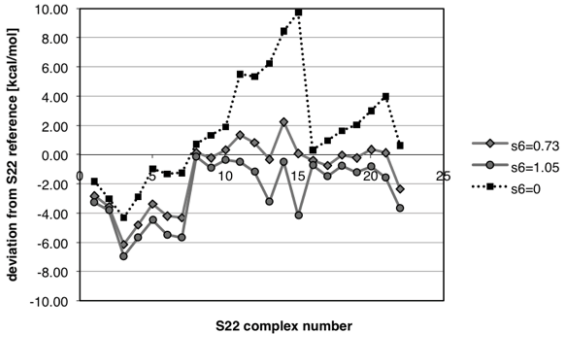

(b) B3LYP-D/cc-pVDZ, $s_6 = 1.05$ *vs.* $s_6 = 0.73$

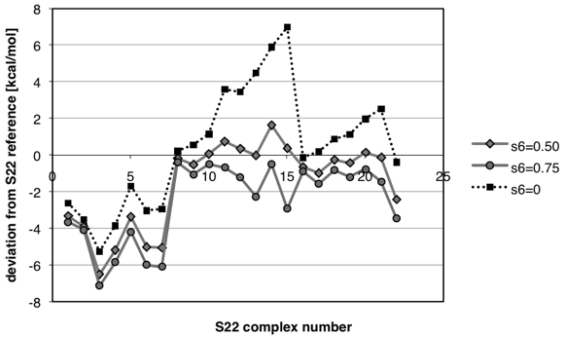

(c) PBE-D/cc-pVDZ, $s_6 = 0.75$ *vs.* $s_6 = 0.50$

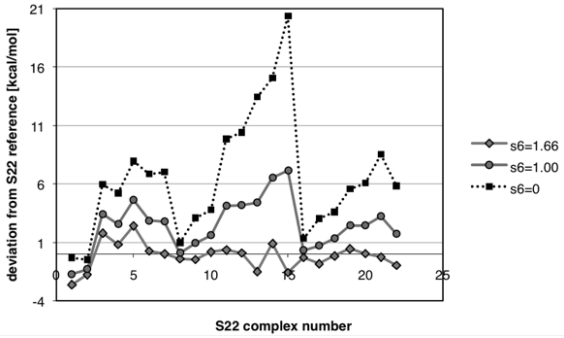

(d) revPBE-D/cc-pVDZ, $s_6 = 1.66$ *vs.* $s_6 = 1.00$

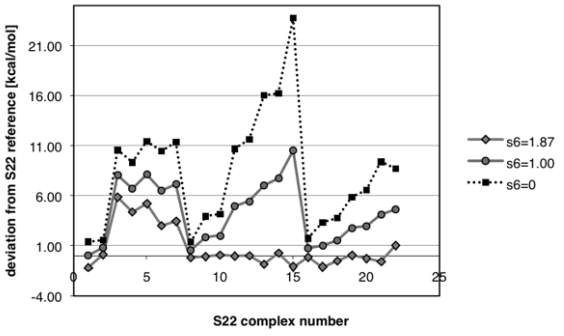

(e) revPBE-D/cc-pVTZ, $s_6 = 1.87$ *vs.* $s_6 = 1.00$

Figure 2.9: Deviation of DFT-D calculated and CCSD(T) reference for the S22 set of complexes for different functionals.

Table 2.2: Mean absolute deviation of S22 complexes for the series of functionals and corresponding basis sets for the optimized s_6 values shown.

DFT Functional	basis set	Optimized s_6 value	MAD (kcal/mol)
B97-D	cc-pVDZ	1.00	1.075
	cc-pVDZ + CP	1.39	0.518
	cc-pVTZ	1.18	0.337
	cc-pVTZ + CP	1.41	0.454
	cc-pVQZ	1.26	0.330
	cc-pVQZ + CP	1.39	0.441
	TZV(2d,2p)	1.25	0.375
	TZV(2d,2p) + CP	1.38	0.425
B3LYP	cc-pVDZ	0.73	1.709
	cc-pVTZ	0.88	0.853
	cc-pVQZ	0.96	0.612
PBE	cc-pVDZ	0.50	2.579
	cc-pVTZ	0.64	1.030
	cc-pVQZ	0.65	0.798
revPBE	cc-pVDZ	1.66	0.826
	cc-pVTZ	1.87	1.326
	cc-pVQZ	1.90	1.536
	cc-pVTZ (8-22)	1.87	0.393
	cc-pVQZ (8-22)	1.90	0.355

optimized values sensibly flatten the curve in the pure dispersion and in the mixed regions, while maintaining acceptable results in the hydrogen-bonded area.

The apparently strange behavior of revPBE with respect to basis set increase can be rationalized through a comparison of the plot in Figure 2.9d for cc-pVDZ with a corresponding plot for cc-pVTZ shown in Figure 2.9e. While errors for complexes 8 to 22 are satisfactorily reduced for the triple-ζ basis set, errors associated with the hydrogen bond complexes (complexes 1 - 7) are actually increased, reducing the global performance (MAD) for this functional. The MAD of complexes from 8 - 22 using revPBE/cc-pVTZ and revPBE/cc-pVQZ is of the same order of that obtained for B97-D using the same respective basis sets, as can be seen in Table 2.2.

Figure 2.10 shows all results together, illustrating the performances of the different functionals. The B97-D with triple-ζ basis set appears to be in general the best choice for accurate calculations. Interestingly, B97-D with cc-pVDZ provides essentially the same performance as B3LYP-D with cc-pVTZ. Oddly, results of revPBE/cc-pVDZ appear to provide the overall best of the other double-ζ basis sets (Figure 2.11), and additionally of nearly all triple-ζ basis sets and even some of the quadruple-ζ basis sets. However, as we observe when applying this functional, these results are a bit misleading, as results for structure and properties of molecules outside the S22 test set are found to be not as good as with, for example, the B97-D functional. The high values of the optimal s_6 for the revPBE functional are evidence that the exchange part of this functional correctly provides little to no bond in the vdW region, forcing the vdW interactions to be treated by

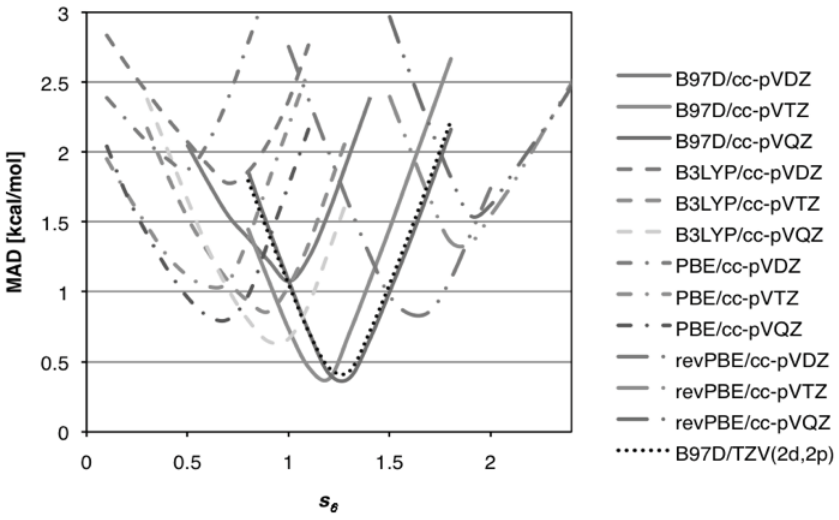

Figure 2.10: Mean absolute deviation at optimal s_6 values for the functionals and basis sets considered in this study

the semiempirical dispersion-like term. For this reason, and also due to its simple GGA implementation and large use in physical and surface science, revPBE/cc-pVDZ appears to be one of the best reference methods for large systems. The B97-D functional is still a very good choice using either double-ζ or triple-ζ basis sets, given its rational balance of exchange and correlation terms, and over all good behavior in general. For use with the cc-pVDZ basis set, a sensible reduction of the optimized s_6 parameter is necessary.

To further validate results, we also looked at small molecule benchmark dimers that have been used in many other investigations of this type, some of our larger models for aryl/aryl interactions, as well as corannulene constructs, given the large focus on these latter systems in our research. The first two small but nontrivial tests include methane dimers and benzene dimers, the latter of which has been the subject of many experimental and theoretical investigations for which there is considerable benchmark data.

Methane Dimers

$(CH_4)_2$ in D_{3d} (staggered) conformations was first considered using B97-D/TZV(2d,2p) in order to verify in accord with literature[23] and experimental results[41–46]. Counterpoise (CP)[47] corrections for basis set superposition error (BSSE) was also investigated for both, the summary of which is in Table 2.3.

Results for the staggered conformation of the methane dimer are in good agreement with those of Grimme as well as experimental data. Small differences from that of Grimme can be attributed to a) Grimme uses resolution of the identity RI approximation for two-electron integrals, and b) a slight difference in basis set: Grimme uses TZV2P basis set[48] (discarded *d*- and *f*- function on first and 2-5-row atoms, respectively), here TZV(2d,2p)[49] as implemented in GAMESS is used.

As previously mentioned, counterpoise corrections need to be treated with caution due to the fact that such effects are partially accounted for within the semiempirical dispersion correction itself. At the double-ζ, such considerations may still be required, but one should be aware that the semiempircal correction might influence the effectiveness of the

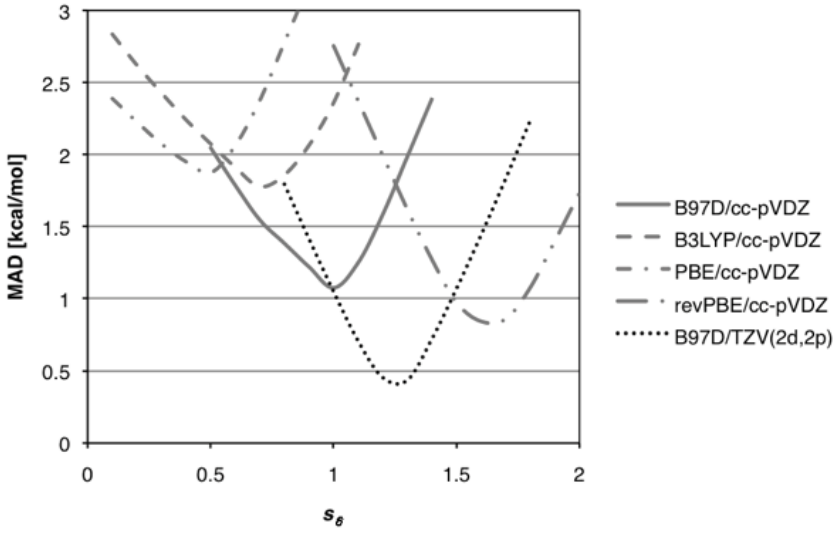

Figure 2.11: Mean absolute deviation at optimal s_6 values for functionals using the cc-pVDZ basis set as compared to B97-D/TZV(2d,2p)

Table 2.3: Summary of DFT-D results as a function of basis set and CP correction for methane dimers

	$(CH_4)_2$ D_{3h} (eclipsed)			$(CH_4)_2$ D_{3d} (staggered)	
method	s_6	ΔE (kcal/mol)	R_e (Å)	ΔE (kcal/mol)	R_e (Å)
B97-D/TZV(2d,2p)	1.25			-0.567	3.792
B97-D/TZV(2d,2p) + CP	1.25			-0.558	3.792
B97-D/cc-pVDZ	1.25	-0.743	3.600	-0.782	3.606
B97-D/cc-pVDZ + CP	1.25	-0.527	3.600	-0.558	3.606
B97-D/cc-pVDZ opt	1.00	-0.521	3.747	-0.548	3.792
B97-D/cc-pVDZ + CP opt	1.39	-0.882	3.595	-0.924	3.518
B3LYP-D/TZV(2d,2p)	1.25	-0.778	3.411	-0.830	3.409
B3LYP-D/TZV(2d,2p) + CP	1.25	-0.518	3.411	-0.545	3.409
B3LYP/cc-pVDZ		unbound		unbound	
B3LYP/cc-pVDZ + CP					
Grimme[a]				-0.56	3.78
experiment[b]				-0.33 to -0.46	3.84 to 4.27

[a]Ref[23] [b]Experimental range of values from refs[41–46]. Counterpoise(CP)[47].

Table 2.4: Relative relationship between contact surface and polar moment in benzene dimer structures

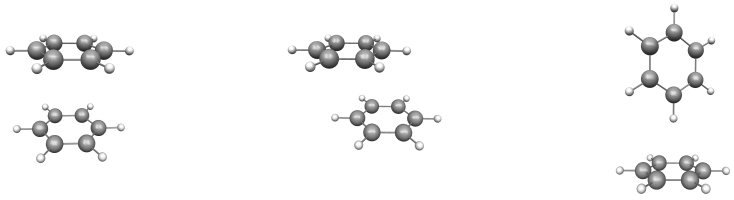

PS PO EF

conformations	contact surface (CS)	polar moment (PM)	relative relationship
PS	maximum attraction	repulsive	CS < PM
PO	medium attraction	attractive	CS $\approx$ PM
EF	minimum attraction	attractive	CS << PM

CP treatment. One immediately sees that B3LYP+CP is very poor, actually predicting methane dimer to be unbound. In contrast, the addition of the semiempirical dispersion correction overshoots the mark, predicting the methane monomers to be too close and too strongly bound. B97-D/cc-pVDZ actually does a comparable job to the larger basis set with the inclusion of CP, albeit again, slightly over bound. Ultimately, the study indicates the need for at least triple-ζ whenever feasible, but that the B97-D functional does a reasonable job even for double-ζ.

Benzene Dimers

Although benzene dimer structures can adopt a continuum of different relative orientations, three prototype structures are typically considered, parallel-stack (PS), parallel-offset (PO), and edge-to-face (EF) (Table 2.4). Whereas the PO and EF are stable minima, the PS is a transition state structure. Two important considerations in these dimers is the balance between contact surface (CS) and polar moment (PM). The polar moment overlap in PS is much larger than in the other two cases, resulting in maximum repulsive polar moment. In the PO structure, the two contributions are quite similar and offer moderate attraction between the two benzenes, while the EF structure has minimal attraction with the contact surface compared to the much larger polar moment attraction.

It is well known that non-dispersive DFT functionals, in particular the popularly exploited B3LYP, give a purely repulsive interaction for the PO configuration of the benzene dimer. Our goal in this work is to see how the DFT-D methods discussed above perform for this complex. The best theoretical estimate of the interaction energy for the PS conformation has been provided by Sinnokrot and Sherrill, at the CCSD(T)/aug-cc-pVQZ* (modified basis set) level of theory[50], enabling us to compare complete disssociation curves.

Here we have investigated the B3LYP-D, B97-D, PBE-D, and revPBE-D, with optimized s_6 parameters for the cc-pVDZ basis set. While it is true that one would choose a more substantial basis set for this small system, our goal is to determine feasibility of double-ζ level basis sets for the purpose of extending these methods to significantly larger aryl/aryl systems shown below. Full dissociation curves have been computed for each of

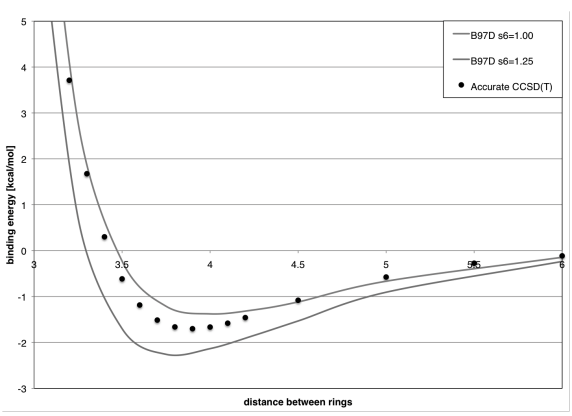

(a) B97-D/cc-pVDZ, $s_6 = 1.25$ *vs.* $s_6 = 1.00$

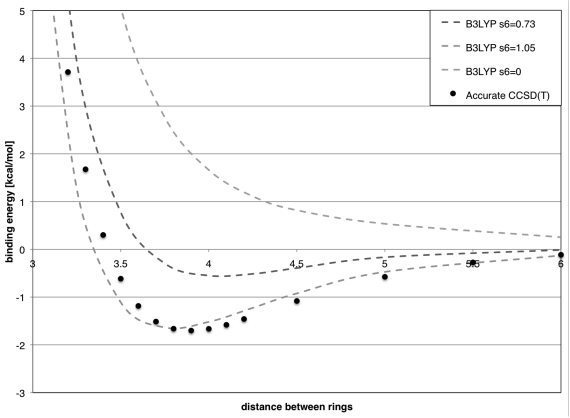

(b) B3LYP-D/cc-pVDZ, $s_6 = 1.05$ *vs.* $s_6 = 0.73$

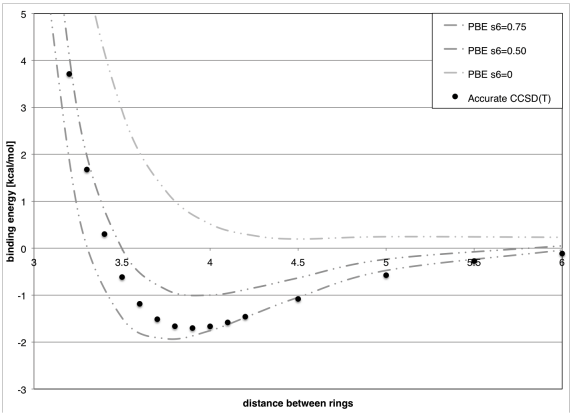

(c) PBE-D/cc-pVDZ, $s_6 = 0.75$ *vs.* $s_6 = 0.50$

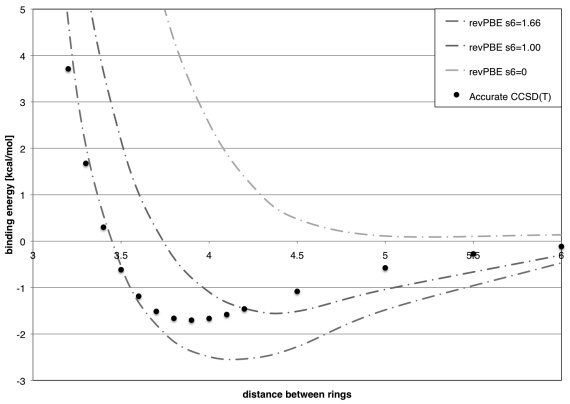

(d) revPBE-D/cc-pVDZ, $s_6 = 1.66$ *vs.* $s_6 = 1.00$

Figure 2.12: energy as a function of intermolecular distance for the benzene face-to-face dimer complex compared to the CCSD(T) reference curve, for different functionals

the four functionals. These dissociation curves, in comparison to the high quality curve of Sherrill and Sinnokrot, provide a better understanding of how the methods appropriately reproduce the strength of the π/π interactions as a function of distance and orientation of the rings. All curves have been constructed using single-point energy calculations of the dimer at variant intermolecular benzene-benzene distance, using experimental benzene internal geometry. Results are shown Figure 2.12 for the different functionals.

Of the functionals investigated, the B97-D functional appears to be one of the better functionals for prediction of the interaction energy profile for the benzene dimer, keeping in mind that the optimization of the s_6 parameter plays a key role when moving from double-ζ to higher order basis sets. For the popularly used B3LYP functional, we note the anomaly that the non-optimized curve ($s_6 = 1.06$) has a better behavior than the optimized curve, primarily due to a cancellation of errors. The s_6 optimization for the PBE functional does not have a particularly large influence on single-point energies at experimental equilibrium geometries. Even if the single-point energy looks worse, the minimum of the optimized curve is nearly predictive of the experimental optimal distance, while the

non-optimized curve predicts over-binding. The two PBE based functionals have globally acceptable results, with errors reduced from 6 kcal/mol using unoptimized s_6 to almost 2 kcal/mol when used with the optimized s_6 parameters. This supports considerations of its general use for significantly large systems.

The best estimate of the interaction energy for the PS conformation, evaluated at the equilibrium intermonomer distance, is provided by the CCSD(T)/aug-cc-pVQZ* (modified basis set) potential energy curve of Sinnokrot and Sherrill, at -1.70 kcal/mol. For reference, their MP2/aug-cc-pVDZ and CCSD(T)/aug-cc-pVDZ numbers are -2.83 kcal/mol and -1.33 kcal/mol, respectively. The experimental dissociation of the benzene dimer, determined by Grover in 1987, is found to be in the range -2.0 to -2.8 kcal/mol. Here, as seen above with the methane dimers, the B3LYP-D functional performs quite poorly. However, using the B97-D functional, we obtain -1.70 kcal/mol with TZV(2d,2p) and optimized s_6 values of Grimme, (-1.559 including CP), and -1.34 kcal/mol using our optimized s_6 values for cc-pVDZ, in very close agreement to that obtained with the CCSD(T)/aug-cc-pVDZ, -1.33.

2.5.2 Research Applications

peri-substituted biphenylene

There is considerable interest, both from an experimental as well as a theoretical perspective, of alkyl-π and aryl-π interactions, due to their importance in many applications from materials to biological systems. Many such studies predict a) that dispersive forces dominate the interaction, b) a repulsive nature of the PS, and attractive nature of the PO and EF, and c) that both electron donating (ED) as well as electron withdrawing (EW) groups enhance stacking interactions[51–55]. Experimental evidence for the repulsive interaction in the PS conformation has been demonstrated by Siegel and Cozzi through a number of investigations[56–59] of substituted 1,8-diarylnapthalenes and confirmed by others[60,61], which aid in the rationalization of a variety of other experimental results in different fields. Experimental evidence for the EF conformation, involving the interaction between the CH groups of the edge ring and the π electron density of the face ring, has been less conclusive, some indicating sensitivity to changes in the local charge distribution on the rings, while others finding no particular sensitivity.

Experimental studies, again by Cozzi and Siegel together with our theoretical contributions, focused on the PO conformation in two conformationally restricted polycyclic systems, and showed that through-space interactions between PO oriented arenes is strongly influenced by electrostatic effects. Therefore, because these same interactions are important in EF and PS structures, polar-π interactions are seen to be a decisive factor for understanding arene-arene interactions.

In a more recent theoretical investigations together with the experimental groups of Siegel and Cozzi[62], we proposed a model for systematic investigation of a PO geometry polar-π interactions between arenes spaced at vdW distances, enabling us to provide a direct comparison of experiment and theory across different functional group modifications. A set of 1,8-diarylbiphenylene comprising two Hammett series was investigated (Figure 2.13). The model provides an excellent test to compare the sensitivity of DFT models to pick up appropriate polar-π interactions between the two arenes. In particular, here compare the following functionals: B97-D, BMK, M06-2X, and B3LYP. Results are

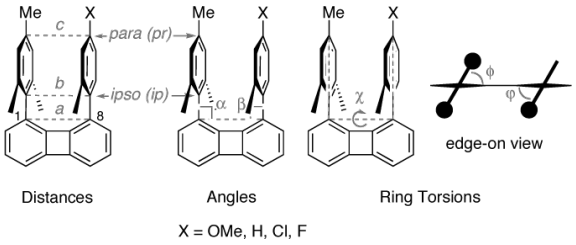

(a) peri-substituted biphenylene as a model for PO benzene dimers

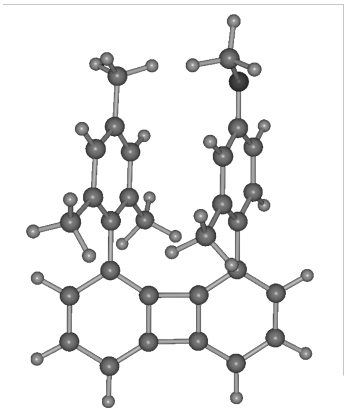

(b) representative OMe-substituted biphenylene

Figure 2.13: biphenylene

shown for the cc-pVDZ basis set, however, triple-ζ, additional polarization, and diffuse functionality, were also investigated, with no significant change in the following trends. The following substituents were considered: OMe, H, Cl, and F. Two possible ground state conformations are possible corresponding to a slight canting of the aryl groups such that the methyl of the probe ring is either endo or exo. All derivatives tend to adopt the endo conformation by $\sim$2-5 kJ/mol, consistent with crystallographic forms found for this series.

In the previous work, we found a distinctly better performance of BMK for predicting geometry in the entire series across ten geometric parameters used to describe this inter-arene interaction. Table 2.5 reports calculated results across these 10 geometric parameters for the substituents X = OMe, H, Cl, and F, using our B97-D implementation. Additionally, the barrier to rotation of the probe aryl ring are determined and compared to experimental values that are derived from dynamic NMR data. The critical distances a, b, c, and the interplanar (ip) stacking distance, in particular show how the different functionals respond to the polarizability and vdW effects.

A regression analysis of experiment *vs.* theory for X = H, Cl, and F, all show excellent prediction, with regression coefficients of $R = 0.9988$, $R = 0.9999$, and $R = 0.998$, respectively. The largest errors occur in the case of X = H and X = F, for the parameters ϕ and ψ, which are associated with the canting of the rings with respect to each other. All barriers are predicted to be within 1.3 kcal/mol of the reported experimental values.

Results of a comparison across four density functionals for two of the substituted diarylbiphenylenes, X = H and X = Cl, was also carried out (Table 2.6a). The B3LYP functional shows the largest deviation from experimental values in both cases as expected. The interaction between the aryl rings is underestimated interaction, as reflected in the greater distance found between the two aryl rings, and the small barrier to rotation of the probe ring. In the opposite extreme is M06-2X, which overestimates the interaction, resulting in aryl rings that are too close, and resulting barrier to rotation that is too large.

Table 2.5: B97-D/cc-pVDZ structure and rotational barrier results for the set of 1,8-diarylbiphenylenes, with substitutents X = OMe, H, Cl, and F

	X = OMe	X = H		X = Cl		X = F	
Parameter	calcd	calcd	expt	calcd	expt	calcd	expt
a (Å)	3.8168	3.8251	3.80(1)	3.8262	3.773(6)	3.8260	3.797(5)
b (Å)	3.7962	3.8276	3.89(1)	3.8312	3.815(6)	3.8263	3.812(5)
c (Å)	3.6768	3.7442	3.84(1)	3.8532	3.776(6)	3.7146	3.715(5)
α (deg)	89.3	89.7	90.7(4)	89.8	90.3(2)	89.8	90.3(1)
β (deg)	89.7	90.3	92.3(4)	90.3	91.2(3)	90.1	90.3(1)
ϕ (deg)	60.1	62.8	61.0(9)	62.8	62.1(6)	62.7	65.8(3)
ψ (deg)	56.9	59.4	65.1(9)	59.5	59.2(7)	58.6	65.8(3)
χ (deg)	8.1	2.8	3.0(2)	2.9	3.7(1)	2.8	2.4(1)
$ip_\perp$ (Å)[a]	3.42	3.43	3.595(6)	3.40	3.456(4)	3.42	3.544(2)
$pr_\perp$ (Å)[a]	3.46	3.39	3.607(7)	3.46	3.481(4)	3.43	3.490(3)
barrier[b]	11.6	10.9	9.7	10.9	10.1	11.9	10.6

[a] $ip_\perp$ and $pr_\perp$ = orthogonal distance from ipso- or para-carbon of reference ring to mean plane of probe ring, respectively. [b]Experimental determinations were performed in solvent.

Table 2.6: **(a)** Structural and rotational barrier results and **(b)** structural and rotational deviations from experimental results for a subset of 1,8-diarylbiphenylenes with substitutents X = H and Cl

(a)

	X = H				X = Cl			
Parameter	B3LYP	M06-2X	BMK	B97-D	B3LYP	M06-2X	BMK	B97-D
a (Å)	3.8699	3.7948	3.8357	3.8251	3.8637	3.7949	3.8291	3.8262
b (Å)	4.0547	3.7677	3.8915	3.8276	4.0177	3.7620	3.8483	3.8312
c (Å)	4.5661	3.6614	4.0101	3.7442	4.3911	3.6316	3.7800	3.8532
α (deg)	93.3	88.6	90.9	89.7	92.7	89.3	90.4	89.8
β (deg)	93.8	90.3	91.2	90.3	93.2	89.4	90.3	90.3
ϕ (deg)	71.1	63.5	65.4	62.8	71.1	63.7	65.5	62.8
ψ (deg)	68.1	61.1	61.6	59.4	67.8	60.2	60.7	59.5
χ (deg)	0.2	1.4	2.1	2.8	0.6	2.0	1.6	2.9
$ip_\perp$ (Å)	3.76	3.51	3.38	3.43	3.75	3.47	3.37	3.40
$pr_\perp$ (Å)	4.22	3.63	3.30	3.39	4.08	3.40	3.27	3.46
barrier	8.8	12.9	9.8	10.9	8.7	13.4	10.0	10.9

(b)

	3b (X = H)				3d (X = Cl)			
Parameter	B3LYP	M06-2X	BMK	B97-D	B3LYP	M06-2X	BMK	B97-D
a (Å)	0.0689	-0.0062	0.0347	0.0241	0.0901	0.0213	0.0555	0.0526
b (Å)	0.1637	-0.1233	0.0005	-0.0634	0.2021	-0.0536	0.0327	0.0156
c (Å)	0.7251	-0.1796	0.1691	-0.0968	0.6145	-0.1450	0.0034	-0.0766
α (deg)	2.6	-2.1	0.16	-1.0	2.4	-1.0	0.10	-0.50
β (deg)	1.5	-2.0	-1.14	-2.0	2.0	-1.9	-0.94	-0.91
ϕ (deg)	10.0	2.4	4.3	1.7	9.0	1.6	3.3	0.68
ψ (deg)	2.9	-4.1	-3.6	-5.8	8.9	0.9	1.5	0.24
χ (deg)	-2.8	-1.6	-0.92	-0.22	-3.1	-1.8	-2.1	-0.77
$ip_\perp$ (Å)	0.16	-0.08	-0.21	-0.16	0.29	0.01	-0.09	-0.05
$pr_\perp$ (Å)	0.61	0.02	-0.31	-0.22	0.60	-0.08	-0.21	-0.01
barrier	-0.90	3.2	0.10	1.2	-1.3	3.3	-0.10	0.80

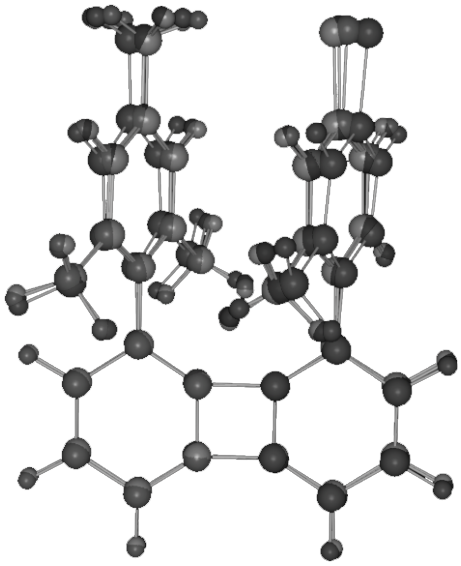

Figure 2.14: peri-substituted biphenylene (X = Cl) for functionals B97-D (brown), BMK (blue), M06-2X (green), and B3LYP (red)

The BMK functional provides very good agreement with experiment. The newest addition, B97-D is very close to the BMK results, the major difference being the amount of canting of one ring with respect to each other, and the predicted barriers for the former are slightly higher. The interplanar distances $ip_{\perp}$ and $pr_{\perp}$ are predicted to be on average 3.4 for both BMK and B97-D, which is what is found experimentally, as this parameters is relatively constant over the series of functional modifications. Figure 2.14 illustrates this phenomenon in an overlay of all four functional predictions for the X = Cl substituted compound. Here, one can clearly see the difference in association of the two aryl rings using the different functionals. Table 2.6b shows the deviations from experimental results across the entire set. Across all parameters, the B97-D provides a uniform agreement with experimental results for all substituents, providing a high degree of predictability. The largest error is, again, associated with the tilt angle of the two rings with respect to each other.

Corannulene

Corannulene as a shallow bowl structure undergoes a dynamical bowl inversion process. The bowl inversion relates two symmetry-equivalent minima through a common flat structure transition state. Our previous investigations[63] involving systematic study of the differences in bowl-inversion barriers and bowl depth for a variety of substituted corannulene derivatives established a predictive structure-energy correlation, wherein deeper bowl depth gives rise to higher inversion barrier, and vice versa. This correlation, $\Delta E = -a\left(x_{eq}\right)^4$ leads to a quartic relationship between the inversion energy (ΔE) and equilibrium bowl depth (x_{eq}), and holds for a large subset of corannulene derivatives.

As well established, the B3LYP/cc-pVDZ level of theory happens to provide highly accurate predictions of structural parameters of corannulene and substituted derivatives as compared to experiment, however, significantly underestimates the barrier to inversion. Møller-Plesset perturbation theory of order 2 (MP2) carried out at the optimized

B3LYP/cc-pVDZ geometry enables accurate predictions of the barrier. This protocol is reliable for many functionalized corannulene derivatives, and appears to be only compromised when secondary structural interactions in specific derivatives, such as additional vdW interactions, can occur.

We have investigated the sensitivity of various density functionals with regard to structure and properties of corannulene, including the simple LDA of SVWN, several GGAs, such as BP86, BLYP, PBE, PBE0, several meta-GGA's and hybrid methods, such as X3LYP, PW91, and most importantly for the structures with secondary interactions, the series of B97 functionals and the BMK and M06-2X functionals. We have added dispersion corrections to many of these functionals (indicated here with the appended "-D" notation), using optimized scale-factors (Table 2.7), and tested them out on the corannulene structure and dynamics.

The high degree of symmetry of corranulene makes it difficult to obtain a precise value for the barrier to the bowl-to-bowl inversion process, but has been estimated from a series of functionalized structures to be about 11.5 kcal/mol. The best theoretical estimate to date is 11.1 kcal/mol, at MP2/cc-pVDZ//B3LYP/cc-pVDZ, including ZPE. The ability to accurately estimate the barrier is directly related to the ability to accurately predict the structural parameters, due to the known structure/energy correlation of bowl depth and inversion barrier. While the bond lengths and angles are quite well reproduced with respect to the experimental predictions, the more difficult geometric feature seems to be the bowl depth and curvature.

As expected, the general functionals can be highly improved using dispersion corrections. The most noticeable difference in the results are a slight increase in bowl depth, resulting in an increase in barrier, as would be predicted from the established bowl/depth functional relationship. The best results are obtained with the B97-D functional, which reaches the performance of the MP2 single point calculations for both reaction barrier and dipole moment predictions. Across all functionals, the barrier is still lower than the experimental value, however, the experimental value is only an estimate due to the high symmetry of the molecule. The BMK functional gives surprisingly good performance across many functionalized corannulenes as well as this unsubstituted case, likely due to the high percentage of HF exchange with terms dependent on the kinetic energy density, suitable for describing the aromatic nature. The M06-2X functional provides quite good agreement with respect to the experiment, although noticeably higher on many of the properties with respect to the other B97-D functionals and BMK.

sym-1,3,5,7,9-pentamanisylcorannulene

Motivated by its deeper bowl depth and higher barrier to inversion, *sym*-1,3,5,7,9-pentamanisylcorannulene has been thoroughly investigated both experimentally as well as computationally. We have previously shown that, without proper treatment of dispersion, one can not adequately predict important structural features or dynamic properties, for example, bowl depth, barrier, and kinetic isotope effects. Further investigations revealed that vdW attractive forces among the peripheral endo methyl groups in this case could contribute to a stabilization of the bowl (ground state) relative to the flat form (transition state), thereby increasing the barrier height. The structure represented a computational challenge for DFT methods, but also for conventional methods due to its large size.

Geometry optimizations carried out using several functionals are reported in Table

Table 2.7: Barrier to interconversion, bowl depth and dipole predictions for corannulene using various density functionals, and the cc-pVDZ basis set

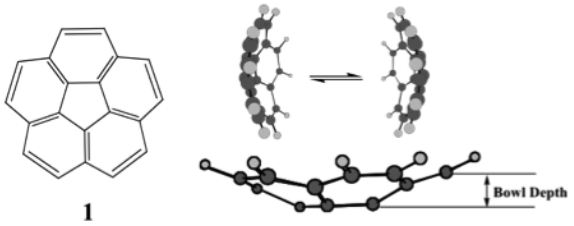

1

Functional	ΔE^a (kcal/mol)	TS frequency (cm^{-1})	Bowl Depth (Å)	dipole (debye)	-(HOMO)^c (eV)
B3LYP	9.33 (9.21)	-109.1	0.87	1.88	6.0 (8.2)
MP2//B3LYP	11.12 (10.99)			2.29	
BLYP	8.74 (8.63)	-105.2	0.88	1.76	5.2 (6.7)
BP86	9.10 (9.09)	-107.9	0.89	2.00	5.6 (7.0)
PBE	9.41 (9.44)	-109.6	0.89	1.97	5.5 (7.0)
SVWN	9.98 (9.71)	-108.3	0.90	2.10	5.7 (7.2)
PBE0	9.50 (9.68)	-112.9	0.88	2.09	6.4 (8.8)
PW91	9.33 (9.31)	-108.9	0.89	1.94	5.5 (7.0)
X3LYP	9.09 (9.13)	-109.5	0.87	1.89	6.2 (8.4)
B97	9.19 (9.29)	-109.7	0.88	2.00	6.1 (8.2)
B97-1	9.25 (9.33)	-109.7	0.88	2.02	6.1 (8.3)
B97-2	9.56 (9.76)	-112.9	0.88	2.06	6.2 (8.4)
B3LYP-D	-9.96		0.90	1.94	6.0 (8.2)
BLYP-D	-9.67		0.91	1.82	5.2 (6.7)
BP86-D	-10.05		0.92	2.07	5.6 (7.1)
PBE-D	-10.19		0.91	2.00	5.5 (7.9)
revPBE-D opt	-9.55		0.92	1.67	4.3 (5.8)
B97-D	-10.39		0.92	2.03	5.4 (6.9)
B97-D opt	-10.10		0.91	2.00	5.4 (6.8)
BMK	8.66 (8.84)	-104.0	0.88	2.14	6.9
M06-2X	9.98 (10.01)	-118.2	0.89	2.19	7.5
MP2/cc-pVDZ	9.11	-115.4	0.91	2.45	8.0
experiment	est. 11.5		0.87	2.071(18)^b	8.37

^{a}Values in parenthesis are without ZPE. Hessians not yet available for dispersion functionals.
^{b}Ref[64]. ^{c}While it has been shown that there is a correlation between HOMO eigenvalue and ionization potential, the absolute estimate is not a reliable measure of I.P. Values in parenthesis have been scaled according to the 3*HOMO - LUMO. Experimental IP is 8.37 eV and MP2/cc-pVDZ Koopmans Theorem = 7.99 eV, ΔSCF = 8.77 eV.[65]

Table 2.8: Computed geometry of *sym*-1,3,5,7,9-pentamanisylcorannulene compared to experimental geometry, for a variety of density functionals

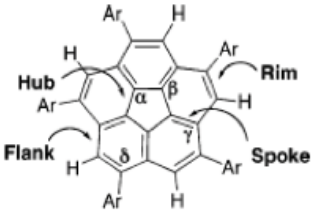

parameter	B3LYP	M06-2X	B97D	B97D opt	revPBE opt	MP2	Expt
C-C hub (Å)	1.418	1.420	1.4264	1.4252	1.4539	1.4245	1.413(4)
C-C spoke (Å)	1.385	1.381	1.3989	1.3975	1.4233	1.4051	1.382(4)
C-C flank (Å)	1.461	1.455	1.4580	1.4601	1.4908	1.4527	1.452(4) leyward
	1.450	1.446	1.4476	1.4496	1.4802	1.4442	1.446(4) wayward
C-C rim (Å)	1.399	1.388	1.4016	1.4033	1.4279	1.4099	1.381(8)
angle α (sym) (deg)	108.0	108.0	108.0	108.0	108.0	108.0	108.0(4)
angle β (sym) (deg)	123.4	122.8	122.5	122.0	122.0	122.4	124.3(4)
angle γ (sym) (deg)	114.8	115.4	115.9	115.6	115.7	115.8	111.9(4)
angle δ (sym) (deg)	120.3	120.6	120.3	120.4	120.3	120.7	122.2(4)
bowl depth (Å)	0.85	0.94	1.02	0.98	1.01	1.01	0.91
$Me_{endo}(1)$-$Me_{endo}(2)$ (Å)	4.62	4.35	4.24	4.37	4.4	4.2	4.4
$Me_{endo}(1)$-$Me_{endo}(3)$ (Å)	7.47	7.04	6.86	7.08	7.14	6.76	7.1
Ar-Cor torsion (deg)	79.6	72.2	82.4	83.7	83.4		79
inversion barrier (kcal/mol)	8.84 (14.09)[a]	12.65	16.6	14.2	14.2	–	12.2-12.5

[a]MP2/cc-pVDZ//B3LYP/cc-pVDZ

2.8. While B3LYP/cc-pVDZ quite accurately predicts basic structural parameters as well as bowl depth and curvature for essentially all previously investigated corannulene derivatives, the functional comes short for sympentamanisylcorannulene. Of the bond lengths, the edge bonds (leyward flank and rim bonds) have the largest error compared to experiment, both overestimated by 1 ppm. M06-2X does much better, but still is off by nearly 1 ppm for the C-C hub bond.

Prediction of bowl depth and associated methyl/methyl distances and torsions are more challenging. B3LYP/cc-pVDZ would predict a bowl depth of 0.85 Å compared to the experimental value of 0.91 Å. Given a structure-correlation formula of $E = ax^4 - bx^2$, this difference in bowl depth would translate into a large underestimation of the barrier to inversion, as is verified in the computation at 8.84 kcal/mol. Correction with the MP2 single point then over-shoots the barrier by a significant amount at 14.09 kcal/mol, but this can be expected since the depth of the bowl is not corrected, but only the dispersion effects at the B3LYP/cc-pVDZ predicted geometry are included. M06-2X predicts the bowl depth to be slightly deeper (0.03 Å) than experimental predictions, and thus the barrier to inversion is also about 1 kcal/mol too high. In all of the semiempircally corrected functionals, B97-D, B97-D with opt s_6, and revPBE with opt s_6, the geometry of the base corannulene nucleus is not as good as with our standard, B3LYP, predicting bonds that are longer than experiment in most cases, although B97-D is quite good. The revPBE with optimized s_6 parameters is quite far off in the bond lengths of the basic corannulene nucleus, and overestimates the bowl depth. In terms of bowl depth and barrier prediction, the B97-D with optimized s_6 parameter is slightly better than MP2/cc-pVDZ, at a significant reduction in computational cost.

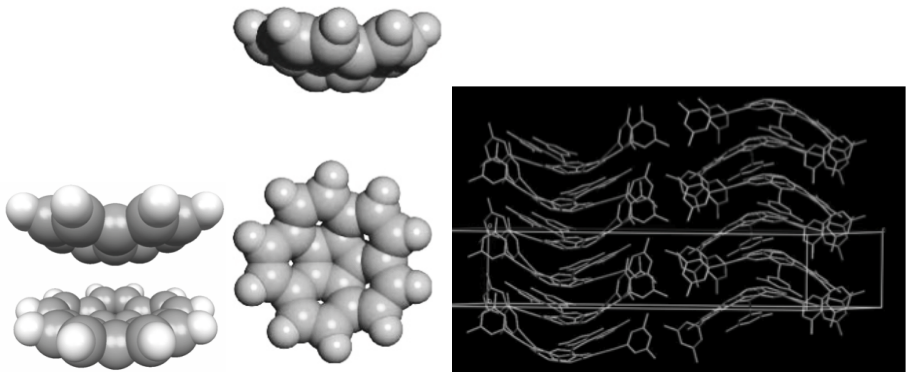

Figure 2.15: Example of stacking motifs and packing of corannulene and functionalized corannulene

Higher order constructs of corannulene

The ability to model inter-corannulene interactions, as associated with packing in the crystal, or complexes of substituted stacked corannulenes, is very much associated with proper modeling of vdW interactions, (Figure 2.15). For example, interesting packing characteristics have been observed in the experimental crystal structures depending on functionalization, resulting in important materials properties[66–71]. Even though corannulene itself is not a $4n+2$ Hückel system, the electronic structure would suggest a configuration that allows for a 6-electron cyclopentadienyl anion in the center, and a 14-electron cation as the outer most ring, each of which does satisfy a $4n+2$ cycle ($n=2$ and $n=3$, respectively). In addition, experimentally, corannulene behaves like other aromatic compounds, for example undergoing electrophilic substitution reactions. As such, one might expect stability for dimers, trimers, and higher order stacks, dominated by vdW interactions. We are therefore in the process of considering larger corannulene dimers and stacks with the new dispersion models. Carrying out the dimer computation on the PS conformation of corannulene, with B3LYP/cc-pVDZ and B97-D/cc-pVDZ, predict inter-stack distances of 4.63 Å and 3.55 Å, respectively. Because of the much larger surface area of corannulene over benzene, we see a much larger effect of dispersion, further illustrating the inadequacy of B3LYP. Additionally, only for the B97-D is the stack predicted to be bound, by 6.23 kcal/mol, significantly more than found for the benzene dimer. Further investigations of stacks and functionalized stacks are now ongoing.

Alternatively, it is of interest to investigate binding characteristics of metal-organic complexes comprised of (substituted) corannulenes with a planar metal surface[72,73]. Such studies enable investigation of molecular self-organization processes of adsorbate molecules on the surface that can be responsible for formation of supramolecular aggregates. Two-dimensional assembly into supramolecular structures is of great interest for studying fundamental processes, such as molecular[74,75] and chiral recognition[76–81]. Moreover, functionalization of surfaces by adsorption of large organic molecules appear as an important route towards new materials or templates for heterogeneous catalysis[82] and molecular electronics[83].

Attempts to incorporate solutions to failures involving nonlocal, long-range electron correlation directly into a density functional can result in rather complicated formulations, leading to expressions at least as complex as some wavefunction methods. Ex-

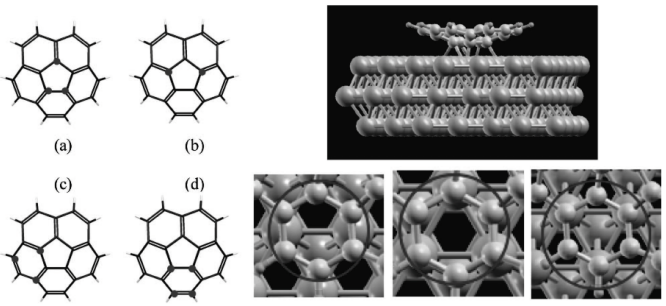

Figure 2.16: (left) Possible binding motifs of corannulene on Cu(111), (a) η^5-hollow site, (b) η^5-bridge site, (c) η^6-hollow site, (d) η^6-bridge site. (right, top) one conformation of corannulene on Cu(111) surface. (right, bottom) hcp hollow site, bridge site, and fcc-hollow site

amples include the vdW-DFT method that has just recently been implemented in the SIESTA software and the first principles approach suggested by Kohn[84], which breaks the Coulomb interaction into a short and long-range (adiabatic connection formula) component of which only the long-range contributes to the vdW energies. Ongoing work with the SIESTA group involves further testing the vdW-DFT method in the SIESTA software and considerations of practicality for the ongoing corannulene on surface computations.

Motivated by the work involving the semiempircally corrected DFT fucntionals, we have in the meantime proceded to implement a protocol for investigations involving complex Cu(111)+corannulene surface interactions, using GAMESS together with the surface modeling software, SIESTA, the latter of which also now has the semiempirical dispersion correction implemented. We have tested this method out on various conformational possibilities of corannulene on a 3 layer Cu(111) surface, as depicted in Figure 2.16. .

While results suggest that functionals such as B3LYP, revPBE, or BLYP, all predict the corannulene + Cu(111) to be repulsive or only weakly bound, depending on the particular conformation of corannulene on the surface, the semiempirical correction enables more realistic modeling of the complexation process (Table 2.9). Using a double-ζ quality basis set supplemented with extra diffuse functions for the copper surface, we are able to perform computation of corannulene in several different conformational possibilities on a 3 layer slab of Cu(111) plus corannulene. These preliminary results show promise for realistic modeling on a metallic surface, as compared to known STM results on the same system, enabling a more detailed research investigation including an increase to a 6 layers slab, which will be the subject of a future publication.

2.5.3 Conclusions

At the onset of this work, our major concerns were to implement more optimal DFT functionals for the purpose of accurate predictions of large molecular polynuclear carbon-based complexes and corannulene on copper surfaces, all of which have dominant dispersion interactions. We have implemented several additional functionals into GAMESS, together with a semiempirical dispersion correction that can be applied with these and other functionals within GAMESS. We have also implemented and tested the B2-PLYP double-hybrid functional. For functionals with a semiempircal correction, we have carried

Table 2.9: Computed geometry of corannulene conformations on Cu(111) surface, comparing the revPBE functional with and without empirical dispersion correction

parameter[a]	revPBE	revPBE-D
η^6-bridge fcc site	2.46 Å	2.23 Å
η^6-hollow fcc site	2.37 Å	2.16 Å
η^6-hollow hcp site	2.38 Å	2.18 Å
η^5-bridge site	detaches	
η^5-hollow hcp site	2.5 Å	2.36 Å

[a] Average C-C bond length for ring.

out a double parameter optimization to understand the variation in the s_R and s_6 coefficients with respect to basis set, functional type, and BSSE, and have proposed optimal values, a summary of which is shown in Table 2.10. We find overall good performance in particular of the B97-D functional. In addition, we find a convenient convergence of optimal s_6 parameter of 1.4 when BSSE is considered for the S22 set of molecules using any of the series cc-pVnZ, $n = 2-4$, as well as TZV2P, a suggested value to use when CP corrections are applied with B97-D, even though it is a relatively large value compared to non CP corrected values. The global performance of B97-D+CP in terms of MAD of the S22 set shows a slight loss of accuracy within the same basis sets, which is attributed to the error associated with the CP corrections, providing a reasonable estimate of the error associated with CP within the S22 set of molecules. Future studies will look at this phenomenon more globally.

Comparative results across functionals were given for several applications with high degree of dispersive interactions, illustrating the strengths and weaknesses in these functionals. Consistently reliable results are found for several of the functional strategies, including the exchange-correlation functional provided by BMK, the M06-2X functional, and the semiempirically corrected B97-D functional. The double hybrid functional, B2-PLYP functional is also seen to provide very good performance, but with an associated higher cost for the MP2 evaluation.

A second purpose of this work was to create a reliable protocol for investigations of polynuclear aromatic carbon species, such as corannulene, on metallic surface. Our investigations here were initially limited to the PBE and revPBE functionals in the SIESTA software, a linear scaling density functional package designed for studies involving materials. Including the semiempirical dispersion correction was seen to greatly enhance predictability of the functionals, as demonstrated in the GAMESS/SIESTA hybrid method for corannulene on Cu(111) surface results, particularly considering other strategies are too costly. Our initial investigations are quite promising, and with the results obtained in our investigations shown here, we are now actively pursuing these new capabilities with a larger Cu(111) surface.

Table 2.10: Summary of density functional plus s_R/s_6 coefficient combinations proposed for a variety of basis sets, as determined from predictions of S22 complexes

DFT Functional	basis set	s_R value	Optimized s_6 value	MAD (kcal/mol)
B97-D	cc-pVDZ	1.1	1.00	1.075
	cc-pVDZ + CP	1.1	1.39	0.518
	cc-pVTZ	1.1	1.18	0.337
	cc-pVTZ + CP	1.1	1.41	0.454
	cc-pVQZ	1.1	1.26	0.330
	cc-pVQZ + CP	1.1	1.39	0.441
	TZV(2d,2p)	1.1	1.25	0.375
	TZV(2d,2p) + CP	1.1	1.38	0.425
B3LYP	cc-pVDZ	1.1	0.73	1.709
	cc-pVTZ	1.1	0.88	0.853
	cc-pVQZ	1.1	0.96	0.612
PBE	cc-pVDZ	1.1	0.50	2.579
	cc-pVTZ	1.1	0.64	1.030
	cc-pVQZ	1.1	0.65	0.798
revPBE	cc-pVDZ	1.1	1.66	0.826
	cc-pVTZ	1.1	1.87	1.326
	cc-pVQZ	1.1	1.90	1.536
	cc-pVTZ (8-22)	1.1	1.87	0.393
	cc-pVQZ (8-22)	1.1	1.90	0.355
B2-PLYP	cc-pVDZ	1.3	0.55	1.394
	cc-pVTZ	1.3	0.55	0.517

Chapter 3

Solvation Methods

Overview

3.1 Basic ideas in solvation methods

As quantum mechanic and quantum chemistry evolved, it became more and more clear the necessity of the inclusion of the environment effects in the standard model of a vacuum calculation[1]. In particular in the experimental laboratory, chemists must address the presence of a solvent in almost every reaction environment.

An obvious way to describe solution phase by mean of quantum mechanics is to move from the description of a single molecule, to small and large clusters of molecules, and ultimately, to large ensembles of molecules. This approach was historical developed by fitting experimental or calulated data for molecules and clusters to simple expressions, *e.g.*, the morse potential. Using such a potential, cluster and ensemble properties are calculated by use of molecular mechanic (MM), molecular dynamics (MD), or Monte Carlo (MC) simulations. This is the general approach of explicit solvation methods (ESMs).

[1] sometimes referred to as gas-phase calculation. We avoid this nomenclature since we find it partially incomplete since it presumes a perfect gas situation with no interactions between molecules.

An alternative approach to solvation was developed starting from the initial idea of Max Born, where the solvent surrounding an ion is approximated asa dielectric continuum. Continuum solvation methods (CSMs) were developed from that original idea, in parallel with ESMs. In many cases, CSMs represent the most affordable, and still accurate method, to treat the effect of the environment in a quantum chemical calculation. In particular we turn our attention to the recent developments in CSMs, as they represent the main solvation methods used during this thesis work.

3.2 Continuum Solvation Methods

As briefly introduced above, continuum solvation methods (CSMs) were first proposed by Born at the beginning of the 1920s. Born's first model for the free energy of solvation of ions was obtained by defining a spherical boundary between the ion and the continuum $\left(R^{\text{ion}}\right)$, as:

$$\Delta G_{\text{S}}^{\text{ion}} = -\frac{\varepsilon_{\text{S}} - 1}{\varepsilon_{\text{S}}} \frac{Q^{\text{ion}^2}}{2R^{\text{ion}}} \tag{3.1}$$

where $\Delta G_{\text{S}}^{\text{ion}}$ is the free energy of solvation of a general ion with integer charge Q^{ion^2} and ionic radius R^{ion}, in a generic solvent with permittivity ε_{S}. We introduce here also the convention to denote the solvent with a suffix (S), and the solute with a superscript index (ion).

Born's idea was further developed by Kirkwood into a rigorous theory for atoms and molecules. The Kirkwood model includes a multipole expression for the free energy of solvation. The multipole expansion includes the electrostatic multiple moments M_l^{X}, charge, dipole, quadrupole, and higher, as:

$$\Delta G_{\text{S}}^{\text{X}} = -\frac{1}{2} \sum_{l=1}^{\infty} f_l\left(\varepsilon_{\text{S}}\right) \frac{M_l^{\text{X}^2}}{R^{\text{X}^{2l-1}}} \tag{3.2}$$

with:

$$f_l\left(\varepsilon\right) = \frac{\varepsilon - 1}{\varepsilon + \chi_l} \tag{3.3}$$

and:

$$\chi_l = \frac{l-1}{l}. \tag{3.4}$$

Since the first electrostatic moment is the total charge, Kirkwood's model reduces to the Born's model for ions. Inclusion of the second term, reduces to the well known Onsager model for the solvation energy of dipolar molecule:

$$\Delta G_{\text{S}}^{\text{X}} = \frac{1}{2} \frac{\varepsilon_{\text{S}} - 1}{\varepsilon_{\text{S}} + \frac{1}{2}} \frac{\mu^{\text{X}^2}}{R^{\text{X}^3}}. \tag{3.5}$$

Kirkwood's formula was used with higher order multipole moments only many years later, when quantum chemical calculations allowed a rigorous decomposition of molecular energies into accurate multipole moments.

A further development in continuum solvation models was achieved by the introduction of the electrostatic field into the self-consistent procedure of quantum chemistry. In

this way, the multiple moments are not considered as fixed any longer, but serve to generate a reaction field that is able to interact with the electronic structures of the molecule. With this improvement, both polarization of the solvent, as well as back-polarization of the solute in the presence of the solvent, are taken into account in the calculation. This reaction field model approach improves results obtained with the Onsager or Kirkwood models by an average 20-30%.

At the same time it became clear that spherical cavities were not sufficiently accurate, particularly as matched with the reaction field models. The introduction of molecular-shaped cavity, however, brought with it the additional problem of the absence of analytical solutions for the reaction field. Three different approaches have been developed to overcome this major limitation:

1. The first approach for the introduction of molecular-shaped cavities is to search for approximated solution of the reaction field equations for this kind of cavity. This approach led to the generalized Born models (usually abbreviated GB), where Cramer and Truhlar's SMx models are the most advanced examples.

2. The second approach is to obtain the reaction field $\mathbf{E}(\mathbf{r})$ by solving the very complicated, but rigorous, mathematical model, called the nonhomogeneous Poisson equation for the volume polarization density $\mathbf{P}(\mathbf{r})$:

$$\mathbf{P}(\mathbf{r}) = \frac{\varepsilon(\mathbf{r}) - 1}{4\pi}\mathbf{E}(\mathbf{r}) \tag{3.6}$$

   followed by search for approximated solution (numerical integration, linearized Poisson-Boltzmann equation, etc.).

3. A third approach is to represent the electronic density distribution of the solute as partial charges on the surface of the cavity, and replacement of the complicated volume polarization density $\mathbf{P}(\mathbf{r})$ with the much simpler surface polarization charge density $\sigma(\mathbf{r})$. The reaction field $\mathbf{E}(\mathbf{r})$ is then obtained using a simpler set of linear equations that can be treated with matrix algebra:

$$4\pi\varepsilon_S\sigma = \mathbf{E}_n + \mathbf{E}_n(\sigma). \tag{3.7}$$

   Different approaches for the calculation of the partial charges and for the algebraic treatment, lead to different solvation methods, including the polarizable continuum model (PCM) of Miertus' and Tomasi's groups, and the conductor like screening model (COSMO) of Klamt and Schüürmann.

The COSMO method and its subsequent developments have been used in this thesis, and will be described in the next paragraph (§ 3.2.1).

3.2.1 COSMO and its ab-initio implementation

The Conductor-like Screening MOdel (COSMO) was introduced by Andreas Klamt and Gerrit Schüürmann in 1993[85]. Klamt's key idea involved use of perfect-conductor boundary conditions to calculate the charges on the cavity surrounding the molecule and their corresponding reaction field.

The ab-initio implementation of COSMO, termed COSab, was first proposed through a collaboration between Andreas Klamt and Kim Baldridge in 1997[86]. Work in this thesis was based on this original COSab implementation. The original concept is, nevertheless, the same, and is briefly present here.

Consider the solute molecule enclosed by a cavity, which represents the boundary to the continuum. Let this cavity consist of m surface segments that are small enough to be handled as homogeneous for the calculation of the electrostatic screening of the solute by the continuum. Let the m-dimensional vector, $\Phi = (\Phi_1, \ldots, \Phi_m)$, be the set of electrostatic potentials arising on the m cavity segments from the charge distribution of the solute. This potential will cause screening charges, $\mathbf{q} = (q_1, \ldots, q_m)$, arising from the polarization of the continuum. Let the matrix $\mathbf{A}$ be the Coulomb interaction matrix of these screening charge, taking into account the self-interaction of a homogeneous charge distribution on a segment, by the diagonal elements A_{ii} . For the details of the evaluation of $\mathbf{A}$ again see the main article of Klamt and Schüürmann[85].

Following the concept "conductor-like screening model", we first consider the ideal screening charges, $\mathbf{q}^*$, which would arise in a conducting continuum. This case is equivalent to a dielectric continuum with infinite permittivity ($\varepsilon = \infty$). For a conductor, we have the condition that the total potential arising on the surface segments due to the solute and the screening charges has to vanish. Since the potential caused by screening charges, $\mathbf{q}$, is given by $\mathbf{Aq}$, we have

$$0 = \Phi + \mathbf{A}\mathbf{q}^* \quad \Longrightarrow \quad \mathbf{q}^* = -\mathbf{A}^{-1}\Phi. \tag{3.8}$$

Now, the screening charges, $\mathbf{q}$, in a finite dielectric are very well approximated as

$$\mathbf{q} = f(\varepsilon)\,\mathbf{q}^*, \tag{3.9}$$

with

$$f(\varepsilon) = \frac{\varepsilon - 1}{\varepsilon + 0.5}. \tag{3.10}$$

The interaction energy of the solute with the screening charges is given by the scalar product

$$E_{\text{int}} = \Phi\mathbf{q}. \tag{3.11}$$

However, half of this energy gain is needed for the creation of the dielectric polarization, *i.e.*, of the screening charge distribution, so that in essence, the net energy gain of the system due to the dielectric screening is given by

$$E_{\text{diel}} = \frac{1}{2}\Phi\mathbf{q} \;=\; \frac{1}{2} f(\varepsilon)\,\Phi\mathbf{A}^{-1}\Phi \tag{3.12}$$

and usually we refer to this as the dielectric energy.

Now, the algorithmic procedure for the evaluation of the self-consistent wavefunction of the solute in the presence of the dielectric continuum at fixed solute geometry is as follows:

1. As usual, we start with an initial guess for the wavefunction, and hence for the charge distribution Q. This can, but need not be, the self-consistent gas phase wave-

function.

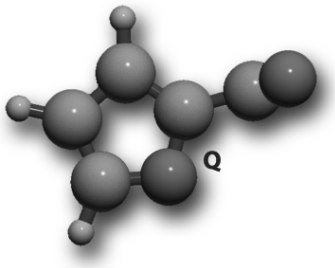

2. We build the molecular-shaped cavity using geometrical considerations. The cavity is generated using iterative refinement of sphere triangulation, following the well-established GEPOL algorithm. In the context of a refined COSab implementation, the cavity is further corrected for misfits in the intersection points of the atomic spheres (crevices).

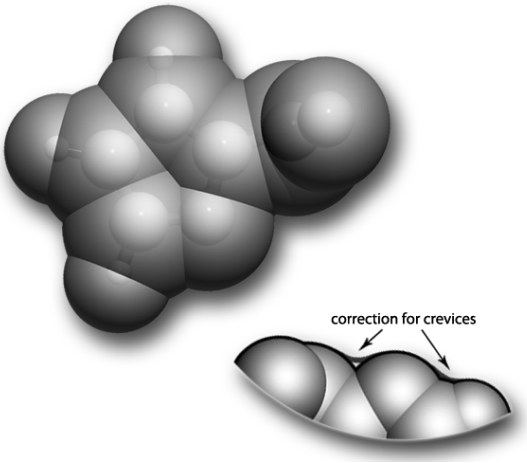

3. We generate the potential Φ and then the screening charges $\mathbf{q}$:
$\mathbf{q} = -f(\varepsilon)\mathbf{A}^{-1}\Phi$.

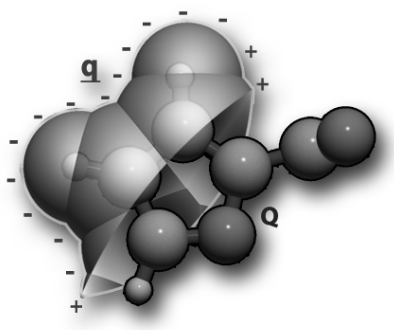

4. At this point, we resubstitute the screening charges into the one-electron Hamiltonian as external point charges, calculate the Fock matrix as usual, and do a single SCF step to yield a new energy as well as a new wavefunction. We now return to step 2 until convergence of the energy and wavefunction is achieved.

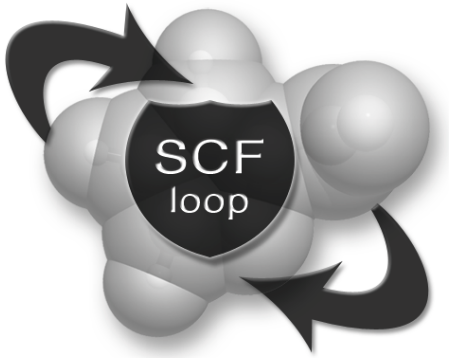

5. Once convergence is achieved, we need to remove the outlying charge error (OCE) arising from the approximation used in 3.12. We remove it using the double cavity method, that build a larger cavity around the molecule at a position that will include the entire electron density of the molecule (usually at $R \approx 2.2 \times R^{\mathrm{vdW}}$). The energy term calculated on the surface of the second cavity is exactly equal to the corrections for the OCE that we need to add to our final energy.

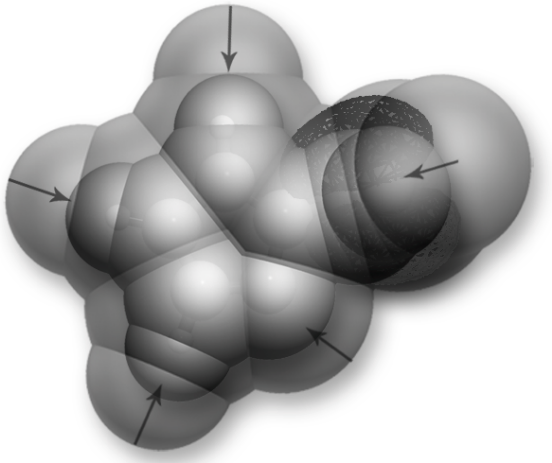

The segmentation of the outer cavity corresponds directly to that of the inner cavity, such that there is a 1:1 correspondence between outer- and inner-cavity charge points, $\mathbf{q}$. The outer cavity-segment charges, $\mathbf{q}'$, are calculated via:

$$0 = \Phi' + \mathbf{A}'\mathbf{q}' \tag{3.13}$$

where $\mathbf{A}'$ is the interaction matrix involving the segment points on the outer cavity, and Φ' represents the potential for interaction of the secondary cavity with the solute and the screening charges from the inner cavity. Since the segmentation points on both surfaces correspond, the final screening charge is represented as a correction,

$$\mathbf{q}'' = \mathbf{q} + \mathbf{q}', \tag{3.14}$$

with associated potential on the original inner cavity $\Phi'' = -\mathbf{A}\mathbf{q}''$. The final corrected energy is, as before, half of the interaction energy needed for the creation of the screening charges:

$$E_{\text{tot}} = E_0 + \frac{1}{2}\Phi''\mathbf{q}'' \tag{3.15}$$

$$= E_0 + E_{\text{diel}}. \tag{3.16}$$

In this expression of the total energy, all OCE's are removed apart from the tiny influence which the use of Φ'' instead of Φ has on the solute wavefunction during the SCF. It should be noted that this total energy does indeed include the back-polarization of the solute by the solvent. Therefore, E_0 is not identical with the self-consistent gas phase energy, E_{gp}, of the solute since it includes the cost for this back-polarization, while the corresponding energy gain, which is about twice as large as the back-polarization cost, is subsumed in the dielectric energy, E_{diel}. In its present state, the total energy E_{tot} only includes the electrostatic interaction of the solute with the solvent. There can be no doubt that a nonelectrostatic term representing the dispersion and cavitation energy, being approximately proportional to the solute surface area (*i.e.*, the cavity area), should also be taken into account. But, since the latter usually is much smaller than the electrostatic part and since its definition is less clear, we have restricted ourselves to the electrostatic part of the solvation energy for this thesis work.

3.2.2 Recent developments of the COSab algorithm

The core of the COSab implementation in GAMESS is based on the original COSMO algorithm of Klamt[85] and was implemented by Kim Baldridge between 1997 and 2000[86]. This first version enabled HF and DFT calculations for single point energies and molecular gradients, with the multipole expansion corrections for the OCE. Extension to include MP2 wavefunctions was presented shortly after by Jonas and Baldridge[87].

A refined version of the method was implemented by Gregerson and Baldridge in 2003[88]. This version introduces the double cavity method for the OCE corrections.

A third implementation was carried by Potier and Baldridge in 2007[2], including a new algorithm for the creation of the cavity, the interface to the COSMO-RS program by COSMOlogic, the D-COSMO method, and general improvements.

The last two versions, however, have not been included in a stable production release of GAMESS because they lacked general stability with large molecular cavities. One of the purposes of this thesis work was to revise the COSab code, in order to improve its stability and to allow its inclusion in a stable release of GAMESS. Our main modifications to the code include:

- Two new routines to call the calculation of the solvation energy, and the OCE, respectively.
- Reorganization of all the `COMMON` groups to reduce memory requirements, especially for large cavities.

[2]Unpublished work

- Refinements in the dynamic memory allocation of large vectors and matrices.
- Implementation of the parallel version of the MP2/COSab within the mp2ddi algorithm.
- Grouping of all the routines related to COSab in the cosmo.src source file.
- Enabling of the DFT-D/COSab methods.
- The new Ahlrichs' triple zeta valence family of basis sets (TZV, TZVP, TZVPP) for the COSMO-RS method.

As discussed in the previous chapter of this thesis, dispersion forces play a significant role in many molecular systems. In the solution phase, not only intra-molecular forces are present, but also inter-molecular interactions can occur. The COSab method can account for, at least part, of the inter-molecular dispersion interactions, but we still need an accurate treatment of the intra-molecular forces. As in the vacuum case, MP2 is one of the pre methods to treat these interactions, but it is not affordable for large molecular systems. As previously described, DFT-D is an accurate, and affordable, alternative for the MP2 method in vacuum calculations, and with a suitable expansion it could be used for solution phase calculations. The accurate implementation and optimization of the DFT-D/COSab method is a major part of this thesis work. We published our results in a recent paper, that we entirely report in the next section.

The actual implementation of COSab will be available in the next major release of GAMESS, and includes all the following features for HF, MP2, and DFT (including DFT-D) wavefunctions, for both the restricted and the unrestricted case:

- COSMO solvation energies using the improved cavity algorithm.
- Analytical molecular gradients.
- Semi-numerical molecular second derivatives (hessian).
- Parallel implementation for all the methods.
- Generation of cosmo files for the interface with the COSMO-RS program.
- D-COSMO method.

3.3 Implementation and Optimization of DFT-D/COSab with Respect to Basis Set and Functional

Following the same scheme of the previous Chapter on DFT, we report in this section our 2009 paper entitled: "Implementation and optimization of DFT-D/COSab with respect to basis set and functional: Application to polar processes of furfural derivatives in solution"[89].

The article present the implementation and the optimization of our combined DFT-D/COSab method, together with an example of its appication to the push-pull system of furan-2-carbaldehyde (furfural) derivatives. Once again we prefer to report here the entire article, including the small application examples. More research example will be reported in the final chapter of this thesis (Chapter 4).

3.3.1 Introduction

The treatment of van der Waals (vdW, dispersive) interactions is an active field of research as of late, particularly in the DFT community[7,10,14,23,24,27,28,33,34,36,90–104]. The importance of vdW interactions is clear when considering molecular systems whose structures are largely influenced, and in some cases totally determined, by dispersion interactions. Moreover, the stability of a given molecular charge distribution may also be affected by its environment, specifically by the polarity of the medium or solvent. In particular, aromatic or π-conjugated molecules display a special sensitivity toward the redistribution of electron density as a function of their nuclear position, photonic excitation, and polar solvation. In general, chemical recognition, whether in materials or biological systems, depends on physio-chemical modulation that may be determined either qualitatively or quantitatively. Molecules in close proximity create competition and selection based on relative free energies of reaction (complexation/association), excitation (change in electronic state), and/or product formation (new chemical bond). Proper treatment of dispersion and solvent effects, both important effects on their own, in combination still leave open several important questions for reliable treatment.

Given that dispersion energies are pure electron correlation effects[105], accurate computations via ab initio based wavefunctions, including at least single and double substitutions, can provide good accuracy with adequate basis sets, (*e.g.*, CCSD(T) method)[106], albeit with a significant computational cost. On the cheaper side of these methods, Møller-Plesset perturbation (MP2, MP4) methods[107], while an improvement over most density functional approaches, tend to be largely over bound for many systems[108,109]. In general, neither computational solution is economical, particularly for large molecular systems and complexes. Recent literature including work of our own, on the other hand, illustrates the effectiveness of dispersion corrected DFT approaches[23,27,32,33,110,111]. Such methods, coupled to effective strategies for treatment of solvent[87,112–117], promise to provide an economical yet accurate method where both solvent and dispersion effects dominate. One approach has already been shown in a recent paper by Riley et al.[94] where a slightly modified version of the semiempirical correction of Grimme[23] applied to the TPSS density functional[118] was coupled with the IEF-PCM approach for continuum solvation[119]. However, still not well understood is a more general view of such DFT-D functionals together with continuum solvent representations, including optimal representations of the dispersion correction, effects of basis set, and representations of the solvent.

Our goals in this work include, a) contribution to the development of semiempirically corrected density functionals, emphasizing functionals and basis sets that are necessary for investigations of structure and properties in solution, b) implementation, optimization and performance analysis of the semiempirically augmented density functional theory (DFT-D) in conjunction with our ab initio implementation of the conductor-like screening model, COSab, within the GAMESS software[1], c) illustration of the combined DFT-D/COSab method on systems with known dispersion and solvation phenomenon, presented with an expanded set of basis sets, functionals, and solvent dielectrics, with consideration of both structure and properties.

3.3.2 Computational Methods

All calculations reported here were carried out using a locally modified version of the GAMESS electronic structure program. In the present work, we consider the semiempirically corrected functional, B97-D[23], and two conventional hybrid functionals, B3PW91[120], and B3LYP[40,120]. Additionally, comparisons are made with the second order Møller-Plesset perturbation theory (MP2)[107] and CCSD(T)[106]. Dispersion corrections were recently implemented and tested in the GAMESS software, using the ansatz proposed by Grimme (2006)[24]. The new parameters in the functional form make B97-D less susceptible to spurious dispersion contamination in the exchange component than the original functional of Becke[28]. The dispersion energy in B97-D is entirely handled by the semiempirical term, leading to smaller errors. For semiempirically corrected functionals, given the importance and dependence of the associated parameters on the choice of functional and basis set, we have carried out parameter optimization for several basis sets, including TZV2P[48], with (2d,2p), and Dunning's correlation consistent basis sets[121], denoted cc-pVnZ, where $n =$ D for double with [3s2p1d] contraction, T for triple with [4s3p2d1f] contraction, and Q for quadruple with [5s4p3d2f1g] contraction. The S22 reference set of data provided by Jurecka et. al.[38] is used as a validation test set, in addition to several test systems.

Solvation was taken into account using the most recent implementation of our COSab solvation method, based on the original COSMO theory of Klamt and modified for ab initio theory[86–88]. Dielectric permittivities of water ($\varepsilon = 78.4$), and ether ($\varepsilon = 4.335$) are used for parameterization studies. An expanded set of dielectrics was used to investigate a set of substituted pyrroles, for illustration of the method, including, toluene ($\varepsilon = 2.38$), chloroform ($\varepsilon = 5.0$), methanol ($\varepsilon = 12.0$), acetone ($\varepsilon = 20.7$), methanol ($\varepsilon = 32.6$), and water ($\varepsilon = 78.4$). The parameters of the cavity construction are: 1082 points for the basic grid, 92 segments on the complete sphere. The outlying charge error was taken into account via the double cavity approach[87,88,122]. The solvent radial extent was optimized in the parameter optimization studies, and taken as 1.3 for the application studies. Solvent atomic radii were taken from Bondi[123] or from Klamt[124].

3.3.3 Theoretical Approach and Discussion

DFT dispersion corrections

Much work has been carried out to revise and enhance density functionals for increased accuracy, the most important component of late being the addition of corrections for dispersion. A particularly effective and consistent strategy to correct failures due to lack of dispersion has involved addition of an empirical potential[34,125] to the final DFT energy. This empirical potential is typically of the form C_6R^{-6}, where R are interatomic distances and C_6 dispersion coefficients. Such a strategy has been formulated and well established by several research groups[23,33,36,126]. In particular, the method of Grimme establishes a semiempirical dispersion correction that can be applied to the final result of any mean field calculation that lacks a sufficient description of dispersion energy[127,128]. Typically, this procedure is used in conjunction with density functional theory (leading to various DFT-D methods)

$$E_{\text{disp}} = -s_6 \sum_{i=1}^{N_{at}-1} \sum_{j=i+1}^{N_{at}} \frac{C_6^{ij}}{R_{ij}^6} f_{\text{dmp}}\left(R_{ij}\right) \tag{3.17}$$

where the dispersion coefficients C6 are calculated from the atomic polarizabilities and the fdmp is a damping function with the form:

$$f_{\text{dmp}}\left(R_{ij}\right) = \frac{1}{1+\exp\left[-d\left(\frac{R_{ij}}{s_R R_{ij}^0}-1\right)\right]} \tag{3.18}$$

This semiempirical correction does not depend on the electronic structure of the system, and therefore, optimization of the relevant parameters must be considered, in particular the s_6 prefactor to the C_6 atomic coefficients, the d damping factor, and the s_R prefactor to the vdW radii. The atomic polarizabilities (which lead to the C_6 coefficients), the vdW radii, and all semiempirical parameters were optimized in the original paper of Grimme[110], and further work was carried out by our own group more recently[32]. Such parameters have to compensate for differences in the electronic descriptions due to basis sets, functionals, and in the present work, effects of solvent. The nonlinear parameter, d, is considered optimal, and fixed to the optimized value of Grimme, $d = 20$[23]. Differences in implementations are mainly in the values of these parameters. The final mean-field (MF) DFT-D energy is the result of the direct addition of this dispersion energy to the computed DFT energy:

$$E_{\text{MF-D}} = E_{\text{MF}} + E_{\text{disp}} \tag{3.19}$$

First Principles Continuum Solvation Theory

We have developed a rigorous self-consistent approach for the inclusion of electrostatic solvation effects in conventional ab initio gas phase computations in GAMESS[86,87]. This model is implemented at the RHF (ROHF, UHF), DFT, HDFT, and MP2 (UMP2) levels, including first and second derivatives. Our approach to continuum solvent modeling (COSab) arises from the concepts of screening in conductors, a modification of the original COSMO theory of Klamt[85]. Significant model features of this approach include: a) molecular-shaped cavity construction, b) efficient solution to energy and derivative quantities, c) efficient ways of including dynamic correlation, d) inclusion of an alternate approach using multipoles up to hexadecapoles, e) assessment of outlying charge effects using a choice of two strategies, f) general electrostatic solvation accuracy within $2-6$ kJ/mol, and g) several strategies for inclusion of first solvation shell effects.

We refer the details of the underlying theory of the COSab method to the first part of this chapter, or to the original paper[86], and instead only point out the main concepts related to the coupling of this theory with the semiempirical dispersion corrections for density functional treatments. The treatment of solvent effects within the continuum model involves the construction of a cavity around a solute system, with a dielectric continuum representing the solvent outside the cavity. The molecular electric field arising from the nuclei and the electronic distribution is screened by the polarization of this dielectric continuum. The iterated solute/solvent interaction can be uniquely represented by the resulting surface charge distribution at the interface to the continuum. Construction of

the molecular cavity relies on van der Waals radii of Bondi[123] scaled by a solvent factor (cos_{rad}) in the range of $1.2-1.3$ that represents the area of approach of solvent molecules to a solute[124]. These radii in fact ensure that the cavity volumes are approximately equal to the molar volumes of the compounds, and therefore are not really free parameters[124], and demonstrated the physically correct screening energy decay behavior[86].

While authors of other solvent models may recommend different sets of vdW radii[129–131], there is a general agreement that the cavity size is closely related to the vdW surface. Recently, Truhlar et. al.[132] provided a systematic study showing variation across four popularly used solvent models, including a discussion of what radii provide the most physical results, and also showing that scaling factors greater than 1.4 produce unphysical cavities. These important insights in fact imply that, for some molecules (*e.g.*, those with diffuse electronic structure), a small but significant portion of the solute electron density can extend outside the molecular cavity. This leads to error in the prediction of solvent phenomenon, since the solute is not fully represented in the proper way in its interaction with the solvent. Such errors are termed outlying charge errors, and are most problematic for systems with diffuse charge localized or anionic systems, and can lead to errors that are substantial (*e.g.*, $40-80$ kJ/mol error). Our present solvation implementation has two effective strategies for the treatment of outlying charge error[88].

It is important to note that the vdW radii involved in the damping function in Equation 3.18 are different than those used in the continuum solvation method, as both are optimized independently using different approaches and for different properties. As such, one cannot use the same set of vdW radii values for both contributions. The model for solvation is in fact independent to that of the semiempirical dispersion model. Any eventual dependencies of the two effects would nevertheless be accounted for through the parameterization of the semiempirical scaling factors within both methods.

Together, the DFT-D+COSab method has a total of 4 parameters to consider for any interdependencies and for optimization. Three parameters, scaling factor s_R and s_6, (vdW radii and dispersion coefficients, respectively) and damping function exponent, d, arise from the DFT-D method. The fourth parameter, cos_{rad}, is related to the creation of the solvent cavity surface. Following the approach used in our previous work (as well as others)[23,32], the value of d is kept fixed at the value of 20. This leaves investigation into the behavior of only three parameters, s_6, s_R, and solvent extent radii (cos_{rad}), simultaneously with respect to basis set and functional.

Parameter Optimization

To perform simultaneous optimization of the three chosen parameters, a suitable database of molecules with accurate solvated interaction energies is required. The S22 set, proposed by Hobza et al.[38], is the standard database used in all previous considerations of the DFT-D method. However, this database provides accurate interaction energies only in vacuum. To obtain solvated interaction energies, the following term, first proposed by Riley et. al.[94], is used to correct the vacuum energies:

$$\Delta E_{\text{solv}}^{\text{CP}} = \Delta E_{\text{vac}}^{\text{CP}} + \Delta\Delta E_{\text{solv}} \tag{3.20}$$

In this way, a value for $\Delta\Delta E_{\text{solv}}$ can be calculated, using a suitable solvation method, to give

$$\Delta\Delta E_{\text{solv}} = \Delta E_{\text{solv}}^{\text{no-CP}} - \Delta E_{\text{vac}}^{\text{no-CP}} \tag{3.21}$$

Using this approach, one can propose a way forward for providing chemical accuracy in solution for a reasonable costs, and including important effects of dispersion and solvation. In addition, this method provides a reasonable way to take basis set superposition error (BSSE) into account in solution. This is very important given that continuum solvation methods do not provide a clear and unique way to take into account BSSE in the calculations, since there is no analogue to the counterpoise CP corrections as used in gas phase. Alternatively, since the optimization of the s_6 parameter for the B97-D functional including counterpoise correction shows a minimum at $s_6 = 1.4$ regardless of basis set, one could carry out CP corrected solvation energies using $s_6 = 1.4$.

Computational solvent models are fundamentally different at the algorithmic level. This results in different accounting of the various aspects of solvation representation within the quantum mechanics ansatz. For example, models have different (or missing) representations for cavity descriptions, solvent radii, outlying charge effects, non-electrostatic effects, or other solvent related phenomenon. In particular, comparison with experimental data has showed substantial difference in predictability with different solvent cavity descriptions, which are a function of solvent radii parameters[133]. The radii used to generate the spheres associated with the cavity ultimately govern the volume of the cavity and the distance between the atoms and the solvent surface. Computed properties depend heavily on the choice of atomic radii.

The specific formalism used by Riley et al.[94] involved the use of the Integral-Equation-Formalism Polarized Continuum Model, IEF-PCM, together with the use of united atom, UA0, solvent radii. The general PCM method uses a cavity of interlocking spheres approximately 20% larger than the vdW radius. The electrostatics are treated using the Poisson equation, with Green's functions used to define the integral operators determining the apparent charge. Non-electrostatic effects are evaluated empirically, using a solvent accessible surface (SAS). In this way, the surface charge depends only on the potential and not on the vector electric field, thereby being less sensitive to numerical instabilities. The specification of the solute cavity, defined using the united atom topological model (UA0), is obtained from spheres centered on non-hydrogen atoms. The radius of each sphere, which is dependent on the atom type, connectivity, and number of hydrogen atoms attached, is based on the Universal Force Field (UFF)[134]. This particular choice of radii used for cavity construction (default for cavity construction in other quantum chemistry software) has been found to lead to relatively high mean unsigned errors for solvation phenomenon[133,135], and is typically not recommended for quantitative calculations of solvation free energies[136–138].

Given the known sensitivities to details of solvation model, it becomes necessary to recalculate solvation reference corrections for the S22 set of molecules for this work. Here, we have calibrated a set of corrections for both high and low dielectric, water ($\varepsilon = 78.4$) and ether ($\varepsilon = 4.33$), respectively. Calculations are performed at the MP2/aug-cc-pVDZ level of theory, as chosen by Riley et al.[94] in order to draw some comparisons. Results are reported in Table 3.1.

Table 3.1: MP2/aug-cc-pVDZ solvent reference energy corrections (kJ/mol) for the S22 set of molecules.

S22 complex reference number	vacuum	$\Delta\Delta E_{\text{solv}}$ MP2/COSab (this work) ether $\varepsilon = 4.33$	$\Delta\Delta E_{\text{solv}}$ MP2/COSab (this work) water $\varepsilon = 78.4$	$\Delta\Delta E_{\text{solv}}$ MP2/IEF-PCM[a] ether $\varepsilon = 4.33$	$\Delta\Delta E_{\text{solv}}$ MP2/IEF-PCM[a] water $\varepsilon = 78.4$
1	-13.26	-3.347	2.301	-4.48	-0.54
2	-21.00	-14.81	-11.21	-14.35	-9.87
3	-77.86	-50.58	-36.65	-32.93	-10.42
4	-66.78	-37.53	-20.67	-33.30	-17.40
5	-86.40	-50.71	-30.79	-39.50	-16.44
6	-69.92	-43.30	-28.83	-36.36	-20.88
7	-68.49	-43.76	-31.25	-36.32	-21.67
8	-2.22	-1.97	-1.84	-2.13	-2.13
9	-6.32	-4.35	-3.39	-4.39	-3.68
10	-6.28	-5.10	-4.48	-5.36	-4.64
11	-11.42	-7.11	-5.10	-7.36	-5.23
12	-18.49	-14.39	-11.89	NA[b]	NA[b]
13	-42.34	-23.81	-12.76	-16.40	-7.95
14	-21.84	-14.64	-11.30	-14.85	-12.09
15	-51.17	-34.31	-24.31	-32.09	-24.90
16	-6.402	-2.720	-0.92	-2.55	-0.50
17	-13.72	-7.24	-3.64	0.38	7.03
18	-9.832	-6.99	-5.44	-7.20	-0.08
19	-18.66	-9.83	-4.60	-10.96	-5.56
20	-11.46	-9.54	-8.58	NA[b]	NA[b]
21	-23.97	-16.11	-11.67	NA[b]	NA[b]
22	-29.50	-21.05	-16.78	-15.61	-7.45

[a] Reference [94].

[b] Riley et al. did not report this value because of problems in the convergence of the energies.

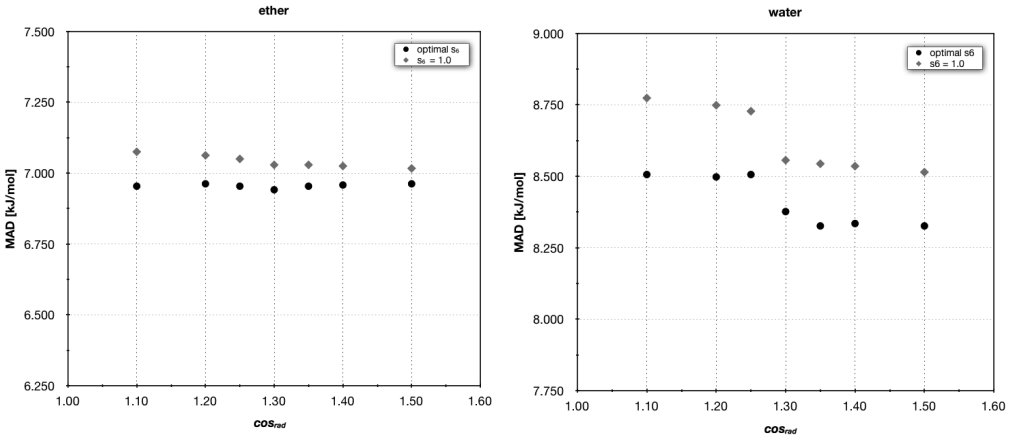

Figure 3.1: Mean absolute deviation of S22 set of molecules as a function of solvent radii extent value (cos_{rad}) at $s_6 = 1.0$ (red), and at the optimal s_6 for the respective cos_{rad} (black), at the B97-D+COSab/cc-pVDZ level of theory.

Table 3.2: Summary of results of Mean Absolute Deviation (MAD, kJ/mol) for the S22 set showing variance in solvent radii extent parameter, cos_{rad}, as a function of s_6, at the B97-D+COSab/cc-pVDZ level of theory.

	water			ether		
solvent extent parameter, cos_{rad}	MAD with $s_6 = 1.0$	corresponding optimal s_6	MAD with optimal s_6	MAD with $s_6 = 1.0$	corresponding optimal s_6	MAD with optimal s_6
1.1	8.774	0.93	8.506	7.075	0.97	6.954
1.2	8.749	0.94	8.498	7.063	0.97	6.962
1.25	8.728	0.95	8.506	7.050	0.97	6.954
1.3	8.556	0.96	8.376	7.029	0.98	6.941
1.35	8.544	0.95	8.326	7.029	0.98	6.954
1.4	8.535	0.95	8.334	7.025	0.98	6.958
1.5	8.514	0.96	8.326	7.017	0.98	6.962
Variance	0.01326	-	0.00784	0.00048	-	0.00005
Std. Error	0.04352	-	0.03346	0.00824	-	0.00270

Optimization of the solvent extent parameter (cos_{rad}).

The algorithm for cavity construction in the COSab-GAMESS method involves construction of a basic grid representing the molecular cavity generated from the vdW surface around the molecule. This is followed by a series of projections onto the solvent surface, extending the cavity to approximately a distance of van der Waals + 20-30%[123,124]. The cavity segmentation is small enough as to assume homogeneous charge distribution on each segment. The standard value for the parameter, cos_{rad}, is typically taken as 1.2 or 1.3. Here, we actually investigate the response in the range from 1.1 to 1.5 to better understand the influence of this parameter on the prediction of solvation.

A first set of calculations were performed at the B97-D+COSab/cc-pVDZ level of theory, with the dispersion parameters fixed at $d = 20$, $s_R = 1.1$ and $s_6 = 1.0$. Further optimization was undertaken of the more critical s_6 parameter for each value of cos_{rad} to confirm results. Figure 3.1 and Table 3.2 summarize these results.

The variation in the mean absolute deviation of the S22 set for the cos_{rad} parameter in the range $1.1 - 1.5$ is within 0.45 kJ/mol for water and 0.13 kJ/mol for ether. An optimal

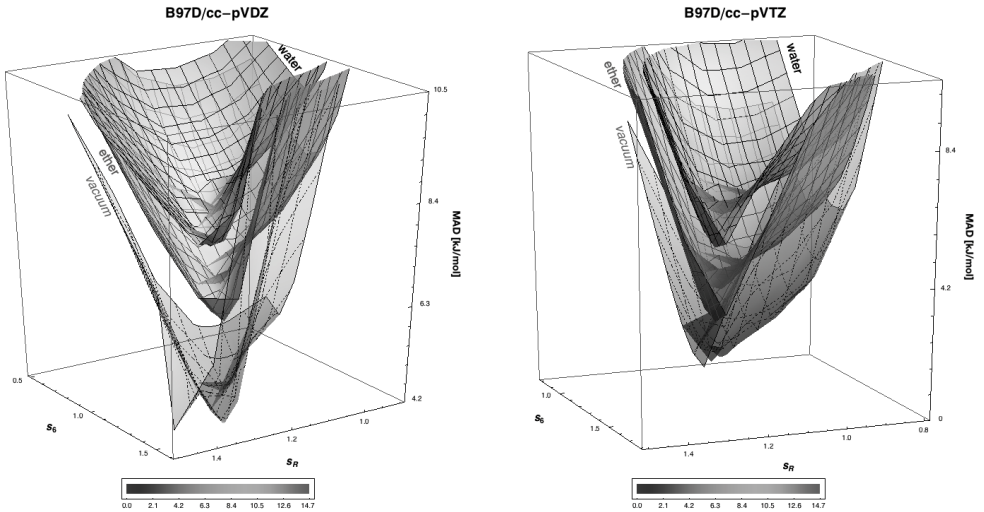

Figure 3.2: Optimized s_6 and s_R empirical dispersion function parameters for the B97-D functional, with cc-pVDZ and cc-pVTZ basis sets, respectively. Plots are given on the same relative scale.

value of $cos_{rad} = 1.30$ is suggested for two reasons. First, the performance is slightly better for the simultaneous optimization of cos_{rad} and s_6 (see black dots on the graphic). Second, 1.30 is one of the possible values suggested for the COSab method (typical values are 1.20 and 1.30). The general message, however, is that values in the range 1.3 ± 0.2 do not affect the general behavior of the method, which could be surprising given the known sensitivity of electrostatic solvation properties to variation in atomic radii, as discussed above.

Optimization of DFT-D parameters (s_6 and s_R).

As in our previous work[32], we investigate the combined behavior of the two DFT-D parameters, s_6 and s_R, using the optimal value determined for $cos_{rad} = 1.3$. The simultaneous optimization of these two parameters is presented in Figure 3.2 as a surface function for three different environments, vacuum, water, and ether, was carried out. Results were investigated for the B97-D functional with both the cc-pVDZ and cc-pVTZ basis sets, and are illustrated in Figure 3.2.

The topology of the curves for the three environments (vacuum, ether, H_2O) appear very similar to each other, but with different relative height on the MAD axis. This similarity in topology suggests that behavior in solvated environments for these complexes with variation in dispersion functional parameters is qualitatively the same. The differences regarding the MAD from that of the gas phase are expected due to the fact that these were determined using MP2/aug-cc-pVDZ in the respective environment, rather than at CCSD(T)/CBS. However, because we are interested here in the optimal values of the s_6 and s_R, if the overall topology in different environments is truly within a small tolerance of that observed for the gas phase environment, this difference in height along the MAD axis can be tolerated.

To compare more closely the variance in surface topology in different medium, we

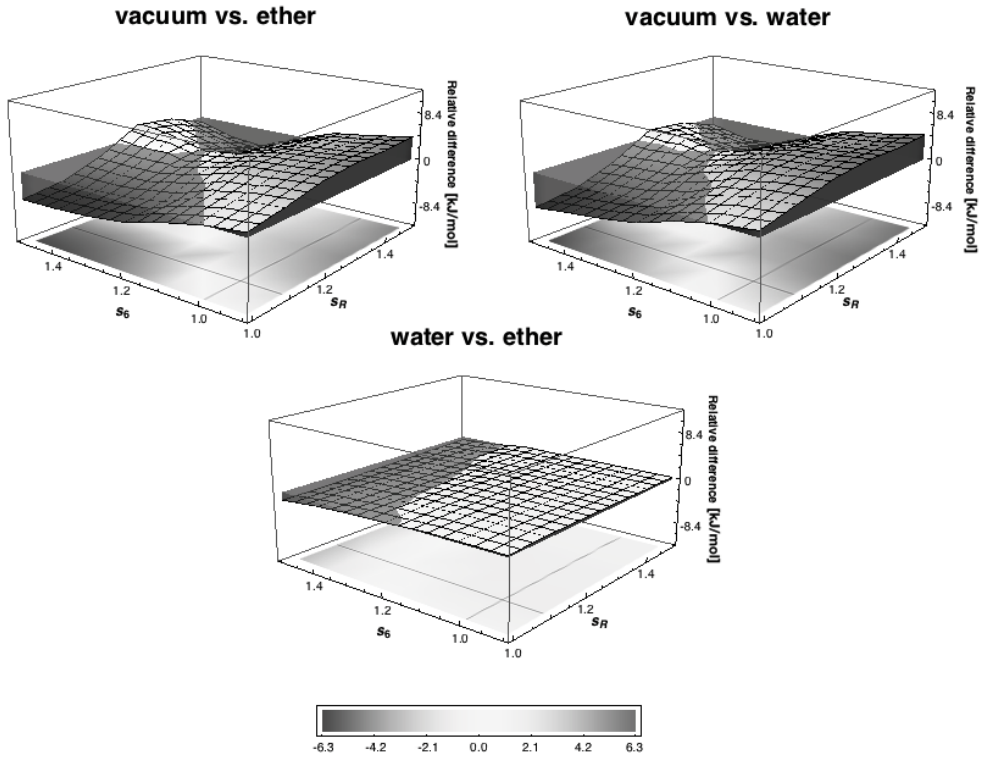

Figure 3.3: water vs. vacuum, ether vs. vacuum, and water vs. ether projection plots, at the B97-D+COSab/cc-pVDZ level of theory.

can project one curve onto either of the other two, and determine any significant point-to-point differences. These differences are plotted as a surface function of the two DFT-D parameters in Figure 3.3, with a color density map projected on the bottom of each diagram, for all three possibilities: water vs. vacuum, ether vs. vacuum and water vs. ether. Only the B97-D+COSab/cc-pVDZ case is shown here, since similar results are obtained at the B97-D+COSab/cc-pVTZ level of theory. In these surface representations (Figure 3.3), blue (negative) means that the solvated curve was lower than the vacuum (ether) curve in Figure 3.2, while red (positive), means that the solvated curve is higher than the vacuum (ether) curve in Figure 3.2.

The deviations from zero (red or blue, Figure 3.3) are in all cases smaller than 4.2 kJ/mol, and in general very small for both basis sets, confirming the fact that the curves overlap almost perfectly. Moreover, the intersection of the optimized s_6/s_R parameters is always in a minimum deviation region. From these results, we can conclude that the method behaves in the same way for both solvents, when the optimization of the two DFT-D parameters is conducted simultaneously. When solvated results are compared to the vacuum case, this general conclusion does not change.

A more detailed slice of the surface functions is shown in Figure 3.4 for $s_R = 1.1$. Numerical values for the corresponding s_6 optimizations are reported in Table 3.3. As can be seen, the values of the optimal s_6 parameter for the solvated cases differ only slightly from that used in the vacuum, for each of the basis sets considered. Additionally, these results also include indirectly, consideration of BSSE, as shown above. Therefore, our overall conclusions made in our previous article, including discussion of BSSE, more ex-

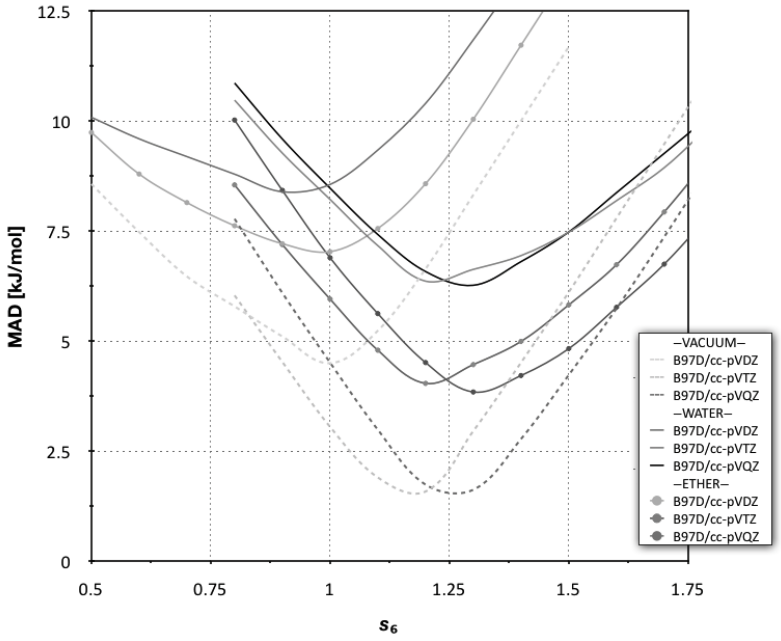

Figure 3.4: water vs. vacuum, ether vs. vacuum, and water vs. ether projection plots at the B97-D+COSab/cc-pVDZ level of theory, represented as a slice through the surface functions from Figure 3.3.

tensive optimization, and summary of values proposed as a function of basis set, can be extended with good accuracy to the DFT-D + COSab procedure, for calculation of interaction energies in solution. As such, these results, together with those of Riley et al.[94] using a different ansatz for including solvation effects together with semiempirically corrected DFT, support that in general, for any treatment of dispersion-governed systems in solution, no additional considerations need be made nor specialized optimizations undertaken.

Geometry Optimization.

The DFT-D method is typically parameterized using single point energy calculations on an accurate gas phase geometry, for each complex in the S22 database. This procedure opens up questions regarding any variations in methodology and subsequent prediction of results, when full optimization of geometry is considered instead of a single point energy calculation. In the case of a vacuum environment, these questions are not considered significant due to the fact that the starting geometry is calculated at a very high level of theory. More specifically, the optimized geometry for most of the complexes in the S22 set has been determined with CCSD(T)/QZ, with a few cases optimized with CCSD(T)/TZ or MP2/TZ-CP. All final single point energies are then calculated at the CCSD(T)/CBS level. Explicit details of the optimizations used in each case can be found in the original paper[38].

In contrast, it is not readily clear that the gas phase optimized geometries are the most appropriate when one is considering a solvent environment, as one can expect changes in the structures of the complexes due to their interactions with the solvent. In particular, one expects a change in distance between the two monomers in the complex. While the

Table 3.3: Summary of results of Mean Absolute Deviation (MAD, kJ/mol) for the S22 set showing variance in s6 with solvent and basis set.[a]

Solvent	basis-set	optimized s_6	MAD [kJ/mol]
vacuum	cc-pVDZ	1.00	4.498
	cc-pVTZ	1.18	1.410
	cc-pVQZ	1.26	1.381
water	cc-pVDZ	0.96	8.376
	cc-pVTZ	1.21	6.356
	cc-pVQZ	1.28	6.192
ether	cc-pVDZ	0.98	6.941
	cc-pVTZ	1.19	4.038
	cc-pVQZ	1.28	3.820

[a] $cos_{rad} = 1.3$, $s_R = 1.1$, $d = 20$

main purpose of this article is not to search for better procedures of parameterization of the DFT-D method, one still must consider possible sources of error due to changes in geometry, and the consequences for the DFT-D + COSab procedure.

In order to carry out such an analysis, we have calculated the gradient for all molecular systems in the S22 set with the B97-D functional across a variety of basis sets, in a water environment. The root mean square deviation (RMSD) and the largest component (MAX) of the gradient are reported in Table 3.4, as a measure of the differences between the geometries as given in the S22 set and their respective optimized equilibrium geometries.

These summarized values for RMSD and MAX gradient indicate that, provided one uses a large enough basis set, a large majority of the complexes are not far from their gas phase optimized geometries. As expected, incremental increase in basis set size provides a more accurate picture of just how close the solution phase complexes are to the optimized gas phase geometry. Cases where there are the greatest RMSD values, an indication of when solvation changes are expected to be significant, are highlighted in bold face in Table 3.4. For example, complexes that have bond length differences in the picometer range represent significant differences when one is trying to obtain chemical accuracy in structure and associated properties.

To further analyze these results, complexes in the S22 set were divided into three subgroups according to the nature of the primary interactions between the molecules. The three categories of complexes are A) hydrogen-bonded complexes (1-7), B) predominant dispersion interactions, complexes (8-15) and C) mixed hydrogen bonding and dispersion, complexes (16-22). Complexes with the highest RMSD and MAX gradient within each group are indicated in boldface in Table 3.4. In each category, we have chosen one complex to illustrate results of a full optimization in solution at the B97-D/cc-pVnZ (n = D,T,Q) level of theory, starting from the accurate vacuum geometry. In category A, H-bond complexes, formamide dimer (#4) is chosen, with the highest RMSD gradient at cc-pVTZ and cc-pVQZ, and the second highest at cc-pVDZ. For category B, the dispersion complexes, the uracil dimer stack (#13) is the complex with highest RMSD and MAX gradient with all considered basis sets. Within category C, the mixed complexes, benzene

Table 3.4: summary of results of RMSD and Maximum (MAX) gradient values for the S22 set as a function of basis set.

molecule	cc-pVDZ		cc-pVTZ		cc-pVQZ	
	RMSD gradient	MAX gradient	RMSD gradient	MAX gradient	RMSD gradient	MAX gradient
1	0.0077984	0.0174154	0.0026740	0.0053823	0.0022662	0.0041095
2	**0.0105507**	0.0191442	0.0056189	0.0124492	0.0051123	0.0120283
3	0.0083584	0.017122	0.0046930	0.0097907	0.0040162	0.0090413
4	0.0090051	0.0234469	**0.0062381**	0.0166286	**0.0058922**	0.0159450
5	0.0078098	**0.0249773**	0.0055591	**0.0178010**	0.0053169	**0.0165761**
6	0.0058952	0.0203691	0.0036121	0.0149223	0.0035065	0.0139418
7	0.0068203	0.0221163	0.0044578	0.0146959	0.0042735	0.0130864
8	0.0055312	0.0107665	0.0020459	0.0040859	0.0018506	0.0037130
9	0.0054494	0.0098256	0.0025617	0.0035783	0.0024370	0.0034128
10	0.0052723	0.0124369	0.0022704	0.0058819	0.0021843	0.0056609
11	0.0044198	0.0094194	0.0016463	0.0035123	0.0015786	0.0032221
12	0.0047943	0.0101749	0.0019266	0.0039867	0.0021137	0.0040012
13	**0.0075948**	**0.0222007**	**0.0055311**	**0.0150658**	**0.0052161**	**0.0132548**
14	0.0042266	0.0099944	0.0017430	0.0037012	0.0016530	0.0037704
15	0.0061554	0.0210383	0.0038124	0.0139875	0.0036075	0.0122721
16	**0.0066904**	0.0164377	0.0025598	0.0047258	0.0026196	0.0057154
17	0.0054453	0.0134867	0.0023467	0.0076936	0.0021896	0.0070529
18	0.0057686	**0.0179676**	0.0022156	0.0057129	0.0020522	0.0045684
19	0.0049909	0.0141728	**0.0063532**	**0.0313533**	**0.0068787**	**0.0340759**
20	0.0044762	0.0109458	0.0017516	0.0041108	0.0016882	0.0038493
21	0.0043044	0.0105029	0.0018935	0.0044323	0.0018214	0.0041939
22	0.0049381	0.0122261	0.0022128	0.0071765	0.0021013	0.0065132
average	0.0061953	0.0157358	0.0033511	0.0095761	0.0031989	0.0090911
maximum value	0.0105507	0.0249773	0.0063532	0.0313533	0.0068787	0.0340759

– HCN (#19) has the highest RMSD and MAX gradient with cc-pVTZ and cc-pVQZ, and also for cc-pVDZ. Data for the fully optimized solvent (water) structures and energetics for these three complexes as compared to gas phase, is illustrated and summarized in Table 3.5.

The most sensitive geometry parameters in these complexes are the inter-monomer distances and the angular relationship between the two monomers. Table 3.5 summarizes these values as a function of basis set and environment for the three complexes considered. The geometry taken from the S22 set has been optimized in the gas phase and in water for the basis sets shown. In the gas phase, each complex shows a different behavior in the variance of the interatomic distance with respect to increase in basis set. The inter-monomer distance in the formamide dimer increases significantly with increase in basis set, with a convergence to the S22 reference value (ΔReference = 0.032 Å, 0.001 Å, and 0.005 Å, respectively). Complex 13, uracil dimer, on the other hand, shows a decrease in inter-monomer distance with increase in basis set, contrary to the reference limit (ΔReference = 0.008 Å, 0.021 Å, and 0.086 Å, respectively). Addition of diffuse functions does not change this trend. The angular relationship between the two monomers is, however, similar to that predicted at the reference level. Complex 19 shows an increase in inter-monomer distance with basis set, but away from the reference value of 3.387 Å (ΔReference = 0.031 Å, 0.024 Å, and 0.043 Å, respectively). The angular dependence in the benzene-HCN system is relatively the same across basis sets, with a total variance of ~5°.

Moving from gas phase to solution phase results in a significant change in geometry,

Table 3.5: comparison of optimized vacuum, optimized solvent (water), and reference S22 gas phase, geometry parameters for three complexes of the S22 set using different basis sets.[a]

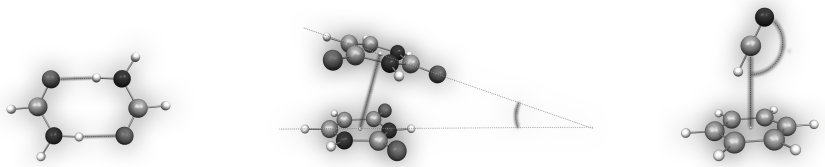

#4 Formamide dimer **#13 Uracil dimer** **#19 Benzene · HCN**

		vacuum			water		
bonds	S22 reference CCSD(T)/CBS	cc-pVDZ	cc-pVTZ	cc-pVQZ	cc-pVDZ	cc-pVTZ	cc-pVQZ
#4	1.841	1.809	1.842	1.846	1.860	1.901	1.905
#13	3.365	3.357	3.344	3.279	3.516	3.459	3.434
#19	3.387	3.418	3.412	3.430	3.279	3.226	3.180
		vacuum			water		
angles	S22 reference CCSD(T)/CBS	cc-pVDZ	cc-pVTZ	cc-pVQZ	cc-pVDZ	cc-pVTZ	cc-pVQZ
#4	-	-	-	-	-	-	-
#13	13.8	18.4	18.0	14.0	19.9	13.6	12.5
#19	174.6	175.7	177.0	179.6	154.3	153.7	149.4

	respective optimized vacuum geometry *vs.* optimized solvated (water) geometry								
	initial RMSD (au) from gas phase geometry			ΔE (kJ/mol) vacuum-water			%max geometry change (vacuum-water)		
	cc-pVDZ	cc-pVTZ	cc-pVQZ	cc-pVDZ	cc-pVTZ	cc-pVQZ	cc-pVDZ	cc-pVTZ	cc-pVQZ
#4	0.00905	0.00624	0.00589	1.46	4.595	3.93	1.1	3.8	3.2
#13	0.00760	0.00553	0.00522	10.70	4.51	2.50	5.9	1.6	0.3
#19	0.00499	0.00635	0.00688	16.74	19.30	18.28	8.0	16.5	3.4

[a]The graphic shows intermolecular distances (blue) and angles (red), as reported in the table.

but again, different trends for the three different cases. In the case of the formamide dimer, the hydrogen bond distance increases by almost 6 pm in going from the gas to the solution phase. It is known that high dielectric solvents have a dramatic effect in the dimerization of formamide[139–141]. The increase in the polarity of the solvent is thought to reduce the dimerization, likely due to competition from the surrounding medium. This then causes the opportunity for other bonded forms, from the rather well-defined double hydrogen bonded form in the gas phase, to single hydrogen-bond dimers (medium dielectric) and less well-defined structures in water.

In the second class of complexes, the uracil dimer, the change in environment from gas phase to solution phase shows an even more dramatic increase in the distance between the two monomers (*e.g.*, ~15 pm for cc-pVQZ). The uracil dimer can exist in both hydrogen-bonded configurations as well as various stacked arrangements[142]. The stacked and T-shaped conformations, with a large dispersive energetic component, are less stable than the hydrogen bonded configurations, albeit less so in the gas phase than in the solution phase.

In the last case, benzene-HCN system, one sees a very large decrease in the inter-monomer distance in the high dielectric water environment, changing from 3.43 Å to 3.18 Å, at the B97-D/cc-pVQZ level of theory. In addition, the angular relationship between the benzene and the HCN changes significantly, from perpendicular in the gas phase, to canted in the solution environment. Other studies have also shown that this interaction weakens with stronger dielectric, with the interaction energy in water being less than half as strong as in the gas phase (~15 kJ/mol vs ~6.5 kJ/mol)[94].

In all of these cases, taking the optimized gas phase geometry as the starting point of the solution phase optimization, one sees that the gradient of the first step is quite high, (on average 0.006 a.u.), an indication that the solution phase structure is still far from the gas

phase structure. For the three molecules considered here, one sees maximum geometry changes as high as 16% from that of the gas phase, depending on the system and level of theory. Such differences between gas and solution phase can constitute significant differences in energetics, for example, if one is trying to determine interaction energies in solution environment with a high level of accuracy but is only using gas phase geometries. In just these three examples, we see over 17 kJ/mol in energy difference (at the cc-pVQZ level of theory) between gas and solution phase. In general, one must carefully consider the implications of geometry optimization in a solution environment depending on the system and associated properties of interest.

3.3.4 Illustrative Example: Ground State Conformational Dynamics of Polar Processes

Despite the general tendency for molecules to adopt electronic configurations with minimal charge separation (*e.g.*, electroneutrality principle), many important structural and dynamical features are mediated by charge-separated states. In particular, the conformational analysis of push-pull conjugated π systems is strongly influenced by contributions from zwitterionic states. In donor-acceptor systems, one can identify a dual-resonance-form model, where the major contributor is determined by the degree of stabilization of the charge-separated state. Typically, one of the two resonance forms contributes local double-bond character, manifesting a higher rotational barrier. Depending on the nature of the donor (D) / acceptor (A) pair and the effect of solvent, the barrier to rotation can span a fairly large range. In addition to kinetic effects, it is often found that the dominant equilibrium conformer varies with the medium, with the conformer of higher dipole moment generally more favored in media of high dielectric constant. A particular case of longstanding interest is the barrier to rotation in push-pull furfural systems, especially due to their importance as components in many biological redox centers and synthetic molecular devices [143–148]. Moreover, these systems have associated experimental as well as computational challenges [149]. For example, the very small energy difference between the *cis* and *trans* isomers, the possibility for secondary interactions in some of the analogues as well as the strong solvent dependencies across a small range of dielectric (particularly for the parent furan-2-carbaldehyde system), creates particular challenges for both experimental as well as computational predictions. Unambiguous assignments of experimental spectral results have made difficult the predictions of the *cis-trans* energy difference, ΔECT, as well as the barrier to interconversion, Ea, with a wide range in experimental predictions in both. Similar details pose challenges for computational solvent methods to accurately predict the small energy differences between isomers and pick up the solvent detail that reproduces the conformational change as a function of dielectric. Solvent effects can actually be large enough to reverse the order of stability between the *cis* isomer and the *trans* isomer. As such, this class of system represents a particularly good test for the present method. In particular, here we investigate the parent furfural system and two analogues, as illustrated in Figure 3.5.

In our 2000 work, together with the experimental group of Bain [150], we investigated a full set of push-pull conjugated pyrrole cognates. Bain and Hazendonk [150] used a combination of three NMR experiments to obtain rate data over 6 orders of magnitude representing an approximately 150 K temperature range, giving very reliable experimental numbers

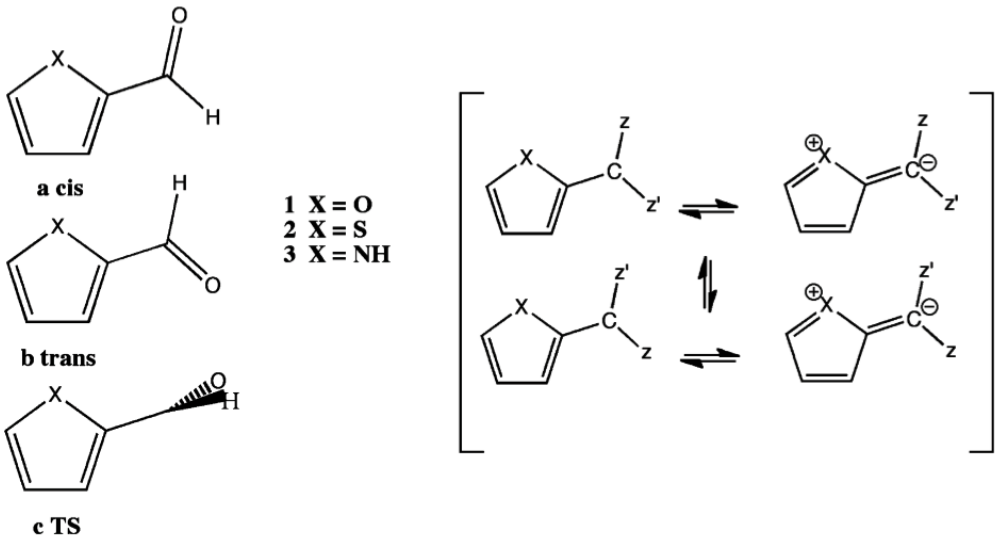

Figure 3.5: Conformations of furan-2-carbaldehyde (X = O), thiophen-2-carbaldehyde (X = S), and pyrrole-2-carbaldehyde(X = NH).

for the furfural system. Experimental activation parameters were obtained with errors less than 1 kJ/mol and 6 J/(mol K) for $\Delta H^{\ddagger}$ and $\Delta S^{\ddagger}$, respectively. The $\Delta H^{\ddagger}$ for toluene, acetone, and methanol do not obey a simple relationship with ε, suggesting that the solvent effect is likely more complex than just the effect of solvent reaction field. Large $\Delta S^{\ddagger}$ values support this and also implied that equating $\Delta G^{\ddagger}$ and $\Delta H^{\ddagger}$, as is often done, is not justified even for aprotic solvents. Using theoretical methods, we previously carried out a full investigation[151] of the effects of method/basis set on prediction of both ΔE_{CT} and barrier to interconversion. A summary of these results is shown in Figure 3.6. Results enable comparison across basis set as well as wavefunction type. Basis sets of at least double-ζ quality with polarization on both heavy and light atoms, and preferably diffuse functions, is shown to be optimal. Our best estimate for ΔE_{CT} (relative to the lower energy *trans* form) and barrier was determined with CCSD(T)/ TZV(2d,2p)//MP2/TZV(2d,2p) [$\Delta E_{CT} = 2.13$, $\Delta E_{CT-ZPE} = 2.48$ $E_{a-ZPE} = 37.62$ kJ/mol]. This provided benchmark values, given the historical controversy regarding the experimental information. However, less expensive but with overall good predictability is the MP2/aug-cc-pVDZ level. Theoretical predictions can be compared to the 1989 IR and Raman spectroscopic study reporting $\Delta E_{CT} = 3.42 \pm 0.28$ kJ/mol and $E_a = 38.96 \pm 0.25$ kJ/mol.[152]

We now compare the earlier, more computationally expensive CCSD(T) and MP2 results, with the present dispersion enabled functional, B97-D, for analogues **1-3** in both gas and solution phase. We first consider the parent, furan-2-carbaldehyde system (furfural), **1**. The energy difference between *trans*, **1a**, and *cis*, **1b**, forms of furfural in gas phase shows the *trans* conformation, **1a**, to be more stable by ~4 kJ/mol, with the exact value dependent on the level of theory, as previously found. In solution, the larger dipole moment of the *cis* isomer, **1b**, can preferentially stabilize this form over the *trans* conformation. In Table 3.6, results with B97-D/cc-pVDZ and B97-D/aug-cc-pVDZ are compared to other functionals as well as our previous MP2 and reference CCSD(T) results, across a wide range of dielectrics. Gas phase ΔE_{CT} values are overestimated with cc-pVDZ with all methods with respect to the benchmark CCSD(T) values. However, the

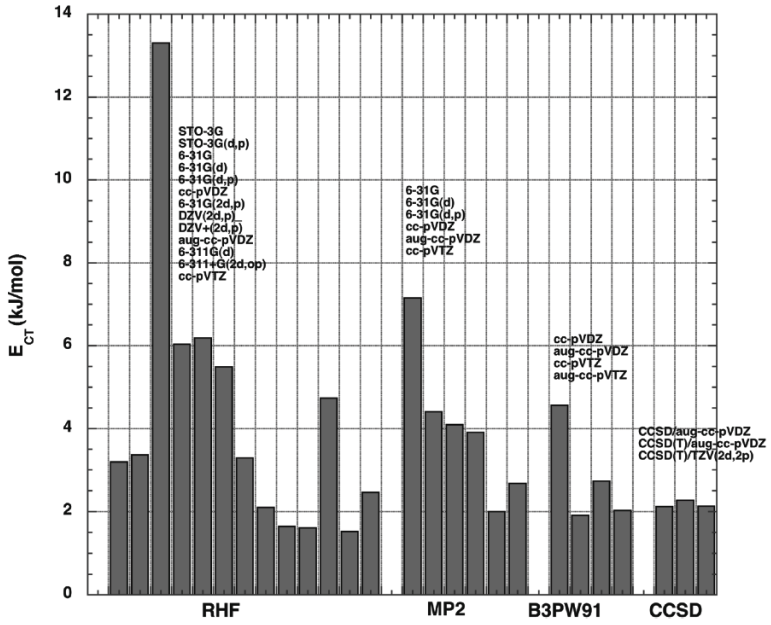

Figure 3.6: Rotational equilibrium of *trans*- vs *cis*-2-furanaldehyde as a function of wavefunction type and basis set, relative to the *trans* isomer.

Table 3.6: rotational equilibrium (kJ/mol) of *trans*- *vs.* *cis*-2-furanaldehyde as a function of wavefunction type and basis set, for gas phase and 6 different solvents.[a,d]

	cc-pVDZ				aug-cc-pVDZ			
ε	MP2	B97-D	B3LYP	B3PW91	MP2	B97-D	B3LYP	B3PW91
1[b]	3.72	4.56 (4.61)	4.82 (4.93)	4.65 (4.75)	2.02	1.92 (2.31)	2.03 (2.50)	1.94 (2.40)
2.38	2.29	3.19 (3.35)	3.15 (3.37)	2.98 (3.13)	0.03	-0.10 (1.28)	0.49 (1.07)	-0.13 (0.38)
5	1.29	1.96 (2.09)	1.60 (1.86)	2.17 (2.37)	-1.47	-1.56 (-1.16)	-1.78 (-1.17)	-1.73 (-1.13)
12	0.55	1.08 (1.16)	1.17 (1.43)	1.01 (1.21)	-2.57	-2.72 (-1.78)	-2.22 (-1.57)	-3.47(-2.87)
20.7	0.29	1.00 (1.10)	0.64 (0.83)	1.65 (1.92)	-3.06	-3.06 (-1.77)	-3.41 (-2.76)	-3.87 (-2.03)
32.6	0.15	0.88 (0.98)	0.66 (0.86)	0.65 (0.86)	-3.23	-3.44 (-2.12)	-3.83 (-3.15)	-3.94 (-3.36)
78.4	0.02	0.56 (0.65)	0.88 (1.09)	0.46 (0.69)	-3.45	-3.74 (-2.19)	-3.09 (-2.39)	-3.98 (-3.35)
average unsigned difference with respect to MP2	-	-0.70 (-0.80)	-0.66 (-0.87)	-0.75 (-0.94)	-	-0.14 (-0.90)	-0.35 (-0.61)	-0.36 (-0.43)
difference with respect to CCSD(T)[c] for $\varepsilon = 1$	1.59	2.43 (2.48)	2.69 (2.80)	2.52 (2.62)	-0.11	-0.21 (0.18)	-0.10 (0.37)	-0.19 (0.27)
difference with respect to experiment for $\varepsilon = 1$	0.30	1.14(1.19)	1.40(1.51)	1.23(1.33)	-1.40	-1.50 (-1.11)	-1.39 (-0.92)	-1.48 (-1.02)

[a] ΔE_{CT} relative to the trans isomer **1a** in kJ/mol. [b] Experimental gas phase value reported as 3.42 ± 0.38 [152]. [c] CCSD(T)/ DZV(2d,p)//MP2/DZV(2d,p) [$\Delta E_{CT} = 2.99$, $E_a = 42.91$ kJ/mol], CCSD(T)/TZV(2d,2p)//MP2/TZV(2d,2p) [$\Delta E_{CT} = 2.13$, $E_a = 39.16$ kJ/mol], and CCSD(T)/aug-cc-pVDZ//B3PW91/aug-cc-pVDZ [$\Delta E_{CT} = 2.26$, $E_a = 41.10$ kJ/mol][151]. [d] Zero point corrected values are given in parentheses.

Table 3.7: B97-D/aug-cc-pVDZ Dipole Moments of *trans*- and *cis*-conformers for 2-furanaldehyde, **1**, in Gas Phase and 6 Different Solvents[b]

	2-furanaldehyde			
	dipole (D)			
ε	*cis*	*trans*	TS	ΔE_{CT_1}[a] kJ/mol
1	4.46	3.85	2.82	-1.92 (-2.31)
2.38	5.29	4.57	3.24	0.10 (-1.28)
5	5.87	5.07	3.52	1.56 (1.16)
12	6.31	5.45	3.72	2.72 (1.78)
20.7	6.47	5.59	3.79	3.06 (1.77)
32.6	6.55	5.66	3.82	3.44 (2.12)
78.4	6.64	5.74	3.86	3.74 (2.19)
Δ(gas-water)	2.18	1.89	1.04	5.66 (4.50)

[a] ΔE_{CT} relative to the *trans* isomer **1a** in kJ/mol.
[b] Zero point corrected values are given in parentheses.

aug-cc-pVDZ basis provides sufficiently accurate results for all considered functionals. The average unsigned difference with respect to MP2 shows that B97-D provides better results than B3LYP or B3PW91, at an overall lower computational cost than for hybrid functionals, MP2, or CCSD(T).

The general trend across the range of dielectrics (natural log scale), from toluene ($\varepsilon = 2.38$ to water $\varepsilon = 78.4$) for the parent system, for a variety of wavefunction types, is shown in Figure 3.7. Notably, the B97-D and MP2 curves are very similar in predictability, while the two hybrid DFT methods show considerable variance, particularly the B3LYP method. We have carried out additional computations for the B3LYP curve around the region of $\varepsilon = 5.0$, and, in fact, the prediction is shown to be continuous around these points, rather than exceptions (see, *e.g.*, Figure 3.7 insert graph). This region corresponds to the cross over between preferences for *cis* over *trans* conformation. The overall dipole moment change over the span of dielectrics is $\Delta\mu = 1.9\,\mathrm{D}$ for a corresponding change in $\Delta\Delta E_{CT} = 4.50$ kJ/mol. The slope of the curve on the $\ln(\varepsilon)$ plot is relatively steep illustrating the strong change preference toward the *cis*-2-furanaldehyde form over the *trans*-2-furanaldehyde form in higher dielectric. While it is true that the *trans*-2-furanaldehyde form relieves the lone-pair/lone-pair oxygen repulsion that is found in the *cis*-2-furanaldehyde form, in higher dielectric the higher dipole moment of the *cis* form relative to the *trans* form will eventually dominate, changing that preference.

To further illustrate donor/acceptor properties in these systems, we have investigated thiophen-2-carbaldehyde (X = S) and pyrrole-2-carbaldehyde (X = NH). Table 3.8 summarizes the gas phase results for the three analogues. Unlike the parent system, thiophene-2-carbaldehyde, **2**, has a more polar S-*cis* conformation and is therefore more stable in the gas phase than is the S-*trans* conformation. Although the dipole difference between S-*cis* and S-*trans* is smaller than in **1**, one still expects preferential stabilization of the former conformation in solvent. Similarly, pyrrole-2-carbaldehyde, **3**, is also found to have a more stable *cis*- conformation in the gas phase. Importantly, the less polar N(H)-*cis* form gains stabilization due to the possibility for intramolecular interaction between the hydrogen of the nitrogen and the oxygen of the furan ring. In this case, however, unlike either

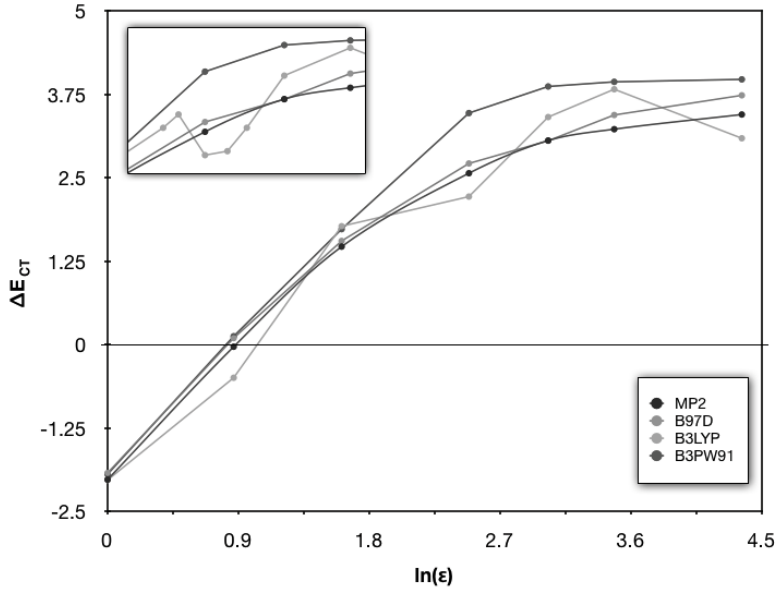

Figure 3.7: Comparison of calculated ΔE_{CT} as a function of dielectric for various wavefunction types using the aug-cc-pVDZ basis set. The insert figure shows an enhanced view with additional calculated points of the x axis region from $\ln(\varepsilon) = 2.5 - 3.5$.

Table 3.8: B97-D/aug-cc-pVDZ calculated gas phase energetics and dipole moments for 1-3

	energetics[a]					dipole				
X	ΔE_{CT}	expt	preferred tautomer in gas phase	E_{a}	expt	*cis*	*trans*	TS	preferred tautomer in solution phase	expt
O	1.9	3.42 ± 0.28[b]	*trans*	55.2	38.96 ± 0.25[b]	4.5	3.8	2.8	*cis*	3.97 (μ_{cis})[c] 3.52 (μ_{trans})[c] 3.52 (μ_{TS})[c]
S	-3.85	4.1 ± 0.4	*cis*	45.5	-	4.1	3.7	2.8	*cis*	3.52 (μ_{cis})[d]
NH	-14.7	-	*cis*	57.1	-	3.1	4.6	2.7	*trans*	2.48 (μ_{cis})[e]

[a] ΔE_{CT} relative to the *trans* isomer, **1a**, in kJ/mol. [b] Reference [152]. [c] *cis* and *trans* from ref [153]. TS value calculated from bond dipoles [154]. [d] reference [155]. [e] reference [156].

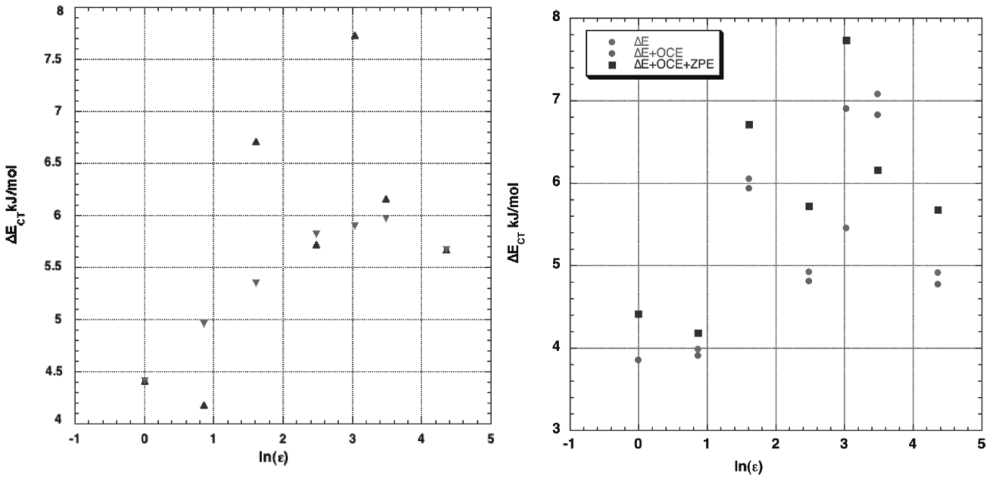

Figure 3.8: Variation in ΔE_{CT} as a function of dielectric for two levels of cavity discretization (a) and as a function of outlying charge and zero point energy (b) for thiophen-2-carbaldehyde, **2**.

1 or **2**, the dipole moment would suggest a substantial preferential stabilization of the *trans* conformation in solution environment, due to the significantly larger dipole of the NH-*trans* structure, so the two effects, weak interactions in the *cis* form and strong dipole stabilization in the *trans* form, are competitive. The tautomeric equilibrium in solution phase is in general found to be dependent on both ΔE_{CT} and $\Delta\mu$. Table 3.9 summarizes the effects of dielectric variance for analogues, **2**, S, and **3**, N(H). One sees a consistent preference for the *cis* isomer in both the calculated ΔE_{CT} as well as the predicted dipole across the full span of dielectrics. In **3**, N(H), as observed in the gas phase results, we see the competition between the hydrogen bond stabilization present in the *cis* isomer, and the stronger dipole component present in the *trans* isomer. The result is a preference for the *cis* isomer across the span of dielectric, since the weak hydrogen bond interaction will only partially compensate for the more dramatic solvent dipole effect in the N(H)-*trans* conformation. A subtle feature of the solvation model capability is observed with system **2**, S, due to the second row element, sulfur. In particular, the detailed nature of the cavity construction algorithm is an inherent part of the quality of the solvation model. Different regions of the molecular cavity can have different sensitivity to surface discretization, depending on how rapidly varying the surface charge is, and may require a higher level of discretization to track this change properly. In the case of thiophen-2-carbaldehyde, one can observe this phenomenon. Figure 3.8 shows a comparison of ΔE_{CT} as a function of $\ln(\varepsilon)$ for a normal cavity discretization and a highly refined cavity discretization. Checking also the effects of outlying charge and zero point energy, one sees that each of these have a consistent effect across dielectric and are not responsible for the inconsistent trend in the data.

Figure 3.9 shows comparison of solvation trends for all three analogues at the B97-D/aug-cc-pVDZ level of theory. The curves illustrate the dipole versus electrostatic trends across the span of dielectrics for the different types of functionalities. In particular, pyrrole-2-carbaldehyde **3**, shows a steep slope in the opposite direction as that of the parent furfural system, for the reasons explained above. In the sulfur substitution, the smaller change in dipole over the span of dielectrics, results in only a small increase in

Table 3.9: B97-D/aug-cc-pVDZ dipole moments of *trans*- and *cis*-conformers for thiophen-2-carbaldehyde, **2** (X = S), and pyrrole-2-carbaldehyde, **3** (X = NH), in gas phase and 6 different solvents.[a]

	S					NH				
ε	*cis*	*trans*	TS	preferred tautomer in solution phase	ΔE_{CT}	*cis*	*trans*	TS	preferred tautomer in solution phase	ΔE_{CT}
1	4.08	3.68	2.82	*cis*	3.85 (4.41)	3.07	4.64	2.74	*trans*	14.7 (14.0)
2.38	4.88	4.39	3.26	*cis*	4.28 (4.96)	3.72	5.54	3.19	*trans*	11.7 (11.5)
5	5.44	4.89	3.56	*cis*	4.66 (5.35)	4.18	6.19	3.49	*trans*	9.36 (9.17)
12	5.87	5.27	3.78	*cis*	5.10 (5.82)	4.53	6.67	3.72	*trans*	7.28 (7.21)
20.7	6.02	5.41	3.86	*cis*	5.06 (5.90)	4.66	6.84	3.79	*trans*	5.37 (5.40)
32.6	6.10	5.48	3.90	*cis*	5.19 (5.97)	4.72	6.94	3.83	*trans*	6.26
78.4	6.20	5.57	3.95	*cis*	4.84 (5.73)	4.80	7.04	3.87	*trans*	4.48 (4.33)

[a] ΔE_{CT} relative to the *cis* isomer, **1b**, in kJ/mol.

stabilization energy across the span of dielectrics.

Comparison of barrier height with available experiment is difficult due to the lack of experimental values for the substituted systems. For **2**, the experimentally available value of 42.27 ± 0.63 kJ/mol in CH_2Cl_2 solution[157,158] and 43.11 ± 1.26 kJ/mol in the pure liquid[159] agrees well with the calculated barrier of 43.60 kJ/mol for $\varepsilon = 12.0$ and 44.57 kJ/mol in water. Figure 3.10 shows a general trend of calculated E_a for the three systems studied. The increase in barrier to interconversion to the *trans* form shows steady increase for both **3** and **2**, corresponding to the stronger preference for the *cis* isomer with increasing dielectric, somewhat attenuated in the parent system as observed above. The sulfur system barrier is considerably less than the other two, again reflecting the relatively small increase in stabilization with increase in dielectric.

3.3.5 Conclusions

Detailed chemical treatments of molecular and electronic structure, including the effects of the environment, can offer significant challenges unless highly accurate methods are employed. We present here an accurate and yet cost efficient way of including solvent effects with dispersion enabled density functional theory, such that a self-consistency is maintained with respect to the solvent charges and the interaction potential. Numerical values for corresponding s_6 semiempircal dispersion parameters are reported. As shown, values of optimal s_6 parameters for solvation theory differ only slightly from that used in the vacuum, for each of the basis sets considered. Results include indirectly, consideration of BSSE. The resulting DFT-D + COSab procedure can be extended with good accuracy for prediction of interaction energies in solution. We have applied the DFT-D + COSab method to one category of push-pull conjugated heterocycles, with known challenges associated with prediction of isomer preference and barrier to interconversion in solution environment. The behavior of changing donor/acceptor on both gas and solution phase, conformational preferences, and internal rotational barrier show the importance of dispersion, hydrogen bonding, and solvation in the computational model. The dispersion corrected DFT model with appropriate basis set reproduces the trends in the known experimental data and projects trends across a large span of dielectric.

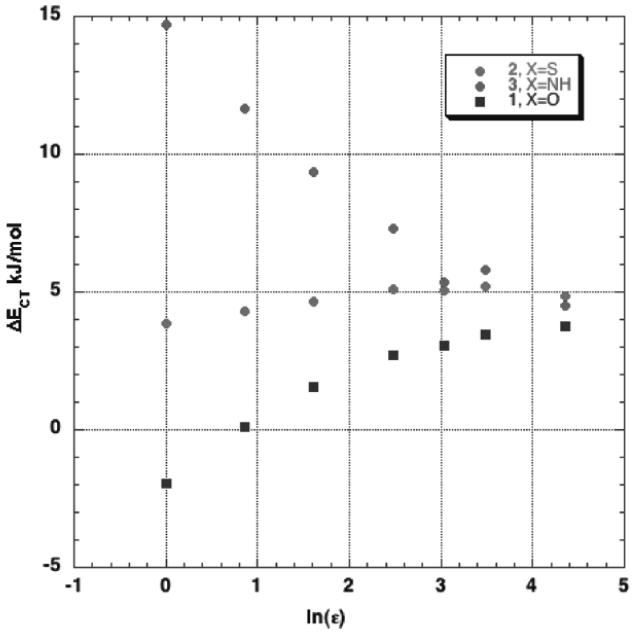

Figure 3.9: Comparison of calculated ΔE_{CT} as a function of dielectric ($\ln(\varepsilon)$).

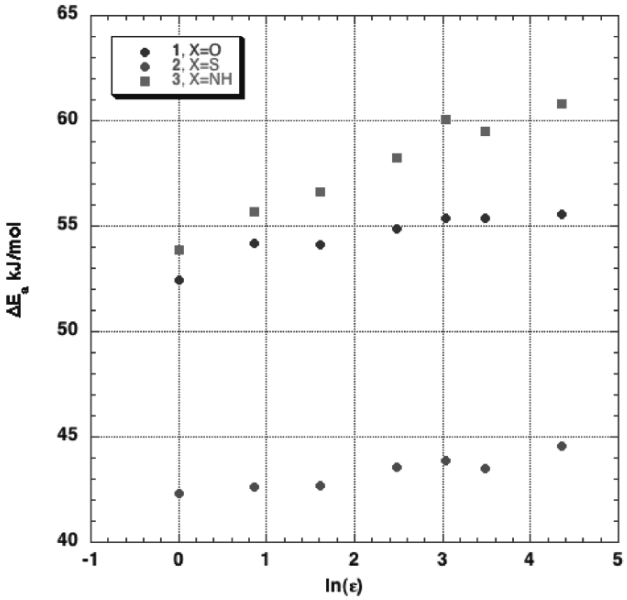

Figure 3.10: Comparison of calculated E_{a} (cis $\rightarrow$ TS) as a function of dielectric ($\ln(\varepsilon)$).

Chapter 4

Applications

Overview

In this Chapter we present a collection of research applications on density functional theory and solvation methods. We'll start from a DFT study on the triaziridine molecule, a small but computationally challenging system that we use to illustrate the capabilities of the common exchange-correlation functionals.

4.1 DFT computations of substituents effects on triaziridine strain energy and heat of formation

4.1.1 Introduction

For the top-row main group elements, cyclopropane $(CH_2)_3$ and ozone O_3 define structural extremes; the former exists solely as a three-membered ring compound[160], whereas the isoelectronic ozone exists principally as an acyclic 1,3 dipolar structure with at best a fleeting three-membered ring high energy intermediate[161?] . Triaziridine (**1**), in contrast, is an isolable three-membered ring isomer of $(NH)_3$[162], which exists also as the 1,3 dipolar isomer azimine (**2**)[163–168] (Figure 4.1). One speculation to the relative stability of **1** concerns its being a 6-electron cycle that might benefit from some type of aromatic stabilization[169,170]. This speculation notwithstanding, one might equally well view **1** as a fully saturated system suffering multiple repulsive vicinal lone-pair effects[171,172]. An assessment of the heat of formation for **1** and the effect of substituents on its ring strain provides a way to address these aromatic *vs*. vincinal lone pair repulsion models.

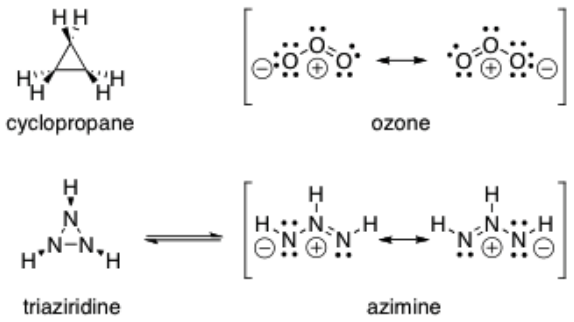

Figure 4.1: Structurally analogous couples cyclopropane/triaziridine and ozone/azmine

In addition to being part of the series $(CH_2)_3$, $(NH)_3$, O_3 , **1** can also be cast as the third member in the series of $(NH)_n$ compounds preceded by nitrene NH and dihydrodiazine NH=NH, and followed by polyimine. Nitrene is a well-studied reactive intermediate for which numerous derivatives are known to alter its stability and electronic structure[173]. Substituted diazines are well known from the extensive chemistry of diazo compounds that display simple double bond *E/Z* stereochemistry[174].

1 and **2** can each display a set of stereoisomeric conformers, the relative energies of which should respond to substitution at N (Figure 4.2). The relative orientation of lone pairs varies among these isomers, and correlates to the ranking of conformer energies. The parent **1** was prepared from the reaction of ammonia with silver(I) impregnated xeolite, and its structure determined as a silver(I) ion complex in the xeolite[162]. The first experimentally characterized triaziridine was the diisopropyl-carboxyethyl derivative, prepared by Dreiding and co-workers, via photolysis of the azimine[166]. The majority of experimental triaziridine research has been conducted on the *N*-aryl, *N*-alkyl or *N*-ester[175–179], or polycyclic derivatives[172,180–182], which appear to impart some stabilization to the ring. The earliest computational study of a triaziridine was an SCF study of the structure and energy of the parent and related N_3H_3 isomers[183]. Additional studies have been carried out on a variety of triaziridine derivatives at various levels of theory[167,169,184–192].

The present work focuses on assessing the heat of formation, ring strain energy, barriers to inversion of nitrogen, and magnetic properties, in the parent and as a function of N-substituents, with the hope of delving into issues of vincinal lone pair repulsion and aromatic stabilization in **1**.

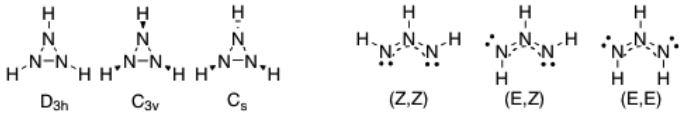

Figure 4.2: Structurally analogous couples cyclopropane/triaziridine and ozone/azmine

4.1.2 Methods

All calculations have been carried out using the GAMESS[1] and GAUSSIAN[193] software packages, employing a variety of levels of theory for comparative purposes. Wavefunction-based methods considered here include second order Møller-Plesset perturbation theory (MP2)[107] and Density Functional Theory (B3LYP[40,120], M06[15]). G3MP2 theory was employed for heat of formation computations[194]. Dunning basis sets were considered, both double- and triple-ζ quality: DZV(2d,p), TZV(2d,p)[49], and cc-pVnZ and aug-cc-pVnZ ($n =$ D double, T triple)[121]. For each optimized geometry, the Hessian (matrix of second derivative) was calculated to determine local minima (positive definite) or nth-order saddle point (n negative eigenvalues), and zero-point energy corrections. Ionization potentials were determined by both Koopmans'[195] and ΔSCF ($E_{\text{neu}} - E_{\text{cat}}$) methods. Nucleus-independent chemical shifts (NICS) properties[196], including NICS(Iso)[197,198], NICS(In-plane), and NICS(ZZ)[199] values, were computed using the GIAO method[200,201]. A NICS-scan[202] was carried out for several molecules considered here. The isotropic chemical shift values are separated into their in-plane (NICS(Iso)) and out-of-plane (NICS(ZZ)) components, by consideration of the eigenvalues of the chemical shift tensors. The NICS(ZZ) values, more closely related to the current density, reflect the magnetic response of a molecule toward a magnetic field applied perpendicular to the plane (*i.e.*, z direction), and are therefore considered primarily associated with the π contribution. Visualization and analysis of structural (including representation of 3D molecular orbitals) and property results were obtained using QMView[203] and MacMolPlt[204].

In the absence of a good experimental structure as a reference, choice of optimal methodology was made by evaluating structure and property convergence on the lead triaziridine compound and its isomers. This revealed the necessity for dynamic correlation and no less than double-ζ valence plus polarization. Comparison of results with and without diffuse functionality indicated little to no effect. With regard to the DFT functional, improved functionals, such as the M06 series of Truhlar have been shown to superior to most other conventional functionals, including B3LYP, across 4 large databases of most every molecular construct. We have found very similar results from these two functionals for the types of molecules considered in this work, and have chosen to emphasize the M06 results, as we have found them to have greater predictability[13–15].

4.1.3 Results and discussion

Aromatic character *vs*. lone-pair repulsion in 1 and 2

The supposition of aromatic character in **1** comes from a purely formalistic analysis of electron counting ($3 \times 2 = 6 = 4 + 2$). Despite the virtues of the aromatic sextet[205], an analysis of the molecular orbitals readily reveals that in **1**, the six electrons fill all the "would-be" π orbitals and therefore the net β from the secular determinant would be zero (Figure 4.3). With no delocalization benefit, one might assume the lone pairs on nitrogen would repel one another Coulombically. This analysis is borne out by the relative energies of the planar (D_{3h}) and non-planar (C_{3v} and C_s) conformations.

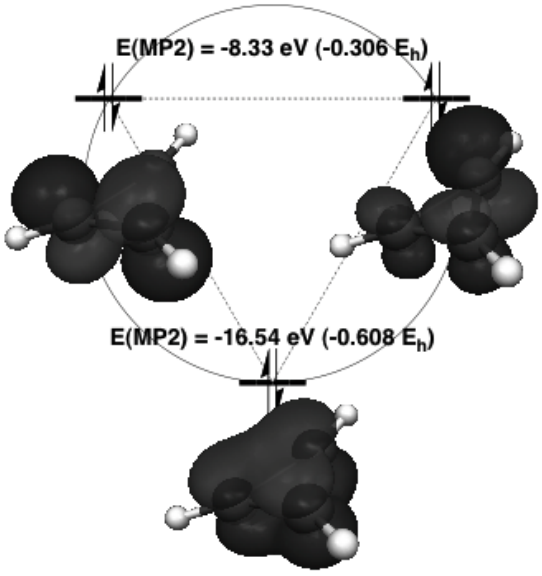

Figure 4.3: Frost's circle for a π-cycle of three π orbitals in D_{3h} **1**

The planar form of **1** is predicted to be substantially higher in energy than the non-planar forms (ca. 129 kcal/mol). Given that the inversion barrier in aziridines and oxaziridines are 18–20 kcal/mol and 24–31 kcal/mol[206–209] respectively[184,191], a ring with 3 electronegative atoms could easily display barriers of > 30 kcal/mol. Three times the single inversion barrier might be taken as a rough approximation for the planar form assuming no dependence among the barrier processes. The possibility of additional vicinal repulsion would raise the energy and therefore a planar form void of aromatic character could easily be expected to be > 100 kcal/mol higher than its non-planar isomers. Earlier computations arrived also at this rough energy estimate for the planar form[167]. Of the two non-planar forms, C_{3v} and C_s, the C_s form with only one *syn*-alpha repulsion is predicted to be lower in energy by about 10 kcal/mol. Thus, the initial data would favor a view of **1** as not aromatic and suffering from neighboring lone pair repulsion.

The open forms of **2**, cannot show this vicinal lone-pair repulsion, because the central nitrogen's electrons are either π or σ bonding. The computed relative energy values for the (*E,E*), (*E,Z*), and (*Z,Z*) conformers are 0.0, 1.3, and 7.9 kcal/mol, respectively. The higher energy of the latter conformer indicates a substantial through-space 1,3-repulsive effect between the lone pairs in the (*Z,Z*) conformer. In contrast, a relatively

small difference in energy between the (*E,Z*) and (*E,E*) conformers reflects the similarity of hydrogen-lone-pair and hydrogen–hydrogen 1,3 interactions. In the triazenes **3**, an isomer set tautomeric to **1** and **2**, the *E* and *Z* conformers show a distinct 15 kcal/mol difference in energy that can be accounted in large portion to vicinal lone-pair repulsion (Figure 4.4)[168].

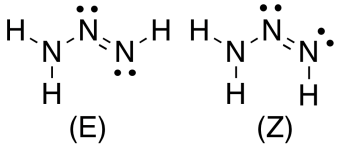

Figure 4.4: Triazine conformers, **3**

Looking to the structural criteria, a paradoxical situation arises for **1**. The planar form of **1** is predicted by QM calculations to have exceptionally short bond lengths of 1.405 Å, something that might be expected for a system profiting from aromatic stabilization. In contrast, the shortening in planar **1** might be attributed to a rehybridization effect independent of any aromatic character.

In cyclopropane, the bond lengths are 1.51 Å, somewhat shorter than the 1.54 Å in ethane. The shortening in cyclopropane bond lengths has been attributed to such hybridization effects. If that were the whole story, one would expect to see some harbinger of the effect in the non-planar forms of **1**; however, they show N–N bond lengths of 1.487 Å, somewhat longer than the reference value of 1.448 for NH_2–NH_2. It has been previously noted that in cyclic compounds like **1**, the bond length shortening associated with replacement of carbon by an electronegative atom is greater for ring systems[188].

The idea has arisen that σ-aromaticity plays a strong role in **1**. Presumably, a geometrical consequence of this σ-aromatic character would lead to shorter and stronger σ-bonds. Further support for a rehybridization at nitrogen toward an sp^2-like idea comes from the ionization potential data. The experimental ionization potentials of ammonia, hydrazine, diazine, and azimine, are 10.070 ± 0.020[210], 8.1 ± 0.15[211], and 9.65 ± 0.08[212], respectively (Figure 4.5, Table 4.1). The ionization potential calculated for **1** is 9.5 eV, indicating an effectively higher electronegativity of N in **1**, which is consistent with greater sp^2 character.

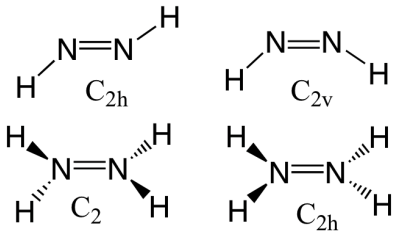

Figure 4.5: Conformers of diazine and hydrazine

Table 4.1: M06/DZV(2d,p) calculated ionization potentials for **1**, NH_3, NH_2NH_2, NH_3NH_3, and NH_2NH_4

Molecule	ΔSCF	-HOMO	Δ*E*
1 (C_{3v})	10.52	7.60	0.0
1 (C_s)	10.86	7.61	9.8
NH_3	10.79	7.43	
N_2H_4 (C_{2h})	9.93	6.96	0.0
N_2H_4 (C_2)	8.86	5.83	3.0
N_2H_2 (C_{2v})	10.30	7.02	4.9
N_2H_2 (C_{2h})	10.18	6.83	0.0
2 (*E*,*E*)	9.52	6.97	0.0
2 (*Z*,*Z*)	9.21	6.72	7.9

A cult phenomenon has risen around the concept of computing nuclear independent chemical shift (NICS) effects as a way to claim aromatic character[196]. NICS values for **1**-D_{3h}, **1**-C_{3v} and benzene-D_{6h} were computed at 1.5 Å, *i.e.* NICS(1.5), the values are 1.4, -0.6 and -7.2, respectively[213,214].

An impression from this single point analysis would be that **1** does not exhibit a chemical shift effect. The best analysis to refute this hypothesis would be a full 3-D plot of the chemical shift field; however profiles along the central axis perpendicular to the to the molecular plane suffice (Figure 4.6); in particular, the generally accepted NICS(*XX*-in-plane), NICS(*ZZ*) and NICS(Iso) curves are depicted. By symmetry the π part of the NICS(*ZZ*) term must vanish in the plane. In contrast, the σ component is neglected at distances around 1.0–1.5 Å above the plane; thus the choice to use these as the classical "aromatic" NICS positions.

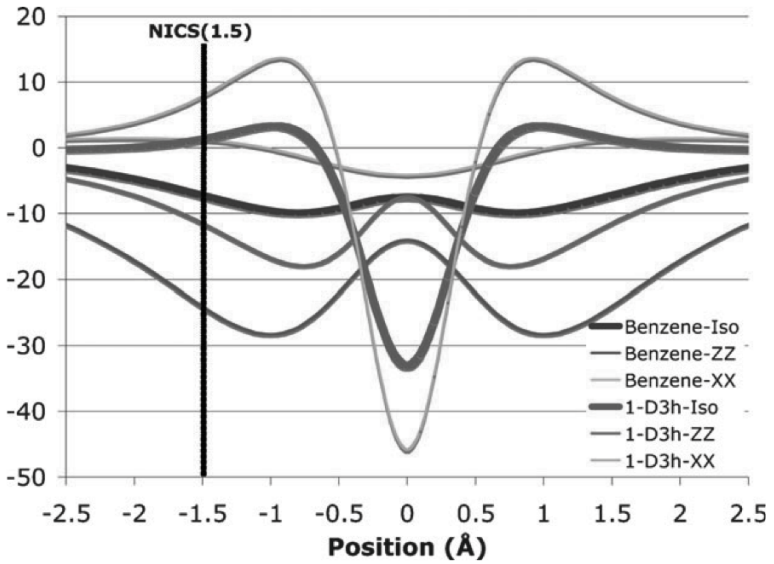

Figure 4.6: Calculated NICS values along the symmetry axis for **1**-D_{3h} (blue) and benzene-D_{6h} (red)

Considering aromatic to mean "benzene-like" the comparison between **1**-D_{3h} and

benzene-D_{6h} NICS(Iso) curves betray a qualitative difference (*i.e.* **1** is not like benzene)[215]. The difference can be seen to come from the fact that the NICS(*XX*-in-plane) contribution dominates the form of the profile for **1**, whereas the NICS(*ZZ*) contribution dominates the form of profile for benzene. Separate analysis of the composite NICS(in-plane) and NICS(*ZZ*) profiles at NICS(1.5) reveals a stronger σ-paramagnetic ring current effect and a weaker π-diamagnetic ring current effect (by NICS(*ZZ*)) in **1**-D_{3h} compared to benzene.

Ultimately, no matter its popularity, NICS does little more to address aromaticity than the myriad of other parameters available in the literature. The reason for NICS failing as a universal "aromaticity" parameter does not lie in NICS but in the basis of the concept of "aromaticity"[216].

Ring strain *vs.* aromatic stabilization in 1

One way to assess the relative energetics of open and cyclic forms is to use an oligomeric structure series, as shown in Figure 4.7. In such an analysis, one considers an infinite cyclic and an infinite linear polymer as equal. Thus, the difference between the energy of an "$m+n$" oligomer and the sum of "m" cyclic monomers and an "n" oligomer should asymptotically approach "m" times the energy difference between open and cyclic monomer forms. This method has been used to assess the energy between the open triene and cyclic benzene to be *ca.* 20 kcal/mol[216].

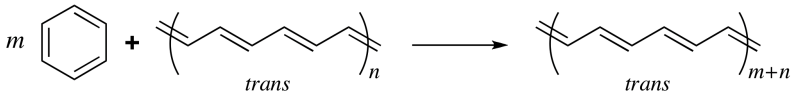

Figure 4.7: Oligomeric series analysis to determine open *vs.* cyclic energy in benzene

A similar analysis could be applied here to assess the idealized open and cyclic forms of $(NH)_3$ (Figure 4.8). Already at $n = 3$, $m = 1$ the ΔE value converges to *ca.* 24kcal/mol endothermic for the formation of the cyclic structure. A similar analysis predicted a value *ca.* -19 kcal/mol for benzene, and 27 kcal/mol for cyclopropane. Such an analysis would categorize the energy difference between open and cyclic forms of **1** as stemming more from ring strain, as in cyclopropane, than resonance as in benzene.

In light of the energetic, structural and NICS phenomena, the understanding of the properties of triaziridine **1**-D_{3h} seems not to be aided by categorization as aromatic. Thus, we turn our attention to lone-pair repulsion effects, specifically to how substituents effect the energy thermodynamic/kinetic relationships among cyclic isomers.

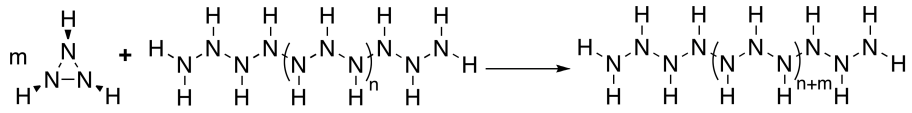

Figure 4.8: Oligomeric series analysis to determine open vs. cyclic energy in **1**

4.1.4 Substituent effects

Ground state conformers

For monosubstituted triaziridines, four conformations exist: a pair of C_1 enantiomers interconvertable by pyramidal inversion at both nitrogens bearing hydrogen and a pair of C_s meso diastereomers (X_{syn} and X_{anti}) related by pyramidal inversion at the nitrogen bearing X (Figure 4.9).

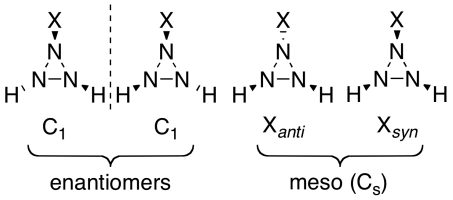

Figure 4.9: Confomers of X-substituted triaziridines.

The energy of twelve X-substituted triaziridines were computed. In all cases, the C_1 pair of conformers were lowest in energy (Table 4.2). In addition to the relative energy with respect to the lowest conformer, the difference between X_{syn} and X_{anti} as well as the differential contribution from zero-point energy (ZPE) were computed.

Table 4.2: M06/DZV(2d,p) calculated energies of conformers X_{syn} and X_{anti} relative to C_1

X	X_{anti}	X_{syn}	$\sum_{syn+anti-}$	$\Delta_{syn-anti}$	Δ_{ZPE}
H	0.00	8.87	8.87	8.87	0.92
CH_3	0.85	7.63	8.48	6.78	0.39
CF_3	1.32	7.70	9.02	6.38	0.31
CN	2.27	7.08	9.35	4.81	0.24
NH_2	1.72	6.42	8.14	4.70	0.07
CCH	2.80	6.32	9.12	3.52	0.26
F	3.44	5.61	9.05	2.16	0.49
Cl	3.46	5.54	9.00	2.08	0.24
BH_2	4.52	4.52	9.04	0.00	0.00
NO_2	5.08	7.01	12.09	1.93	0.11
OH[a]	1.67	5.01	6.68	3.34	0.99
O^-	6.10	-0.12	5.98	-6.22	-1.10

[a] For X = OH there are additional conformations with OH pointing in or out. Thus the relative energies with respect to C_1 out (the lowest energy conformer) follow as C_1 in = 0.87 kcal/mol, OH_{anti} in = 1.67 kcal/mol, OH_{anti} out = 4.03 kcal/mol, OH_{syn} out = 5.01 kcal/mol, OH_{syn} in = 13.41 kcal/mol.

When compared to the C_1 isomers, the X_{syn} and X_{anti} isomers show a compensation effect wherein stabilization of the X_{syn} form generally correlates to a destabilization of X_{anti}. Thus, the relative energy of $X_{anti} + X_{syn} =$ constant (ca. 9 ± 0.5 kcal/mol) for nine of the twelve derivatives. One might expect a common set of effects would rationalize

these somehow related cognates. In contrast, three of the twelve derivatives lay at least six standard deviations away from the norm (X = NO_2, OH, and O^-). One can look for special interactions that might separate these from the pack.

To look for common factors, the structures were analyzed as a collection of bilateral eclipsing interactions. There are six eclipsing interactions in a triaziridine conformer and they can present themselves in seven types: (1) X/H; (2) LP_X/H; (3) X/LP_H; (4) LP_X/LP_H; (5) H/H; (6) H/LP_H; (7) LP_H/LP_H (*cf.* Table 4.3, footnote a). Each of the conformers C_1, X_{anti} and X_{syn}, can be characterized by a pattern of eclipsing interactions (Table 4.3). Over a series of substituted triaziridines, the interplay of these interactions may be deciphered.

Table 4.3: Characterization of conformers by eclipsing interactions[a]

Interaction	C_1	X_{anti}	X_{syn}
X/H	1	0	2
LP_X/H	1	2	0
X/LP_H	1	2	0
LP_X/LP_H	1	0	2
H/H	0	1	1
H/LP_H	2	0	0
LP_H/LP_H	0	1	1

[a] X and H stand for substituents X and hydrogen, respectively; similarly LP_X and LP_H stand for the lone pair of a nitrogen bearing either X or hydrogen, respectively. The / is used to mean eclipsing interaction.

For the parent triaziridine with X = H, the C_1 and X_{anti} become equivalent. The difference between X_{anti} and X_{syn} is 4 fewer H/LP interactions, compensated by 2 additional H/H plus 2 additional LP/LP interactions and *ca.* 9 kcal/mol (Figure 4.10). Assuming an H/H interaction to be about the same as in ethane (*i.e.*, 1 kcal/mol per H/H interaction) and inferring an H/LP interaction to be about 0.5 kcal/mol, then one arrives at an LP/LP interaction in the parent triaziridine of about 4.5 kcal/mol. This value is similar to that derived from diazine, where in the nitrogen atoms also are roughly sp^2 hybridized[211,217]. For sp^3 hybridized nitrogen atoms, as in hydrazine, the interaction energy is expected to be much higher[190,210].

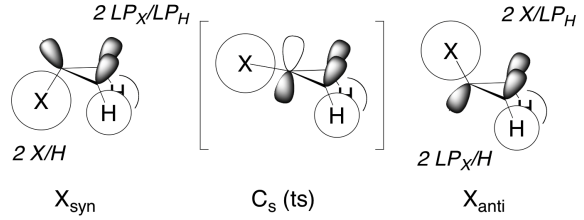

Figure 4.10: Conformers with differential eclipsing interactions indicated. Nitrogen atom labels suppressed for clarity. LP_H/LP_H and H/H interactions omitted because they are constant.

Already at this stage one can discern that the LP/LP interactions are much stronger than H/H or H/LP in the parent system. Therefore, a primary substituent effect could arise from the influence of X on the LP/LP interaction. One can imagine chemical effects that

might affect these eclipsing interactions: the electronegativity of X and π conjugation with LP_X, are those classically discussed. Ritchie has already discussed that for systems in which X is directly bonded to N, as in NH_2X, the classical ideas of linear free energy effects are at best qualitatively helpful[218]. Indeed, Calvin developed a special parameter to deal with such interactions for pyramidal inversion barriers (see below)[219]. Qualitatively the influence of X on LP_X comes from sigma inductive factors, which induce a rehybridization at nitrogen a la Bent's rule[220], in combination with π conjugation factors (*e.g.* vicinal lone-pair repulsion). Greater σ character for a given LP lowers its interaction energy. Greater π character increases its interaction energy, unless it is involved in a π bond.

At one extreme, are substituents like F and Cl, with strong s acceptor character that reduces the interaction energy of LP_X by giving it more s character. At the other extreme, BH_2 acts as s donor but has a strong π acceptor character that pulls LP_X into π conjugation and away from further interaction.

The LP_X/LP_H and LP_H/LP_H interaction model accounts for the compensation of energy betweenX_{syn} and X_{anti} as well as for the constant lower energy of the C_1 isomer. In those cases where the substituent causes the LP_X/LP_H interactions to drop off, the differential eclipsing model described above predicts that X_{syn} and X_{anti} should become roughly equal in energy, as it is primarily one LP_X/LP_H that differentiates them. The difference between C_1 and X_{syn} and X_{anti} is modeled as 1 LP_H /LP_H ± 1 LP_X /LP_H interaction, respectively. Assuming the substitutent does not play a role in any long-range effect on the LP_H , then the LP_H /LP_H interaction would remain roughly 4-5 kcal/mol and therefore the C_1 isomer would be lower in energy than X_{syn} and X_{anti} by 0-5 kcal/mol and 5-10 kcal/mo, respectively. This model is consistent quantitatively and qualitatively with the computed data for the 9 "regular" substituent examples. What then of the three outliers?

For the three outliers NO_2, OH and O^-, an estimate of the "expected" X_{syn} and X_{anti} relative energies can be made in order to see from where the anomaly stems. NO_2 being a group of electronegative atoms and having the possibility of π conjugation should be effective at reducing the LP_X/LP_H interaction, therefore X_{syn} and X_{anti} should each be around 4–5 kcal/mol higher in energy than the C_1 isomer. Indeed, X_{anti} is at the higher border of the expected range whereas X_{syn} is destabilized. Examination of the detailed structure shows steric transannular interactions in X_{syn}.

An estimate for the OH substituted conformer comes from the expectation of OH to be between F and NH_2 (*i.e. ca.* 6 kcal/mol for X_{syn} and 3 kcal/mol for X_{anti}). For X = OH there are additional conformations with OH pointing *in* or *out*; Table 4.2 presents the most stable for each conformer in the body of the table and the others in the footnote. Recounting the relative energies here with respect to C_1 *out* (the lowest energy conformer), they follow as C_1 *in* = 0.87 kcal/mol, OH_{anti} *in* = 1.67 kcal/mol, OH_{anti} *out* = 4.03 kcal/mol, OH_{syn} *out* = 5.01 kcal/mol, OH_{syn} *in* = 13.41 kcal/mol. The midpoint between OH_{anti} *in* and *out* (*ca.* 3 kcal/mol) sits in the expected range, indicating a small H-bonding *vs.* electron repulsion term depending on the specifics of the OH conformation. The midpoint of OH_{syn} *in* and *out* (*ca.* 9 kcal/mol) is still too high and seems to arise from a strong transannular repulsion in the OH_{syn} *in* conformer. Comparison of OH_{anti} conformations with *in* and *out* pointing H gives an estimate of the bifurcated H-bond energy in OH_{anti} in (*ca.* 2.5 kcal/mol).

In special instances there can be strong X/H and X/LP_H interactions, for example in the case of O^- where O^-/LP_H is strongly destabilizing and O^-/H is strongly stabilized due to Coulombic interactions. This effect is evident in the strongly destabilized X_{anti} and strongly stabilized X_{syn} energies compared to the expected values.

Overall, such a lone-pair repulsion model accounts for the general trend in substituent effects on conformer energies. The energetics of any outliers can be explained by additional transannular interactions. Thus, this approach highlights two key factors that account for the variance in the data (*i.e.*, the σ and π factors that affect LP/LP repulsions). Albeit a simple model, it is insightful.

Another effect that could alter the LP_X/LP_H interaction is the degree of resonance conjugation between X and LP_X. It is known for substituted amines that such conjugation can be gauged by the energy of pyramidal inversion at N[221]. Let us turn our attention now to pyramidal inversion in the series **1**-X.

Barriers

If lone pair repulsion is a major component in determining relative energies in **1**, then it should be possible to modulate these energy differences through conjugation of substituent to nitrogen. Computational investigation included consideration of several mono-substituted variants of **1**. In the monosubstituted systems, there are three different local minima possibilities to consider: two C_s symmetric conformers (X_{syn} and X_{anti}) and one C_1 isomer. Starting from the C_1 conformer, inversion at the nitrogen bearing X proceeds through a C_2 symmetric state to a homomeric C_1 product conformer; from the C_s *syn* or *anti* conformer a C_s transition state with near flat geometry at nitrogen. The respective differences in minima and transition states as a function of X gives some insight to the substituent effects (Table 4.4).

Table 4.4: Barriers to inversion at N–X

X	$\Delta(C_2[ts]-C_1)$/min	$\Delta(C_s[ts]-X_{anti})$	$\Delta(C_s[ts]-X_{syn})$	Calvin-splitter	ΔNH_2X
F	78.3	77.7	75.5	-7.8	
O^-	52.2	60.0	66.2	-5.5	
Cl	52.8	53.2	51.1	-2.5	
NH_2	43.8	48.9	44.2	-1.6	
H	34.6	38.4	29.5	0	5.8
NO_2	35.0	34.7	32.6	2.1	2.7
CCH	18.5	19.9	16.4	2.3	1.7
CN	18.6	20.9	16.1	2.6	1.4
BH_2	0.00	0.00	0.00		0.00

Substituent effects on the pyramidal inversion barrier of aziridines and related nitrogen-containing small-ring heterocycles has been categorized as dominated by electronegativity, σ_p^-, or σ_{inv} parameters[219,222]. Electronegativity effects can be related to "Bent's rule"[220], which states that, as the electronegativity of X becomes greater, the orbital, contributed to the bond by the partner atom to X, adopts more π character. In the case of an N–X bond, this means the lone pair must be more purely σ in character and that should lead to an increase in the barrier.

The nature of σ_p^- is to characterize resonance effects that stabilize a neighboring lone pair through a π type interaction. A greater σ_p^- parameter value for X predicts a lowering of the barrier by involving the lone pair at N in a π-bond with an optimally planar geometry[223].

The σ_{inv} parameter was a construction of Splitter and Calvin to deal with the unusual behavior of nitrogen centered barriers to pyramidal inversion[219]. They studied a number of heterocycles and attempted to establish a Hammett relationship by empirical regression on the rate of inversion data. This method provides a simple semi-quantitative model from which one can predict the barrier to inversion in derivatives of **1**. It does not necessarily provide any more insight into the physical mechanisms of the variance, but empirically takes into account a complex admixture of the elements stated above.

A plot of C_1 X_{anti} or X_{syn} barrier *vs.* electronegativity shows a trend that can be fit to a line with a regression R^2 value no better than 0.84. A simple plot of barrier *vs.* σ_p^- provides a substantially worse linear correlation. The σ_{inv} parameter performs well, with R^2 for C_1 X_{anti} or X_{syn} barriers of 0.95, 0.94, 0.89, respectively, as shown in Figure 4.11. As with the simple lone-pair repulsion model for ground state conformations, the Splitter–Calvin model allows one to identify outliers and discuss them relative to an empirically "expected" context. The consistent outlier in the barrier series is NO_2. It seems the full conjugation benefit expected from NO_2 is not realized in these systems. Although one could rationalize this as coming from some combined strain and steric effect in the transition state, we are still working to understand this better.

Observation of the outliers in the barrier *vs.* electronegativity plot indicated that a conjugation effect was missing. Indeed, a plot of barrier *vs.* $[E_{\mathrm{neg}} - C\sigma_p^{0-}]$ provides a substantially better fit with $C = 1$ and can be optimized for $0.5 < C < 0.75$ to give an R^2 value of 0.95. This analysis is intended to illustrate that a combination of electronegativity and conjugation effects are at play; it is not intended to suggest yet another convoluted correlation scheme is needed. It supports the idea that the Splitter–Calvin model accounts empirically for these two effects. An added feature of the Splitter–Calvin model is that one can extrapolate an expected *r* slope for the correlation of around 5, on the basis of ring strain and atomic composition. Indeed, the slopes of the correlations in Figure 4.11 all come between 4.8 and 5.5. Thus, one can conclude that rehybridization and conjugation effects are important to determine the barrier to pyramidal inversion in the series **1**-X, and that the series **1**-X is not anomalous compared to other systems displaying pyramidal inversion barriers at nitrogen.

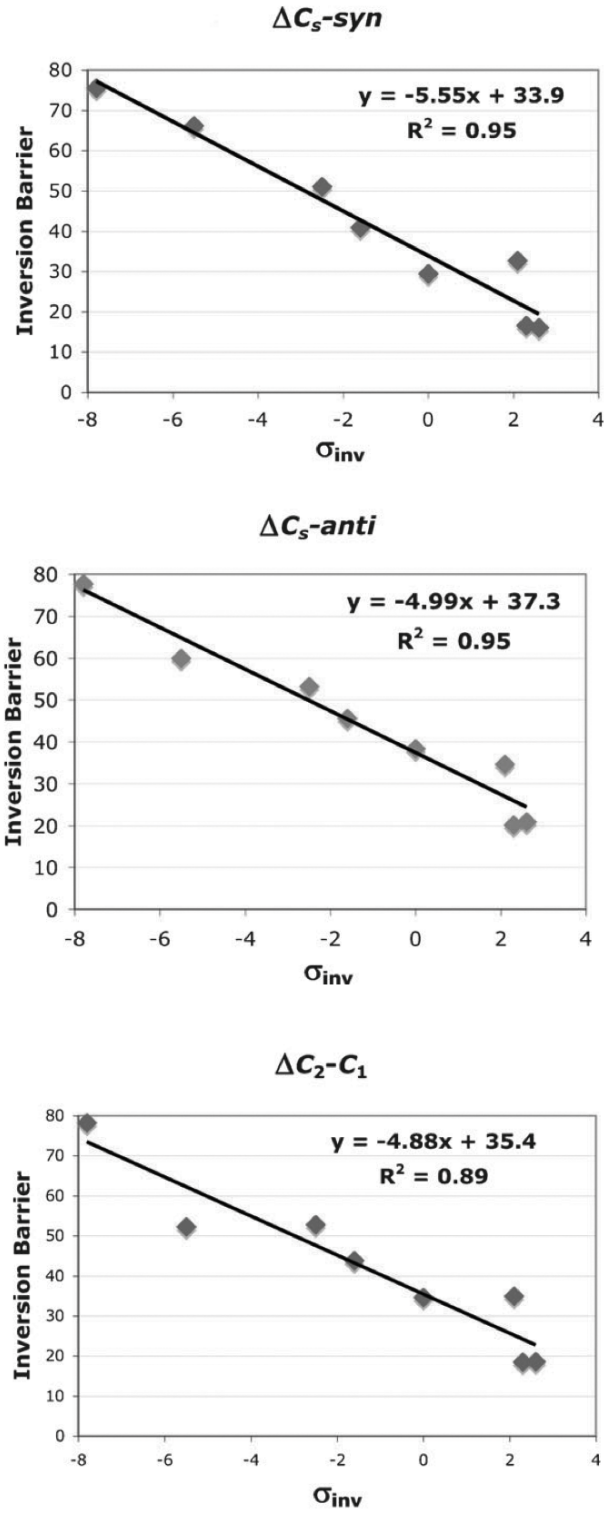

Figure 4.11: Correlation of computed inversion barrier to Calvin's parameter for nitrogen inversion.

Substituent effects on the heat of formation and strain

The effect of the substituents on the stability of the ring was evaluated considering two energetic properties: ring strain[188,224] and enthalpy of formation[169,225]. Ring strain is evaluated using the homodesmotic reaction in equation (4.1) for the substituted systems.

$$N_3H_2X + 3\ NH_2{-}NH_2 \rightarrow 2\ NH_2{-}NH{-}NH_2 + NH_2{-}NX{-}NH_2 \tag{4.1}$$

The standard enthalpy of formation was evaluated using Equation (4.2).

$$\frac{3}{2}N_2\,(g) + \frac{3}{2}H_2\,(g) \rightarrow trans - N_3H_3\,(g) \tag{4.2}$$

The enthalpy of formation of the ring involves calculation of the enthalpy of formation of the HX molecule, using the same method as that used for the cyclic molecule. Subtracting this value from the total ΔH_f° provides a "corrected" value for the enthalpy of formation. Calculations of ΔH_f° and ΔG_f° at 298 K for **1**-X were performed using the G3MP2 method (Table 4.5).

Table 4.5: G3MP2 calculated ΔH_f° and ΔG_f° at 298 K for **1**-X

X	ΔH_f	ΔG_f	HX	ΔH_f^{corr}
F	83.75	101.93	-65.44	149.19
O^-	81.89	104.27	-57.41	139.39
Cl	117.53	143.60	-10.00	127.53
NH_2	147.49	164.17	31.20	116.29
H	94.37	118.93	-17.84	112.21
NO_2	-60.99	-32.23	-166.54	105.56
CCH	99.59	116.52	-1.14	100.73
CN	104.08	127.88	8.71	95.36
BH_2	103.17	122.65	27.16	76.01

Depending on the type of substituent, one can evaluate substitutent interactions in terms of their atoms donor or acceptor properties on the ring through σ and/or π interactions. Evaluation of CRS across the series **1**-X reveals stabilization by σ acceptors and destabilization for σ donors (Table 4.7). The predicted trends across MP2, B3LYP, and M06 are the same, with MP2 consistently predicting much lower strain energies than the DFT methods. Between the two strategies of DFT functional, the M06 predictions lie intermediate between B3LYP, and MP2.

A plot of calculated ΔH_f^{corr} results against the substituent electronegativity Taft parameters[226] (a slight modification to Hammett's parameter) shows a reasonable linear correlation (Table 4.6; Figure 4.12). Overall, the results support the idea that substituent electronegativity plays a dominant role on the stability of the triaziridine ring. A convenient rationalization of this effect stems from Bent's rule (*i.e.* lone-pair rehybridization).

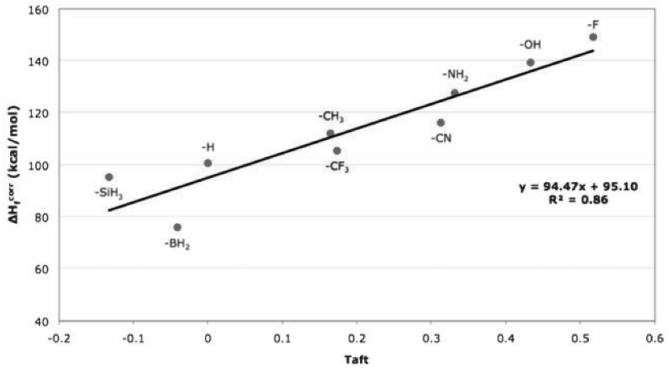

Figure 4.12: Taft correlation diagram for ΔH_f°. Molecular orbital analysis of the π system of $N_3(BH_2)_3$, **4**.

Table 4.6: Calculated ΔH_f^{corr} and Taft values for **1**-X

X	Taft	ΔH_f^{corr}
F	0.517	149.19
O^-	0.434	139.39
Cl	0.332	127.53
NH_2	0.313	116.29
H	0.165	112.21
NO_2	0.174	105.56
CCH	0	100.73
CN	-0.133	95.36
BH_2	-0.041	76.01

Table 4.7: Substituent analysis of triaziridine system in terms of conventional ring strain (CRS) for substituents with s and p effects

X	MP2/DZV(2d,p)	B3LYP/DZV(2d,p)	M06/DZV(2d,p)
F	21.98	27.61	25.22
O^-	21.14	24.57	28.39
Cl	23.51	27.29	27.31
NH_2	30.22	36.19	35.38
H	25.31	29.82	28.46
NO_2	29.64	34.14	33.55
CCH	25.93	32.59	30.43
CN	29.88	35.18	33.78
BH_2	27.27	39.56	38.50

Extended aromatic constructs

The results obtained from the analysis of **1**-X systems point to a special direct p bonding in N-BH_2 that is dramatically stronger than in N-NO_2. Indeed, a similar effect is present even in the simple NH_2-BH_2 *vs.* NH_2–NO_2 analogs. Whereas NH_2–BH_2 is flat

and has a 30 kcal/mol orthogonal torsional barrier, NH_2-NO_2 is slightly pyramidalized with a twisted cognate that is only 11 kcal/mol higher in energy. Given the *ca.* 30 kcal/mol barrier to inversion for traziridine **1**-H, it is not surprising that **1**-BH_2 attains a flat minimum energy structure.

From these data, however, one can propose a potentially flat structure with a π aromatic-like triaziridine system, such as $N_3\left(BH_2\right)_3$ (Figure 4.13).

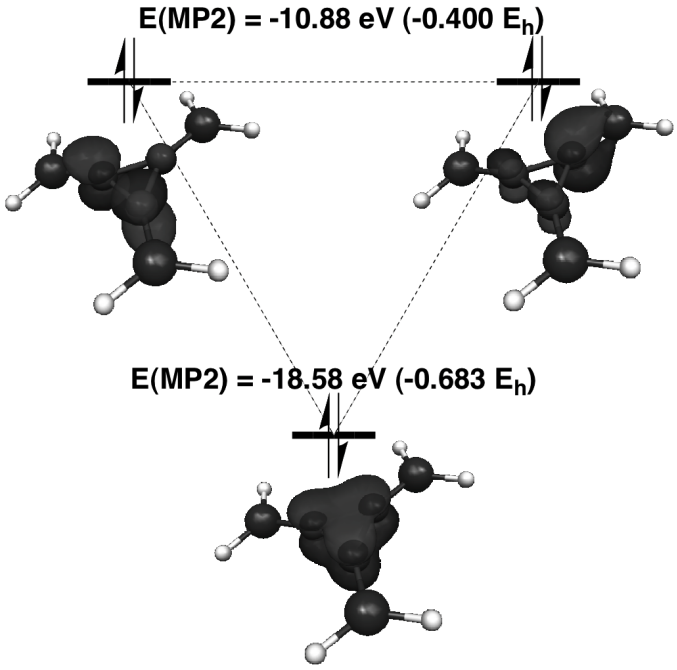

Figure 4.13: Molecular orbital analysis of the π system of $N_3\left(BH_2\right)_3$, **4**.

As in **1**-BH_2, there is a partial delocalization of the π orbitals onto the boron atoms. Here, the π system is lower in energy with respect to that of D_{3h} triaziridine but has a very similar π system.

The absolute minimum on the $N_3H_3H_6$ potential energy surface is the six-membered ring aromatic inorganic system of borazine. MP2/DZV(2d,p) calculations place borazine approximately 240 (220, M06) kcal/mol lower in energy with respect to **4**. Nonetheless, within the manifold of cyclic N_3 structures, **4**, is flat and the relative minimum. The structure of **4** well illustrates the strength of the BN π interaction and the power this has to control molecular structure and properties (Table 4.8)[227].

Table 4.8: Calculated triaziridine results (Å) for *tri*-substituted triaziridine.

MP2		B3LYP		M06	
r(N-N)	*r*(N-B)	*r*(N-N)	*r*(N-B)	*r*(N-N)	*r*(N-B)
1.398	1.389	1.395	1.383	1.383	1.382

4.2 Assessment of DFT and DFT-D for Potential Energy Surfaces of Rare Gas Trimers – Implementation and analysis of functionals and extrapolation procedures

4.2.1 Introduction

Rare gas compounds are, in many cases, simple models for study of complex properties. In particular, weak interactions of van der Waals bound dimers, n-body interaction energies in trimers, tetramers, etc., and complex aggregations of large clusters, are of significant importance. Few body, rare gas compounds are heavily used for parameterizations of semi-empirical potentials, for example, for empirical force fields or ab initio molecular dynamics methods. In these cases, highly accurate ab initio potential energy surfaces (PES) are extremely important for such parameterizations. Also significant are three-body atomic systems, which present intriguing properties, such as "Efimov physics"[228,229], and "Borromean states"[230,231] with the presence of bound states even when the analogous 2-body systems are unbound.

Homo-dimers present a well-known, simple, one-dimensional PES[232], commonly used in parameterizations. Equilateral homo-trimers as well as homo-dimers, present an analogue one-dimensional PES but with a much larger (Borromean) bound state. Because of a less profound knowledge of the nature of their bonds, their use in parameterizations is restricted mainly to 3-body correction components[233,234]. For the same reasons, accurate results of rare gas dimers, are mainly used as test systems for theoretical models, but homo-trimers are very rarely used in this sense.

The study of rare gas trimers is nevertheless a very well established first step in the investigation of the stability of large clusters, and significant data is available in this direction[235–245]. Some experimental results have been carried out on rare gas triatomic systems[246], revealing less sensitivity in measurements than the weaker binding dimers. We believe that rare gas trimers represent ideal candidates for parameterization and validation of new theoretical models, in the same way that dimers have been used up to now.

In terms of theoretical models for modeling intermolecular interactions in the study of the properties of gases, much is being learned about the different regions of the potential energy surface and the correct importance and representation of short, intermediate, and long-range interaction, particularly since the introduction of entire new generations of approximations for the exchange-correlation potential (*e.g.*, see Table 4.9). The local density approximation (LDA) and its analogue, local spin density approximation (LSDA), were the first approximations to the exchange-correlation potential v_{xc} used by Kohn and coworkers with high success, particularly for applications in solid-state physics. Initial strategies to improve results of LDA/LSDA involved inclusion into the exchange-correlation functional terms that depends on the gradient of the density, leading to the generalized gradient approximation (GGA) functionals. These functionals were the major contribution to the introduction of DFT in quantum calculation on molecules with chemical accuracy. Despite their great success, GGA approximations fail in the description of properties that depend mainly on the correlation of electrons, such as is the case for vdW complexes. To overcome the main limitations of GGA functionals, different strategies have been developed in the recent literature (Table 4.9).

Table 4.9: Categories of strategies of density functionals beyond GGA.

Density Functional Type	**Main Feature**	**Examples**	**Reference**
meta-GGA	Depend on the Kohn-Sham kinetic energy density	Minnesota family	Zhao/Truhlar[9,14,15,247]
		τ-HCTH family	Handy[16]
		BMK	Boese/Martin[17]
Range-separated hybrid (RSH)	Coulomb operator is separated into long-range and short-range terms, the extent of which determines the exact variant of the functional	LC-BLYP CAM-B3LYP	Savin[18,19]
		HSE	Scuseria[248,249]
		ωB97	Chai/Head-Gordon[20]
Empirical/semi-empirical	vdW dispersion interactions described empirically with a damped inter-atomic R^{-6} potential	B97-D	Grimme[23]
Double-hybrid	Includes terms derived from correlated wave function methods (*e.g.,* MP2 theory)	B2-PLYP, mPW2-PLYP	Grimme[24,250]
		MC3BB MC3MPW	Zhao/Truhlar[25]
		B2K-PLYP mPW2K-PLYP	Martin[93]
Andersson-Langreth-Lundqvist functional	Long-range exchange correction scheme together with the Andersson-Langreth-Lundqvist vdW functional	vdW-DF	Langreth[26]

In this work, we have evaluated the latest dispersion sensitive density functional theory (DFT) based methodologies for their ability to accurately represent the potential energy surface of the rare gas trimer systems. While one can find several literature investigations concerning rare-gases dimers, very few articles involve accurate calculations of the potential energy surfaces of the rare gas trimers. Moreover, to our knowledge, none of the more recent dispersion-enabled DFT functionals have been tested on these systems, despite their relevance for understanding the intermolecular interactions, and the implications on the overall computational cost saving compared to traditional benchmark level methods. Also of fundamental importance in this analysis is the use of complete basis set (CBS) extrapolation, for which there are several established procedures. In this context, it is also of interest to compare convergence properties and behavior of basis set superposition error (BSSE) across these models. In the present contribution, we show high

accuracy calculations of the PES of the main Rg_3 molecules (Rg = He, Ne, Ar), across a full suite of density functional classes and several established extrapolation schemes, referenced against CCSD(T)/CBS theory.

4.2.2 Computational Methods

All calculations reported here were carried out using a locally modified version of the GAMESS electronic structure program, running on our group cluster hardware. Associated visualization and analysis was carried out using MacMolPlt[204] and Qutemol[251]. In the present work, we apply our recently implemented suite of density functionals, including the semi-empirically corrected functionals, in addition to key functionals implemented by several other GAMESS DFT contributors. Evaluated functionals include B97[28], B97-1[252], B97-2[253], B97-3[254], B97-D[23], B98, HCTH/93[252], HCTH/120 and HCTH/147[255], HCTH/407[256], τ-HCTH and τ-HCTHhyb[16], BMK[17], ωB97 and ωB97X[20], ωB97X-D[21], BLYP[6,257**?**], B3LYP[6**?**], B2-PLYP[24], CAM-B3LYP[19], VS98[258], PKZB[259], TPSS[118,260], TPSSH[261,262], TPSSM[263], M05[9], M05-2X[10], M06 and M06-2X[15], M06-L[12], M06-HF[13], M08-HX and M08-SO[247]. The ultrafine (96,1202) Lebedev grid (corresponding to army grade) has been used for all calculations. In accord with our previous study on the performance of the B97-D functional[32], the scaling factor for the semi-empirical dispersion was taken as $s_6 = 1.00$ for all the double-ζ basis sets considered, and $s_6 = 1.25$ for all the triple-ζ basis sets considered. Basis set superposition error (BSSE) is corrected with the counterpoise (CP) method[264]. A detailed analysis of the BSSE results is also reported in this work.

In addition to density functional theory, computations were also carried out using the Hartree-Fock (HF)[265], Møller-Plesset perturbation theory of order (MP2)[107], coupled-cluster with single and double excitations (CCSD)[266], and two methods of coupled-cluster with single, double and iterative triple excitations CCSD[T] (also known as CCSD+T(CCSD)) and CCSD(T)[267,268] methods, as implemented in GAMESS. The latter method is the highest level of theory applied in this study, and arguably one of the best methods available for single-reference computations. Additional renormalized (R-), and completely renormalized, (CR-), CCSD(T) calculations[266,269,270] are presented for the case of He, for comparative purpose.

Several basis sets were employed in this study in order to investigate consistency and predictability across the full set of molecules studied. The basis sets include the correlation consistent basis set of Dunning**?** , with augmented functions, denoted aug-cc-pVnZ, with n = T for triple, Q for quadruple, and 5 for quintuple. We note that relative contractions for each split shell differ from He to Ne and Ar, and refer readers to the original articles for more details. Extrapolation to the complete basis set (CBS) limit is presented, using comparative expressions for the respective He_3 cases. Theoretical Methodology and Approach Accurate calculations of the PES of rare-gas trimers: The potential energy surfaces (PESs) of three Rg_3 systems (Rg = He, Ne, Ar), are investigated with high-level computational methods up to CCSD(T) with complete basis set extrapolation (CBS). The potential energy surface of each D_{3h} Rg_3 molecule is determined with respect to the ground state of the respective three separated Rg atoms along the radial coordinate of the trimer (Figure 4.14). In greater detail, the He_3 molecule is used to carefully investigate performance across all methods, the results of which are then extended to the other two

trimer systems, Ne and Ar trimers. For highly accurate comparison, we carry out an extrapolation to the complete basis set limit with coupled cluster, as described in the next sections, for all three trimers.

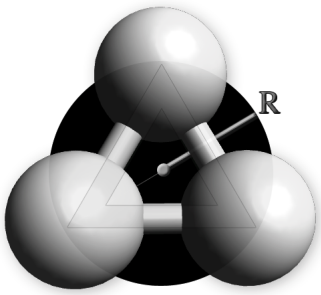

Figure 4.14: The radial coordinate of the Rg_3 D_{3h} trimer molecule.

Convergence of the results with respect to basis set size

For the He_3 trimer molecule, we have carried out accurate calculations using CCSD(T) showing the convergence of the PES with respect to increasing basis set size, including extrapolation to the complete basis set limit. In addition, an extra set of calculations was carried out with the aug-cc-pVnZ (n = 2-5) series of basis sets to investigate the convergence properties of this family of basis sets. The correlation consistent basis sets of Dunning and co-workers are used to minimize error associated with finite one-particle expansions. Together with extrapolation to the complete basis set (CBS) limit, provides high accuracy for electronic energies, enabling quantitative comparison between different ab initio methods.

An important component in establishing reliable potential energy surface data involves consistent extrapolation to complete basis set and complete correlation limits[271? –287]. While there has been much discussion associated with carrying out complete basis set extrapolation procedures in the literature across a variety of molecular systems, including challenges associated with the type of molecule, family of basis sets being used, treatment of BSSE, or properties being extrapolated, the most accurate and reliable extrapolation methodology is not a matter of consensus. In this work, we compare several of the important extrapolation schemes used in the literature, and therefore we first briefly discuss the different approaches in what follows.

The original purpose of Dunning and coworkers in the construction of the aug-cc-pVnZ basis sets was to enable the extrapolation of properties using a simple 3-points exponential formula, denoted here as [n,n',n";Feller]-CBS, with [n,n',n" the cardinality of the employed basis]:

$$f(n) = f^{\mathrm{CBS}} + \mathrm{A}\exp(-\mathrm{B}n) \tag{4.3}$$

where n is the cardinal number of the basis set, for example, n = 2 for DZ, 3 for TZ, etc., $f(n)$ is the property (here, this is energy) obtained using the aug-cc-pVnZ basis set, and f^{CBS} is the extrapolated value for the same property.

Several authors assert that Equation 4.3 is suitable for the extrapolation of energies at the Hartree-Fock (HF) level, while in many cases the effective decay for a correlated

method (*e.g.*, coupled-cluster) is reasonably slower than the exponential decay[273,285]. Many other extrapolation techniques have been developed as alternatives. In 1962, Schwartz[284] proposed an extrapolation procedure for energies of atoms that incorporates an inverse power series function of the basis set extension, n. While this extrapolation has quite a simple expression for atoms, it tends to became very complicated for molecules containing different types of nuclei, requiring further approximations[277,288]. In the simple case of Helium homo-trimer, however, such a formulation can be applied as,

$$E(n) = E^{\mathrm{CBS}} + \mathrm{A}n^{-3} + Bn^{-5} + \mathrm{C}n^{-7} + \ldots \tag{4.4}$$

Truncation of Equation 4.5 leads to simple n-points formulas. In the present study, we denote the simple 2-point formula as [n,n';Schwartz]-CBS, the 3-point formula as [n,n',n";Schwartz]-CBS, and so on.

Another set of extrapolation methods of interest was proposed by Truhlar[285] and by Halkier[273], that couple HF together with correlation methods to obtain a formulation of the type,

$$E^{\mathrm{CBS}}(\mathrm{TOT}) = E^{\mathrm{CBS}}(\mathrm{HF}) + E^{\mathrm{CBS}}(\mathrm{corr}) \tag{4.5}$$

The HF component, $E^{\mathrm{CBS}}(\mathrm{HF})$, and the correlation component, $E^{\mathrm{CBS}}(\mathrm{corr})$, are obtained using different power expansion extrapolations for their respective methods. In the method of Truhlar, a power expansion n^{-A} with variant coefficients is used, while Halkier uses an exponential + Schwartz-type expansion.

In the present work, we also employ a hybrid approach that makes use of the 3-point Feller exponential formula, denoted [TQ5;Feller]-CBS, for the HF component, and the 3-point Schwartz formula, [TQ5-Schwartz]-CBS, for the correlation component. This method will be denoted simply as [TQ5;Mixed]-CBS.

Results for several extrapolation techniques at the CCSD(T) level of theory are presented in Table 4.10 and Figure 4.15, for the He_3 trimer system. Comparing results without extrapolation using aug-cc-pVQZ and aug-cc-pV5Z basis sets, one observes evidence of reaching the complete basis set limit. A suitable extrapolation technique with these large basis sets should therefore provide results very close to that of the complete basis set limit. Extrapolations that incorporate double-ζ basis sets are largely insufficient, including the [DTQ5;Schwartz]-CBS method. The simple 2-point [TQ;Schwartz]-CBS extrapolation method, although an improvement over formulas containing double-ζ basis, still carries substantial error in the minimum region (Figure 4.15, insert graph). The best results are achieved with the exponential [TQ5;Feller]-CBS and the simple 2-point [Q5;Schwartz]-CBS extrapolation procedures.

Table 4.10: CCSD(T) dissociation energies, D_e (μE_h), of the He_3 molecule along the radial coordinate R (Å) for various basis sets and CBS extrapolation formulas.

R	auc-cc-pVQZ	aug-cc-pV5Z	[DT;Schwartz]-CBS	[TQ;Schwartz]-CBS	[Q5;Schwartz]-CBS	[DTQ5;Schwartz]-CBS	[TQ5;Feller]-CBS	[TQ5;Mixed]-CBS
1	16,898.453	16,880.903	16,662.095	16,678.638	16,862.491	16,969.085	16,907.242	16,929.423
1.2	3,258.231	3,248.334	3,168.221	3,204.032	3,237.950	3,256.623	3,250.149	3,247.306
1.4	408.852	403.973	368.067	405.416	398.855	393.902	400.204	394.924
1.6	-66.532	-66.212	-55.895	-70.121	-65.877	-62.974	-65.200	-67.486
1.65	-88.653	-88.249	-73.032	-92.438	-87.825	-84.551	-87.120	-89.150
1.7	-96.628	-96.593	-79.897	-99.753	-96.556	-94.093	-95.933	-97.864
1.75	-96.165	-96.696	-81.360	-97.913	-97.253	-96.367	-96.829	-98.739
1.8	-91.039	-92.075	-80.020	-91.028	-93.161	-94.070	-93.023	-94.917
1.9	-75.574	-76.837	-73.213	-72.331	-78.162	-81.585	-78.645	-80.344
2	-60.082	-60.582	-63.301	-55.358	-61.106	-64.696	-61.991	-63.248
2.2	-36.916	-35.964	-41.031	-33.435	-34.964	-36.085	-35.794	-36.235
2.4	-22.355	-21.700	-24.573	-20.490	-21.014	-21.442	-21.478	-21.696
2.6	-13.564	-13.383	-15.280	-12.294	-13.192	-13.805	-13.472	-13.636
2.8	-8.487	-8.417	-9.926	-7.570	-8.343	-8.864	-8.537	-8.633
3	-5.511	-5.447	-6.532	-4.921	-5.380	-5.697	-5.508	-5.551

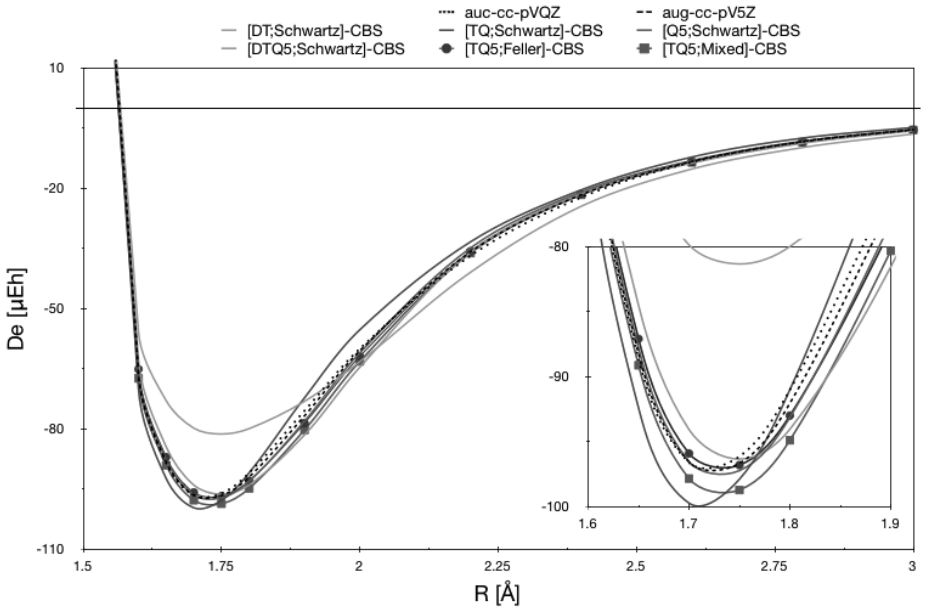

Figure 4.15: CCSD(T) dissociation energies D_e (μE_h) of the He_3 molecule along the radial coordinate R (Å) for as a function of basis set and CBS extrapolation formula. Dashed lines are aug-cc-pVQZ and aug-cc-pV5Z.

Basis set convergence and overall extrapolation behavior can also be viewed by evaluating the interaction energies at fixed distance near the minimum, R = 1.75 Å (Figure 4.16). Figure 4.16 shows that the convergence of the He_3 trimer energy with the aug-cc-pVnZ basis sets is very well approximated by the original exponential formula of Feller. These results are perhaps not a great surprise due to the simple nature of the high-symmetry trimer, with only six electrons. For similar reasons, however, the mixed extrapolation technique appears to be slightly over-bound for this simple case, while it

might provide more accurate results for more complicated molecular systems. The Feller extrapolation formulation will be used for the other two trimer systems.

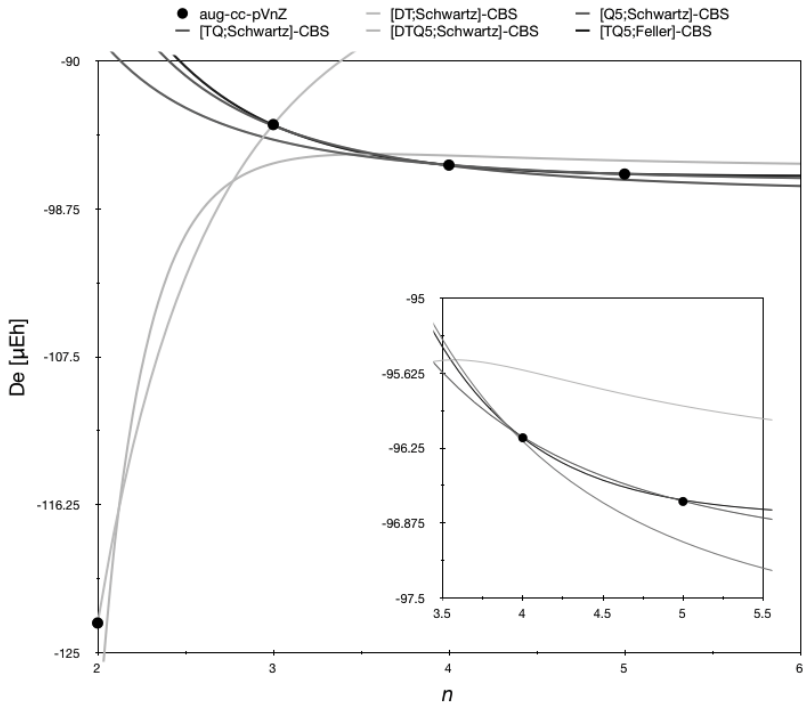

Figure 4.16: Evaluation of extrapolation formulas at the complete basis set limit as a function of basis set size, n, for He_3 at R = 1.75 Å.

Convergence of results with respect to wavefunction method

We next consider optimization of the wavefunction method. In particular, the dissociation energies, D_e, of the He_3 trimer along the radial coordinate R are calculated using the [TQ5;Feller]-CBS extrapolation with different wavefunction methods. Wave functions types include Hartree-Fock (HF) up to coupled cluster methods, as available in GAMESS. In addition to the standard CCSD, CCSD[T], and CCSD(T) methods, GAMESS also has the renormalized, R-, and completely renormalized, CR-, versions of these methods, based on the more general formalism of the method of moments of coupled-cluster equation[266,269,270]. These modified methods remove the failing of their standard counterpart approximations at larger internuclear separations (as well as for diradical systems), while keeping the method economical. The R- and CR- versions of CCSD(T), CCSD[T] make improvements to the CCSD results by a posteriori noniterative corrections to the CCSD energies, and the latter CR- versions are able to eliminate the unphysical nature of potential energy surfaces that arise in single bond breaking with the standard versions. Table 4.11 summarizes the set of computational results across the different wavefunction types.

Table 4.11: Dissociation energies D_e (μE_h) of the He_3 molecule along the radial coordinate R (Å) using the [TQ5;Feller]-CBS extrapolation procedure as function of wavefunction type.

R	HF	MP2	CCSD	CCSD[T]	CCSD(T)	R-CCSD(T)	CR-CCSD(T)
1	19,939.089	17,188.729	17,118.047	16,906.642	16,907.242	16,912.298	16,914.667
1.2	4,578.912	3,422.801	3,350.505	3,249.986	3,250.149	3,252.551	3,253.497
1.4	996.278	497.297	446.164	400.149	400.204	401.302	401.719
1.6	211.559	-14.427	-44.193	-65.224	-65.200	-64.699	-64.498
1.65	143.137	-43.978	-69.766	-87.140	-87.120	-86.707	-86.537
1.7	96.179	-59.226	-81.553	-95.950	-95.933	-95.591	-95.447
1.75	63.878	-65.549	-84.872	-96.843	-96.829	-96.544	-96.423
1.8	41.764	-66.325	-83.043	-93.034	-93.023	-92.785	-92.681
1.9	17.039	-59.104	-71.609	-78.654	-78.645	-78.478	-78.402
2	7.006	-47.580	-56.944	-61.997	-61.991	-61.871	-61.815
2.2	2.042	-27.704	-33.066	-35.798	-35.794	-35.729	-35.698
2.4	0.455	-16.700	-19.913	-21.480	-21.478	-21.441	-21.422
2.6	-0.256	-10.544	-12.529	-13.473	-13.472	-13.450	-13.439
2.8	-0.261	-6.689	-7.944	-8.537	-8.537	-8.523	-8.515
3	-0.135	-4.306	-5.122	-5.508	-5.508	-5.499	-5.494

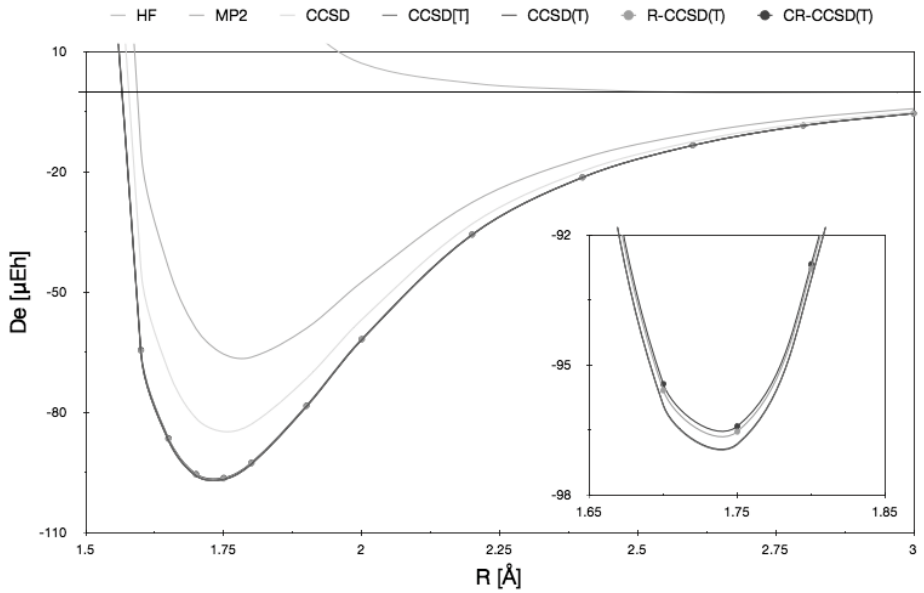

Figure 4.17: Dissociation energies D_e (μE_h) of the He_3 molecule along the radial coordinate R (Å) using the [TQ5;Feller]-CBS extrapolation procedure as a function of wave function type.

From the results, we find that HF predicts an essentially unbound system, as might be expected. MP2 theory shows differences on the order of 30 μE_h in the region of the minimum, with respect to the more accurate wavefunction types. As such, both HF and MP2 wave functions are largely insufficient for the description of the PES of this trimer. A slight improvement is observed with CCSD, which shows a difference on the order of 12 μE_h in the region of the minimum. However, it is clear that triple excitations are necessary to achieve an accurate description of the trimer system. Both CCSD[T] and CCSD(T) show essentially the same description in the region of the minimum, on

the order of 0.02 μE_h. The R-CCSD(T) and the CR-CCSD(T) methods do not provide significant improvements over that of their standard counterparts, CCSD(T) or CCSD[T], in this particular system, again showing differences on the order of 0.2 μE_h in the region of the minimum.

Reference calculations for the PES of the set of rare gas trimers, Rg_3

From the results obtained for He_3 in the previous sections, the potential energy surfaces for all three Rg_3 are determined. Results using the CCSD(T) method and the [TQ5;Feller]-CBS extrapolation are detailed in Table 4.12. The predicted minimum radial coordinate distance is 1.75 Å, 1.80 Å, and 2.20 Å, for He_3, Ne_3, and Ar_3, respectively. The dissociation energies show the drastic difference in binding characteristics along this series. In particular, while the radial distance difference between He_3 trimer and Ne_3 trimer is only 0.05 Å, the difference in dissociation energy is 284 μE_h. Moving to the Ar_3 trimer, the radial distance increases by a significant amount, 0.40 Å (0.45 Å), as does the dissociation energy, with a difference of 973 μE_h (1257.3 μE_h), compared to Ne_3 (He_3). These reference calculations will be used in the comparative analysis across density functional classes in the results section below.

Table 4.12: CCSD(T) reference dissociation energies D_e (μE_h) of the Rg_3 molecules along the radial coordinate R (Å) using the [TQ5;Feller]-CBS extrapolation procedure.

He		Ne		Ar	
R [Å]	D_e [μE_h]	R [Å]	D_e [μE_h]	R [Å]	D_e [μE_h]
1.00	16,907.2	1.00	132,743.7	1.00	1,035,602
1.20	3,250.1	1.20	25,043.9	1.20	351,542.3
1.40	400.2	1.40	3,794.8	1.40	105,027.2
1.60	-65.200	1.60	57.43	1.60	26,759.2
1.65	-87.120	1.70	-310.907	1.80	4,589.3
1.70	-95.933	1.80	-380.858	2.00	-657.443
1.75	-96.829	1.90	-336.865	2.20	-1,354.108
1.80	-93.023	2.00	-265.582	2.30	-1,247.063
1.90	-78.645	2.20	-155.338	2.40	-1,068.008
2.00	-61.991	2.40	-97.182	2.50	-881.626
2.20	-35.794	2.60	-62.580	2.60	-714.031
2.40	-21.478	2.80	-41.109	2.80	-458.702
2.60	-13.472	3.00	-27.786	3.00	-296.944
2.80	-8.537	4.00	-4.331	4.00	-50.669
3.00	-5.508	6.00	-0.342	6.00	-3.599

Density Functional Theory Classes

In order to carry out a full analysis of the series of rare gas trimers across various classes of density functional types, we have implemented a large variety of functionals of different class type into the GAMESS software. The descriptiom and the implementation

of these new classes of density functional types have been largely described in Chapter 2 of this thesis.

4.2.3 Potential Energy Surfaces of Rare Gas Trimers

We now compare performance across several density functional class types for the prediction of the potential energy surfaces of the Rg_3 trimers, as referenced against the accurate CCSD(T) [TQ5;Feller]-CBS extrapolated results provided above in Table 4.12. The aug-cc-pVnZ family of basis sets, with n = D and T, is used for all reported calculations here, in combination with 34 different exchange-correlation functional approximations. The ultrafine (96,1202) Lebedev grid (corresponding to army grade in GAMESS) has been used for all calculations. Basis set superposition error (BSSE) is accounted for using the counterpoise (CP) method[289], and further elaborated on in the discussion.

To evaluate the performance of each functional, a mean absolute deviation with respect to the accurate CCSD(T)/CBS data (Table 4.12) has been calculated on the usual 15 points grid used for the PES calculation. For this evaluation, one could argue that the mean absolute deviation, MAD, evaluated as

$$\mathrm{MAD} = \sum_{X=1}^{X_{tot}} \frac{D_e^{xc}(X) - D_e^{\mathrm{CCSD(T)}}(X)}{X_{tot}} \tag{4.6}$$

is not the best parameter for the evaluation of the functional performance due to the fact that it accounts for equal weighting of each point on the grid. To establish a single reliable evaluation parameter for the problem at hand, errors in the region of the minimum should count more than errors in regions far from the minimum. For example, points in the repulsive region at short range should be more heavily weighted. For this reason, a weighted mean absolute deviation, denoted wMAD, is calculated in addition to the usual MAD. The wMAD values are calculated by giving a weight factor to each point of the grid according to the distance of that point from the equilibrium, and the relative shape of the accurate PES. The weight factors are calculated with the CCSD(T)/CBS PES by scaling each point according to the relative heights of the PES at that point, and by renormalization of the total weight to the total number of points in the grid, (Figure 4.18).

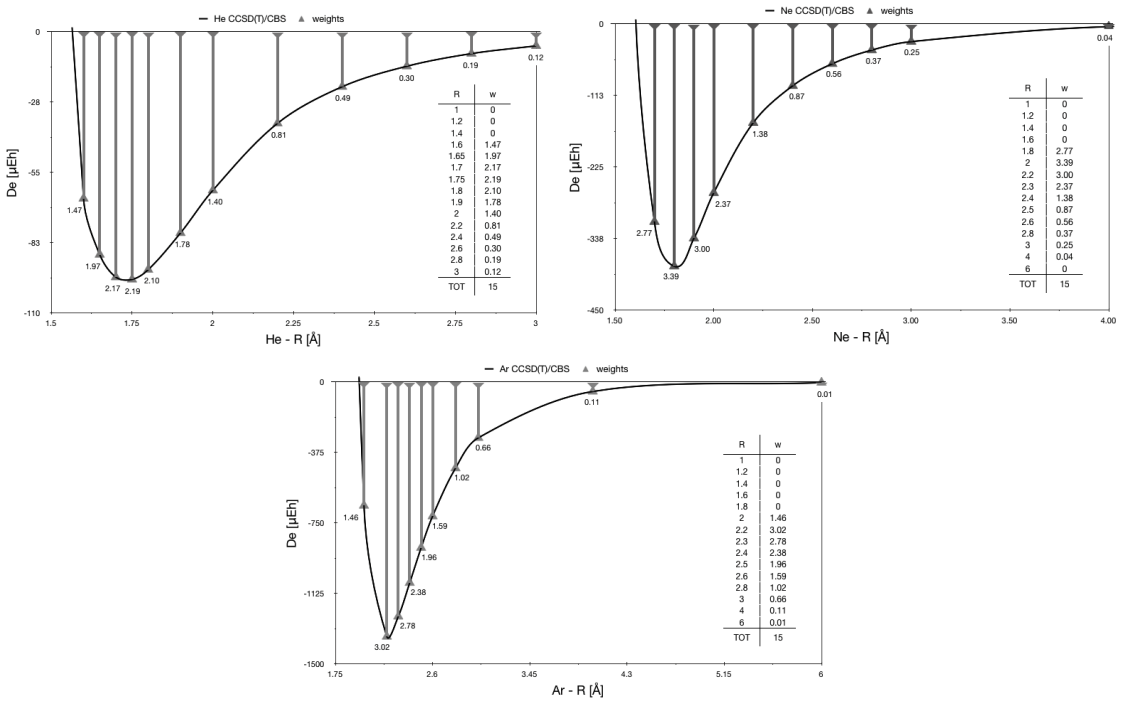

Figure 4.18: Weights used in the wMAD in accord with the shape of the accurate CCSD(T)/CBS PES for a) He (blue), b) Ne (red), and Ar (green).

In addition to the mean absolute deviation parameters, the difference from the absolute CCSD(T)/CBS value (deviation from reference, abbreviated DFR) in the region of the minimum (R = 1.75 Å for He_3, R = 1.80 Å for Ne_3, and R = 2.20 Å for Ar_3) is also determined in the evaluation of the performance of each density functional approximation. The MAD and wMAD values with respect to the accurate PES for 34 different DFT functionals and two basis sets are collected in Table 4.13 for He, Table 4.14 for Ne, and Table 4.15 for Ar.

For the He_3 trimer, the two functionals that perform the best are the τ-HCTHhyb and ωB97X functionals. Relative to the majority of the data, reasonable performance is also obtained with several of the other functionals, including B97, B97-2, B98, TPSS, TPSSH, M05 and M05-2X, M08-HX and M08-SO, and ωB97X and ωB97X-D. Interestingly, the semi-empirical dispersion correction does not seem to improve the results in the cases included, B97-D and ωB97X-D, compared to their uncorrected counterparts. In several cases, we also note that the BSSE does not necessarily improve the results, a point that will be revisited below.

Moving on to the heavier trimers, Ne_3 and Ar_3, which have stronger (covalent) bonding, we see a difference in the trends of the set of functionals. This might be anticipated based on the difference in bonding in the heavier trimers, which have more covalent character. For the Ne_3 trimers, the B97 family of functionals performs very well, particularly the B98, B97, B97-1, and B97-K functionals. Other functionals also have relatively good performance including M05, M05-2X, M06-HX and M06-SO, TPSS and TPSSH, and τ-HCTHhyb. However, while the DFR value is fairly low, the wMAD values are noticeably large. Also, several of these functionals need to be used with caution givcn the known spurious oscillatory behavior in the kinetic energy density component of several of the functionals[290,291].

Finally, the more difficult case, the Ar_3 trimer, we notice considerably fewer functionals provide reasonable performance. In this case, the ωB97X functional stands out, with the M05-2X functional being also reasonable relative to the other functionals. This would indicate a type of bonding in this trimer that is not well represented by most of these functionals.

In general, several meta-GGA functionals, such as VS98 and PKZB, show results that are highly dependent on the system as well as the basis set, with acceptable results in many cases, but quite poor results in others. As with the other meta-GGA functionals these also show oscillating behavior. The BLYP, B3LYP, CAM-B3LYP, and BMK functionals also have overall poor performance, something that could be a result of specialized parameterization for specific properties, *e.g.*, for kinetic data, rather than structural. The B2-PLYP functional also provides relatively unsatisfactory results in all cases.

Table 4.13: MAD, wMAD, and deviation from reference near the equilibrium distance for 34 different density functionals and Helium trimer. Results shown are BSSE corrected (BSSE uncorrected).

Helium Trimer	aug-cc-pVDZ			aug-cc-pVTZ		
	MAD	wMAD	DFR R=1.75	MAD	wMAD	DFR R=1.75
Functionals Implemented in the current work						
B97	198.3(195.0)	45.9(56.8)	-59.0(-71.8)	201.0(201.8)	65.7(68.9)	-78.2(-81.7)
B97-1	113.9(116.8)	88.4(98.9)	-97.2(-109.6)	132.3(134.3)	113.6(116.7)	-125.7(-128.9)
B97-2	474.1(455.0)	56.6(42.2)	39.4(23.0)	453.5(449.6)	43.3(39.8)	32.4(28.7)
B97-3	590.1(571.3)	472.0(458.6)	528.8(513.0)	707.1(690.5)	518.2(510.9)	583.7(576.9)
B97-D	705.9(700.5)	76.1(84.4)	-103.0 (-117.6)	679.6(681.3)	73.3(78.6)	-102.4(-108.9)
B97-K	258.0(269.1)	95.5(104.4)	-87.6(-99.2)	276.9(283.6)	118.5(122.3)	-119.8(-123.2)
B98	118.6(118.7)	52.1(63.3)	-62.1(-75.3)	134.5(135.1)	73.4(76.5)	-84.2(-87.5)
HCTH/93	1,239.9(1,223.8)	291.2(278.6)	285.6(271.2)	1,227.9(1,220.7)	306.2(298.8)	318.5(310.4)
HCTH/120	427.3(432.0)	273.1(286.7)	-321.2(-334.9)	436.9(438.1)	318.2(324.2)	-368.1(-374.7)
HCTH/147	544.1(543.5)	120.2(133.2)	-140.7(-171.0)	515.3(515.5)	149.5(155.7)	-183.6(-190.5)
HCTH/407	654.0 661.0)	554.6(571.0)	-637.2(-653.3)	696.9(700.3)	637.8(644.9)	-732.7 -(740.4)
τ-HCTH	471.8(466.5)	218.3(239.1)	-273.1(-297.3)	487.5(489.9)	271.0(277.3)	-325.6 -(332.7)
τ-HCTHhyb	349.7(336.3)	22.1(18.4)	0.1(-15.6)	313.4(312.0)	13.9(15.2)	-17.2(-21.0)
BMK	930.2(907.1)	795.2(779.4)	842.3(822.8)	1,128.9(1,085.6)	871.6(854.3)	947.9(932.3)
ωB97	162.3(158.2)	194.6(181.4)	228.5(214.9)	147.8(148.2)	185.9(180.6)	214.1(208.6)
ωB97X	57.3(62.0)	35.5(25.0)	37.8(22.7)	31.4(26.9)	13.7(14.6)	-5.6(-10.6)
ωB97X-D	491.1(464.2)	85.0(65.9)	59.8(33.9)	549.1(541.0)	73.3(71.1)	46.9(41.8)
Additional functionals available in GAMESS						
BLYP	529.5(509.8)	390.2(372.8)	438.3(421.2)	516.6(511.1)	400.7(395.4)	457.1(451.4)
B3LYP	263.8(248.0)	251.2(238.3)	286.0(272.9)	253.8(248.9)	258.1(254.2)	297.7(293.8)
B2-PLYP	117.8(83.6)	148.4(123.8)	172.6 (145.1)	111.4(112.6)	147.8(141.6)	174.3(168.3)
CAMB3LYP	210.9 (208.8)	75.6(59.8)	95.1(79.5)	221.7(221.0)	75.8(71.2)	95.6(90.7)
VS98	461.2(465.6)	139.4(135.6)	42.1(28.7)	501.9(505.4)	224.7(227.5)	-224.5(-231.4)
PKZB	854.0(855.4)	170.8(186.0)	-216.7(-231.8)	796.2(796.8)	209.3(216.0)	-256.8(-264.2)
TPSS	188.8(184.4)	46.0(62.8)	-67.9(-87.6)	166.7(166.3)	69.7(74.4)	-87.1(-92.6)
TPSSH	158.9 (153.9)	24.4(42.8)	-40.06(-62.2)	141.8(141.2)	46.0(49.5)	-58.7(-63.0)
TPSSM	247.6(243.6)	61.8(77.3)	-85.4(-103.4)	219.9(219.3)	87.2(92.3)	-106.71(-112.6)
M05	163.0(180.4)	47.4(57.2)	-11.3(-29.3)	140.3(148.7)	82.2(84.5)	-63.1(-68.8)
M05-2X	147.0(142.9)	60.7(58.3)	45.7(34.3)	128.5(126.2)	49.6(49.1)	5.9(-1.7)
M06	226.8(263.4)	331.3(365.0)	-466.4(-508.0)	278.9(250.0)	317.6(332.6)	-422.9(-438.9)
M06-2X	234.6(237.0)	297.9(309.8)	-370.4(-383.0)	226.7(226.5)	314.8(319.2)	-383.5(-387.5)
M06-L	141.2(182.8)	99.2(145.3)	-146.1(-210.6)	140.7(109.8)	60.5(92.9)	-98.7(-134.5)
M06-HF	493.7(495.1)	330.0(347.8)	-406.2(-423.5)	497.4(492.7)	365.7(382.3)	-422.9(-439.3)
M08-HX	226.3(238.8)	41.1(25.0)	47.7(17.2)	104.8(108.7)	65.3(61.9)	70.1(62.5)
M08-SO	90.8(95.6)	40.0(54.0)	-54.9(-69.9)	87.9(54.8)	37.8(42.5)	-33.4(-48.7)

Table 4.14: MAD, wMAD, and deviation from reference near the equilibrium distance for 34 different density functionals and Neon trimer. Results shown are BSSE corrected (BSSE uncorrected).

Neon Trimer		aug-cc-pVDZ				
	MAD	wMAD	DFR R=1.80	MAD	wMAD	DFR R=1.80
Functionals Implemented in the current work						
B97	1,303.1(1,096.9)	61.2(63.1)	-16.6(-95.0)	1,378.3(1,252.5)	107.2(51.5)	27.5(-3.0)
B97-1	771.0(626.2)	44.8(127.6)	-38.8(-118.6)	808.5(735.8)	50.7(101.4)	-12.6(-41.7)
B97-2	1,753.8(1,493.6)	282.1(203.8)	78.8(13.8)	1,938.4(1,786.4)	391.3(323.3)	146.7(106.9)
B97-3	2,143.4(1,937.2)	1,121.1(1,048.0)	612.2(548.7)	1,786.3(1,652.3)	1,082.0(1,024.8)	703.9(668.8)
B97-D	2,720.4(2,543.2)	387.1(474.0)	-502.5(-577.3)	2,850.1(2,726.7)	242.8(266.5)	-390.4(-430.1)
B97-K	711.8(622.5)	87.2(148.9)	23.0(-55.6)	731.6(689.0)	147.7(189.2)	12.0(-13.4)
B98	917.0(711.6)	46.5(50.5)	-5.8(-83.0)	980.5(848.8)	74.3(21.6)	30.6(-3.1)
HCTH/93	3,951.4 (3,692.6)	776.7(693.9)	280.8(213.6)	4,098.9(3,969.8)	990.5(931.3)	413.6(381.5)
HCTH/120	1,786.5(1,640.0)	415.8(513.6)	-365.0(-452.9)	1,827.5(1,771.6)	316.0(365.9)	-314.4(-341.0)
HCTH/147	2,207.4(2,001.4)	135.5(173.2)	-186.5(-267.2)	2,328.1(2,231.7)	133.5(121)	-114.0(-142.4)
HCTH/407	2,386.8(2,232.4)	925.8(1,035.2)	-720.4(-819.3)	2,417.0(2,374.8)	840.4(893.3)	-707.6(-733.5)
τ-HCTH	1,796.8(1,570.0)	260.9(356.6)	-342.8(-419.4)	2,157.1(1,987.3)	187.3(220.8)	-250.1(-315.0)
τ-HCTHhyb	1,138.9 (903.1)	173.7(109.5)	29.0(46.0)	1,404.2(1,233.8)	259.6(184.0)	90.9(45.7)
BMK	1,976.1(1,818.1)	1,790.5 (1,715.3)	917.8(845.5)	1,439.0(1,242.8)	1,831.5(1,750.6)	1,033.8(974.0)
ωB97	535.2(456.5)	569.4(467.5)	425.6(325.9)	503.4(464.5)	404.6(358.5)	402.4(379.2)
ωB97X	422.5(251.1)	340.2(260.7)	204.2(131.1)	418.2(275.7)	209.4(147.0)	187.5(150.8)
ωB97X-D	1,459.8(1,263.3)	309.1(287.9)	-98.4(-153.9)	1,580.1(1,372.4)	326.2(258.9)	-49.3(-114.8)
Additional functionals available in GAMESS						
BLYP	1761.4(1,536.0)	645.5(516.4)	510.7 (383.1)	1855.3(700.0)	749.6(700.0)	579.4(555.7)
B3LYP	848.9(619.9)	435.0 (330.0)	360.6(259.9)	926.8(445.5)	501.6(445.5)	415.6(385.9)
B2-PLYP	547.8(192.3)	284.7(128.0)	253.5(109.1)	454.1(191.7)	287.4(191.7)	265.2(200.4)
CAMB3LYP	558.9(710.1)	132.8(66.2)	188.0(77.5)	499.3(122.2)	137.9(122.2)	238.7(211.7)
VS98	1014.2(935.1)	419.0(335.1)	402.1(312.5)	1220.3(444.0)	457.3(444.0)	573.0(548.8)
PKZB	2936.5(2,734.0)	155.7(233.0)	-233.2(-304.3)	3163.1(137.6)	125.7(137.6)	-171.4(-193.5)
TPSS	1132.0(940.3)	88.8(100.6)	-79.1(-148.5)	1383.9(112.0)	157.3(112.0)	-11.1(-52.3)
TPSSH	934.7(719.8)	93.5(74.1)	-15.5(-80.0)	1182.3(110.6)	184.0(110.6)	39.0(-4.5)
TPSSM	1438.7(1,246.7)	82.6(114.0)	-103.4(-173.2)	1677.4(108.4)	138.2(108.4)	-36.2(-73.5)
M05	452.2(443.6)	114.7(193.4)	3.4(-83.9)	608.8(193.0)	143.0(193.0)	79.8(35.2)
M05-2X	391.6(354.7)	131.8(91.0)	188.7(106.5)	402.3(219.6)	172.1(219.6)	134.7(78.9)
M06	1024.0(844.3)	262.1(276.1)	-341.6(-396.5)	996.4(269.6)	218.3(269.6)	-310.1(-400.5)
M06-2X	652.0(887.0)	282.6(352.4)	-293.0(-352.2)	552.9(392.5)	315.5(392.5)	-306.8(-356.5)
M06-L	677.6(473.6)	124.4 (64.1)	53.2(10.0)	183.7(303.2)	178.4(303.2)	-128.4(-256.4)
M06-HF	421.4(699.9)	339.2(456.0)	-498.0(-601.2)	551.9(560.3)	292.9(560.3)	-410.5(-655.9)
M08-HX	466.8(392.4)	235.6(186.1)	-22.1(-97.3)	529.8(72.5)	214.3(72.5)	87.4(-21.3)
M08-SO	400.2(351.0)	205.7(153.7)	0.2(-91.4)	590.8(47.1)	108.4(47.1)	15.6(-52.4)

Table 4.15: MAD, wMAD, and deviation from reference near the equilibrium distance for 34 different density functionals and Argon trimer. Results shown are BSSE corrected (BSSE uncorrected).

Argon Trimer		aug-cc-pVDZ				
	MAD	wMAD	DFR R=2.20	MAD	wMAD	DFR R=2.20
Functionals Implemented in the current work						
B97	5,368.9(4,970.7)	957.4(769.2)	1,335.1(1,090.6)	2,912.7(2,837.5)	916.3(848.6)	1,268.1(1,186.7)
B97-1	4,236.6(3,853.4)	569.2(387.6)	715.7(480.2)	2,028.4(1,952.3)	513.2(445.3)	643.2(561.0)
B97-2	4,556.7(4,135.0)	1,476.4(1,283.6)	2,138.7(1,889.5)	4,035.9(3,955.6)	1,466.5(1,395.3)	2,101.4(2,015.9)
B97-3	6,920.7(6,547.2)	1,984.8(1,812.4)	2,579.2(2,361.0)	3,701.8(3,486.0)	1,981.4(1,889.8)	2,573.0(2,458.1)
B97-D	4,565.8(4,242.2)	394.7(338.6)	564.7(311.2)	4,722.7(4,670.1)	377.2(350.0)	528.0(439.7)
B97-K	9,392.4(9,016.7)	525.2(353.5)	621.5(398.0)	5,986.0(5,850.1)	460.5(403.2)	541.4(470.4)
B98	4,748.1(4,362.4)	814.6(632.3)	1,101.9(865.9)	2,286.4(2,200.8)	773.4(698.6)	1,041.9(951.7)
HCTH/93	6,430.9(6,249.9)	2,694.6(2,488.3)	3,983.1(3,714.3)	7,934.2(7,868.7)	2,690.4(2,626.7)	3,905.5(3,830.6)
HCTH/120	3,379.5(3,257.3)	465.0 (337.3)	697.9(451.5)	4,941.3(4,938.9)	363.0(334.0)	539.2(485.2)
HCTH/147	4,161.1(3,999.2)	1,086.5(892.2)	1,621.6(1,366.7)	5,610.7(5,559.5)	1,008.0(956.0)	1,479.6(1,418.9)
HCTH/407	4,476.3(4,461.2)	633.0(772.7)	-297.6(-567.2)	5,901.9(5,900.4)	733.8(767.0)	-614.0(-665.6)
τ-HCTH	3,447.1(3,271.8)	822.2(599.0)	1,296.5(996.8)	6,003.0(5,985.4)	773.9(675.1)	1,204.6(1,089.7)
τ-HCTHhyb	3,060.4(2,627.5)	1,160.6(958.6)	1,650.7(1,389.9)	3,191.2(3,169.4)	1,146.1(1,056.9)	1,617.8(1,511.5)
BMK	8,742.2(8,331.2)	3,144.6(2,963.0)	4,276.2(4,052.5)	5,738.6(5,302.1)	3,258.8(3,090.5)	4,430.9(4,217.3)
ωB97	3,943.9(3,726.5)	713.3(594.3)	521.1(309.3)	1,015.7(1,021.3)	658.0(616.8)	581.1(489.8)
ωB97X	3,769.7(3,569.2)	326.8(270.0)	60.1(-152.0)	729.9(733.2)	242.6(205.4)	80.9(-9.9)
ωB97X-D	4,841.2(4,417.8)	626.9(445.1)	1,005.5(758.7)	2,114.3(1,991.7)	666.3(569.4)	1,087.3(957.5)
Additional functionals available in GAMESS						
BLYP	6911.9(6,493.1)	2304.6(2,095.3)	3135.5(2,868.7)	4259.9(4,185.0)	2293.3(2,226.4)	3077.(2,998.8)
B3LYP	6443.7(6,076.8)	1791.4(1,612.0)	2414.4(2,183.1)	3402.2(3,248.0)	1780.2(1,713.6)	2369.9(2,290.3)
B2-PLYP	7526.0(6,593.9)	1196.2(972.4)	1598.0(1,317.8)	2517.8(1,979.8)	1086.3(970.6)	1426.7(1,278.9)
CAMB3LYP	4564.4(4,208.2)	1123.9(948.3)	1444.3(1,219.3)	1477.1(1,331.0)	1110.6(1,049.7)	1418.5(1,345.6)
VS98	5721.9(5,576.5)	1619.3(1,774.9)	-2771.4(-3,035.4)	2732.7(2,706.4)	1778.7(1,813.2)	-2847.6(-2,905.2)
PKZB	7799.4(7,328.9)	1159.6(944.0)	1716.3(1,431.9)	5547.3(5,502.8)	1089.1(1,041.2)	1615.0(1,559.5)
TPSS	3488.1(3,018.7)	1231.3(1,013.1)	1838.0(1,555.1)	3294.5(3,268.6)	1204.5(1,119.3)	1766.3(1,665.3)
TPSSH	3855.5(3,392.7)	1232.4(1,020.8)	1814.9(1,541.2)	2822.0(2,794.2)	1208.2(1,123.2)	1751.3(1,650.8)
TPSSM	4258.0(3,785.7)	1234.6(1,014.7)	1847.1(1,560.9)	3455.6(3,371.8)	1194.2(1,116.3)	1753.4(1,661.5)
M05	3436.6(2,951.9)	406.1(189.1)	311.0(27.8)	3157.4(3,072.1)	443.6(364.9)	425.7(334.0)
M05-2X	4299.0(3,986.5)	281.0(155.5)	159.5(-46.7)	1054.6(753.1)	196.6(120.3)	87.3(-62.6)
M06	2817.5(2,309.8)	437.2(248.8)	600.4(316.4)	1724.4(1,497.2)	610.6(439.3)	897.1(646.2)
M06-2X	3712.4(3,534.3)	187.5(81.4)	364.4(181.2)	621.8(503.3)	241.0(167.3)	472.5(346.0)
M06-L	3916.4(3,427.7)	305.2(114.1)	334.8(46.9)	1456.6(1,157.1)	347.0(113.5)	436.9(42.5)
M06-HF	2526.6(2,109.1)	447.8(278.8)	686.7(399.8)	1299.9(1,678.5)	534.8(351.2)	878.4(511.3)
M08-HX	4372.9(4,063.2)	671.8(504.8)	534.1(231.8)	1645.6(1,337.4)	719.6(570.5)	797.6(598.2)
M08-SO	4323.0(4,019.8)	451.6(287.1)	438.3(158.3)	1639.2(1,279.9)	463.6(284.3)	496.0(272.0)

For a global view of the behavior of the series of density functionals, Figure 4.19 shows the results of PES data for the set of density functional class types. The first class consists of non-hybrid (local) GGA functionals, including B97-D, HCTH/407, BLYP, as well as τ-HCTH, TPSSH, and M06-L, that are included also in this class because they are non-hybrid meta-GGAs. The second class consists of a selection of hybrid functionals, as well as range-separated hybrid, including the most complete reparameterization of the B97 functional (called B98), the commonly used B3LYP functional, the double-hybrid B2-PLYP analogue of B3LYP, the range-separated modification of B3LYP, CAM-B3LYP, and the new ωB97 functionals of Chai and Head-Gordon, ωB97, ωB97X and ωB97X-D. The third class includes a selection of hybrid meta-GGA functionals, including VS98, TPSSH, M05, M05-2X, M06, M06-2X, M08-HX and M08-SO.

In these graphs, one can see a more clear comparison of the behavior of the functionals. For helium, with the first class of functionals, the local GGA functionals, none of the functionals come close to the reference curve, with the exception of the tails. The τ-HCTH and HCTH/407 functionals are way over-binding, and the BLYP functional is dissociative. The others in the set are much closer to the reference data, but still not with

in acceptable tolerance. In the second class of functionals, the hybrid GGA functionals, nearly all the functionals are seen to have a fairly poor predictive nature compared to the reference data. The TPSSH functional is perhaps the closest to at least representing the correct shape of the potential, including the placement of the minimum, although the dissociation energy is predicted to be much too low. Looking at the M0X family of functionals, we see that the M06/M06-2X functionals are seriously over binding, the M05/M05-2X versions are quite unphysical, and the more recent M08-HX functional is predicting a far weaker helium interaction distance, albeit a similar binding energy, compared to the reference. The VS98 functional is completely unrealistic for this system. All functionals in this set, however, have a convergent behavior that does mimic the reference curve. In the last class of functionals, the hybrid-meta-GGA functionals, the ωB97X functional is really the only functional that comes close to the reference data. The B98 functional predicts short interaction distance with a dissociation energy that is much too large, while the CAM-B3LYP functional is completely unphysical throughout. The rest of the functionals are dissociative, including the B2-PLYP functional. The effect of the semi-empirical correction on the ωB97X functional is a displacement of the curve to considerably longer interaction distances, such that the long range dispersion part of the curve follows more closely the CCSD(T) results, with a consequence that the repulsive wall is now occurring at longer distances of the helium atoms in the trimer. The minimum energy structure is also pushed out by about 0.5 Å.

Looking at the classes of functionals for the case of Ne_3 we observe some differences in functional performance, due to the difference in bonding character for this heavier rare gas trimer. For the local GGA functionals, we see only one functional that has the general shape of the reference data, that being the TPSS functional. However the TPSS minimum is at a longer distance than the reference curve (1.9 *vs.* 1.8 Å, respectively), and is under-binding, although the long-range dispersion part of the curve is reproduced. The other functionals are actually fairly poor. For the second class of functionals, hybrid GGA, we see quite a bit of erratic character in many of the functionals, with none of them coming close to the reference data. As in the helium trimer, the TPSSH functional at least represents the general shape of the PES curve, albeit too under-binding and too weak of a bonding distance. Finally, in the hybrid-meta-GGA functionals, it is no longer the case that the ωB97X functional has the best performance, but instead has too shallow of a well and poor dissociation characteristics. Also, unlike in the He_3 trimer, the semi-empirically corrected version of the ωB97X functional now shows a much more reasonable curve than its uncorrected version, with reasonable well depth (albeit too shallow) and good dissociation characteristics. Similar to the helium trimer, however, the curve is displaced to much longer distances, with the minimum predicted to be closer to 2 Å instead of 1.8 Å. The B98 functional has a fairly good performance, albeit too shallow of a well, and the adjacent curve to the left of B98, the CAM-B3LYP functional, has completely unphysical dissociation. In this trimer, the B2-PLYP, while considerably far from the reference data, is at least binding. The remaining two functionals, B3LYP and ωB97 are both dissociative.

Finally, we look at the three classes of functionals for the final trimer, Ar3, which has even more binding character. In the local GGA functional class, we again have very poor performance for all functionals considered. The B97-D functional is probably the most well behaved of all of considered, however, with significant under binding and cor-

respondingly longer Argon interaction distance. In the hybrid GGA functional class, we again see disappointing results for most all functionals. The M05-2X functional has fairly good performance except in the dissociation. In contrast, the M06-2X upgrade of this functional has a good dissociative characteristic, but the minimum is much too shallow and occurs at a much longer Ar distance. The M06 functional has a quite strange performance for this trimer, as does the M08-HX functional. While the M05 and M08-SO functionals have a good representation of the minimum energy distance, the wells are much too shallow and the dissociative part of the curve is way off. In the final class, the hybrid meta-GGAs, none of the functionals are showing good performance. In this case, the ωB97X functional has a good repulsive wall, but the dissociative part of the curve is completely off. In contrast, as might be expected, the semi-empirically corrected version of this functional now has the write dissociative feature, but is way off in the rest of the curve. In this set, now only the B3LYP is predicted to be dissociative.

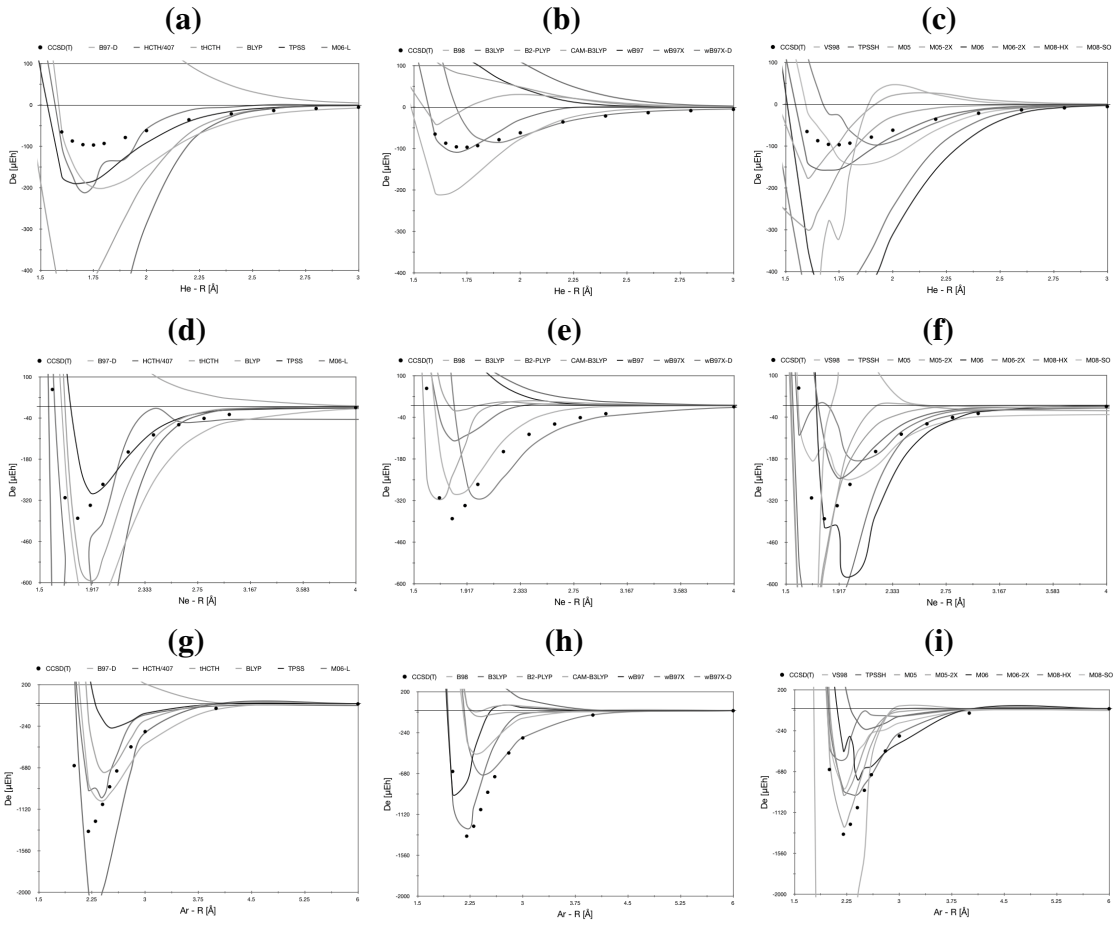

Figure 4.19: Dissociation energies, D_e (μE_h) of the Rg_3 trimers [6a-6c. He (blue), 6d-6f. Ne (red), and 6g-6i. Ar (green)] along the radial coordinate R (Å) using the aug-cc-pVTZ basis set together with local GGA [6a,6d,6g], hybrid GGA [6b,6e,6h], and hybrid meta-GGA [6c,6f,6i], DFT functionals, referenced against the CCSD(T)/CBS results in Table 4.12. Results are presented on the same relative scale; the ultrafine Lebedev grid has been used.

One noticeable defect in the behavior of a number of the functions for the description of the potential energy surfaces is the spurious behavior in several regions, as already men-

tioned above. This behavior was pointed out in a recent article by Johnson and coworkers, within the context of a meta-GGA functional analysis of the PES for a set of dispersion-bound complexes, including the Ar dimer. This erroneous behavior originates from the divergence of the τ-dependent term in these functionals. The suggestion from Johnson and coworkers to avoid this spurious behavior was to use an ultrafine grid.

In the results displayed in Figure 4.19, we see that the erroneous oscillation in the potential energy surfaces actually persist despite the use of grid refinement, contrary to the literature suggestion. The dependency of the meta-GGA results on the grid size appears in this case very large. In a more recent publication of Wheeler and Houk concerning only the M06 suite of functionals, it was determined that the spurious behavior, originates from grid sensitivity in the kinetic energy density enhancement factor used in the exchange component of these functionals. While it is not completely clear to us the exact source of the spurious behavior in all functionals, is an inherent problem of the meta-GGA class of functionals, and therefore the functionals should be used with caution.

4.2.4 Elaboration on BSSE in the PES analysis of the rare gas trimers

Looking carefully at the results in Table 4.13, in some cases the BSSE uncorrected results are moderately better than those that are BSSE corrected. On the other hand, it is well known that BSSE plays a key role accurate treatment of weakly bounded complexes interaction energies, associated with basis sets that are too small, resulting in poor prediction of binding energies and intermolecular distances. Although it is generally believed that DFT is much less affected by BSSE than other wavefunction types, a basis set of at least triple-ζ quality is typically necessary to significantly reduce the BSSE. The counterpoise correction (CP) is a standard method used to correct for BSSE, and while the procedure itself has an associated error (typically results in an overestimation of BSSE) and requires additional effort, the method generally provides good results for the vast majority of cases where it is used. Table 4.16 shows the BSSE as a function of interatomic distance across 5 common DFT functionals using the aug-cc-pVDZ basis set for the He_3 trimer. The data is expressed as both absolute value as well as percentage of the total binding energy. The absolute value of the BSSE at the binding distance is, in general, larger than 13 μE_h for all of the considered functionals, in the order M06 > B2-PLYP > BMK > BLYP > B3LYP > 13 μE_h. Considering that the dispersion energy near the equilibrium distance, evaluated using the semi-empirical dispersion formula of Grimme (namely, the unscaled -D contribution of the B97-D functional), is -140.2 μE_h, the BSSE energy is always larger than 10% of the dispersion energy. With the exception of the B2-PLYP method, the value of the BSSE in the region close to the minimum represents about 5-7% of the total binding energy. The B2-PLYP method, on the other hand, shows a value considerably larger, representing about 35% of the binding energy, with a large basis set dependency. This is most likely due to the presence of the MP2 term. The general behavior of the BSSE with respect to the interatomic distance is fairly unpredictable, ranging significantly across the various functionals, as perhaps seen more clearly in Figure 4.20. These results show that BSSE plays a substantial role in the determination of the binding energies of the rare gas trimers, particularly with double-ζ quality basis sets, although to a different extent across the functionals.

Table 4.16: BSSE as a function of interatomic distance for 5 common DFT functionals, expressed as absolute value in μE_h, ABS, and as percentage of the total binding energy, %.

R	BLYP		B3LYP		BMK		M06		B2-PLYP	
	ABS	%	ABS	%	ABS	%	ABS	%	ABS	%
1	60.24	0.31	63.81	0.36	161.38	0.85	295.65	1.80	179.00	1.05
1.2	29.84	0.64	22.38	0.59	30.92	0.52	71.28	2.15	68.56	2.05
1.4	34.63	2.47	29.01	3.15	26.14	0.80	48.94	27.40	54.96	9.08
1.6	24.75	4.30	22.16	6.85	26.98	1.57	54.80	13.84	42.92	30.40
1.65	21.89	4.60	19.16	7.26	25.59	1.88	52.62	11.07	38.14	35.25
1.7	19.26	4.83	15.99	7.27	22.98	2.22	47.98	8.91	32.83	37.52
1.75	17.08	5.00	13.01	6.88	19.46	2.61	41.55	7.38	27.43	36.23
1.8	15.52	5.36	10.53	6.54	15.54	2.92	34.23	7.45	22.40	34.50
1.9	14.34	6.79	7.64	6.43	8.34	3.43	20.31	5.12	14.64	29.74
2	14.92	9.73	7.24	8.37	3.74	4.07	10.49	3.77	10.35	28.80
2.2	15.69	19.45	8.63	19.36	1.37	30.43	2.85	2.21	7.76	45.87
2.4	12.58	28.70	7.74	33.34	1.49	39.72	1.37	2.34	6.18	84.21
2.6	8.08	32.54	5.28	41.92	1.17	38.03	0.68	2.81	4.09	130.13
2.8	4.50	30.52	3.09	42.36	0.75	41.23	0.33	2.95	2.37	165.88
3	2.24	23.91	1.61	35.05	0.44	53.45	0.19	3.48	1.25	159.86

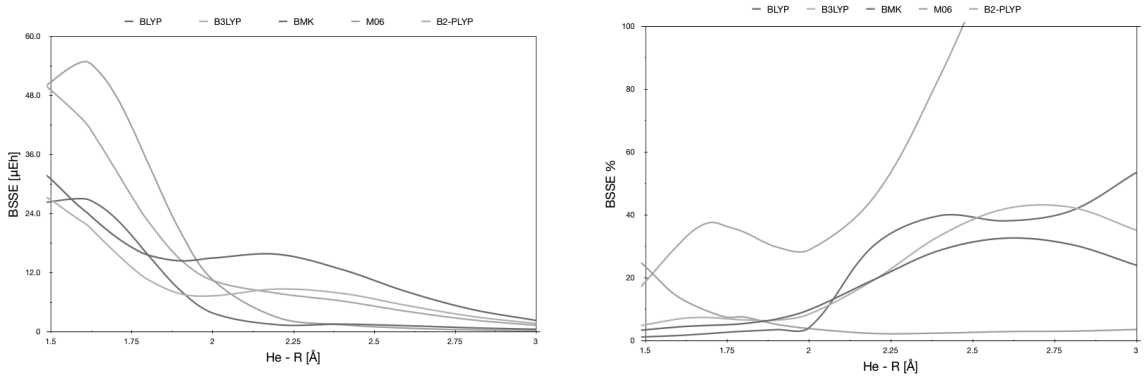

(a) **(b)**

Figure 4.20: BSSE as a functional of interatomic distance, expressed as a) absolute value, and b) percentage of the total binding energy.

A reasonable question on the noted effective performance of the BSSE uncorrected combination of DFT and double-ζ quality basis sets arises from this analysis. The proliferation of use of DFT/double-ζ methods in computational chemistry is primarily due to the relatively cheap computational cost of the combination for a general good performance. However, in many cases, the good performance is amplified by a cancellation of errors in the parameterization of the DFT functional and any associated semi-empirical dispersion correction, in combination with the BSSE and the incompleteness of the basis set. In particular, we have previously shown, for small basis sets, that BSSE can be of the same order of magnitude as the dispersion corrections in those functionals that have

semi-empirical corrections, but the two corrections have different asymptotic behavior. As such, care should be taken in the selection of method and basis set, in particular, for computations involving weak interactions.

4.2.5 Conclusions

A systematic investigation into potential energy surfaces characteristics of a series of rare gas trimers across a wide range of methodology been presented. In the considered equilateral D_{3h} case, the series presents a simple one-dimensional potential energy surface, for which methodology can be easily compared. These systems represent a challenging test for new methodology because of the variation in bonding character, which ranges from weak van der Waals interactions in He_3, to the strong more covalent bond character in the heaviest case, Ar_3. In addition, because of the much smaller literature with respect to rare gas dimer counterparts, this series of rare gas trimers represents an interesting research system, in particular for parameterization of empirical potentials.

For this study, we have implemented a large set of Kohn-Sham DFT density functionals into the GAMESS software package in order to fully test performance across a wide range of functional class types, including several of the new dispersion enabled functionals strategies. In the process, we also facilitate future implementations and parameter testing of a variety of density functional types. Reference data for the series of rare gas trimers is established using CCSD(T) showing convergence with respect to increasing basis set size, including extrapolation to complete basis set limit, using aug-cc-pVnZ (n = 2-5) basis sets. Several extrapolation procedures are compared in this work, including several well-established procedures and one additional one of our own (error in this sentence, but basically this is not true, since we used the Feller formula, so I would cut the sentence after procedures).

Results obtained with the a set of 34 different DFT functionals is evaluated on the same PES grid, using double and triple-ζ quality basis sets, with correction for basis set superposition error, is presented for each of the three rare gas trimers. Results strongly vary depending on the rare gas system, such that no unique best functional can be recommended across the whole series. Local functionals provide a general poor behavior, while hybrid GGAs provide better results overall. Meta-GGA functionals are largely unsatisfactory, but still represent the best functionals for some of the cases presented. Oscillations in the behavior of the PES are found for many meta-GGA functionals, despite the use of an ultrafine Lebedev integration grid. We therefore suggest that these functionals be used with caution. The newly implemented range-separated hybrids, and semi-empirical corrected functionals, present satisfactory global results. The same does not hold for the B2-PLYP double hybrid functional, which performs quite poorly for all considered cases. The behavior of the BSSE was also considered in more detail, posing a reasonable question on the effective performance of the BSSE uncorrected combination of DFT and double-ζ quality basis sets.

4.3 Ion-Quadrupole Interactions In Solution: Generalizations of the DFT-D/COSab approach

4.3.1 Introduction

The chemistry of ions in condensed phases often differs greatly from that observed in the gas phase. These differences can be categorized as coming from either bulk solvent effects or specific ligand effects. For bulk effects, it is empirically observed, but justified because of the dependence of ion screening on dielectric constant, that the difference between the gas phase and hydrocarbon solvent is often comparable with the difference between hydrocarbon solvent and aqueous media. The gas phase chemistry is also strongly influenced by specific ligand effects, particularly polarizability. The nature of benzene interactions is characterized by relative contribution from ion-ion, ion-pole, pole-pole, and vdW interactions. The face of the benzene ring is very electron rich and the quadrupole moment is oriented such that the negative poles coincide with the center of these faces. Thus, the ion-multipole interaction enables strong ion-π attractions. Many research groups have pointed to the importance of the electron rich faces of a benzene ring as a source of stabilization for cations, resulting in several model systems proposed to characterize aryl/aryl interactions. In particular, the so-called polar-π effect has lead to models that include dispersion, polarity, and induced dipolar effects. Extensive theoretical work has been carried out to further support the basic model, providing a simple empirical way to understand a variety of arene/arene interactions. Importance of solvent polarity is also an important component to understanding the stability of a given molecular charge distribution. Cation-π systems display a special sensitivity toward the redistribution of electron density as a function of their nuclear position, photonic excitation, and polar solvation, which also needs to be considered.

Computationally, systems involving weak interactions have posed challenges for chemical accuracy. However, recent developments illustrate the effectiveness of dispersion corrected DFT approaches, including the effects of the environment. However, still not well understood is a more general view of theoretical prediction of solvation phenomenon across a wide variant of dielectric. In the present contribution, we consider optimization and performance analysis of the semiempirically augmented density functional theory (DFT-D) in conjunction with our ab initio implementation of the conductor-like screening model, COSab, within the GAMESS software, and further illustrate the performance of the combined DFT-D/COSab method on a series of cation-π systems for structure and property prediction across a wide range of dielectric.

4.3.2 Computational methods

All calculations reported here were carried out using a locally modified version of the GAMESS electronic structure program, running on our group cluster hardware. Associated visualization and analysis was carried out using MacMolPlt and Qutemol. In the present work, we apply our recently implemented semi-empirically corrected functional, B97-D, according to the ansatz proposed by Grimme (2006). The B97-D exchange-correlation functional is a special re-parameterization of the original B97 hybrid functional of Becke, which is more neutral to spurious dispersion contamination in the ex-

change part than the original functional. The dispersion energy is entirely handled by the semiempirical term, leading to smaller errors. A 302 point Lebedev angular grid was used in the evaluation of the DFT integrals. In accord with our previous study on the performance of the B97-D functional, the scaling factor for the semi-empirical dispersion was taken as $s_6 = 1.00$ for all the double-ζ basis sets considered, including the LANL2DZ, and $s_6 = 1.25$ for all the triple-ζ basis sets considered.

Several basis sets were employed in this study in order to investigate consistency and predictability across the full set of molecules studied. The basis sets employed include the Dunning-Hay all-electron basis sets, DZV(*m*d,*l*p), for Li and K, and TZV(*m*d,*l*p), for Li, Na, and K (where *m* and *l* indicate the number of polarization on heavy and light atoms, respectively), Dunning's correlation consistent basis sets, cc-pV*n*Z (*n* = D,T for double and triple zeta), for Li and Na, and Hay-Wadt LANL2DZ ECP basis for K. The LANL2DZ basis uses the DZV basis set for all atoms, with adjusted orbitals coefficients for ECPs on atoms heavier than Ne. Solvation is taken into account using the most recent implementation of our COSab solvation method, based on the original COSMO theory of Klamt and modified for ab initio theory. An expanded set of dielectrics was used for the applications presented, including, $\varepsilon = 2.38$, (toluene) 5.0, (chloroform) 12.0, 20.7,(acetone) 32.6, (methanol) and 78.4 (water). The parameters of the cavity construction are: 1082 points for the basic grid, 92 segments on the complete sphere. The outlying charge error was taken into account via the double cavity approach. The solvent radial extent was optimized in the parameter optimization studies, and taken as 1.3 for the application studies. Solvent atomic radii were taken from Bondi[123], or from Klamt[85].

4.3.3 Theoretical approach and discussion

Gas phase DFT-D and alkali-metal cations

Systematic investigations of complexes that include alkali metals are challenging from the perspective of finding common, yet good quality, basis sets across the series of metals. While for Li most all common basis sets are available, already at sodium, there are limited choices of basis set, and number decreases down the family, Na, K, Rb, Cs, and Fr. In addition, starting with potassium it becomes necessary to consider relativistic effects, as exemplified in the literature using both standard all-electron basis set and basis sets that include relativistic effects.

In this work, we limit the investigation to the first three alkali metals, the series of which serves to illustrate the DFT-D methodology. Initial investigation involves computation of the structure and interaction energy of the alkali metal/benzene complex across a variety of wave function methods and basis sets, as reported in Table 4.17. The general trend observed shows that, for each split shell added in the basis set, there is a reduction in the interaction energy of about 1 kcal/mol, addition of an extra d orbital on heavy atoms (C and K) increases this energy of almost 1 kcal/mol, and a simultaneous addition of extra p orbitals on hydrogens reduces the interaction energy by about 0.3 kcal/mol. The best compromise between basis set functionality appears to be accomplished with the TZV(d,p) basis, despite the overestimation from experiment of 1.8 kcal/mol. A significant improvement in the result is obtained using the LANL2DZ basis. While being only double-ζ, the global error in interaction energy is reduced to less than 0.5 kcal/mol. However, this appears to be the result of a compensation of errors (as also with the DZV basis).

Comparing results of DZV (no polarization) with LANL2DZ, which are different only by the inclusion of the pseudopotential in the latter basis set, the ECP appears to be important only for the equilibrium distance, since quite different equilibrium cation/benzene distances are found for the two, but nearly the same Energy.

Table 4.17: DFT-D interaction energies, equilibrium distances, dispersion energies, and ΔE(expt-calc) for benzene-alkali metal ion complexes, using different basis sets.

	Li				Na				K			
Method	ΔE [kcal/mol]	Re (Å)	-D	ΔE (expt-calc)	ΔE [kcal/mol]	Re (Å)	-D	ΔE (expt-calc)	ΔE [kcal/mol]	Re (Å)	-D	ΔE (expt-calc)
B97-D:												
6-31G(d,p)	-49.5		-9.96	-11.6	-34.2		-8.23	-6.2	-22.1	2.868	-5.54	-3.8
6-31++G(d,p)	-44.7		-9.92	-6.8	-30.1		-7.99	-2.1	-19.4	2.886	-5.44	-1.1
DZV	-43.0	1.953	-9.90	-5.1	-	-	-	-	-18.9	2.898	-5.35	-0.6
DZV(d,p)	-47.3	1.930	-10.01	-9.4	-	-	-	-	-21.2	2.815	-5.74	-2.9
DZV(2d,p)	-49.1	1.911	-10.05	-11.2	-	-	-	-	-21.9	2.821	-5.73	-3.6
DZV(2d,2p)	-48.8	1.910	-10.05	-10.9	-	-	-	-	-21.7	2.822	-5.73	-3.4
cc-pVDZ	-46.5	1.928	-10.02	-8.6	-31.3	2.394	-8.57	-3.3	-	-	-	-
aug-cc-pVDZ	-45.3	1.918	-10.03	-7.4	-30.3	2.388	-8.57	-2.3	-	-	-	-
LANL2DZ	-	-	-	-	-30.2	2.390	-8.56	-2.2	-18.8	2.943	-5.11	-0.5
cc-pVDZ+LANLDZ(M)	-46.5	1.928	-10.02	-8.6	-29.9	2.402	-8.54	-1.9	-18.9	2.919	-5.20	-0.6
TZV(d,p)	-45.9	1.914	-10.05	-8.0	-32.5	2.381	-10.84	-4.5	-20.1	2.877	-6.88	-1.8
TZV(2d,p)	-46.5	1.912	-10.06	-8.6	-33.1	2.378	-10.87	-5.1	-21.1	2.846	-7.07	-2.8
TZV(2d,2p)	-46.1	1.911	-10.06	-8.2	-32.8	2.378	-10.87	-4.8	-20.8	2.848	-7.06	-2.5
cc-pVTZ	-46.5	1.912	-10.05	-8.6	-32.8	2.382	-10.85	-4.8	-	-	-	-
6-311G(d,p)	-49.1		-12.50	-11.2	-32.7		-9.88	-4.7	-22.3	2.829	-7.14	-4.0
6-311++G(d,p)	-48.0		-12.51	-10.1	-31.6		-9.82	-3.6	-21.6	2.836	-7.10	-3.3
6-311++G(2d,2p)	-48.2		-12.52	-10.3	-32.0		-9.97	-4.0	-21.6	2.831	-7.15	-3.3
aug-cc-pVTZ	-45.9	1.911	-10.05	-8.0	-32.3	2.381	-10.92	-4.3				-
Def2-TZVPP	-45.2		-10.00	-7.3	-30.4		-8.00	-2.4	-19.6		-5.56	-1.3
Def2-QZVPP	-45.7		-10.01	-7.8	-32.1		-8.05	4.1	-22.2		-5.65	-3.9
M06/cc-pVDZ1	-36.9	1.980	-	1.0	-23.9	2.524	-	4.1	-18.7	2.875	-	-0.40
MP2/cc-pVTZ//M06/cc-pVDZ	-37.9	-	-	0.0	-23.5	-	-	4.5				-
ACCURATE MP2	-40.2	1.865		-2.3	-24.9	2.396		3.1	-18.5	2.894		-0.2
ACCURATE CCSDT	-38.13	1.92	-0.59	-0.23	-22.95	2.480	-0.59	5.05	-18.77	2.900	-3.57	-0.47
EXP	**-37.9**				**-28.0**				**-18.3**			

It is clear from the data in Table 4.17 that the dispersion component of DFT-D is significantly overestimated from that predicted from the accurate CCSDT value. Additionally, the error in ΔE is in the range of 5-12 kcal/mol, in contrast to that found with the accurate MP2, CCSDT, and even the M06 functionals. One expects some level of variance in prediction of dispersion among the various methods as compared to the more conventional highly accurate methods (*e.g.*, CCSDT) that incorporate dispersion in a rigorous manner. In particular the DFT methods have a relatively wide range of strategy for accounting for such effects, from direct parameterization of the functional components to incorporation of dispersion via the parameterized function with the DFT-D methods. However, even beyond this, the differences found from the accurate reference are quite substantial, particularly for the DFT-D method. This is very likely due to the fact that the semi-empirical parameters associated with the DFT-D were originally optimized for neutral alkali metals, rather than for cations. The parameters for the neutral state should not be expected to be optimal for the respective charged species, given the significant difference in the electronic structure of the neutral vs cationic states in this series. The C_6 parameter is a function of the effective number of electrons and polarizability of the atom. Therefore,

with increasing number of electrons available to screen outer electrons effectively, one should see an associated increase in the polarizability. Additionally, the effective difference in polarizability between the neutral and the cation should be more dramatic for the earlier alkali metals with fewer electrons, than for the later metals. For example, in the case of Li the difference between the polarizability of the neutral with three electrons vs the cation, Li^+, with 2 electrons will be more dramatic, than say Cesium with 55 electrons compared to the cation, Cs^+, with 54 electrons, due to the significant screening in the latter case. From Table 4.17, already with the potassium cation complexes, the value of the dispersion contribution is significantly less than the other two metals, even with the existing parameters.

Gas phase DFT-D and alkali-metal cations - Optimization of dispersion parameters for alkali metals.

To investigate further the semiempirical dispersion representation for alkali metals, optimization of the C_6 coefficient for each metal was investigated. Optimization was carried out at several levels of theory, to verify convergence. For each of the alkali metals considered, optimizations were carried out with increasing values of C_6, beginning with $C_6 = 0$ (no dispersion accounted for). From these results, a simple error function was constructed, of the form,

$$f(C_6) = \Delta E^{\mathrm{B97-D}} - \Delta E^{\mathrm{CCSD(T)/CBS}} \tag{4.7}$$

where $\Delta E^{\mathrm{B97-D}}$ are B97-D binding energies calculated with a variety of basis sets, and $\Delta E^{\mathrm{CCSD(T)/CBS}}$ are accurate CCSD(T) values at the complete basis set limit, recently proposed by Singh and coworkers[292]. The appropriate optimized parameters for the dispersion term of the B97-D functional were used according to the basis set quality (see Table 2.10).

Table 4.18: Optimized C_6 parameters for the M^+-benzene (M = Li, Na, K) complexes with different basis sets, compared to the respective original values proposed by Grimme for neutral atoms. The appropriate s_6 parameter of the semiempircal term is indicated in parenthesis.

basis set	Li	Na	K
cc-pVDZ ($s_6 = 1.00$)	0.075	0.10	10.45
aug-cc-pVTZ ($s_6 = 1.25$)	0.075	0.10	5.5
6-311++G(2d,2p) ($s_6 = 1.25$)	0.075	0.10	3.8
Def2-TZVPP ($s_6 = 1.25$)	0.075	0.10	4.8
Grimme original parametrization	1.61	5.71	10.61

As previously mentioned, the difficulty associated with determination of the parameters for this set is amplified due to the limited number of high quality basis sets that span all of the alkali metals. Here we have chosen several basis functions, with three in particular that span Li, Na, and K. These include the following: cc-pVDZ (cc-pVDZ + LANL2DZ, for K), aug-cc-pVDZ (Li and Na only), aug-cc-pVTZ, 6-311++G(2d,2p), TZV(2d,2p) (K only). In general, relatively consistent values were obtained for optimized

C_6 parameters across these basis sets, with the exception of potassium, which will be further detailed below. Table 4.18 summarizes the optimal C_6 values obtained for the three metals for each basis set. We note the difference between these optimally determined C_6 values and those determined by Grimme. For the neutral alkali metals, the most dramatic differences are the two more highly polarizable elements, Li and Na.

In attempt to better understand the variance of the optimized C_6 parameters across the series of alkali metals, one can plot the error function for all three cases on the same plot. Figure 4.21 shows a plot of the error functions with respect to the variable $x' = x - x_{med}$, where x_{med} is the optimal C_6 value found for each case. In this way, the curves should look like parabolas, with all minima at $x' = 0$. What we find is that Li and Na each show tight, deep parabolas, reflecting large error sensitivity with respect to variation of the C_6 parameter. Also, the minima are in the same region for each case, regardless of basis set considered (0.075 for the Li system, 0.100 for the Na system), however, it is readily observed that the double-ζ basis set is not sufficient for chemical accuracy, particularly for the Na cation complex.

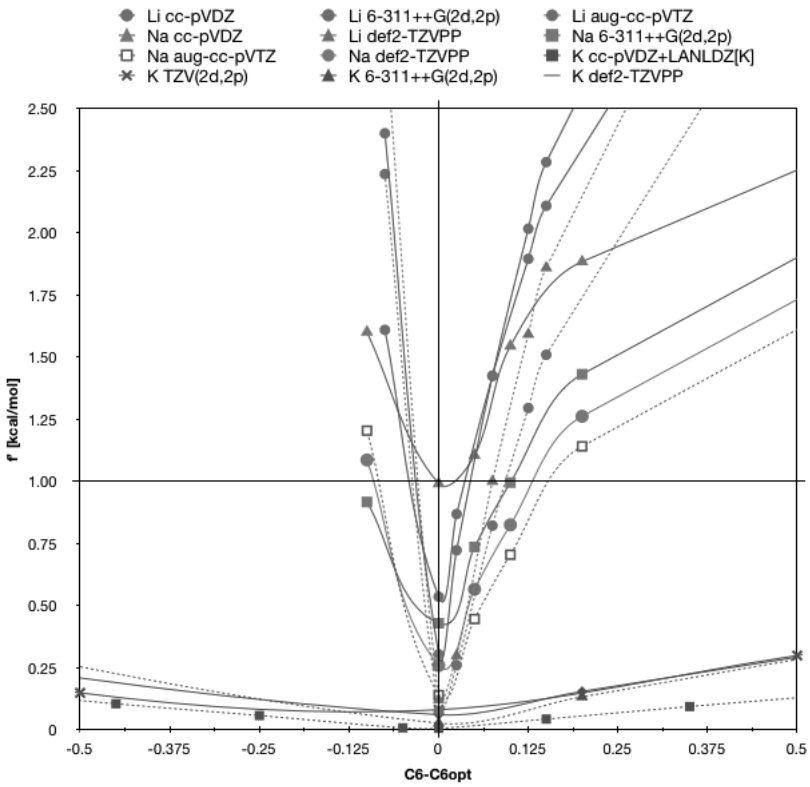

Figure 4.21: Optimized C_6 dispersion function parameters as a function of basis set quality. Chemical accuracy is highlighted with a horizontal black line at 1 kcal/mol.

In contrast, the potassium system shows much less sensitivity with respect to variation of the C_6 parameter, within any particular basis set. Of one takes as reference a $f(C_6)$ under 1 kcal/mol, the range is on the order of 5 C_6 units for all basis sets. If one further reduces the reference value to under 0.25 kcal/mol the range reduces to about 1 C_6 unit.

In either case, this range is quite large, and considerably larger compared with the other two metals. Unlike the other two alkali metals, the minimum of each basis set is located at quite different C_6 values. Also, as noted for Na, the double-ζ basis set is particularly poor for this metal. In fact, while the cc-pVDZ+LANLDZ[K] C_6 value of 10.45 is quite close to the double-ζ basis value as initially proposed by Grimme ($C_6 = 10.61$) provides quite consistent results, however in direct disagreement with the results obtained with the larger basis sets ($C_6 = 5.5$ and $C_6 = 3.8$). This large difference might be justified by a compensation of two different kind of errors: the first resulting from the general over-estimation of the dispersion term with the original Grimme parameter, and the second resulting from an underestimation of the binding energy due to the small flexibility of the double-ζ quality basis set for this system. The quality of the core potential is difficult to analyze, but would not be considered alone enough to justify the large difference observed.

Table 4.19: DFT-D/ modified alkali metal parameters interaction energies, equilibrium distances, dispersion energies, and ΔE(expt-calc) for benzene-alkali metal ion complexes, using different basis sets.

	Li				Na				K			
Method	ΔE [kcal/mol]	Re (Å)	-D	ΔE (expt-calc)	ΔE [kcal/mol]	Re (Å)	-D	ΔE (expt-calc)	ΔE [kcal/mol]	Re (Å)	-D	ΔE (expt-calc)
B97-D:												
6-31G(d,p)	-41.7	1.935	-2.16	-3.8	-27.0	2.425	-0.96	1.0				
6-31++G(d,p)	-37.0	1.942	-2.15	0.9	-23.0	2.452	-0.94	5.0				
DZV	-35.350	1.994	-2.084	2.5	-	-	-					
DZV(d,p)	-39.538	1.948	-2.144	-1.6	-	-	-					
DZV(2d,p)	-41.178	1.914	-2.163	-3.3	-	-	-					
DZV(2d,2p)	-40.985	1.914	-2.163	-3.1	-	-	-					
cc-pVDZ	-38.665	1.944	-2.148	-0.8	-24.056	2.471	-1.063	3.9	-	-	-	
aug-cc-pVDZ	-37.429	1.929	-2.156	0.5	-22.987	2.457	-1.072	5.0	-	-	-	
LANL2DZ	-	-	-		-22.997	2.472	-1.058	5.0				
cc-pVDZ+LANLDZ(M)	-	-	-		-22.706	2.478	-1.057	5.3	-18.775 (C6=10.45)	2.920	-4.723	-0.5
TZV(d,p)	-39.699	1.916	-3.840	-1.8	-23.259	2.458	-1.354	4.7				
TZV(2d,p)	-40.266	1.911	-3.839	-2.4	-23.882	2.447	-1.369	4.1				
TZV(2d,2p)	-39.933	1.911	-3.839	-2.0	-23.562	2.447	-1.369	4.4	-18.850 (C6=4.80)	2.876	-4.924	-0.6
cc-pVTZ	-40.288	1.910	-3.837	-2.4	-23.565	2.455	-1.361	4.4	-	-	-	
6-311G(d,p)	-39.4	1.914	-2.70	-1.5	-24.0	2.460	-1.17	4.0				
6-311++G(d,p)	-38.2	1.912	-2.70	-0.3	-23.0	2.465	-1.16	5.0				
6-311++G(2d,2p)	-38.4	1.913	-2.70	-0.5	-23.4			4.6	-18.796 (C6=3.80)	2.867	-4.118	-0.5
aug-cc-pVTZ	-39.055	1.910	-3.839	-1.2	-23.089	2.453	-1.413	4.9	-	-	-	
Def2-TZVPP	-37.4	1.912	-2.16	0.5	-23.3	2.451	-0.94	4.7	-18.830 (C6=4.80)	2.881	-4.577	-0.5
Def2-QZVPP	-37.9		-2.16	0.0	-22.8		-0.94	5.2	-	-	-	
M06/cc-pVDZ1	-36.9	1.980	-	1.0	-23.9	2.524	-	4.1	-18.7	2.875	-	
MP2/cc-pVTZ//M06/cc-pVDZ	-37.9	-	-	0.0	-23.5	-	-	4.5				
ACCURATE MP2	-40.2	1.865		-2.3	-24.9	2.396		3.1	-18.5	2.894		
ACCURATE CCSDT	-38.13	1.92	-0.59	-0.2	-22.95	2.480	-0.59	5.1	-18.77	2.900	-3.57	-0.5
EXP	**-37.9**				**-28.0**				**-18.3**			

Using the optimized parameters obtained for the alkali metal cations, the calculations reported in Table 4.17 are repeated and summarized in Table 4.19. In particular, now the ΔE(expt-calc) values between DFT-D and CCSDT is substantially smaller, with the maximum -3.8 kcal/mol with the 6-31G(d,p) basis, but on average ~1 kcal/mol or less. As well, the values of the dispersion energy are much more reasonable, albeit still on the high side as referenced to CCSDT. These results are also further supported by recent results obtained by Singh et al.[292], where CCSD(T)/CBS and corrected SAPT partition energies were used to establish the nature of the interactions in several $\pi - \pi$ complexes. In that study, the dispersion energies for Li-Benzene and Na-benzene complexes were found to

be -0.59 kcal/mol for both cases. Our optimization results are in general agreement with these more expensive albeit highly accurate calculations, predicting equal dispersion coefficients, for the two cases and a dispersion contribution, -D, on the order of ~1 kcal/mol. Considering the large number of spurious contributions that the -D component compensates for within the semi-empirical parameters (*e.g.*, BSSE, exchange effect, etc), this is quite good.

Even though one can minimize a trial function such as shown in Equation 4.7, and obtain reasonable "case by case" C_6 parameters that enable prediction within the global accuracy of the B97-D functional, the general message is that extreme care must be taken in using the B97-D method for systems outside of which the original dispersion parameters provide for. Moreover, care must be taken in assigning a quantitative assessment of the amount of dispersion energy inherent in a particular system, except within a relative setting. While it is not in the focus of the present work to find an accurate and general values of the C_6 coefficients for all alkali-metal ions in all their reference states as a function of DFT type and basis set, a general study is warranted based on what we see for the alkali metals. In the present study, we accept the optimized values we have determined for Li, Na, and K-containing cations, which should be consistent for application. With these proposed optimized dispersion parameter values, we move on to the solution phase, and the behavior of cation-π complexes in solution environment.

4.3.4 Application of theoretical approach: alkali-metal benzene cations in solution environment

DFT-D/COSab method for benzene-guanidinium

Solvent effects were taken into account using the combined DFT-D/COSab that we recently detailed in the literature. We initially consider a single complex, the benzene-guanidinium ion complex. The potential energy surface of this system shows a local minimum in the T-shape conformation (Figure 4.22), analogous to the benzene dimer case.

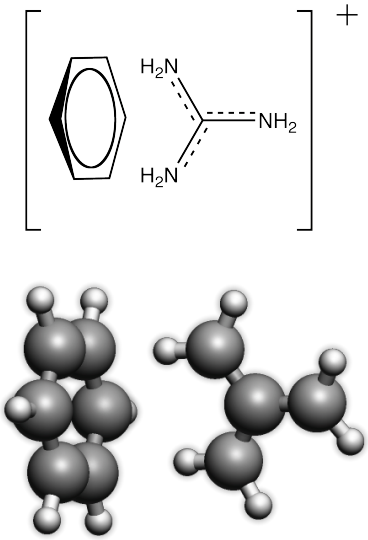

Figure 4.22: T-shape conformation of the benzene-guanidinium complex.

The interaction energy is calculated as the difference in energy of the fully optimized dimer in solution minus the single point energies of each monomer under the same solvated conditions, at the B97-D/cc-pVDZ level of theory. The basis set superposition error (BSSE) is considered, as previously presented, using

$$\Delta E_{\text{solv}} = E_{\text{solv}}^{\text{complex}} - \left(E_{\text{solv}}^{\text{mon.A}} + E_{\text{solv}}^{\text{mon.B}}\right) + \Delta\Delta E_{\text{vacuum}}^{\text{CP}} \tag{4.8}$$

$$\Delta\Delta E_{\text{vacuum}}^{\text{CP}} = E_{\text{vacuum}}^{\text{CP}} - E_{\text{vacuum}}^{\text{no-CP}} \tag{4.9}$$

where $E_{\text{vacuum}}^{\text{CP}}$ and $E_{\text{vacuum}}^{\text{no-CP}}$ are both evaluated as single-point energies of the solvated geometries of the corresponding dimer and monomers.

Results of interactions energy in gas versus high dielectric phase (water, as well as perfect conductor) are summarized in Table 4.20. The high dielectric environment clearly has a large influence on the interaction energy of the complex, lowering the binding energy by more than 13 kcal/mol, from gas phase to perfect conductor. Comparison with the B3LYP/cc-pVDZ method, which does not account for dispersion, allows a gauge of the extent of dispersion in these two different phases. In the gas phase, the difference between the two density functional methods is nearly ~4 kcal/mol, while in the water environment, the difference is on the order of ~3 kcal. Results can also be compared to a more traditional method, MP2/cc-pVTZ+CP, where BSSE correction is made using the counterpoise correction (CP) method. Here, B97-D/cc-pVDZ and MP2/cc-pVTZ+CP give comparable results in both the gas phase as well as in high dielectric, even with a smaller basis set in the former case. This further supports both the parametrization of B97-D for method as well as the efficient method of treating BSSE in solvated complex systems. The B97-D method significantly lowers the computational cost over that of MP2, but also with respect to the hybrid method, as shown in Table 4.20.

Table 4.20: Summary of results for complexation energy of the benzene-quanidinium complex in gas phase, water, and assuming a perfect conductor, for various levels of theory. The cpu time in seconds is also provided.

Level of theory	interaction energy [kcal/mol]			time [s]
	vacuum ($\varepsilon = 1$)	water ($\varepsilon = 78.4$)	perfect conductor ($\varepsilon = \infty$)	
B3LYP/cc-pVDZ	-11.22	1.02	1.42	2705.6
B97-D/cc-pVDZ	-14.94	-1.83	-1.75	2646.4
MP2/cc-pVTZ+CP	-14.68	-1.52	-1.35	6150.4

Following these promising results, a full dielectric scan was next carried out. A good linear correlation is obtained between the interaction energy and the dielectric function of the COSab method,

$$f(\varepsilon) = \frac{(\varepsilon - 1)}{(\varepsilon + 0.5)} \tag{4.10}$$

as depicted in Figure 4.23.

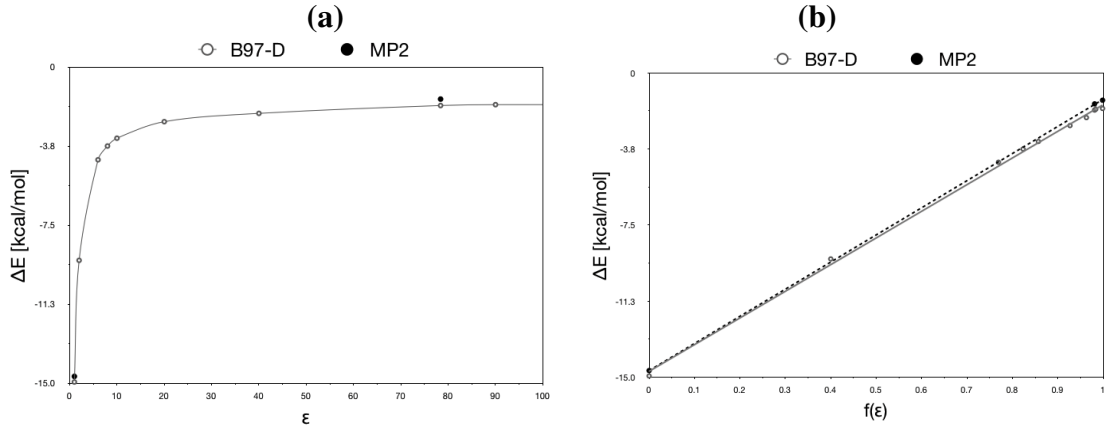

Figure 4.23: Plot of binding energy as a function of dielectric (a), and dielectric function $f(\varepsilon)$ (b), for the benzene-quanidinium system, calculated using B97-D/COSab, and compared to MP2/COSab.

General comparison of properties as a function of dielectric for an expanded set of cations

We next used the B97-D/cc-pVDZ methodology on an expanded set of benzene cation complexes, including benzene-M^+, benzene-NH_4^+, and benzene-$N(CH_3)_4^+$. As for the benzene-guanidinium cation complex, computations were carried out to determine the interaction energy for each complex, as a function of dielectric envionrment.

Using this relationship established above for benzene-guanadinium, one finds near perfect linearity for all complexes considered (Figure 4.24, first plot), resulting in a general equation of the form,

$$\Delta E_{\text{solv}} = a\frac{(\varepsilon-1)}{(\varepsilon+0.5)} + b \tag{4.11}$$

where the values of a and b are the characteristic binding properties of the particular complex, $\left|\Delta E^{\infty}_{\text{solv}} - \Delta E_{\text{vacuum}}\right|$ and ΔE_{vacuum}, respectively.

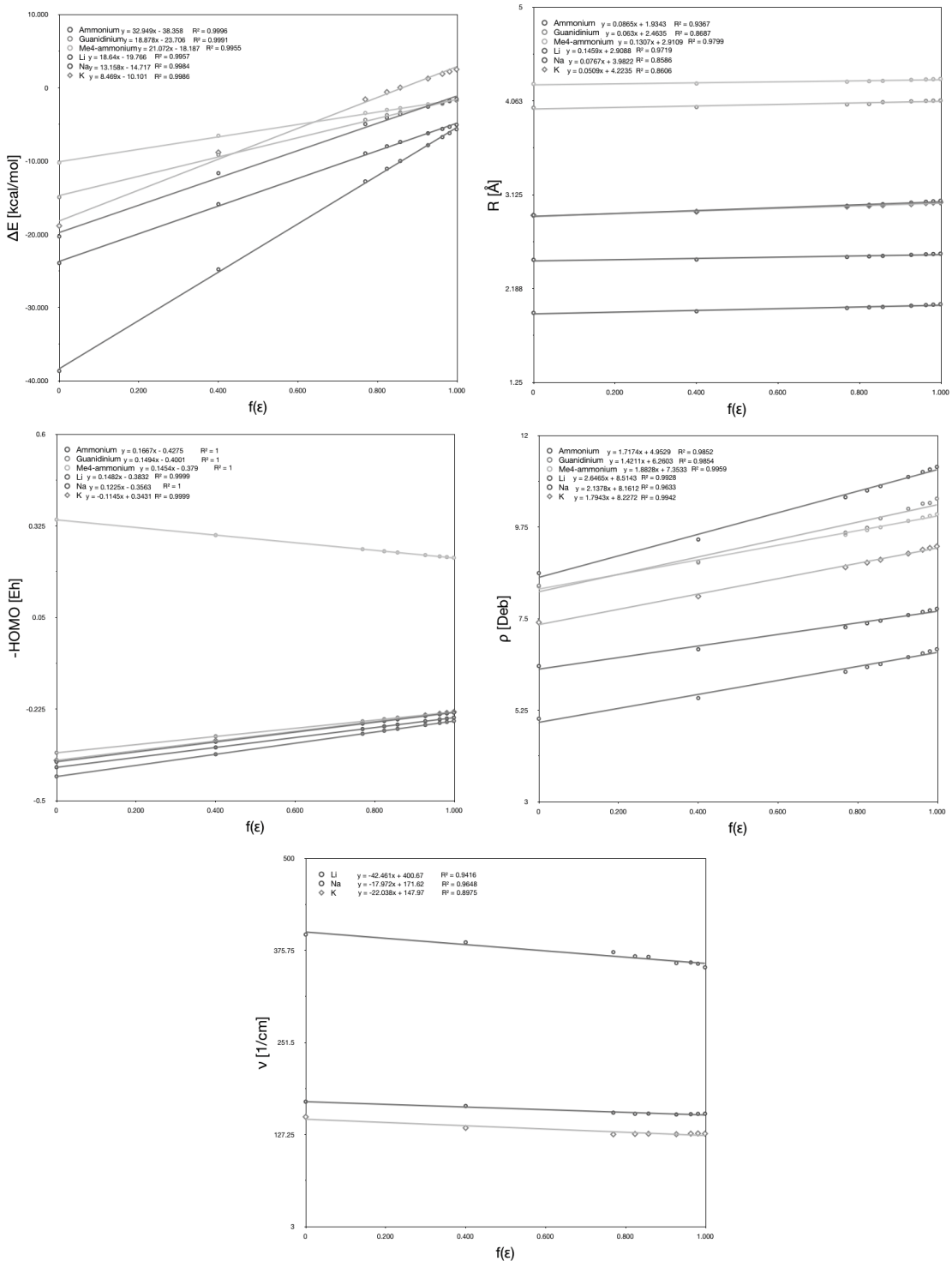

Figure 4.24: Correlation curves for the full set of cation complexes considered.

Table 4.21 summarizes the binding energies in gas phase, ΔE_{vacuum}, the binding energies in a perfect conductor (the infinite dielectric limit), ΔE_{∞}, and the absolute difference in the two mediums, $\left|\Delta E^{\infty}_{\text{solv}} - \Delta E_{\text{vacuum}}\right|$, for each complexes considered. One sees the close relationship between b (y-intercept) and the gas phase interaction energy of the respective cation complex. The value of a is an indication of how the system reacts to

variation in dielectric. For example, if a small change in dielectric corresponds to a large change in the binding energy, a will be large. This property is very well described by $\left|\Delta E^{\infty}_{\text{solv}} - \Delta E_{\text{vacuum}}\right|$, the absolute difference between the binding energy in vacuum and the binding energy in a perfect conductor, as also seen in Table 4.21. (A plot of a as a function of $\left|\Delta E^{\infty}_{\text{solv}} - \Delta E_{\text{vacuum}}\right|$, again shows near perfect correlation, with slope 1 and y-intercept 0.

Table 4.21: Summary of results for complexation energy of the cation complexes 1-5, in gas phase compared to that in an assumed a perfect conductor, for various levels of theory, together with the determined values of a and b in Equation 4.11.

	$-\Delta E_{\text{vacuum}}$	$-\Delta E_{\infty}$	$\left\lvert\Delta E^{\infty}_{\text{solv}} - \Delta E_{\text{vacuum}}\right\rvert$	a	b
Li^+	38.66	5.68	32.99	32.95	38.36
Na^+	23.94	5.07	18.87	18.88	23.71
NH_4^+	20.31	1.54	18.77	18.64	19.77
guanidinium	14.95	1.75	13.19	13.16	14.72
$N(CH_3)_4^+$	8.64	1.09	7.55	7.51	8.57

From these considerations we can obtain a general equation for the calculation of interaction energies in solution, by use of only two calculations, one in gas phase and the second in infinite dielectric. Rewriting equation 4.11, using the notation of the binding energy in vacuum E_1^{bnd} (positive value of the interaction energy), and a simpler notation for the term $\left|\Delta E^{\infty}_{\text{solv}} - \Delta E_{\text{vacuum}}\right| = \Delta E^{\text{bnd}}_{1-\infty}$, we obtain a simple approximated formula:

$$E_{\varepsilon}^{\text{bnd}} = E_1^{\text{bnd}} - f(\varepsilon)\, \Delta E^{\text{bnd}}_{1-\infty} \tag{4.12}$$

The final binding energy of a cation-π system in a solvent with dielectric ε is very well approximated as the binding energy of the complex in gas phase diminished by the energy difference term between the two limit cases of $\varepsilon = 1$ (gas phase) and $\varepsilon = \infty$ (perfect continuum), scaled by a function of ε.

Other properties as a function of dielectric

The equation derived above serves as a useful predictive tool for the binding energy of these complexes in solution. It is also interesting to investigate the behavior of other properties as a function of dielectric. For this purpose, a similar analysis can be carried out for other properties of general interest, such as the equilibrium distance between the monomers (R^{eq}), energy of highest occupied molecular orbital (E^{HOMO}), molecular dipole (ρ), and stretching frequency (ν^{stretch}). For the 5 cation complexes, these properties are summarized by the plot of Figure 4.24.

As shown in Figure 4.24, the HOMO energies show a very high correlation as a function of dielectric, with slope (a-value of Equation 4.11) and y-intercept (b-value of Equation 4.11), derived as with the binding energy property. A general equation for the prediction of HOMO energy is therefore

$$E_{\varepsilon}^{\text{HOMO}} = E_1^{\text{HOMO}} - f(\varepsilon)\, \Delta E^{\text{HOMO}}_{1-\infty} \tag{4.13}$$

Using Koopmans' theorem, would could extrapolate this relationship to Ionization Potential. Due to the problematic interpretation of DFT frontier orbital eigenvalues, however, perhaps a better measure of Ionization Potential, ΔSCF, could be used.

The other properties shown, dipole, equilibrium distance, and stretching frequency, are not energy properties, and therefore show a less precise correlation. Nevertheless, the R^2 value each respective correlation is still significant. The correlation relationships that can be derived for each property, together with their respective R^2 values are:

$$R_{\varepsilon}^{\mathrm{eq}} = R_{1}^{\mathrm{eq}} - f(\varepsilon)\,\Delta R_{1-\infty}^{\mathrm{eq}} \tag{4.14}$$

$$\nu_{\varepsilon}^{\mathrm{stretch}} = \nu_{1}^{\mathrm{stretch}} - f(\varepsilon)\,\Delta \nu_{1-\infty}^{\mathrm{stretch}} \tag{4.15}$$

$$\rho_{\varepsilon} = \rho_{1} - f(\varepsilon)\,\Delta \rho_{1-\infty} \tag{4.16}$$

4.3.5 Conclusions and perspectives

The results presented in the first part of this work on cation-π interactions, clearly show an inconsistency in the DFT-D approach. This limitation can be compensated by using a "case by case" optimization of the semiempirical terms that are included in the E_{disp} term, in particular of the atomic dispersion coefficient, the van der Waals radii, or both. With such *ad hoc* corrections, the DFT-D/COSab approach used in the second part, provides very promising results in the study of quadrupole-ion interaction systems in solution, confirming the broad applicability of the combined approach.

Despite results with the *ad hoc* optimization are interesting for this particular case, the wrong behavior of DFT-D is definitely not desirable, and somehow limits the potential of the method. An uncontrolled use of DFT-D, in fact, can lead to wrong results, analyses, and conclusions. For such this reason, Stefan Grimme was highly stimulated by our results to correct the behavior of the original DFT-D algorithm, in order to make it more consistent over the entire periodic table. For this purpose, he will present a new approach called DFT-D3, that will not make use of semiempirical, pre-stored, atomic C_6 anymore. An additional term dependent on C_8 atomic coefficients, will also be included in the expansion of the dispersion energy term. The atomic dispersion coefficients, C_6 and C_8, will be calculated on the fly from atomic polarizabilities data obtained from atomic densities, by use of the Casimir-Polder expression.

Implementation and optimization of the DFT-D3 method in GAMESS are currently under development in our group, and will be presented in a future paper. The new DFT-D3/COSab will also be matter of investigations in the next future, and will probably lead to a reformulation of the quadrupole-ion interaction study presented here.

Chapter 5

Conclusion and Perspective

Overview

5.1 Outcome

The work of this thesis involved the optimization, implementation, and application of several/ accurate *ab initio* models for calculation of molecular systems and their environment. The methods for molecular energies and properties, described in chapter 2, belong to the framework of Density Functional Theory. Particular emphasis was on the development of methodology for modeling of weakly interacting systems, thereby targeting the vdW component of interaction. A simple semi-empirical term was implemented into the standard density functional, optimized, and tested. The work enabled correction of one of the main limitations of the most used approximation of the exchange-correlation functional: the inability to treat dispersion interactions. The resulting work was incorporated into the suite of density functional capabilities of the GAMESS quantum chemistry package of software, thereby enabling distribution to the community at large. In particular, a large number of new DFT functionals were implemented and are already available in the production version of GAMESS, including:

LDAs: PZ81 correlation.

GGAs: P86 correlation, revPBE, EDF1, B97, B97-1, B97-2, B97-3, B97-D, B97-K, B98, HCTH/93, HCTH/120, HCTH/147, HCTH/407.

meta-GGAs: τ-HCTH, τ-HCTH hybrid, BMK.

RSHs: ωB97, ωB97X, ωB97X-D.

DFT-D: the semiempirical dispersion term is available in addition to Hartree Fock, and the vast majority of DFT functionals of GAMESS (like the common revPBE and B3LYP).

DH: the B2-PLYP double hybrid functional, together with all its possible variation B2*x*-PLYP (*e.g.*, B2K-PLYP, B2T-PLYP, B2GP-PLYP)

The treatment of environment effects used in this work belongs to the class of continuum solvation methods, and is described in chapter 3. The particular solvation method presented in this work, COSab, was developed in this group and has in the past been used successfully on small organic molecules to predict free energy of solvation in agreement with available experimental data. With the efforts described in this thesis, the algorithm can now be used on molecules of arbitrary size, with the default solvation cavity able to manage about 200 atoms (arbitrary extension can be easily obtained by simple increasing of the memory demand in the GAMESS source code). The COSab method was also optimized together with the semiempirically corrected DFT-D, enabling application to molecular systems that are complicated by treatment of dispersion interactions in condensed phase environment. Many other theoretical techniques are also now accessible with these developments, for example theories and applications associated with excited state processes. The revision of the COSab algorithm presented in chapter 3 has also been made available in the production version of GAMESS, and includes the following features:

- Two new routines to enable the calculation of solvation energies, and outlying charge effects, respectively.
- Reorganization of all the `COMMON` groups to reduce memory requirements, especially for large cavities.
- Refinements in the dynamic memory allocation of large vectors and matrices.
- Implementation of the parallel version of the MP2/COSab within the mp2ddi algorithm.
- Grouping of all the routines related to COSab in the cosmo.src source file.
- Enabling of the DFT-D/COSab methods.
- The new Ahlrichs' triple zeta valence family of basis sets (TZV, TZVP, TZVPP) for the COSMO-RS method.

Several interesting research applications that exemplify the methodologies developed in this work, were reported in chapter 4. In particular, a computational investigation was carried out on the parent triaziridine and as a function of N-substituents. Assessment of heat of formation, ring strain energy, barriers to inversion of nitrogen, and NMR criteria lead to understanding of issues related to vicinal lone pair repulsion and aromatic stabilization. Results also lead to the proposal of a potentially flat structure with a π aromatic-like triaziridine system, $N_3(BH_2)_3$.

A second full investigation was carried out on a set of rare gas trimers, molecules that are notoriously difficult in that their interactions are dominated by weak dispersion interactions. At the same time they represent simple models for study of complex properties. While one can find several literature investigations concerning rare-gases dimers, very few articles involve accurate calculations of structure and properties for the rare gas trimers. Moreover, none of the more recent DFT functionals have been tested on these systems, despite the relevance of such functionals for understanding interactions of the type that are present in rare gas trimers. Therefore, in this work, accurate calculations of the structure and properties of the main Rg_3 molecules (Rg = He, Ne, Ar), across a full suite of density functional classes is presented, as compared to highly accurate CCSD(T)/CBS theory.

The third research example presented is a ion-quadrupole interaction analysis, by use of the combined DFT-D/COSab method. The results presented for this case, clearly show an inconsistency in the DFT-D approach. Only a "case by case" optimization of the semiempirical term allowed us to obtain a good validation of the combined method. For such this reason, Stefan Grimme was highly stimulated by our results to correct the behavior of the original DFT-D algorithm, in order to make it more consistent over the entire periodic table. Implementation and optimization of the new DFT-D3 method in GAMESS are currently under development in our group, and will be presented in a future paper.

5.2 Future Work

5.2.1 The problem of electronic correlation in quantum chemistry

The electronic correlation is generally defined as the interaction between electrons in the electronic structure of a quantum system. Despite its relatively small value, compared to the repulsion between nuclei, the nuclei-electron attraction, and the Pauli repulsion (electronic exchange), electron correlation is in general a non-negligible part of the binding energy of a quantum system. Moreover, in many systems, electron correlation is key to important chemical effects, as governed by the weak van der Waals interactions.

In the context of standard approximation for the solution of the nonrelativistic, time independent Schrödinger equation in quantum chemistry (Eqn 5.1),

$$\hat{H}\Psi = E\Psi \tag{5.1}$$

the Hartree-Fock (HF) methodRoothaan[265] represents one of the traditionally best approximations to the total energy of the system, that does not, however, include the opposite-spin electron-electron interaction.[1] According to Löwdin, the electron correlation energy is defined as the energy difference between the exact, non-relativistic, electronic energy and the HF energy (Figure 5.1).

A first approach to treat the correlation problem is to use the general Rayleigh-Schrödinger perturbation theory. In this context, Møller and Plesset developed a method that takes the unperturbed (zeroth-order) Hamiltonian to be the sum of the one-electron Fock operators, and treats electron correlation as the perturbation to the zeroth-order Hamiltonian (Eqn 5.2).

[1] Correlation between electrons with the same spin is included in HF theory in an implicit manner through the Slater determinant, that impose the Pauli principle.

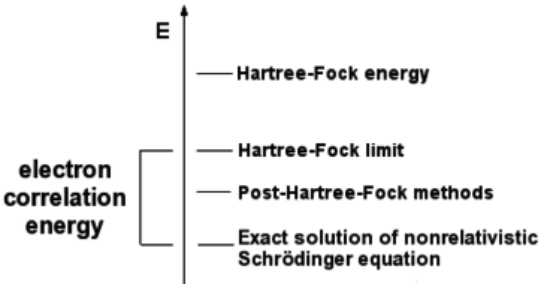

Figure 5.1: Common methodologies in quantum chemistry, and definition of electron correlation energy.

$$\hat{H}_\lambda = \hat{H}_0 + \lambda \hat{V} \tag{5.2}$$

The perturbation theory expansion for the total Schrödinger equation takes the form:

$$\begin{aligned} \Psi_\lambda &= \Psi_0 + \lambda \Psi_1 + \lambda^2 \Psi_2 + \dots \\ E_\lambda &= E_0 + \lambda E_1 + \lambda^2 E_2 + \dots \end{aligned} \tag{5.3}$$

where Ψ_0 is the Hartree-Fock (HF) single-determinant wavefunction, $E_0 = \sum_i^{occ} \varepsilon_i$ is simply the sum of the orbital energies, E_1 is the HF energy, and higher terms are the MPx corrections (MP2, MP3, ...). The energy correction for the widely used MP2 approximation incorporates the second order term as shown in Eqn 5.4.

$$E_2 = \sum_{i<j}^{occ} \sum_{a<b}^{virt} \left(\varepsilon_a + \varepsilon_b - \varepsilon_i - \varepsilon_j\right)^{-1} \left| \left(\phi_i \phi_j \,|\, \phi_a \phi_b\right) \right|^2 \tag{5.4}$$

where the summations are carried out over all double substitutions of electrons between occupied (*occ*) and unoccupied (*virt*) orbitals. This term essentially represents the simplest approximate expression for the dispersion energy.

5.2.2 beyond GGA: new solution for the correlation problem

At the heart of this thesis, and my future plans is the treatment of electron correlation. As presented in Chapter 2 of this Thesis, Density Functional Theory is a reliable and efficient method to treat the correlation problem. Regular LDA and GGA approximations to the exchange-correlation functional, up to the second rung of Perdew's ladder, are insufficient for many quantum chemical calculations. However, two main strategies have been proposed for accurate treatment in chemical systems, that correspond to the third and fourth rungs of Perdew's ladder.

The first strategy is the inclusion of terms that depend on the kinetic energy density, τ, into the functional expression, leading to the meta-GGA functionals (third rung):

$$E_{xc}^{\text{meta}-\text{GGA}} = E_x^{\text{GGA}} + E_x^{\tau} + E_c^{\text{GGA}} + E_c^{\tau} \tag{5.5}$$

The second strategy involves inclusion of terms from wavefunction theory into the Kohn Sham Hamiltonian, in particular the inclusion of a scaled HF-like exchange term. This has lead to the class of hybrid functionals (fourth rung):

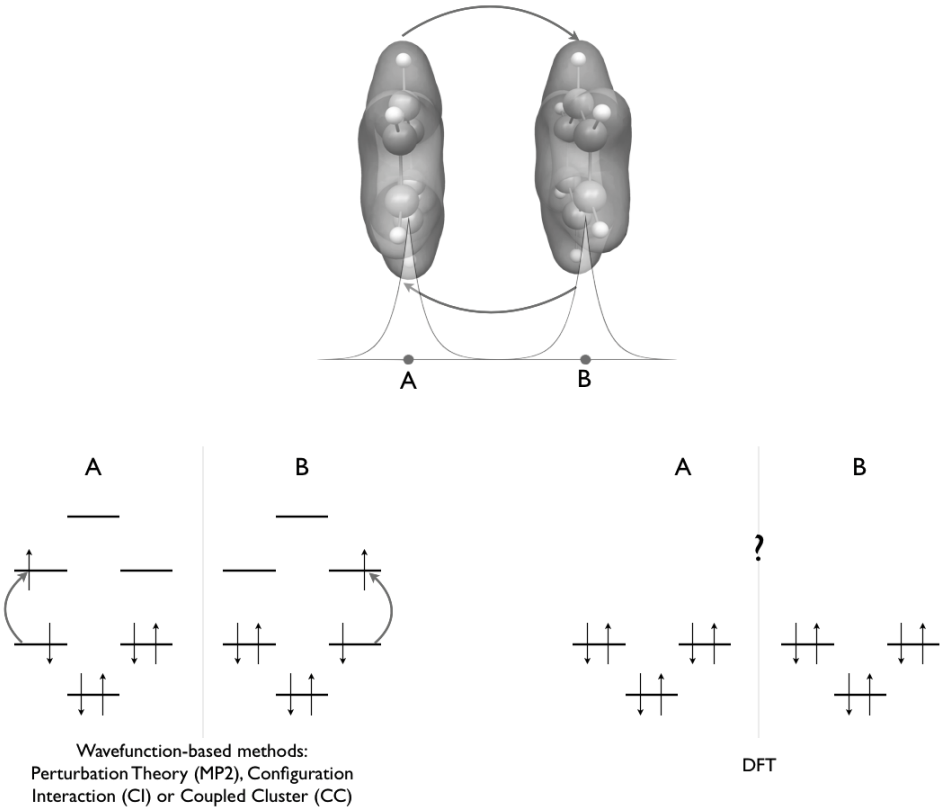

Figure 5.2: Wavefunction theory, and DFT approach to correlation effects

$$E_{xc}^{\text{hybrid}} = E_x^{\text{GGA}} + c_x E_x^{\text{HF}} + E_c^{\text{GGA}} \tag{5.6}$$

The recently developed range separated hybrids (RSH), still belongs to this class of functionals:

$$E_{xc}^{\text{RSH}} = E_x^{\text{SR-GGA}} + (1 - c_x) E_x^{\text{LR-HF}} + c_x E_x^{\text{HF}} E_c^{\text{GGA}} \tag{5.7}$$

A mixed third+fourth rung approach is very popular, and has lead to the class of hybrid meta-GGA functionals:

$$E_{xc}^{\text{hybrid/meta-GGA}} = E_x^{\text{GGA}} + E_x^{\tau} + c_x E_x^{\text{HF}} + E_c^{\text{GGA}} + E_c^{\tau} \tag{5.8}$$

These latter approaches have been very successful, and were the major contribution to the introduction of high accuracy DFT as applied to molecular systems.

On the other side, it is important to stress that DFT always remains a single determinant theory, that treats the correlation problem as a local (mean) effect. The above DFT formalism provides no information on virtual orbitals, and for this reason, even meta-GGA and hybrid functionals are unable to describe effects with non-local correlation components. Such effects mainly occur at large distances, where the electron density of two fragments do not overlap, and for example, play a key role in the description of van der Waals interactions (Figure 5.2).

To overcome the main limitations of GGA functionals, different strategies have been developed in the recent literature (Table 5.1). A large selection of these functionals were

Table 5.1: Future plans for treatments of density functionals beyond GGA.

Density Functional Type	**Examples**	**Reference**	**Personal experience**
meta-GGA	Minnesota family	Zhao/Truhlar[9,14,15,247]	will be considered in postdoc
	τ-HCTH family	Handy[16]	implemented in this work
	BMK	Boese/Martin[17]	–
Range-separated hybrid (RSH)	LC-BLYP CAM-B3LYP	Savin[18,19]	will be considered in postdoc
	HSE	Scuseria[248,249]	will be considered in postdoc / implemented in this work
	ωB97	Chai/Head-Gordon[20]	will be considered in postdoc / implemented in this work
Empirical/semi-empirical	B97-D	Grimme[23]	implemented in this work
Double-hybrid	B2-PLYP, mPW2-PLYP	Grimme[24,250]	implemented in this work
	MC3BB MC3MPW	Zhao/Truhlar[25]	will be considered in postdoc
	B2K-PLYP mPW2K-PLYP	Martin[93]	implemented in this work
Andersson-Langreth-Lundqvist functional	vdW-DF	Langreth[26]	–

investigated in the work of this thesis, as reported in Table 4.9. We repeat the main features of the previous Table in Table 5.1, and indicate the possible future work in the last column.

The aim of my postdoc experience will be to a) investigate, improve, and extend several of these strategies, and b) to propose and implement new strategies that enable higher order calculations. The main strategies for my postdoctoral work, as well as how it deviates from my PhD work, will be presented in the next section.

5.2.3 Postdoctoral work

My goals for the work during the postdoc fellowship are mainly three. The first is to understand how to improve beyond-GGA, DFT types of functionals. Substantiation of the new functionals will involve expansive databases of accurate and experimental chemical data that are available in the host research groups. Second is to improve my knowledge of wavefunction methods, in order to formulate more reliable and efficient DFT + wavefunction approaches. Third is the implementation of these methods into

the major community quantum chemistry software, such as GAMESS, Gaussian, and QChem.

The first approach to the problem will be to explore the meta-GGA range-separated hybrid class of functionals. Comparing the exchange expression of range separated hybrids, and the hybrid meta-GGA functionals (Eqns 5.7 and 5.8), one finds large similarities between the two. The long-range Hartree-Fock term (nonlocal by definition) of Eqn. 5.7 is substituted by the τ–dependent exchange in Eqn. 5.8. The GGA exchange is limited to short-range in the first case, and the last two terms, the GGA correlation and the scaled HF exchange, are the same for both functional forms. A mixed RSH/meta-GGA approach will be the next natural step for functional development, and, up to now, a relatively unexplored field. The proposed RSH/meta-GGA functional will assume the generic form:

$$E_{xc}^{\mathrm{RSH/meta-GGA}} = E_x^{\mathrm{SR-GGA}} + c_\tau E_x^\tau + c_x^{\mathrm{LR}} E_x^{\mathrm{LR-HF}} + c_x E_x^{\mathrm{HF}} + E_c^{\mathrm{GGA}} + E_c^\tau \tag{5.9}$$

A second approach would be the optimization of the double hybrid (DH) class of methods, whose efficiency and performance is largely unsatisfactory, despite the large effort of a large part of the DFT community. A DH/meta-GGA functional, will have the following generic form:

$$E_{xc}^{\mathrm{DH/meta-GGA}} = E_x^{\mathrm{GGA}} + E_x^\tau + c_x E_x^{\mathrm{HF}} + E_c^{\mathrm{GGA}} + E_c^\tau + c_2 E_2 \tag{5.10}$$

where E_2 is the MP2 energy correction described in eq. 4. In order to carry out this development, both the meta-GGA and the scaled wavefunction energy terms will need optimization and adjustment. The wavefunction term, moreover, will need special attention in terms of efficiency, in order to improve the applicability, and consequently the success, of these kind of functionals for application on large chemical and bio-chemical systems.

A third approach is suggested by a major criticism to DFT. Specifically, in many cases, the density itself is a quantity that does not contain enough information to describe a quantum system. In a more rigorous mathematical description, the electron density is only the diagonal part of a more complex object called the density matrix:

$$\rho(r_1, r_2) = \sum_{i=1}^{N} \Psi(r_1)\Psi^*(r_2) \tag{5.11}$$

Density matrices contain all the necessary quantities for the treatment of quantum systems, since they are directly related to the total wavefunction, For this reason, the extension of DFT to density matrix, called density matrix functional theory (DMFT), holds promise as another reasonable approach to the correlation problem. Unfortunately, DMFT methods are not yet well formulated in the field of quantum chemistry, due to a more complicated formulation and implementation. Efforts in my postdoc will involve work towards reliable density matrix methods in widely used quantum chemistry software.

After the postdoc experience I plan my career in academics, possibly in Switzerland. The high level of the Swiss University system (among the top in Europe, and the entire world), and the many research opportunities provided by the Swiss National Science Foundation, make Switzerland the first place to consider for a possible top-level academic career.

The background that I will develop during the postdoctoral Fellowship, will provide me the opportunity and the competences to manage new research lines in the field of quantum chemistry. Development and refinement of electronic structure methods will always be the basic platform for my future research, but training has and will continue in these key research groups, to provide me with important understanding of how to apply state-of-the-art methodology as valuable support to experimentalists across a wide variety of fields for filling in important gaps in the experimental picture.

Bibliography

[1] Schmidt, M.; Baldridge, K. K.; Boatz, J.; Elbert, S.; Gordon, M.; Jensen, J.; Koseki, S.; Matsunaga, N.; Nguyen, K.; Su, S.; Windus, T.; Dupuis, M.; Montgomery, J. *J. Comput. Chem.* **1993**, *14*, 1347–1363.

[2] Kohn, W. *Rev Mod Phys* **1999**, *71*, 1253–1266.

[3] Pople, J. *Rev Mod Phys* **1999**, *71*, 1267–1274.

[4] Perdew, J. P.; Ruzsinszky, A.; Constantin, L. A.; Sun, J.; Csonka, G. I. *J Chem Theory Comput* **2009**, *5*, 902–908.

[5] Perdew, J. P. *Physical Review B* **1986**, *33*, 8822–8824.

[6] Becke, A. D. *Phys Rev A* **1988**, *38*, 3098–3100.

[7] Perdew, J. P.; Burke, K.; Ernzerhof, M. *Phys. Rev. Lett.* **1996**, *77*, 3865–3868.

[8] Becke, A. D. *J Chem Phys* **1993**, *98*, 1372–1377.

[9] Zhao, Y.; Schultz, N. E.; Truhlar, D. G. *J Chem Phys* **2005**, *123*, 161103.

[10] Zhao, Y.; Truhlar, D. G. *J Chem Theory Comput* **2006**, *2*, 1009–1018.

[11] Zhao, Y.; Schultz, N.; Truhlar, D. G. *J Chem Theory Comput* **2006**, *2*, 364–382.

[12] Zhao, Y.; Truhlar, D. G. *J Chem Phys* **2006**, *125*, 194101.

[13] Zhao, Y.; Truhlar, D. G. *J Phys Chem A* **2006**, *110*, 13126–13130.

[14] Zhao, Y.; Truhlar, D. G. *Accounts Chem Res* **2008**, *41*, 157–167.

[15] Zhao, Y.; Truhlar, D. *Theoretical Chemistry Accounts: Theory, Computation, and Modeling (Theoretica Chimica Acta)* **2008**, *120*, 215–241.

[16] Boese, A.; Handy, N. C. *J Chem Phys* **2002**, *116*, 9559–9569.

[17] Boese, A. D.; Martin, J. M. L. *J Chem Phys* **2004**, *121*, 3405.

[18] Leininger, T.; Stoll, H.; Werner, H.; Savin, A. *Chemical Physics Letters* **1997**, *275*, 151–160.

[19] Yanai, T. *Chemical Physics Letters* **2004**, *393*, 51–57.

[20] Chai, J.-D.; Head-Gordon, M. *J. Chem. Phys.* **2008**, *128*, 084106.

[21] Chai, J.-D.; Head-Gordon, M. *Phys. Chem. Chem. Phys.* **2008**, *10*, 6615–6620.

[22] Chai, J.-D.; Head-Gordon, M. *J Chem Phys* **2009**, *131*, 174105.

[23] Grimme, S. *J. Comput. Chem.* **2006**, *27*, 1787–1799.

[24] Grimme, S. *J Chem Phys* **2006**, *124*, 034108.

[25] Zhao, Y.; Lynch, B.; Truhlar, D. G. *J Phys Chem A* **2004**, *108*, 4786–4791.

[26] Dion, M.; Rydberg, H.; Schroeder, E.; Langreth, D. C.; Lundqvist, B. I. *Phys. Rev. Lett.* **2004**, *92*, 246401.

[27] Schwabe, T.; Grimme, S. *Phys. Chem. Chem. Phys.* **2007**, *9*, 3397–3406.

[28] Becke, A. D. *J Chem Phys* **1997**, *107*, 8554–8560.

[29] Perdew, J. P.; Zunger, A. *Physical Review B* **1981**, *23*, 5048–5079.

[30] R.D. Adamson, P. G.; Pople, J. *Chem. Phys. Lett.* **1998**, *284*, 6–11.

[31] Zhang, Y.; Yang, W. *Phys. Rev. Lett.* **1998**, *80*, 890–890.

[32] Peverati, R.; Baldridge, K. K. *J Chem Theory Comput* **2008**, *4*, 2030–2048.

[33] Jurecka, P.; Cerny, J.; Hobza, P.; Salahub, D. R. *J. Comput. Chem.* **2007**, *28*, 555–569.

[34] Wu, Q.; Yang, W. *J Chem Phys* **2002**, *116*, 515–524.

[35] Williams, R.; Malhotra, D. *Chemical Physics* **2006**, *327*, 54–62.

[36] Grimme, S. *J. Comput. Chem.* **2004**, *25*, 1463–1473.

[37] Ducere, J.-M.; Cavallo, L. *J Phys Chem B* **2007**, *111*, 13124–13134.

[38] Jurecka, P.; Sponer, J.; Cerny, J.; Hobza, P. *Phys. Chem. Chem. Phys.* **2006**, *8*, 1985–1993.

[39] Zhao, Y.; Lynch, B.; Truhlar, D. G. *Phys. Chem. Chem. Phys.* **2005**, *7*, 43–52.

[40] Lee, C.; Yang, W.; PARR, R. *Physical Review B* **1988**, *37*, 785–789.

[41] Schamp, H.; Mason, E.; Richardson, A.; Altman, A. *Phys Fluids* **1958**, *1*, 329–337.

[42] Dymond, J.; Rigby, M.; Smith, E. *J Chem Phys* **1965**, *42*, 2801–&.

[43] Snook, I.; Spurling, T. *J Chem Soc Farad T 2* **1972**, *68*, 1359–&.

[44] Hanley, H.; Klein, M. *J Phys Chem-Us* **1972**, *76*, 1743–&.

[45] Pope, G.; Chappele, P.; Kobayash, R. *J Chem Phys* **1973**, *59*, 423–434.

[46] Matthews, G.; Smith, E. *Molecular Physics* **1976**, *32*, 1719–1729.

[47] Boys, S.; Bernardi, F. *Molecular Physics* **1970**, *19*, 553–&.

[48] Schafer, A.; Huber, C.; Ahlrichs, R. *J Chem Phys* **1994**, *100*, 5829–5835.

[49] Dunning, T. *J Chem Phys* **1971**, *55*, 716–&.

[50] Sinnokrot, M.; Sherrill, C. *J Phys Chem A* **2004**, *108*, 10200–10207.

[51] Lee, E. C.; Kim, D.; Jurecka, P.; Tarakeshwar, P.; Hobza, P.; Kim, K. S. *J Phys Chem A* **2007**, *111*, 3446–3457.

[52] Ringer, A.; Sinnokrot, M.; Lively, R.; Sherrill, C. *Chem-Eur J* **2006**, *12*, 3821–3828.

[53] Sinnokrot, M. O.; Sherrill, C. D. *J Phys Chem A* **2006**, *110*, 10656–10668.

[54] Sinnokrot, M.; Sherrill, C. *J Am Chem Soc* **2004**, *126*, 7690–7697.

[55] Sinnokrot, M.; Sherrill, C. *J Phys Chem A* **2003**, *107*, 8377–8379.

[56] Cozzi, F.; Cinquini, M.; Annunziata, R.; Dwyer, T.; Siegel, J. *J Am Chem Soc* **1992**, *114*, 5729–5733.

[57] Cozzi, F.; Cinquini, M.; Annuziata, R.; Siegel, J. S. *J Am Chem Soc* **1993**, *115*, 5330–5331.

[58] Cozzi, F.; Ponzini, F.; Annunziata, R.; Cinquini, M.; Siegel, J. *Angew Chem Int Edit* **1995**, *34*, 1019–1020.

[59] Cozzi, F.; Siegel, J. *Pure Appl Chem* **1995**, *67*, 683–689.

[60] Zoltewicz, J.; Maier, N.; Fabian, W. *J Org Chem* **1998**, *63*, 4985–4990.

[61] Kaneta, N.; Mitamura, F.; Uemura, M.; Murata, Y.; Komatsu, K. *Tetrahedron letters* **1996**, *37*, 5385–5388.

[62] Cozzi, F.; Annunziata, R.; Benaglia, M.; Baldridge, K. K.; Aguirre, G.; Estrada, J.; Sritana-Anant, Y.; Siegel, J. S. *Phys. Chem. Chem. Phys.* **2008**, *10*, 2686–2694.

[63] Seiders, T.; Baldridge, K. K.; Grube, G.; Siegel, J. *J Am Chem Soc* **2001**, *123*, 517–525.

[64] Lovas, F.; McMahon, R.; Grabow, J.; Schnell, M.; Mack, J.; Scott, L.; Kuczkowski, R. *J Am Chem Soc* **2005**, *127*, 4345–4349.

[65] Seiders, T.; Baldridge, K. K.; Siegel, J. S.; Gleiter, R. *Tetrahedron letters* **2000**, *41*, 4519–4522.

[66] Wu, Y.-T.; Bandera, D.; Maag, R.; Linden, A.; Baldridge, K. K.; Siegel, J. S. *J Am Chem Soc* **2008**, *130*, 10729–10739.

[67] Zhao, Y.; Truhlar, D. G. *Phys. Chem. Chem. Phys.* **2008**, *10*, 2813–2818.

[68] Filatov, A. S.; Petrukhina, M. A. *J Organomet Chem* **2008**, *693*, 1590–1596.

[69] Wu, Y.-T.; Siegel, J. S. *Chem Rev* **2006**, *106*, 4843–4867.

[70] Prinzbach, H.; Wahl, F.; Weiler, A.; Landenberger, P.; Woerth, J.; Scott, L. T.; Gelmont, M.; Olevano, D.; Sommer, F.; von Issendorff, B. *Chem-Eur J* **2006**, *12*, 6268–6280.

[71] Diudea, M. *Phys. Chem. Chem. Phys.* **2005**, *7*, 3626–3633.

[72] Parschau, M.; Fasel, R.; Ernst, K.-H.; Groening, O.; Brandenberger, L.; Schillinger, R.; Greber, T.; Seitsonen, A. R.; Wu, Y.-T.; Siegel, J. S. *Angew Chem Int Edit* **2007**, *46*, 8258–8261.

[73] Xiao, W.; Passerone, D.; Ruffieux, P.; Ait-Mansour, K.; Groening, O.; Tosatti, E.; Siegel, J. S.; Fasel, R. *J Am Chem Soc* **2008**, *130*, 4767–4771.

[74] Theobald, J.; Oxtoby, N.; Phillips, M.; Champness, N.; Beton, P. *Nature* **2003**, *424*, 1029–1031.

[75] Yokoyama, T.; Yokoyama, S.; Kamikado, T.; Okuno, Y.; Mashiko, S. *Nature* **2001**, *413*, 619–621.

[76] Fasel, R.; Wider, J.; Quitmann, C.; Ernst, K.-H.; Greber, T. *Angew. Chem. Int. Ed.* **2004**, *43*, 2853–2856.

[77] Parschau, M.; Romer, S.; Ernst, K. *J Am Chem Soc* **2004**, *126*, 15398–15399.

[78] Chen, Q.; Richardson, N. *Nat Mater* **2003**, *2*, 324–328.

[79] Fasel, R.; Parschau, M.; Ernst, K. *Angew Chem Int Edit* **2003**, *42*, 5178–5181.

[80] Greber, T.; Sljivancanin, Z.; Schillinger, R.; Wider, J.; Hammer, B. *Phys. Rev. Lett.* **2006**, *96*, 056103.

[81] Schillinger, R.; Sljivancanin, Z.; Hammer, B.; Greber, T. *Phys. Rev. Lett.* **2007**, *98*, 136102.

[82] WAN, K.; DAVIS, M. *Nature* **1994**, *370*, 449–450.

[83] Ratner, M. *Nature* **2005**, *435*, 575–577.

[84] Kohn, W.; Meir, Y.; Makarov, D. *Phys. Rev. Lett.* **1998**, *80*, 4153–4156.

[85] Klamt, A.; Schuurmann, G. *J Chem Soc Perk T 2* **1993**, 799–805.

[86] Baldridge, K. K.; Klamt, A. *J Chem Phys* **1997**, *106*, 6622–6633.

[87] Baldridge, K. K.; Jonas, V. *J Chem Phys* **2000**, *113*, 7511–7518.

[88] Gregerson, L.; Baldridge, K. K. *Helvetica chimica acta* **2003**, *86*, 4112–4132.

[89] Peverati, R.; Baldridge, K. K. *J Chem Theory Comput* **2009**, *5*, 2772–2786.

[90] Benighaus, T.; DiStasio, R. J.; Lochan, R. C.; Chai, J.-D.; Head-Gordon, M. *J Phys Chem A* **2008**, *112*, 2702–2712.

[91] Hill, J. G.; Platts, J. A.; Werner, H.-J. *Phys. Chem. Chem. Phys.* **2006**, *8*, 4072–4078.

[92] Silvestrelli, P. L. *Phys. Rev. Lett.* **2008**, *100*, 053002.

[93] Tarnopolsky, A.; Karton, A.; Sertchook, R.; Vuzman, D.; Martin, J. M. L. *J Phys Chem A* **2008**, *112*, 3–8.

[94] Riley, K. E.; Vondrasek, J.; Hobza, P. *Phys. Chem. Chem. Phys.* **2007**, *9*, 5555.

[95] Grimme, S.; Antony, J.; Schwabe, T.; Mueck-Lichtenfeld, C. *Org. Biomol. Chem.* **2007**, *5*, 741.

[96] Grimme, S.; Mueck-Lichtenfeld, C.; Antony, J. *J Phys Chem C* **2007**, *111*, 11199–11207.

[97] Neese, F.; Schwabe, T.; Grimme, S. *J Chem Phys* **2007**, *126*, 124115.

[98] Grimme, S.; Neese, F. *J Chem Phys* **2007**, *127*, 154116.

[99] Grimme, S.; Steinmetz, M.; Korth, M. *J Chem Theory Comput* **2007**, *3*, 42–45.

[100] von Lilienfeld, O.; Tavernelli, I.; Rothlisberger, U.; Sebastiani, D. *Phys. Rev. Lett.* **2004**, *93*, 153004.

[101] Wu, X.; Vargas, M.; Nayak, S.; Lotrich, V.; Scoles, G. *J Chem Phys* **2001**, *115*, 8748–8757.

[102] Mooij, W.; van Duijneveldt, F.; van Duijneveldt-van de Rijdt, J.; van Eijck, B. *J Phys Chem A* **1999**, *103*, 9872–9882.

[103] Meijer, E.; Sprik, M. *J Chem Phys* **1996**, *105*, 8684–8689.

[104] Hobza, P.; Zahradnik, R. *Chem Rev* **1988**, *88*, 871–897.

[105] Kutzelnigg, W. *Journal of Molecular Structure: THEOCHEM* **1988**, *181*, 33–54.

[106] Helgaker, T.; Jorgensen, P.; Olsen, J. **2000**, 960.

[107] Moller, C.; Plesset, M. *Phys Rev* **1934**, *46*, 0618–0622.

[108] Bates, D. M.; Anderson, J. A.; Oloyede, P.; Tschumper, G. S. *Phys. Chem. Chem. Phys.* **2008**, *10*, 2775–2779.

[109] Bachorz, R. A.; Bischoff, F. A.; Hoefener, S.; Klopper, W.; Ottiger, P.; Leist, R.; Frey, J. A.; Leutwyler, S. *Phys. Chem. Chem. Phys.* **2008**, *10*, 2758–2766.

[110] Antony, J.; Grimme, S. *Phys. Chem. Chem. Phys.* **2006**, *8*, 7.

[111] Cerny, J.; Jurecka, P.; Hobza, P.; Valdes, H. *J Phys Chem A* **2007**, *111*, 1146–1154.

[112] Cammi, R.; Frediani, L.; Mennucci, B.; Tomasi, J.; Ruud, K.; Mikkelsen, K. *J Chem Phys* **2002**, *117*, 13–26.

[113] Chen, W.; Gordon, M. *J Chem Phys* **1996**, *105*, 11081–11090.

[114] Christiansen, O.; Mikkelsen, K. *J Chem Phys* **1999**, *110*, 8348–8360.

[115] Cossi, M.; Rega, N.; Scalmani, G.; Barone, V. *J Chem Phys* **2001**, *114*, 5691–5701.

[116] Giesen, D.; Gu, M.; Cramer, C.; Truhlar, D. *J Org Chem* **1996**, *61*, 8720–8721.

[117] Tomasi, J.; Mennucci, B.; Cammi, R. *Chem Rev* **2005**, *105*, 2999–3093.

[118] Tao, J.; Perdew, J.; Staroverov, V.; Scuseria, G. *Phys. Rev. Lett.* **2003**, *91*, 146401.

[119] Miertus, S.; Scrocco, E.; Tomasi, J. *Chemical Physics* **1981**, *55*, 117–129.

[120] Becke, A. D. *J Chem Phys* **1993**, *98*, 5648–5652.

[121] Dunning, T. *J Chem Phys* **1989**, *90*, 1007–1023.

[122] Klamt, A.; Jonas, V. *J Chem Phys* **1996**, *105*, 9972–9981.

[123] Bondi, A. *J Phys Chem-Us* **1964**, *68*, 441–&.

[124] Klamt, A.; Jonas, V.; Burger, T.; Lohrenz, J. *J Phys Chem A* **1998**, *102*, 5074–5085.

[125] Zimmerli, U.; Parrinello, M.; Koumoutsakos, P. *J Chem Phys* **2004**, *120*, 2693.

[126] Kubar, T.; Jurecka, P.; Cerny, J.; Rezac, J.; Otyepka, M.; Valdes, H.; Hobza, P. *J Phys Chem A* **2007**, *111*, 5642–5647.

[127] Ahlrichs, R.; Penco, R.; Scoles, G. *Chemical Physics* **1977**, *19*, 119–130.

[128] Hepburn, J.; Scoles, G.; Penco, R. *Chemical Physics Letters* **1975**, *36*, 451–456.

[129] Fortunelli, A.; Tomasi, J. *Chemical Physics Letters* **1994**, *231*, 34–39.

[130] Luque, F.; Bachs, M.; Orozco, M. *J. Comput. Chem.* **1994**, *15*, 847–857.

[131] Stefanovich, E.; Truong, T. *Chemical Physics Letters* **1995**, *244*, 65–74.

[132] Marenich, A. V.; Cramer, C. J.; Truhlar, D. G. *J Chem Theory Comput* **2008**, *4*, 877–887.

[133] Chiorescu, I.; Deubel, D. V.; Arion, V. B.; Keppler, B. K. *J Chem Theory Comput* **2008**, *4*, 499–506.

[134] Rappe, A.; Casewit, C.; Colwell, K.; Goddard, W.; Skiff, W. *J Am Chem Soc* **1992**, *114*, 10024–10035.

[135] Mu, W.-H.; Chasse, G. A.; Fang, D.-C. *Int. J. Quant. Chem* **2008**, *108*, 1422–1434.

[136] Cramer, C. J.; Truhlar, D. G. *Accounts Chem Res* **2008**, *41*, 760–768.

[137] Klamt, A.; Mennucci, B.; Tomasi, J.; Barone, V.; Curutchet, C.; Orozco, M.; Luque, F. J. *Accounts Chem Res* **2009**, *42*, 489–492.

[138] Cramer, C. J.; Truhlar, D. G. *Accounts Chem Res* **2009**, *42*, 493–497.

[139] Colominas, C.; LUQUE, F.; OROZCO, M. *J Phys Chem A* **1999**, *103*, 6200–6208.

[140] Podolyan, Y.; Gorb, L.; Leszczynski, J. *J Phys Chem A* **2002**, *106*, 12103–12109.

[141] Bende, A.; Suhai, S. *Int. J. Quant. Chem* **2005**, *103*, 841–853.

[142] Kratochvil, M.; Engkvist, O.; SPONER, J.; Jungwirth, P.; Hobza, P. *J Phys Chem A* **1998**, *102*, 6921–6926.

[143] Benassi, R.; Bertarini, C.; Hilfert, L.; Kempter, G.; Kleinpeter, E.; Spindler, J.; Taddei, F.; Thomas, S. *Journal of Molecular Structure* **2000**, *520*, 273–294.

[144] Benassi, R.; Bertarini, C.; Kleinpeter, E.; Taddei, F.; Thomas, S. *J Mol Struc-Theochem* **2000**, *498*, 201–215.

[145] Kleinpeter, E.; Schroth, W.; Pihlaja, K. *Magnetic Resonance in Chemistry* **1991**, *29*, 223–230.

[146] Neuvonen, H.; Fueloep, F.; Neuvonen, K.; Koch, A.; Kleinpeter, E. *J Phys Org Chem* **2008**, *21*, 173–184.

[147] Hinchliffe, A.; Mkadmh, A.; Nikolaidi, B.; Soscun, H. J.; Abu-Awwad, F. M. *Cent Eur J Chem* **2006**, *4*, 743–759.

[148] Puterova, Z.; Krutosikova, A.; Lycka, A.; Durcekova, T. *Molecules* **2004**, *9*, 241–255.

[149] Dahlqvis, K.; Forsen, S. *J Phys Chem-Us* **1965**, *69*, 4062–&.

[150] Bain, A.; Hazendonk, P. *J Phys Chem A* **1997**, *101*, 7182–7188.

[151] Baldridge, K. K.; Jonas, V.; Bain, A. *J Chem Phys* **2000**, *113*, 7519–7529.

[152] Little, T.; Qiu, J.; Durig, J. *Spectrochim Acta A* **1989**, *45*, 789–794.

[153] Monnig, F.; Dreizler, H.; Rudolph, H. *Z Naturforsch Pt A* **1965**, *A 20*, 1323–&.

[154] Abraham, R.; Siverns, T. *Tetrahedron* **1972**, *28*, 3015–&.

[155] Bertran, J.; Ortiz, E.; Balleste, L. *Journal of Molecular Structure* **1973**, *17*, 161–162.

[156] Marstokk, K.; Mollenda, H. *Journal of Molecular Structure* **1974**, *23*, 93–101.

[157] Casarini, D.; Lunazzi, L.; Macciantelli, D. *J Chem Soc Perk T 2* **1985**, 1839–1844.

[158] Lunazzi, L.; Placucci, G.; Chatgilialoglu, C.; Macciantelli, D. *J Chem Soc Perk T 2* **1984**, 819–822.

[159] Pethrick, R.; Wynjones, E. *J Chem Soc A* **1969**, 713–&.

[160] Gauss, J.; Cremer, D.; Stanton, J. *J Phys Chem A* **2000**, *104*, 1319–1324.

[161] Ju-Xiang, S.; Zheng-He, Z.; Duo-Hui, H.; Jun, W.; Xin-Lu, C.; Xiang-Dong, Y. *Chinese Phys* **2007**, *16*, 2650–2655.

[162] Kim, Y.; Gilje, J.; Seff, K. *J Am Chem Soc* **1977**, *99*, 7057–7059.

[163] Kerber, R. *J Org Chem* **1972**, *37*, 1587–&.

[164] Kerber, R.; Heffron, P. *J Org Chem* **1972**, *37*, 1592–&.

[165] Kaupp, G.; Dohle, J. *Angew Chem Int Edit* **1986**, *25*, 828–830.

[166] Leuenberger, C.; Hoesch, L.; Dreiding, A. *J Chem Soc Chem Comm* **1980**, 1197–1198.

[167] Magers, D.; Salter, E.; Bartlett, R.; Salter, C.; Hess, B.; Schaad, L. *J Am Chem Soc* **1988**, *110*, 3435–3446.

[168] Pye, C.; Vaughan, K.; Glister, J. *Can J Chem* **2002**, *80*, 447–454.

[169] Glukhovtsev, M.; Bach, R.; Laiter, S. *Int. J. Quant. Chem* **1996**, *62*, 374–383.

[170] Gimarc, B.; Trinajstic, N. *Pure Appl Chem* **1980**, *52*, 1443–1458.

[171] Kaupp, G.; Dohle, J.; Burger, K.; Rademacher, P.; Poppek, R. *J Phys Org Chem* **1988**, *1*, 267–273.

[172] Gleiter, R.; Sigwart, C.; Irngartinger, H.; Gries, S.; Marterer, W.; Klingler, O.; Prinzbach, H. *Tetrahedron letters* **1988**, *29*, 185–188.

[173] Gilchrist, T. L. **1969**.

[174] Chevallier, F.; Mongin, F. *Chem Soc Rev* **2008**, *37*, 595–609.

[175] Hilpert, H.; Hollenstein, R. *Helvetica chimica acta* **1986**, *69*, 136–140.

[176] Hilpert, H.; Hoesch, L.; Dreiding, A. *Helvetica chimica acta* **1987**, *70*, 381–389.

[177] Hilpert, H.; Hoesch, L.; Dreiding, A. *Helvetica chimica acta* **1986**, *69*, 2087–2097.

[178] Hilpert, H.; Hoesch, L.; Dreiding, A. *Helvetica chimica acta* **1987**, *70*, 390–395.

[179] Hilpert, H.; Dreiding, A. *Helvetica chimica acta* **1988**, *71*, 277–291.

[180] Klingler, O.; Prinzbach, H. *Angew Chem Int Edit* **1987**, *26*, 566–567.

[181] Marterer, W.; Fritz, H.; Prinzbach, H. *Tetrahedron letters* **1987**, *28*, 5497–5500.

[182] Irngartinger, H.; Kallfass, D.; Prinzbach, H.; Klingler, O. *Chem Ber* **1989**, *122*, 175–178.

[183] Nguyen, M.; Kaneti, J.; Hoesch, L.; Dreiding, A. *Helvetica chimica acta* **1984**, *67*, 1918–1929.

[184] Rajyaguru, I.; Rzepa, H. *J Chem Soc Perk T 2* **1987**, 359–363.

[185] Song, H.; Xiao, H.-M.; Dong, H.-S.; Huang, Y. *Journal of Molecular Structure: THEOCHEM* **2006**, *767*, 67–73.

[186] Alcami, M.; Depaz, J.; Yanez, M. *J. Comput. Chem.* **1989**, *10*, 468–478.

[187] Alcami, M.; Mo, O.; Yanez, M. *J Am Chem Soc* **1993**, *115*, 11074–11083.

[188] Alcami, M.; Mo, O.; Yanez, M. *J. Comput. Chem.* **1998**, *19*, 1072–1086.

[189] Alcami, M.; Mó, O.; Yáñez, M.; Alkorta, I.; Elguero, J. *Phys. Chem. Chem. Phys.* **2002**, *4*, 2123–2129.

[190] Schlegel, H.; Skancke, A. *J Am Chem Soc* **1993**, *115*, 7465–7471.

[191] Ebrahimi, A.; Deyhimi, F.; Roohi, H. *J Mol Struc-Theochem* **2001**, *535*, 247–256.

[192] Salter, E.; Hinrichs, R.; Salter, C. *J Am Chem Soc* **1996**, *118*, 227–228.

[193] Frisch, M. J. et al. *Gaussian, Inc.,* **2004**, *GAUSSIAN 03 (Revision C.02)*, year.

[194] Curtiss, L.; Redfern, P.; RAGHAVACHARI, K.; Rassolov, V.; Pople, J. *J Chem Phys* **1999**, *110*, 4703–4709.

[195] Koopmans, T. *Physica* **1934**, *1*, 104–113.

[196] Schleyer, P.; Maerker, C.; Dransfeld, A.; Jiao, H.; Hommes, N. *J Am Chem Soc* **1996**, *118*, 6317–6318.

[197] Schleyer, P.; Jiao, H.; Hommes, N.; Malkin, V.; Malkina, O. *J Am Chem Soc* **1997**, *119*, 12669–12670.

[198] Schleyer, P.; Manoharan, M.; Wang, Z.; Kiran, B.; Jiao, H.; Puchta, R.; Hommes, N. *Org Lett* **2001**, *3*, 2465–2468.

[199] Cernusak, I.; Fowler, P.; Steiner, E. *Molecular Physics* **2000**, *98*, 945–953.

[200] Wolinski, K.; Hinton, J.; Pulay, P. *J Am Chem Soc* **1990**, *112*, 8251–8260.

[201] Ditchfield, R. *J Chem Phys* **1972**, *56*, 5688–&.

[202] Stanger, A. *J Org Chem* **2006**, *71*, 883–893.

[203] Baldridge, K. K.; Greenberg, J. *J Mol Graphics* **1995**, *13*, 63–66.

[204] Bode, B.; Gordon, M. *J Mol Graph Model* **1998**, *16*, 133.

[205] Clar, E. J. **1972**, 128.

[206] Forni, A.; Garuti, G.; Moretti, I.; Torre, G.; Andreetti, G.; Bocelli, G.; Sgarabotto, P. *J Chem Soc Perk T 2* **1978**, 401–405.

[207] Bjorgo, J.; Boyd, D. *J Chem Soc Perk T 2* **1973**, 1575–1577.

[208] Bjorgo, J.; Boyd, D.; Campbell, R.; Thompson, N.; Jennings, W. *J Chem Soc Perk T 2* **1976**, 606–609.

[209] Sliwa, W. *Rocz Chem* **1976**, *50*, 667–676.

[210] Walker, W.; Weissler, G. *J Chem Phys* **1955**, *23*, 1540–1541.

[211] Meotner, M.; Nelsen, S.; Willi, M.; Frigo, T. *J Am Chem Soc* **1984**, *106*, 7384–7389.

[212] Foner, S.; Hudson, R. *J Chem Phys* **1978**, *68*, 3162–3168.

[213] Li, Z.; Moran, D.; Fan, K.; von Rague Schleyer, P. *J Phys Chem A* **2005**, *109*, 3711–3716.

[214] Hirsch, A.; Chen, Z.; Jiao, H. *Angew Chem Int Edit* **2001**, *40*, 2834–2838.

[215] Juselius, J.; Sundholm, D. *Phys. Chem. Chem. Phys.* **1999**, *1*, 3429–3435.

[216] Baldridge, K. K.; Siegel, J. *J Phys Org Chem* **2004**, *17*, 740–742.

[217] Matus, M. H.; Arduengo, A. J.; Dixon, D. A. *J Phys Chem A* **2006**, *110*, 10116–10121.

[218] Ritchie, J. *J Am Chem Soc* **1989**, *111*, 2517–2520.

[219] Splitter, J.; Calvin, M. *Tetrahedron letters* **1973**, 4111–4114.

[220] Bent, H. *J Inorg Nucl Chem* **1961**, *19*, 43–50.

[221] Rauk, A.; Allen, L.; Mislow, K. *Angew Chem Int Edit* **1970**, *9*, 400.

[222] Andose, J.; Lehn, J.; Mislow, K.; Wagner, J. *J Am Chem Soc* **1970**, *92*, 4050–&.

[223] Shorter, J. **1973**, 119.

[224] Zhao, M.; Gimarc, B. *J Phys Chem-Us* **1994**, *98*, 7497–7503.

[225] Karahodza, A.; Knaus, K.; Ball, D. *Journal of Molecular Structure: THEOCHEM* **2005**, *732*, 47–53.

[226] Marriott, S.; Reynolds, W.; Taft, R.; Topsom, R. *J Org Chem* **1984**, *49*, 959–965.

[227] Baldridge, K. K.; Siegel, J. *J Am Chem Soc* **1993**, *115*, 10782–10785.

[228] Efimov, V. *Nucl Phys A* **1973**, *A210*, 157–188.

[229] Suno, H.; Esry, B. D. *Phys Rev A* **2008**, *78*, 062701.

[230] Richard, J. *Few-Body Syst* **2006**, *38*, 79–84.

[231] Zhukov, M.; Danilin, B.; Fedorov, D.; Bang, J.; Thompson, I.; Vaagen, J. *Phys Rep* **1993**, *231*, 151–199.

[232] Cybulski, S.; Toczylowski, R. *J Chem Phys* **1999**, *111*, 10520–10528.

[233] Bressanini, D.; Morosi, G. *Phys. Rev. Lett.* **2003**, *90*, 133401.

[234] Bressanini, D.; Morosi, G. *Few-Body Syst* **2004**, *34*, 131–135.

[235] Cencek, W.; Jeziorska, M.; Akin-Ojo, O.; Szalewicz, K. *J Phys Chem A* **2007**, *111*, 11311–11319.

[236] Cencek, W.; Patkowski, K.; Szalewicz, K. *J Chem Phys* **2009**, *131*, 064105.

[237] Giese, T. J.; York, D. M. *Int. J. Quant. Chem* **2004**, *98*, 388–408.

[238] Giese, T. J.; York, D. M. *J Chem Phys* **2004**, *120*, 590.

[239] Ichihara, A.; Itoh, R. *B Chem Soc Jpn* **1990**, *63*, 958–960.

[240] Kim, Y. *Phys Rev A* **1975**, *11*, 796–803.

[241] Blume, D.; Greene, C.; Esry, B. *J Chem Phys* **2000**, *113*, 2145–2158.

[242] Chakravarty, C.; Hinde, R.; Leitner, D.; Wales, D. *Phys Rev E* **1997**, *56*, 363–377.

[243] Gonzalez-Lezana, T.; Rubayo-Soneira, J.; Miret-Artes, S.; Gianturco, F.; Delgado-Barrio, G.; Villarreal, P. *J Chem Phys* **1999**, *110*, 9000–9010.

[244] Bruch, L.; Novaro, O.; Flores, A. *J Chem Phys* **1977**, *67*, 2371–2374.

[245] Lim, T.; Duffy, K.; Nakaichi, S.; Akaishi, Y.; Tanaka, H. *J Chem Phys* **1979**, *70*, 4782–4785.

[246] Sandhas, W.; Kolganova, E.; Ho, Y.; Motovilov, A. *Few-Body Syst* **2004**, *34*, 137–142.

[247] Zhao, Y.; Truhlar, D. G. *J Chem Theory Comput* **2008**, *4*, 1849–1868.

[248] Hetzer, G.; Pulay, P.; Werner, H. *Chemical Physics Letters* **1998**, *290*, 143–149.

[249] Heyd, J.; Scuseria, G. *J Chem Phys* **2004**, *120*, 7274–7280.

[250] Schwabe, T.; Grimme, S. *Phys. Chem. Chem. Phys.* **2006**, *8*, 4398–4401.

[251] Tarini, M.; Cignoni, P.; Montani, C. *Ieee T Vis Comput Gr* **2006**, *12*, 1237–1244.

[252] Hamprecht, F.; Cohen, A.; Tozer, D. J.; Handy, N. C. *J Chem Phys* **1998**, *109*, 6264–6271.

[253] Wilson, P.; Bradley, T.; Tozer, D. J. *J Chem Phys* **2001**, *115*, 9233–9242.

[254] Keal, T.; Tozer, D. J. *J Chem Phys* **2005**, *123*, 121103.

[255] Boese, A.; Doltsinis, N.; Handy, N. C.; Sprik, M. *J Chem Phys* **2000**, *112*, 1670–1678.

[256] Boese, A.; Handy, N. C. *J Chem Phys* **2001**, *114*, 5497–5503.

[257] Miehlich, B.; Savin, A.; Stoll, H.; Preuss, H. *Chemical Physics Letters* **1989**, *157*, 200–206.

[258] Voorhis, T. V.; Scuseria, G. *J Chem Phys* **1998**, *109*, 400–410.

[259] Perdew, J.; Kurth, S.; Zupan, A.; Blaha, P. *Phys. Rev. Lett.* **1999**, *82*, 2544–2547.

[260] Perdew, J.; Tao, J.; Staroverov, V.; Scuseria, G. *J Chem Phys* **2004**, *120*, 6898–6911.

[261] Staroverov, V.; Scuseria, G.; Tao, J.; Perdew, J. *J Chem Phys* **2003**, *119*, 12129–12137.

[262] Staroverov, V.; Scuseria, G.; Tao, J.; Perdew, J. *J Chem Phys* **2004**, *121*, 11507–11507.

[263] Perdew, J. P.; Ruzsinszky, A.; Tao, J.; Csonka, G. I.; Scuseria, G. E. *Phys Rev A* **2007**, *76*, 042506.

[264] Su, P.; Li, H. *J Chem Phys* **2009**, *131*, 014102.

[265] Roothaan, C. *Rev Mod Phys* **1951**, *23*, 69–89.

[266] Piecuch, P.; Kucharski, S.; Kowalski, K.; Musial, M. *Comput Phys Commun* **2002**, *149*, 71–96.

[267] Bentz, J. L.; Olson, R. M.; Gordon, M. S.; Schmidt, M. W.; KENDALL, R. A. *Comput Phys Commun* **2007**, *176*, 589–600.

[268] Olson, R. M.; Bentz, J. L.; KENDALL, R. A.; Schmidt, M. W.; Gordon, M. S. *J Chem Theory Comput* **2007**, *3*, 1312–1328.

[269] Kowalski, K.; Piecuch, P. *J Chem Phys* **2000**, *113*, 18–35.

[270] Kowalski, K.; Piecuch, P. *J Chem Phys* **2000**, *113*, 5644–5652.

[271] de Lara-Castells, M.; Krems, R.; Buchachenko, A.; Delgado-Barrio, G.; Villarreal, P. *J Chem Phys* **2001**, *115*, 10438–10449.

[272] Feller, D.; Sordo, J. *J Chem Phys* **2000**, *112*, 5604–5610.

[273] Halkier, A.; Helgaker, T.; Jorgensen, P.; Klopper, W.; Koch, H.; Olsen, J.; Wilson, A. *Chemical Physics Letters* **1998**, *286*, 243–252.

[274] Martin, J. M. L. *Chemical Physics Letters* **1996**, *259*, 669–678.

[275] Martin, J. *Chemical Physics Letters* **1996**, *262*, 97–104.

[276] Martin, J. *Chemical Physics Letters* **1998**, *292*, 411–420.

[277] Martin, J. M. L.; Taylor, P. *J Chem Phys* **1997**, *106*, 8620–8623.

[278] Nyden, M.; Petersson, G. *J Chem Phys* **1981**, *75*, 1843–1862.

[279] Peterson, K.; Dunning, T. *J Phys Chem A* **1997**, *101*, 6280–6292.

[280] Peterson, K.; Woon, D.; Dunning, T. *J Chem Phys* **1994**, *100*, 7410–7415.

[281] Petersson, G.; Bennett, A.; Tensfeldt, T.; Allaham, M.; Shirley, W.; Mantzaris, J. *J Chem Phys* **1988**, *89*, 2193–2218.

[282] Petersson, G.; Frisch, M. *J Phys Chem A* **2000**, *104*, 2183–2190.

[283] Petersson, G.; Yee, A.; Bennett, A. *J Chem Phys* **1985**, *83*, 5105–5128.

[284] Schwartz, C. *Phys Rev* **1962**, *126*, 1015–&.

[285] Truhlar, D. G. *Chemical Physics Letters* **1998**, *294*, 45–48.

[286] Wilson, A.; Dunning, T. *J Chem Phys* **1997**, *106*, 8718–8726.

[287] WOON, D.; Dunning, T. *J Chem Phys* **1994**, *100*, 2975–2988.

[288] Martin, J. M. L. *Chemical Physics Letters* **1996**, *259*, 679–682.

[289] Jansen, H. B.; Ros, P. *Chemical Physics Letters* **1969**, *3*, 140–143.

[290] Johnson, E. R.; Becke, A. D.; Sherrill, C. D.; Dilabio, G. A. *J Chem Phys* **2009**, *131*, 034111.

[291] Johnson, E.; Wolkow, R.; DiLabio, G. *Chemical Physics Letters* **2004**, *394*, 334–338.

[292] Singh, N. J.; Min, S. K.; Kim, D. Y.; Kim, K. S. *J Chem Theory Comput* **2009**, *5*, 515–529.